CHAPTER SIX

MODTRAN SIMULATIONS

6.1 Motivation

The main objectives of this chapter are to use the atmospheric modelling program MODTRAN to:

1- Illustrate some of the general aspects and dominant features of the clear sky infrared (IR) spectral radiance and show the importance of some emission processes and the effect of changing zenith angles. Overcast IR spectra will also be shown.

2- Investigate the influence of some of the atmospheric parameters on the spectral distribution of the thermal IR from clear skies, and determine their impact on the IR clear sky temperatures. These, according to their importance, are screen level temperature, the precipitable water vapor PWV, aerosol type and altitude of the site.

3- Investigate the wavelength response of the IR cloud detectors whose data are used in this project. In the early days of using the cloud monitors, it was thought that 17 μm was the upper limit for both the detectors and the lens assemblies.
4- Use MODTRAN, with its standard atmospheric profiles, to assess the compatibility of the measured sky temperatures with those generated by MODTRAN.
5- Use MODTRAN, with appropriate real radiosonde atmospheric profiles for Adelaide, to assess the applicability and the validity of the proposed clear IR sky temperature formulae, observationally derived in the previous chapters, firstly at the zenith, and then at different zenith angles.

This chapter is divided into three main parts. MODTRAN software will be introduced in the first part, section 6.2. This will include an overview of the package, its method of calculation, and its main features, which will discuss the required information and program cards for a desired run. In the second part, section 6.3, the methodology of running MODTRAN with an appropriate input, preferred outputs and the method of converting these outputs to get the desired temperatures will be given. The last part is the result section; this will be divided to many subsections according to the various investigations.

6.2 MODTRAN Software

6.2.1 Overview

MODTRAN is a "Moderate Resolution Transmission" program calculating atmospheric radiance/transmittance at a moderate resolution. MODTRAN is one of a number of atmospheric radiation algorithms developed by the U.S. Air Force Research Laboratory (AFRL) program beginning in the early 1970's. Some other important ones are LOWTRAN 2 (Selby *et al.* 1972), LOWTRAN 3 (Selby. and McClatchey 1975), LOWTRAN3B (Selby, Shettle and McClatchey 1976), LOWTRAN 4 (Selby *et al.* 1978), LOWTRAN 5B (Robertson *et al.* 1981), LOWTRAN 5 (Kneizys *et al.* 1983), LOWTRAN 6 (Kneizys *et al.* 1983), LOWTRAN7 (Kneizys, 1988) and MODTRAN (Berk *et al.* 1989). Each of the developed version of these codes is a modified version

of the previous one. In each newly modified version more features and upgrades are added to overcome limitations found in the previous one. MODTRAN itself also went through some upgrades to its first versions developed 1989. The original MODTRAN2 code and the upgrades of following MODTRAN versions, including the version used in this study, have been discussed in many articles e.g. Anderson. (1993), Acharya *et al*.(1993), Berk.(1995), Berk. (1996) and Berk *et al.* (1998). Details of these upgrades are covered in Abreu and Anderson, (1996). MODTRAN has been used in various applications and studies, including atmospheric science, environmental hazards, military ecology, remote sensing and energy deposition, Wang *et al* (2002). It is one of the most successful radiative transport models.

The MODTRAN program is a computationally rigorous radiation transfer algorithm that is used to calculate the spectral absorption, transmission, emission and scattering characteristics of the atmosphere for wavelengths extending at moderate resolution from thermal infrared (IR) through the visible and into the ultraviolet. The spectral resolution of MODTRAN is 2 cm^{-1} in averaged steps of 1 cm^{-1}, in comparison to LOWTRAN 7, which has a resolution of 20 cm^{-1} in average steps of 5 cm^{-1} (Anderson *et al* 1995). MODTRAN is two-parameter equivalent-width band model (Molecular absorption coefficient calculated as a function of line strength and line half-width) that employs large pre-stored spectral databases. The parameters are derived directly from the HITRAN database from heights of 0 to 120 km. The HITRAN database includes spectral information for more than one million spectral lines for 13 minor and trace species (Rothman *et al*. 1992 and Rothman *et al*. 2003). These include water vapor, carbon dioxide, nitrous oxide, carbon monoxide, methane, oxygen, nitric oxide, sulfur dioxide, nitrogen dioxide and nitric acid.

The current version of MODTRAN used in this study, MODTRAN 4 version3 Revision1 (Mod4v3r1) uses a HITRAN 2k database, (Berk *et al*. 1999). This version of MODTRAN encompasses all the capabilities of previous versions of LOWTRAN and MODTRAN. However, many upgrades have been added in order to facilitate accurate calculations with higher resolutions and higher speeds. A technical description of the MODTRAN approach of calculations and the recent upgrades can be found in any MODTRAN report. (e.g. MODTRAN 4 version 3 revision 1 report Berk *et al*. 1999)

The MODTRAN package includes six cloudless standard atmospheres representing average seasonal and latitudinal variations of atmospheric properties. MODTRAN also allows the user to define an atmospheric profile (e.g. radiosonde data) with any specific

set of parameters. The MODTRAN package includes several parameters to define the aerosol background. Several aerosol types are available e.g. rural, urban, desert, Navy and fogs. Clouds, their types and properties, can be defined. The geometry of lines-of-sight between the observer and the target can also be specified. Solar and lunar source functions and scattering (Rayleigh, Mie, single and multiple) and default profiles can be chosen.

6.2.2 Radiation Transfer and MODTRAN Approach of Calculations

MODTRAN formulations, approximations and methods of calculating the atmospheric radiance are similar to those summarized in section 2.8 and discussed in more details in many references; see for example McClatchy *et al*.(1970), McClatchy *et al.* (1972).
The basic approach in MODTRAN is to approximate the atmosphere as a sequence of homogeneous layers, for which each layer's radiance contribution from each of the source terms is considered. Spectroscopic information for each spectral line, needed to calculate the absorption coefficient for a spectral line, at standard pressure and temperature are derived from the HITRAN database. For each layer the absorption coefficient parameters are then adjusted for the pressure and temperature variations. The absorption coefficients obtained for each atmospheric constituent are then multiplied by the amount of absorber for each layer to get the optical depth. The optical depth of that layer is then converted to transmission through that layer. The total transmittance is obtained as the product of the full-path individual species transmittance, along with the transmittance associated with scattering attenuation and continuum. Finally, MODTRAN calculates the total radiance accounting for all the source terms with aid of the radiation transfer equation, Selby *et al.* (1972).

6.2.3 MODTRAN Input/Output

An attempt has been made in MODTRAN4 to make it easier for the users to keep track of input and output (I/O) files, Berk *et al*. 1999. This includes easier ways of handling input and output files than in previous versions of MODTRAN.
A single input text file known as *tape5* controls MODTRAN. This file contains the data and parameters that MODTRAN needs to run. Within the tape5 file there are six *required* "cards" (fig 6.1) input lines and a few *optional* sub-cards, which are not shown

in the main card. The required cards contain either letters or numbers (floating or integer), which assign different values or trigger different models in MODTRAN. Except when specifying file names, character inputs are case insensitive. Also, blanks are read as zeroes for numerical inputs, and as default values otherwise.

Each card or sub-card in tape5 handles a different aspect of the atmosphere or MODTRAN itself. MODTRAN models the atmosphere as a set of homogenous layers. The characteristics of these layers are either pulled from several internal model atmospheres (urban, rural. etc) or can be characterized by radiosonde data collected from a specific atmosphere.

The output of MODTRAN is several text "tape" files, which describe the details for the atmosphere modelled during the run (sun location, meteorological descriptions, concentrations of aerosols, etc.) and the spectral behaviour of the atmosphere

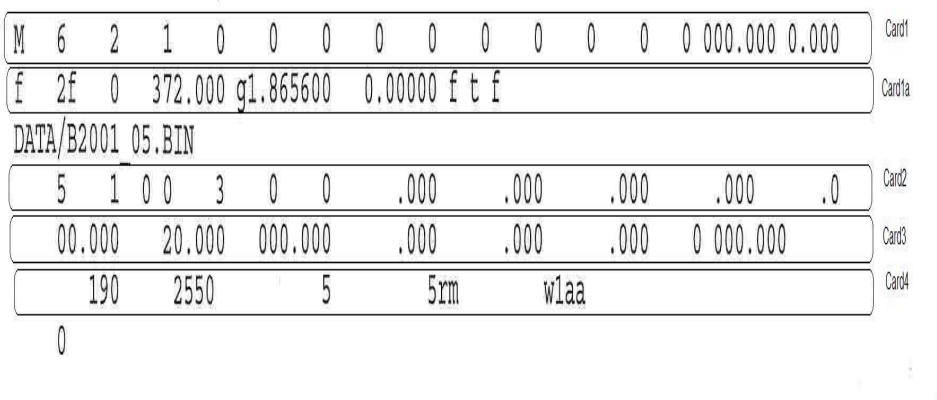

Figure 6. 1: MODTRAN's input. A typical example of Tape5 file shows the required six cards that control MODTRAN.

A primary one is the tape7 file, which contains all of the spectral data. It has data at the specified resolutions and the results of the convolutions with the slit function specified in card4. MODTRAN also produces a tape6 file, which helps in diagnosing and locating errors. It records the individual components of the tape5 file and analyzes them. It also reports the procedures MODTRAN goes through and gives details of the individual atmospheric profiles for different species. The tape6 file is a huge file. However, if MODTRAN crashes at the end of this file it can be easy to find where and why it crashed. Total integrated atmospheric radiance and transmission of the run over specific wavelengths and resolutions are also found in this file. Sets of "pltout" and

other types of files are also produced. The plotout file contains the value of the radiance or the transmittance with a corresponding wavelength or frequency. The file has a great importance in this study since its output was used for further analysis to plot the spectral distribution and deduce the sky temperature.

6.2.4 Required MODTRAN Cards

A brief summary for each of the six main required cards will be given in this sub-section. These are card1, card1a, card2, card3, card4 and card5. The main inputs needed in these cards and required in this study will be given. For a complete coverage for all the cards and their detailed formats and options see Berk *et al*. (1999).

Card1

In card 1 options for running MODTRAN can be selected. For example, the band model algorithm used for the radiative transport. For an atmospheric model, one of the six geographical seasonal model atmospheres, or specified user meteorological radiosonde data, can be used. For a user-defined atmosphere other optional cards are required. The geometry type and mode of executing the program can be chosen. Output preferences (either transmission or radiance or both), with or without multiple scattering, can be defined. Specific profiles for temperature and pressure for molecular gases and 13 heavy molecules can be selected.

In this project, the MODTRAN band model was selected. MODTRAN was then run with slow speed for a slant path between two heights and executed without multiple scattering in spectral thermal radiance. All available standard atmospheres in this version of MODTRAN were used. In addition, radiosonde profiles for Adelaide were used and triggered. In this case, an additional 2C card is required for additional required inputs. The rest of the options in this card were left at the default values.

Card 1a

This card enables the selection of multiple scattering options, the scaling of molecular profiles, customizing of the top-of atmosphere (TOA), trigger specification of data files, and scaling of the solar irradiance and solar constant. Manipulation of water vapor,

ozone gas column amounts and the carbon dioxide CO_2 mixing ratio can be defined. Some preliminarily sensor characteristics can be selected here.

Most of the parameters were set to the default values, including the ozone O_3. Carbon dioxide CO_2 was set to the recently reported value for Adelaide 372 ppmv, while the amount of water vapor column (PWV), in g/cm^2, was varied for each run of MODTRAN as will be illustrated later.

Card2

This card deals with the main aerosol profiles presented in the atmosphere, and cloud options. A seasonal dependence of the profiles for both the tropospheric (2 to 10 km) and stratospheric (10 to 30 km) aerosols can be chosen. Options to select both the profile and extinction types for the stratospheric aerosols, and to determine transition profiles through the stratosphere to 100 km, exist in this card. Cloud options, types, density of clouds and precipitation rate can be controlled here. Card 2 has many optional cards that must be specified when related options in this card or other cards are triggered.

An urban extinction aerosol model without background stratospheric extinction with different visibilities was used here. MODTRAN was also run for clear skies; in this case cloud options were not triggered. The rest of the options in this card were left unused.

Card3

Card3 controls the geometry of the sensor–target relationship for a given problem. For example the initial and final height of the sensor and the target, and the viewing angle are required here.

Firstly at the zenith, and then at different zenith angles, MODTRAN was run in upward looking mode between two altitudes. H1 was set to a ground level and H2 was set to 25 km. The radius of the earth and the other options in this card were set to default values. As in card 2, card 3 has many other optional cards. These were left at the default values.

Card4

This card specifies the spectral characteristics of the given problem and allows the user to choose the desired spectral range, resolutions, and frequency/wavelength increments of the output using the desired slit function. The spectral response was obtained at spectral resolution of 10 cm^{-1} with 10 cm^{-1} full width at half maximum (FWHM) across the spectral range of 190-2550 cm^{-1}.

Card5

This card is used if there is a series of runs to be done for later comparisons.

A summary of required inputs used in this study are given in table (6.1) and will be discussed in detail in the following section.

6.3 Methodology

The methodology of the simulations conducted here using MODTRAN consists of four steps.

1. We choose the desired atmospheric profile and the required main inputs.
2. Run MODTRAN for the chosen profile and specific input.
3. Process the MODTRAN outputs with an appropriate code.
4. Do the desired investigations and statistical assessment of the output.

In the following subsections each one of the other four steps will be discussed separately.

6.3.1 Atmospheric Profiles

6.3.1.1 Standard Atmospheric profiles

The MODTRAN package includes six cloudless standard atmospheres each defined by temperature, pressure, density, and mixing ratios for H_2O, O_3, CH_4, CO and N_2O as a function of altitude. These are Tropical (Trop.), mid-latitude summer (MLS), mid-latitude winter (MLW), sub-Arctic summer (SAS), sub-Arctic winter (SAW), and 1976 US standard (US). Each atmosphere contains 34 layers with specified properties between the earth surface and 100 km altitude (Skatviet *et al*. 2002). In this study, the maximum height set was 25 km. There are two reasons for this selection. Firstly, most of the IR radiation originates in the lower atmosphere (see section 2.2). Hence if heights greater than 25 km are used the contributions from the upper atmosphere will be negligible. Secondly, the maximum height of measurements reached by the radiosonde itself was 25 km, hence for creating the Adelaide profiles (see next section) a consistent height between the standard atmospheres and the created atmosphere must be identically chosen. The standard atmospheres were also used to investigate the response of the cloud monitors. Fig (2.2) in chapter 2 shows an example of the temperature profiles of six standard atmospheres provided by MODTRAN.

6.3.1.2 Adelaide Profiles

The proposed IR formulae found in the previous chapters could be tested accurately if ground level parameters could be varied for every run of MODTRAN, along with the availability of representative upper air atmospheric profiles.

Due to the difficulties of having all the radiosonde data available at all times, reasonable radiosonde profiles were created and were used as approximations to the atmospheric conditions over Adelaide.

In this study, data from the available clear-night meteorological balloon launches from Adelaide Airport were used to define the pressure, temperature, and relative humidity profiles over Adelaide. These radiosonde data were averaged over the months of December to February and assumed to be a good representation of atmospheric

conditions during summer over Adelaide. Similarly, radiosonde data for the period between June and September were averaged and assumed to be representative of observing conditions in winter over Adelaide. Fig (6.2) shows the temperature, water vapor mixing ratio and relative humidity profiles over Adelaide.

These interpolated profiles were used as inputs into MODTRAN, as user defined atmosphere models. Since the MODTRAN model can only have a maximum of 34 levels the data were chosen to create curves that can reasonably present the radiosonde data (up to 25 km). The difference in height between one layer and the subsequent one did not exceed 100 meters from the ground to the first kilometer. Above that a 1 km difference between two layers was used.

The profiles for other atmospheric constituents (CH_4, CO, O_2, NO…. etc) were set to those from the MODTRAN standard MLS model, which was assumed to be close to the conditions at Adelaide in both seasons.

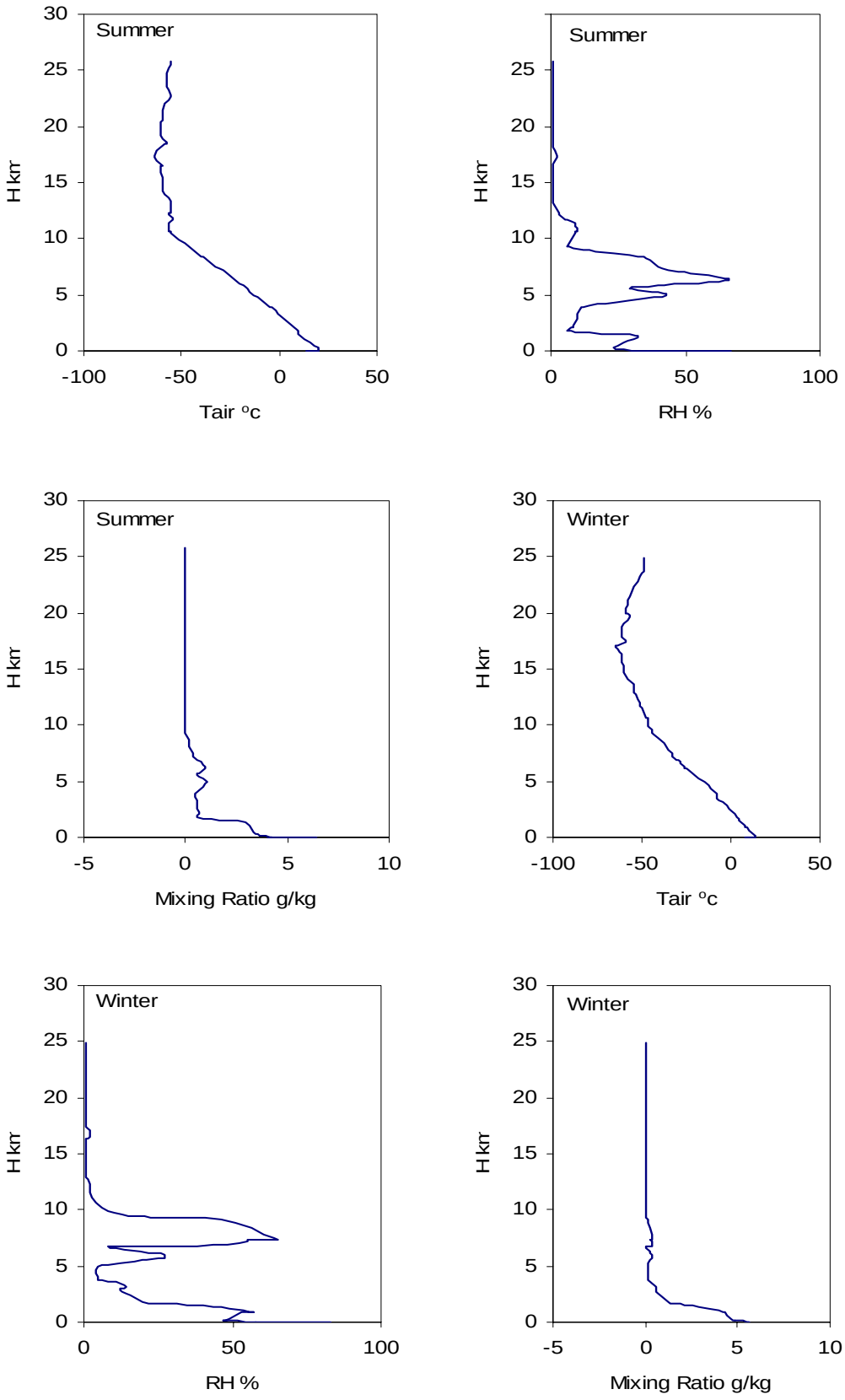

Figure 6. 2: Assumed atmospheric profiles over Adelaide showing the temperature relative humidity and the water vapour mixing ration as a function of altitude for both summer and winter conditions.

6.3.1.3 General inputs

All the primary atmospheric information needed for the desired calculations of the IR clear sky temperatures with MODTRAN mentioned in section (6.2.4) are summarized in table (6.1). These inputs can be divided into four classes.

1. Parameters never used in this project: Their values were left blank or set to zero.
2. Parameters that are used in this project and their values were set only once: These are the MODTRAN band model, the geometry type between two altitudes, executing MODTRAN without multiple scattering, choosing radiance as an output and run MODTRAN for nighttimes only with cloudless atmospheres.
3. Parameters, which were used for specific purposes. The values of these parameters were varied as their effects were studied. For example, the aerosol types and the PWV were set at fixed values when investigating the zenith angle distributions. On the other hand, at fixed zenith angle the PWV was changed every time to investigate the effect of the PWV. Also, different standard atmospheres were run for different amounts of PWV and for different zenith angles. To study the effect of altitude on sky temperature the altitude of the observer was also changed to different values.
4. For a user-defined atmosphere card 2C was triggered. In this case, the number of layers must be entered and the values of pressure, temperature, and relative humidity at each level must be defined.
5. Fig (6.3) is an example of the winter atmospheric profile input card.

Card #	Column	Variable Name	Value of Variable	Does What
1	1	MODTRAN	0	Selects MODTRAN
	5	MODEL	1-7	6 standard atmosphere plus the Adelaide profile
	10	ITYPE	2	Slant path between altitudes
	15	IEMSCT	0	Radiance mode of calculations
	20	IMULT	0	No multiple scattering
	25-50	M1-M6	0	Reset to "MODEL"
1a	20	CO2MX	370 ppmv	CO_2 mixing ratio in ppmv.
	30	H2OSTR	Varies each run	Vertical water vapor column
	40	O3STR	0 default	Vertical ozone column
2	1	APLUS		modify aerosol profiles
	5	IHASE	1-9	Use different aerosol profiles
	10	ISEASON	1	Spring-Summer , Winter-fall
	15	IVULCAN	2	No volcanic profile
	71-80	GNDALT	0.272	Altitude of surface to S.L.
2c	5	ML	30	No. of radiosonde layers to be read
	1-10	ZMDL(i)	for i=1,ZMLD(1)= 0.272	Altitude (km)
	11-21	P(i)	for i=1, P(1)=976.	Pressure in mb
	21-30	T(i)	for I=1, T(1)=17.9	Temperature in ^{o}c
	31-40	WMOL(1)(i)	for I=1, WHOL(1)(1)=77.	Water in relative humidity units
	61	JCHAR(1)	A	Pressure in mb
	62	JCHAR(2)	B	Temperature in deg Celsius
	63	JCHAR(3)	H	Relative Humidity in %
3	1-10	H1	0	Initial altitude (km)
	11-20	H2	24	Final Altitude (km)
	21-30	ANGLE	0-90	Vary the zenith Angle
	51-60	RO	0.	Default to nominal radius.
4	1-10	V1	190	Initial Frequency cm^{-1}
	11-20	V2	2550	Final Frequency cm^{-1}
	21-30	DV	20	Frequency Increment
	31-40	FWHM	5	Slit function Full Width at Half Maximum.
	41	YFLAG	r	Radiance in output
	42	XFLAG	m	Wavelength in microns; radiances in $W/sr/cm^2/\mu m$.
5		IRPT	0	STOP program.

Table 6. 1: Explains the primary atmospheric inputs and its MODTRAN card and column, its corresponding value and what it does.

```
M   7    2    1    0    0    0    0    0    0    0    0    1    0 000.000 0.00
f   2f   0   372.000 g0.888000   0.00000 f t f
DATA/B2001_05.BIN
    5    2    0    3    0    0  05.00000   0.00000   0.00000   0.00000   0.000
   29    0    0
     0.085  1022.300    13.200    56.000     0.000     0.000ABH2222222222222
     0.124  1004.600    12.100    41.000     0.000     0.000ABH2222222222222
     0.572   952.100     9.500    33.000     0.000     0.000ABH2222222222222
     1.026   901.000     5.600    55.000     0.000     0.000ABH2222222222222
     1.500   849.700     3.000    11.000     0.000     0.000ABH2222222222222
     2.043   794.500     1.000     8.000     0.000     0.000ABH2222222222222
     3.005   704.100    -3.300     7.000     0.000     0.000ABH2222222222222
     4.044   616.700    -9.300     5.000     0.000     0.000ABH2222222222222
     5.061   539.400   -17.200    10.000     0.000     0.000ABH2222222222222
     6.067   470.700   -23.000     8.000     0.000     0.000ABH2222222222222
     7.066   409.700   -32.200    24.000     0.000     0.000ABH2222222222222
     8.069   355.200   -35.500     3.000     0.000     0.000ABH2222222222222
     9.000   310.200   -42.100     3.000     0.000     0.000ABH2222222222222
    10.024   266.500   -42.000     2.000     0.000     0.000ABH2222222222222
    11.005   230.700    42.000     1.000     0.000     0.000ABH2222222222222
    12.022   198.300   -46.000     1.000     0.000     0.000ABH2222222222222
    13.058   169.300   -52.700     1.000     0.000     0.000ABH2222222222222
    14.014   145.800   -56.700     1.000     0.000     0.000ABH2222222222222
    15.032   124.000   -59.300     1.000     0.000     0.000ABH2222222222222
    16.022   105.700   -64.500     1.000     0.000     0.000ABH2222222222222
    17.025    89.500   -68.800     1.000     0.000     0.000ABH2222222222222
    18.025    75.800   -68.800     1.000     0.000     0.000ABH2222222222222
    19.009    64.400   -61.900     1.000     0.000     0.000ABH2222222222222
    20.037    54.500   -63.000     1.000     0.000     0.000ABH2222222222222
    21.031    46.500   -59.400     1.000     0.000     0.000ABH2222222222222
    22.050    39.500   -56.400     1.000     0.000     0.000ABH2222222222222
    23.023    33.900   -56.300     1.000     0.000     0.000ABH2222222222222
    24.037    28.900   -54.300     1.000     0.000     0.000ABH2222222222222
    24.551    26.700   -52.500     1.000     0.000     0.000ABH2222222222222
    00.000    20.000   000.000         0         0         0                 0
       190     2550.        20         8rm           w1aa
    0
```

Figure 6. 3: Example of a MODTRAN input card for an Adelaide winter profile.

6.3.2 Running MODTRAN

Having chosen all the appropriate atmospheric profiles with the desired parameters selected, MODTRAN is now ready for running. MODTRAN was run using the command Mod34.f. The output from MODTRAN is now ready for the purpose of aimed investigations. Tape6 and Plotout files were the two important output files used in this study. The first was investigated after each run to check that MODTRAN was

correctly running the specified inputs and was also used to diagnose any odd or any unreasonable output. The Plotout file is the main file used for plotting and calculations.

The outputs were generally used either to *investigate the spectral distributions* of the atmosphere when one or more atmospheric variables were changed or to *calculate the integrated sky temperature* of a specific run for further assessments and comparisons. For the former we only need to plot the output radiance against wavelength using appropriate plotting software. However, for the latter, several steps need to be done and these will be the topic of the following subsection.

6.3.3 Procedures for Sky Temperatures Calculations from MODTRAN

MODTRAN calculates thermal infrared radiation for a desired wavelength interval and resolution, and outputs the calculated atmospheric spectral radiance R in (watt / (str.cm^2.µm)).

A *Mathematica* algorithm was designed to interface with the MODTRAN output file, *Plotout*, and plot the radiance as a function of wavelength. This step was employed to test the spectral distribution of the run and it then calculates the final sky temperature. The calculation of the sky temperature from MODTRAN output with Mathematica algorithm involves:

1- Integrating over a spectral interval to get the total radiance between the desired wavelength ranges, see equation (6.1) below. For example for the G15 cloud monitor the broadband radiance was calculated between 6.6 µm and 17 µm, and also for 6.6 and 50 µm.

$$R = \int_{\lambda_1}^{\lambda_2} R \; d\lambda \qquad \text{(Watt / (str.cm}^2\text{))} \tag{6.1}$$

2- Integrating equation (6.1) over the sky dome.

3- By assuming the atmosphere as a uniform blackbody having a uniform temperature, T_{sky}, and using the Stefan Boltzman law,

$$\sigma \, T_{sky}^{4} = R_{total} \Rightarrow T_{sky} = \frac{R}{\sigma} \quad (6.2)$$

The total integrated radiance for the specific wavelength interval is thus converted to a temperature, which is conventional for the purposes of investigations and comparisons conducted in this study.

The Mathematica algorithm was usually interfaced to the output of each MODTRAN run.

The results presented in the following are divided into two main sections. The study of the IR spectra and the key factors that affect these spectra will be discussed in section (6.4). Comparisons between MODTRAN simulated temperatures and those measured by the cloud monitor and those predicted by the models proposed in the previous chapters will be discussed in section (6.5).

6.4 Initial Results (Spectra and Investigations)

6.4.1 Typical IR Atmospheric Spectra

6.4.1.1 At the Zenith

The typical clear sky spectral distribution of energy emitted by the atmosphere at the zenith for clear nights in the region of 5μm - 50 μm, for mid-latitude summer profile is shown in fig (6.4).

The main features of the IR atmospheric emission obtained from the figure can be summarized as follows:

1- The atmosphere emits as a blackbody at the ground level temperature below 7.6 μm, between 14 μm and 16 μm, and beyond 22 μm. Water vapor, H_2O, is the main absorber and emitter in these wavelengths.

2- A wide band of absorption/emission from 13μm and 17 μm is due to carbon dioxide, CO_2.

3- Ozone O_3 absorption/emission is peaked at 9.6 μm. It is formed by photochemical reactions, and occurs mainly between 10 and 30 km altitudes. Its emission is largely limited to a narrow spectral interval. Hence the total

thermal IR radiation reaching the ground level is not greatly influenced by ozone variations.

4- A weak band of absorption/emission at 7.6 µm due to methane, CH_4.

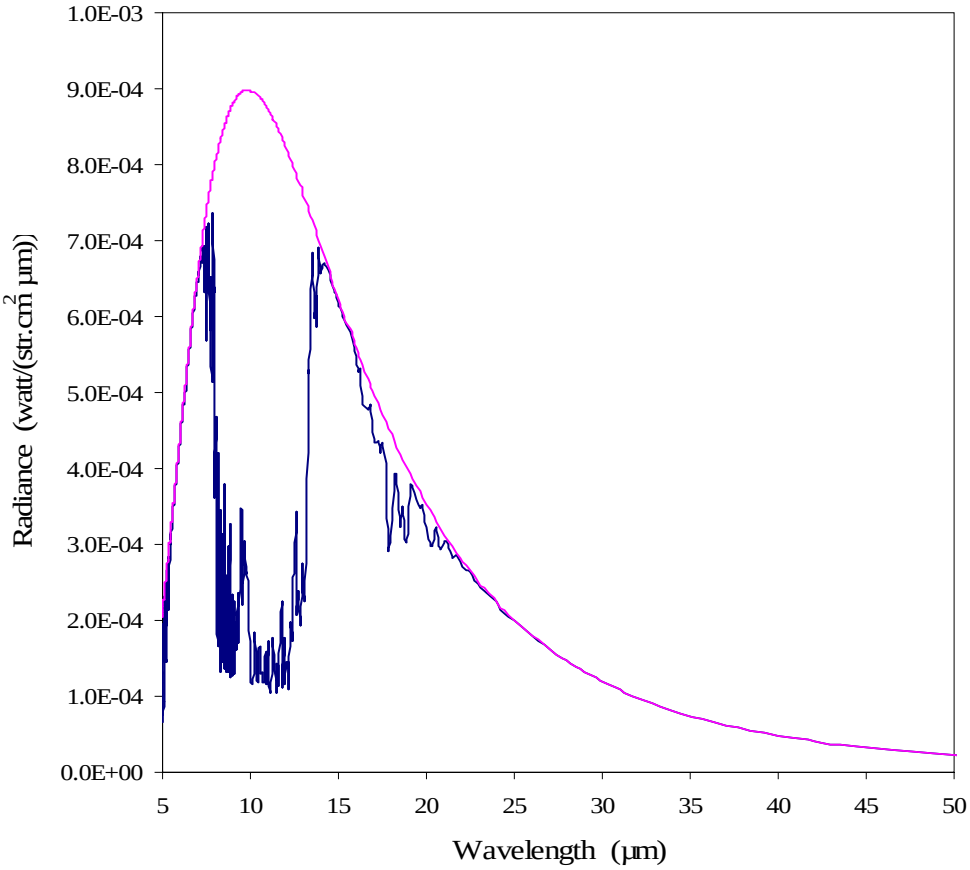

Figure 6. 4: Shows an example of MODTRAN output for IR clear sky spectrum (blue curve) superimposed by a black body curve (pink curve) at air temperature for a typical MLS profile with T_{air} =21 ^{o}C, RH = 75.9 % and PWV = 1 cm.

5- Relatively little energy is emitted by the atmosphere in the "atmospheric window" extending from 8 µm to 13µm. This background emission has not yet been explained. One of the most acceptable proposed reasons that this emission is due to the wings of water vapor and carbon dioxide bands, Ayotte *et al.*(1999). Idso (1981) has pointed that the water dimer is another possible explanation for this emission. However, the purpose of this thesis is not to do further investigations in this regard.

6.4.1.2 At Different zenith Angles

Fig (6.5) shows the clear sky spectrum obtained at different zenith angles for the mid-latitude summer profile.

The most observable spectral change observed in these curves is the increase in the sky emission in the atmospheric window as the zenith angle increases. This increase is due to increasing the amount of the atmosphere (optical path) as one moves toward the horizon where the system reaches that of a black body. Also, it is clear that the effect of the ozone emission increases as the elevation angle increases.

Figure (6.6) shows a plot of the simulated sky temperature, for two different wavelength bands 6.6 μm to 17 μm and 6.6 μm to 50 μm, along with measured sky temperatures from a G15 detector, as a function of the logarithm of the secant of the zenith angle from the zenith to 87^{o}. Adelaide summer profile was used as input to MODTRAN for this simulation. At each zenith angle the simulated temperature was obtained by integrating the area under the spectral distribution curve e.g. fig (6.5) for that angle (see Mathematica procedures) and for the desired wavelength bands. Two important facts can be noted from this figure. Firstly, for either wavelength range the sky temperatures increase monotonically as one moves toward larger air masses and this variation is almost linear with the logarithm of the air mass as we have established experimentally in chapter5. Secondly, the 6.6 μm to 50 μm sky temperatures are very close to the measured temperatures. The maximum difference between the measured and 6.6 μm to 50 μm simulated temperatures was 1.6 ^{o}C. On the other hand, a difference of 40 ^{o}C can be noticed between the measured and the simulated sky temperatures for 6.6 μm to 17 μm wavelength bands. This evidence along with others found in the following sections will help us to draw a final conclusion about the upper limit of the wavelengths of the detectors.

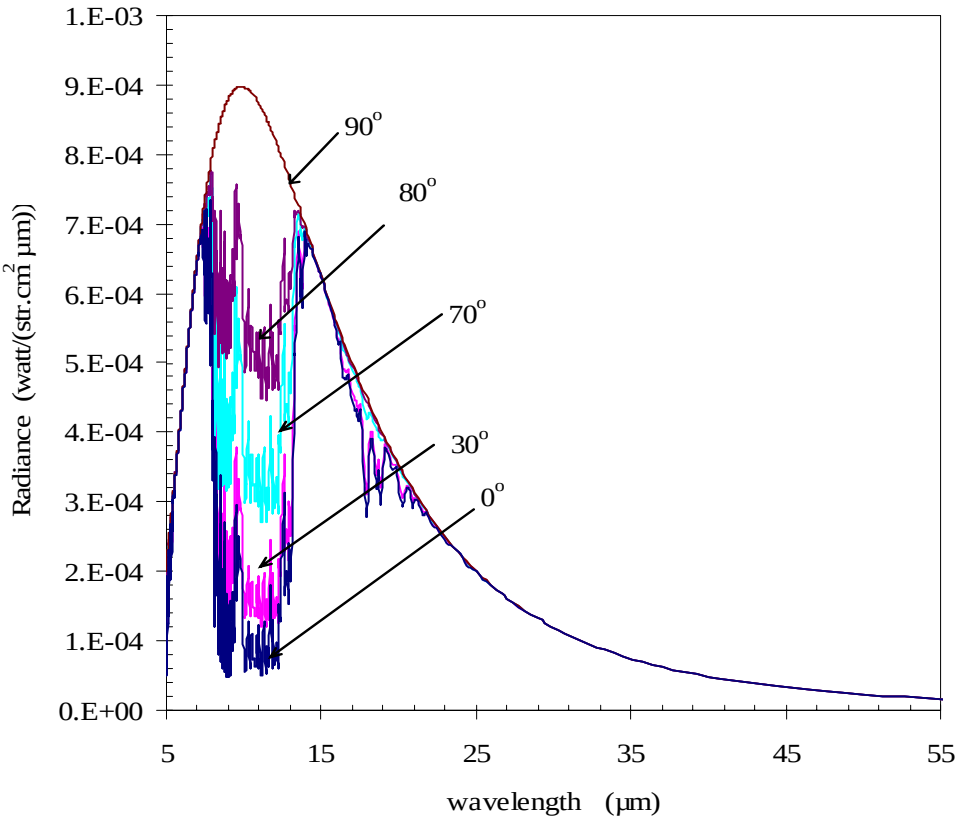

Figure 6. 5: Shows IR clear sky radiance of typical MLS profile with Tair = 21 °C, RH = 75.9 % and the PWV = 1 cm for zenith angles of 0° (zenith),30°, 70°, 80° and 90°(horizon).

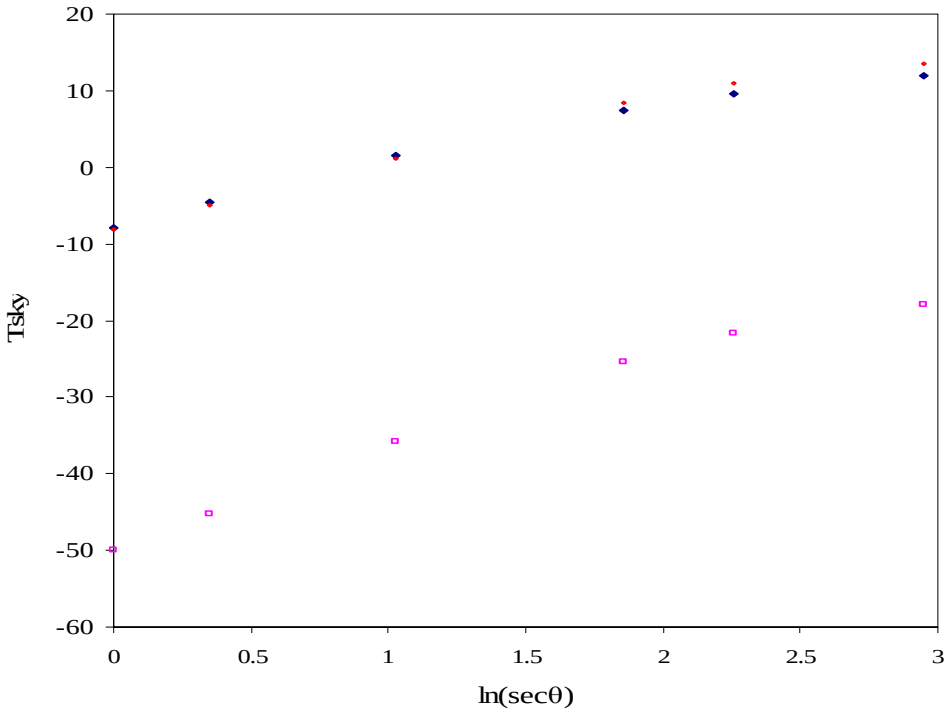

Figure 6. 6: Shows the sky temperatures for two-wavelength band obtained by MODTRAN for an Adelaide summer profile (21 December 2002) and measured temperatures as a function of logarithm of air mass. Measured (Dark Blue), 6.6 µm –50 µm (Red) and 6.6 µm –17 µm (Pink) Tair =17 °C, RH = 80 % and the PWV = 0.71 cm.

6.4.1.3 Cloudy sky Spectrum

Cloud has strong effect on the IR atmospheric radiation. This decreases in importance with altitude because higher clouds are usually colder than low clouds (Kondratyev 1965).

The effect of clouds upon the atmospheric radiation may be seen in figure (6.7). Here MODTRAN, with similar inputs to these used in previous two sections, is used to simulate an atmospheric radiation spectrum for MLS standard atmosphere for cirrus and stratus cloud types at zenith. Both spectra are plotted with that for clear sky for the purpose of comparisons. The graph shows the effect of clouds of different altitudes on the spectral distribution of the IR atmospheric radiation. Due to their higher altitude, the spectrum of the cirrus cloud is similar to that of clear skies. The integrated sky temperatures between 6.6 μm to 50 μm for cirrus were -10.5 ^{o}C and for the clear sky was -12 ^{o}C. On the other hand, the basic effect of the low level clouds (stratus) is to close off the atmospheric window (8 μm to 14 μm) to the atmospheric radiation and emit as a black body with temperature close to that of the screen level. The integrated sky temperature for the stratus spectrum between 6.6 μm to 50 μm was 15 ^{o}C.

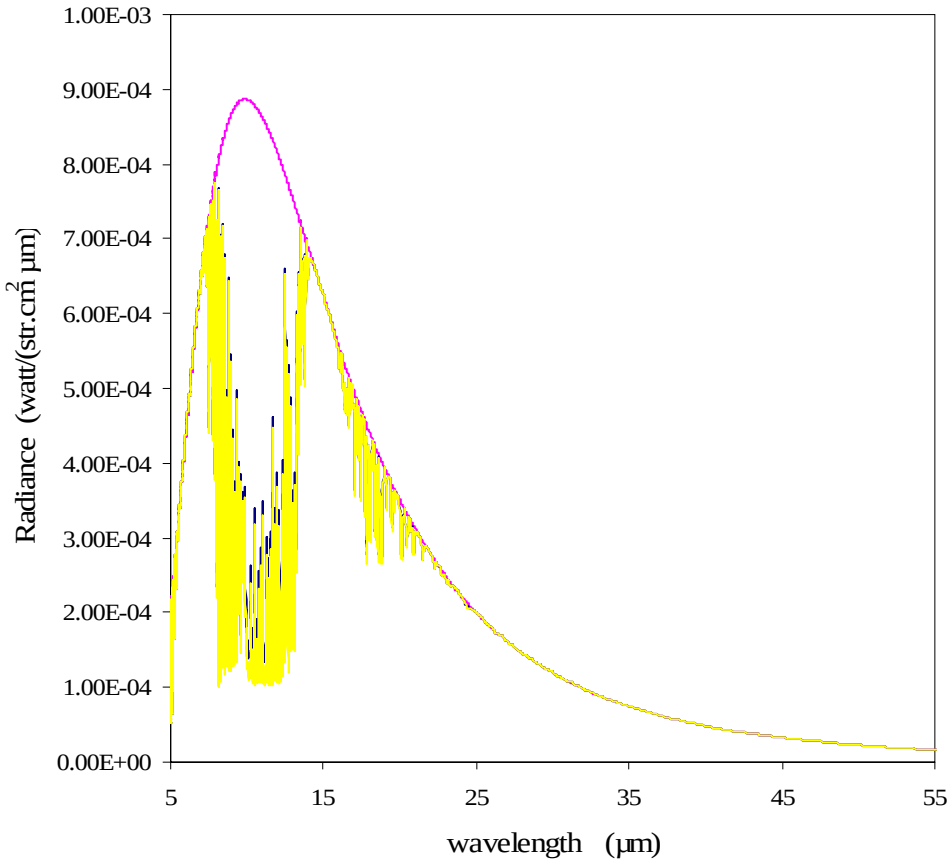

Figure 6. 7: Shows a typical IR spectrum of the cloudy sky at the zenith for MLS standard atmosphere (Tair = 21 °C, RH = 75.9 % and the PWV = 1 cm) for Stratus (pink), Cirrus (blue) compared with the clear sky spectrum (yellow).

6.4.2 The Effect of Screen Temperatures

It was found in the previous chapter that the sky temperatures increase almost linearly as the screen temperatures increase.

The aim of this section is to investigate, using MODTRAN, the impact of the screen temperatures on the clear sky atmospheric emission.

MODTRAN has six standard atmospheres that cover a wide range of screen level temperatures from warm conditions at the tropics of 27 °C to very extreme cold conditions found in the sub-Antarctic winter –15 °C. MODTRAN was run at the zenith for the entire range of standard atmospheres. For each run of a specific atmosphere, the amount of water content (PWV) was varied. Using the Mathematica algorithm and the procedures discussed in section 6.3.3, the sky temperatures for each atmosphere and for every amount of PWV were calculated for two different wavelength ranges, for G15

6.6µm to 17µm and 6.6µm to 50µm. Results of these simulations are summarized in table (6.2).

Fig (6.8) shows a plot of sky temperatures as a function of screen level temperatures for a value of 1 cm of PWV, for the 6.6 µm to 50 µm and 6.6 µm to 17 µm wavelength ranges.

6.6µm -50 µm					
Atmosphere	T ^{o}C	PWV 0.5 cm	PWV 1 cm	PWV 2 cm	PWV 3 cm
Tropical (Trop)	26.6	-12.6	-8.5	-3.6	0.4
Mid latitude summer (MLS)	21.0	-16.2	-12.2	-7.3	-3.2
Mid latitude Winter (MLW)	-0.9	-33.7	-29.4	-28.0	-28.0
Sub-Antarctic Summer(SAS)	14.0	-22.5	-18.4	-13.4	-9.6
Sub-Antarctic Winter(SAW)	-15.8	-44.2	-43.1	-43.1	-43.1
US STD	15.0	-22.5	-18.2	-13.2	-9.5
6.6µm -17 µm					
Tropical(Trop)	26.6	-54.1	-50.7	-44.5	-38.3
Mid latitude summer (MLS)	21.0	-57.9	-54.6	-48.2	-42.0
Mid latitude Winter (MLW)	-0.9	-77.0	-73.7	-72.0	-72.0
Sub-Antarctic Summer (SAS)	14.0	-64.8	-61.5	-55.2	-49.3
Sub-Antarctic Winter (SAW)	-15.8	-88.4	-87.8	-87.8	-87.8
US STD	15.0	-64.9	-61.5	-55.1	-49.5

Table 6. 2: Integrated sky temperature results at the zenith (in ^{o}C) of MODTRAN simulations for six standard atmospheres for different amount of PWV. The upper portion of the table shows the 6.6-50µm simulations while the lower portion represents the 6.6-17µm sky temperatures. T column is the screen level temperature for the standard atmosphere.

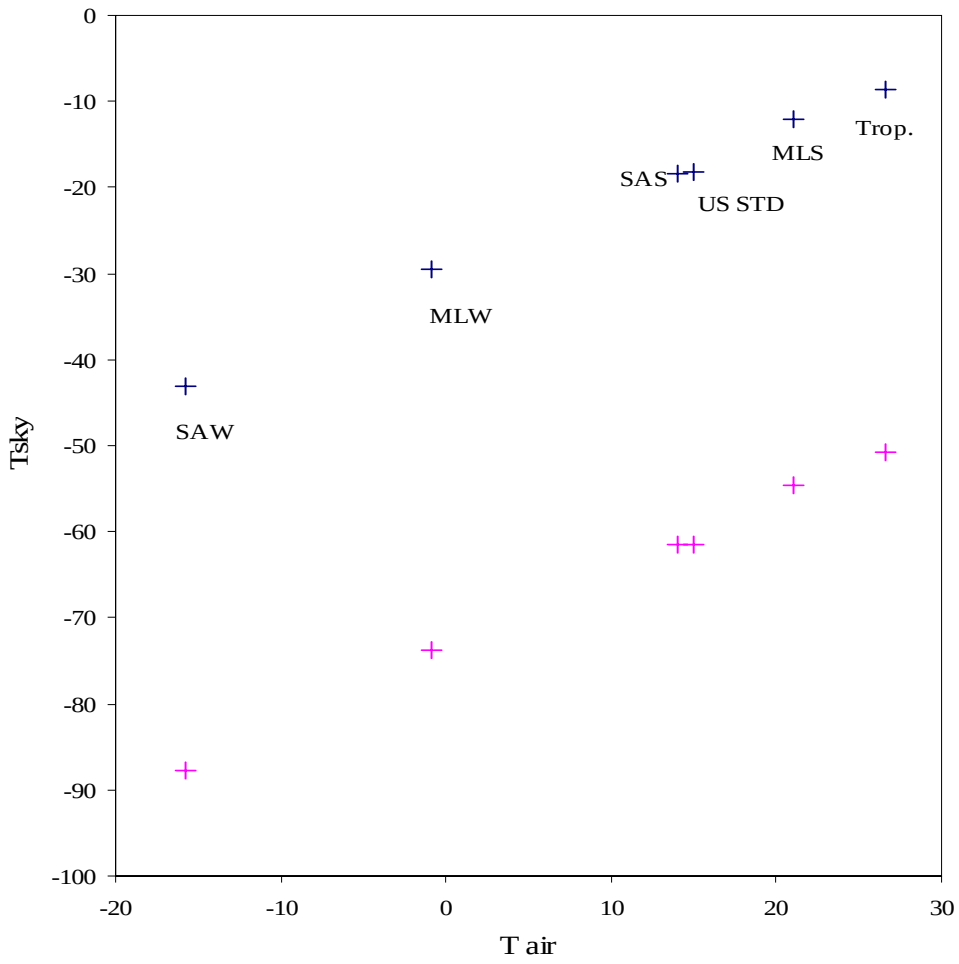

Figure 6. 8: The simulated sky temperatures at the zenith for 6.6 µm -50 µm(Dark Blue) and 6.6µm - 17µm (Pink) for different screen level temperatures for six standard atmospheres as marked for 1cm of PWV.

From the data presented in table (6.2) and figure (6.8), it is clear that, for the same amount of PWV, sky temperatures are increasing progressively with increasing screen level temperatures. This trend is observable for both wavelength ranges. However, the atmospheric emission for the range of wavelengths between 6.6 µm to 50 µm is higher in comparison to those in the 6.6 µm to 17 µm range due to the emission by water vapor which is similar to that of black body, see fig (6.4).

The results of the linear regression analysis between the two temperatures (in ^{o}C) for both wavelength ranges for MLS atmosphere were:

$$Tsky_{(6.6\mu m-50\mu m)} = 0.81 \times Tair - 29.75 \quad (6.3)$$

$$Tsky_{(6.6\mu m-17\mu m)} = 0.81 \times Tair - 73.7 \quad (6.4)$$

and the correlation coefficient for both fits was 0.998. It is obvious that apart from the different of the intercepts in both equations, the slopes are the same,

A similar relation between the screen level temperatures and the sky temperatures was experimentally found in chapter 4 for G15 and STD detector (see table 4.2). For example for G15 the regression analysis between the measured sky temperatures and the screen level temperatures was:

$$Tsky = 0.74 \times Tair - 29.3 \quad (6.5)$$

and the correlation coefficient was 0.80

Comparing equation (6.3) and (6.4) with (6.5) shows that the slope of the experimental formula is close to that obtained theoretically. It is also clear that the intercept of (6.5) is similar to that of (6.3), wavelength range of 6.6 μm to 50 μm, shows the proximity between the simulated sky at this wavelength range and the measured sky temperature and will assist us to confirm the wavelength of response of the detectors.

6.4.3 The Effect of Amount of Water Contents

Apart from the screen level temperature, the existence of water vapor in the atmosphere has the greatest impact on the IR flux or temperatures from clear skies. Water vapor is a very abundant atmospheric constituent and contributes to a large part of thermal IR radiation from the atmosphere. It shows wide fluctuations, which may be ascribed mainly to the variations of air temperatures, and may occur within a short scale of time. The emission spectrum of water vapor is very complex and the IR radiation varies strongly over very narrow ranges of wavelength. The actual spectrum of water vapor is made up of thousands of spectral lines, in which the monochromatic IR sky flux varies rapidly from line to line, creating a complex spectral distribution. It is practically impossible to evaluate this accurately over the entire spectrum of interest, and thereby obtain the total emission by integrating over the spectrum.

Fig (6.9) shows the spectral distribution of IR flux obtained by MODTRAN for mid-latitude summer at the zenith for various amounts of PWV. An increase of the area under the curves can be observed as the amount of water is increased.

At very low values of water (0.00005 cm), the emission due to water vapor is negligible and the atmospheric emission is only due to carbon dioxide and ozone and some other minor gases e.g. methane. As the amount of PWV is increased, the emission from the water vapor first approaches the blackbody emission in the spectral region on each side of the relatively low emissive atmospheric window. The ratio between the area under the curve and under the blackbody is related to the atmospheric emissivity. A further increase of the PWV is accompanied by an increase of emission from the spectral atmospheric window towards the blackbody values. At a value of 20 cm of PWV the atmosphere is nearly emitting as a black body, and when the PWV gets to its maximum value, the atmosphere become totally black body emitter at the screen level temperature. This situation can be imagined as if the observer is in the middle of a fog.

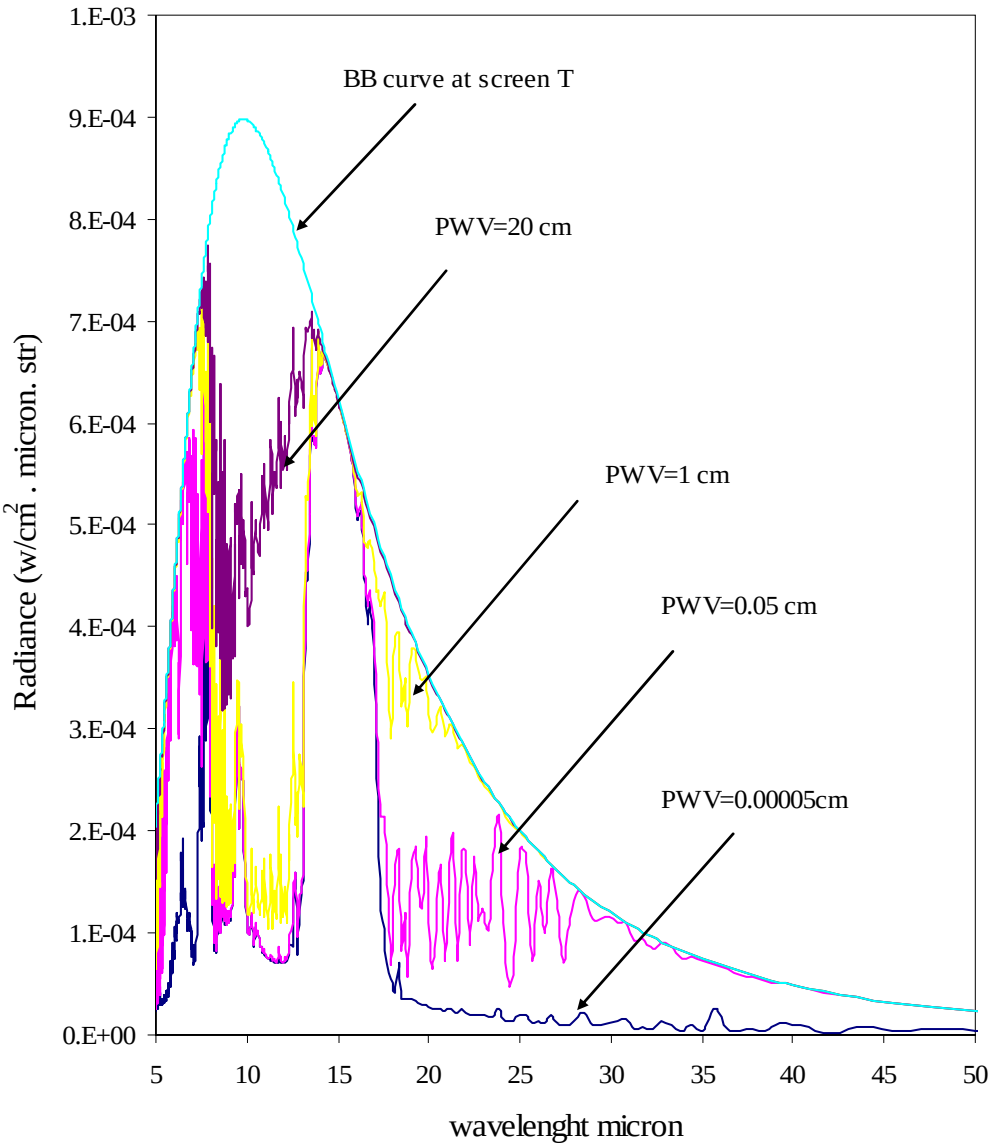

Figure 6. 9: The spectral distributions for IR clear sky radiance at the zenith for different amounts of PWV. The simulations were conducted for a mid-latitude summer (MLS) at the specified amounts of water.

Fig (6.10) shows a plot of the PWV values against the integrated sky temperatures for three standard atmospheres for the two different wavelength ranges. It shows how the sky temperatures increase monotonically with increasing the amount of PWV. With the exception of the Sub Arctic Winter (SAW) standard atmosphere (not shown in this figure, but illustrated in figure 6.11), similar results are found for all standard atmospheres. This deviation is due to the SAW extremely dry conditions where it is impossible to achieve higher amount of PWV, see table 6.2.

The regression analysis between the PWV and the simulated sky temperature using MODTRAN for MLS atmosphere, for example, for both wavelength ranges were:

$$Tsky_{(6.6\mu m-50\mu m)} = 0.48 \times PWV - 17.4 \quad (6.6)$$

$$Tsky_{(6.6\mu m-17\mu m)} = 0.63 \times PWV - 60.9 \quad (6.7)$$

and the correlation coefficients were 0.98 and 0.99 respectively.

Although with some scatter in the data, this relation between the sky temperature, and the PWV was found experimentally in chapter 4 over the measured ranges of PWV and sky temperatures.

The regression analysis found between these two variables a for G15 detector was:

$$Tsky = 0.88 \times PWV - 26.3 \quad (6.8)$$

with a correlation coefficient of 0.73 see table (4.2).

The slope and the intercept of equation (6.8) are different from those in equations (6.6) and (6.7). However, the slope of this equation was not far from those of both equations, while the intercept of (6.8) was closer to that of equation (6.6).

One explanation for these differences between the measured and simulated sky temperatures is that the range of the PWV values covered experimentally was between 0.2 to 2 cm. This is narrower than that covered by the simulations. It can bee seen in figure (6.10) that the slope is greater in the range. Instrumental error either in the IR cloud monitors or in the GPS receiver may cause part of this deviation. We expect also the variations of the measured screen temperature have an impact in causing the scatter in equation (6.8) while the fixed screen temperature at MLS gives a perfect fit represented by either equations (6.6) or (6.7).

Fig (6.11) and table (6.2) summarize the results of this section and the previous section. The figure shows the relationship between the sky temperatures as predicted by MODTRAN for the wavelength range between 6.6 μm to 50 μm, for different atmospheres (different screen temperatures) and for different values of the PWV. Generally speaking, in the normal conditions such that found in the MLS, US STD and tropical atmospheres (which have similar range of temperatures experienced in Adelaide) the amount of the atmospheric water content and screen level temperature can be used together and assumed to be the most effective parameters in modeling the IR radiation with a high accuracy. For example from the table and the figure, a difference

of 5 degrees can be observed in MLS if the amount of PWV increased by 1 cm. This value is similar to that value found experimentally for the same increase in the amount of PWV.

However, in very extreme conditions such as those found in the SAW and MLW, even increasing or decreasing the PWV (RH up to 100%) the amount of water will have no practical impact on the sky temperatures. This mainly due to the fact that in such extreme conditions of very low screen temperature the atmosphere is very dry and it is impossible to achieve a higher PWV. As pointed by Hidas *et al*(2001) that the actual amount of water vapor above the Antarctic is on average of the order of micro-meters of PWV.

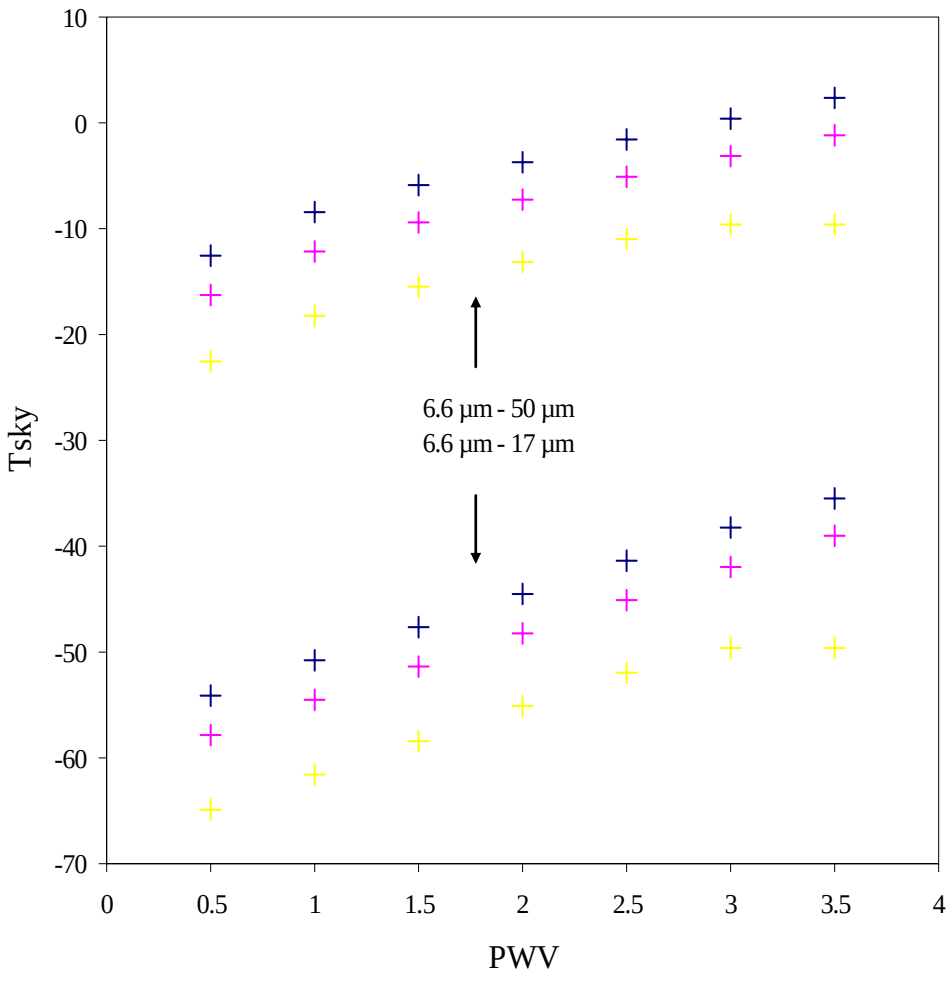

Figure 6. 10: *The simulated sky temperatures in ^{o}C for 6.6µm -50µm upper part of the figure and 6.6µm -17µm (lower part of the figure), for three standard atmospheres as a function of the PWV in cm. These atmospheres are (bottom to top) US STD., MLS and Trop. atmospheres.*

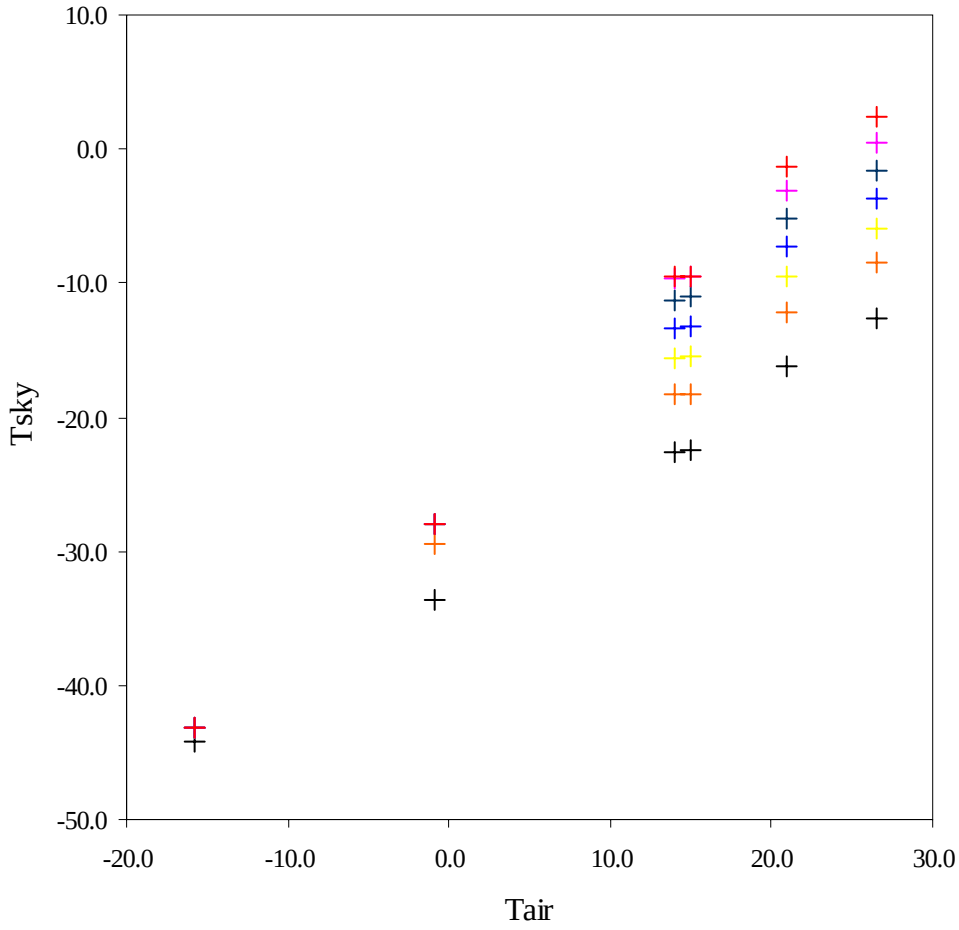

Figure 6. 11: The simulated sky temperatures (in oC) for 6.6µm -50µm for different screen level temperatures (in oC) for six standard atmospheres (from top right diagonally to the bottom left (and see figure 6.8 to identify the atmospheres by their T values.) they are, tropical, MLS, US standard atmosphere, SAS, MLW, and SAW atmosphere each atmosphere with 0.5cm (black), 1cm (orange), 1.5cm (yellow), 2cm (light blue), 2.5cm (dark blue), 3cm (pink) and 3.5cm (red) of PWV .

6.4.4 The Effect of Other Parameters

In the previous sections we found that the screen temperature and the amount of atmospheric water content have a great impact on the on the IR clear sky atmospheric emission and they both can be used to model the IR clear sky radiance. However other parameters are expected to have some effect on the atmospheric emission. Their effects vary in importance according to the wavelength, atmospheric conditions and other factors such as the geography and the altitude of the site. For example Hidas *et al.* (2001) have shown that, at some IR wavelengths, the clear sky atmospheric emission is affected by the aerosol content. Similarly, Chamberlain *et al.* (2000) found that the modelled atmospheric flux in the atmospheric window was strongly dependent on the amount of aerosols included in the model.

Also, Berger *et al.* (1992) used some radiosonde data incorporated in LOWTRAN code to study the clear sky radiation as a function of a site's altitude, in which they concluded that this parameter has an influence on the atmospheric emission.
Here MODTRAN will be used to briefly study the effect of these two parameters on the clear sky temperatures.

6.4.4.1 The Effect of Atmospheric Aerosol

The effect of aerosol on the atmospheric emission was examined first. MODTRAN's standard aerosol type, "urban", was used and spectra and sky temperature were obtained for different visibilities.
Visibility is a measure of the distance at which an object or light can be seen in optical light. It is important to all forms of traffic: roads, sailing and aviation. In extremely clean air such as in Arctic or mountainous areas, the visibility can be up to 70 or 100 km. However, visibility is often reduced in conditions of air pollution and high humidity conditions. Visibility is related to the presence of aerosols in the atmosphere and has an effect on the visible range of wavelengths. Their influence may be extended to the IR part of the spectrum if the size of the aerosol particles becomes comparable with the IR wavelengths. Starting with a high visibility, increasing amount of urban aerosols were added, corresponding to visibilities of 100 km, 70 km , 50 km, 30 km, 20 km, 10 km, 5 km,1 km and 0.5 km. Figure (6.12) shows the resulting spectra for visibilities 100 km, 10 km, 5 km, and 1 km. (The reason for plotting the selected spectra of these visibilities is because with visibilities greater than 10 km the spectra are almost the same (see data in table 6.3), and they overlapped with each other). For a visibility of 1 km and below, apart from the atmospheric window and the 15 μm CO_2 emission, the sky is almost radiating as a black body at all wavelengths. The effect of increasing the aerosols amount (decreasing visibility) is to increase the atmospheric emission in the atmospheric window until for a very low visibilities, the emission in this window resembles that of a blackbody at the screen temperature. In chapter 10 we will see that simulating MODTRAN with such very low visibilities gives a feasible reason for some inconsistent IR sky temperature measurements at the Riyadh site in Saudi Arabia.
Table (6.3) gives the integrated sky temperature for the values of visibilities used here for the wavelength ranges between 6.6 μm to 17 μm and 6.6 μm to 50 μm. For both wavelength ranges the clear sky temperatures for visibilities above 20 km do not vary

much with further decreases in the amount of the aerosols (increasing the visibility range). The sky temperature increases by 1.2 ^{o}C for visibility ranges between 20- 100 km. This is an important consequence for many applications. For example observatories having visibility of more than 20 km are optimum places for IR astronomical observations.

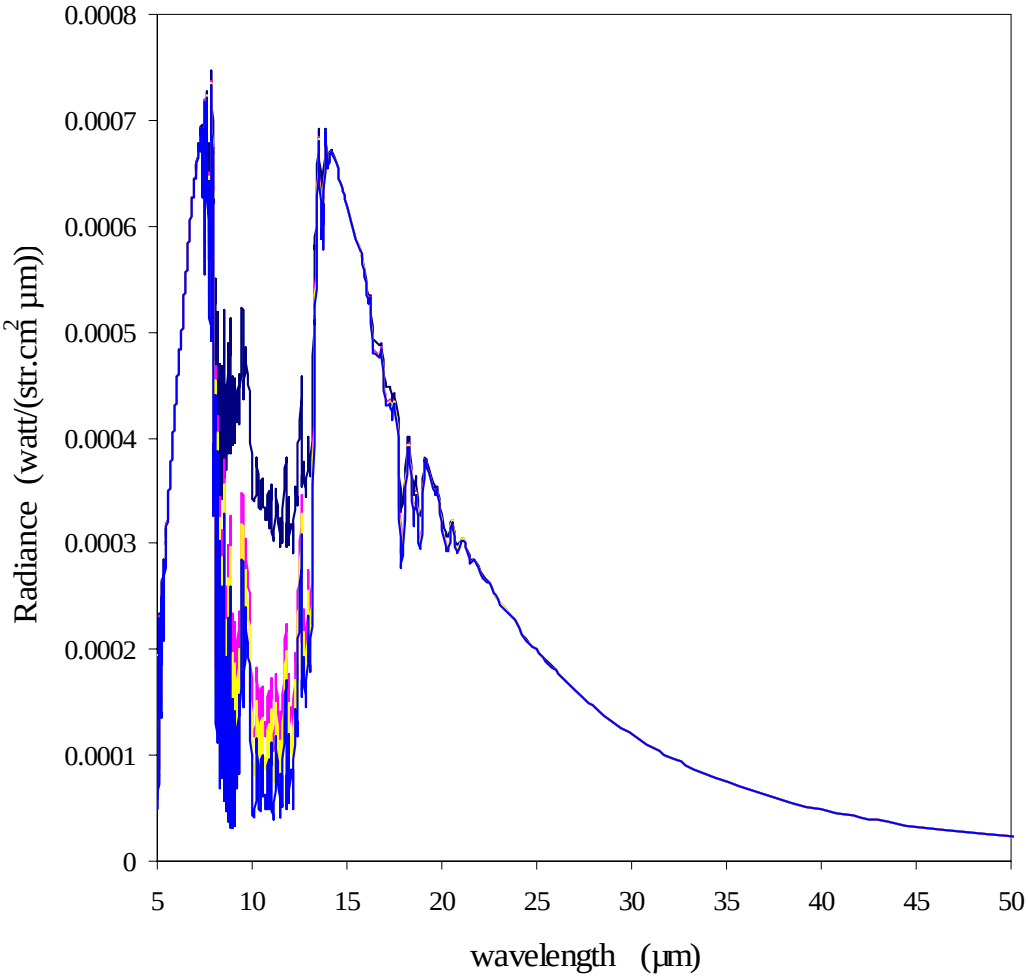

Figure 6. 12: The clear sky atmospheric spectra for MLS atmosphere with varying visibility of aerosols (light blue vis = 100 km, yellow vis = 10 km, pink vis = 5 km, dark blue vis = 1 km). The model has 1 cm of PWV.

Visibility km	Tsky ^{o}C 6.6µm -17µm	Tsky ^{o}C 6.6µm -50 µm
0.5	-32.9	2.3
1	-41.9	-3.2
5	-54.1	-11.5
10	-56.3	-12.8
20	-57.7	-13.6
30	-58.2	-13.9
50	-58.6	-14.1
100	-58.9	-14.3

Table 6. 3: Integrated clear sky temperature over two spectral ranges for MODTRAN MLS atmosphere showing the effect of varying aerosol visibility.

6.4.4.2 The Effect of Site's Altitude

In investigating the effect of the site elevation upon the IR atmospheric emission for clear sky, MODTRAN was run for a MLS standard atmosphere at 6 arbitrary altitudes: 0, 0.5, 1, 2, 3 and 4 km. Figure (6.13) shows the IR clear sky spectra obtained at these altitudes. For lower altitudes (0, 0.5 and 1 km) the main features of the atmospheric IR spectra do not change very much. The absorption band by CO_2, O_3 and H_2O and other minor gases dominate. As the altitude increases, the amount of the total water vapor above the considered base altitude decreases. However, the CO_2 amount remains sufficient to close the window between 14 and 16 µm. Inside the atmospheric window, ozone emission is visible at any altitude. Outside the atmospheric window the atmospheric radiance is that of a black body at an air temperature corresponding to the considered base altitude (not shown in the figure).

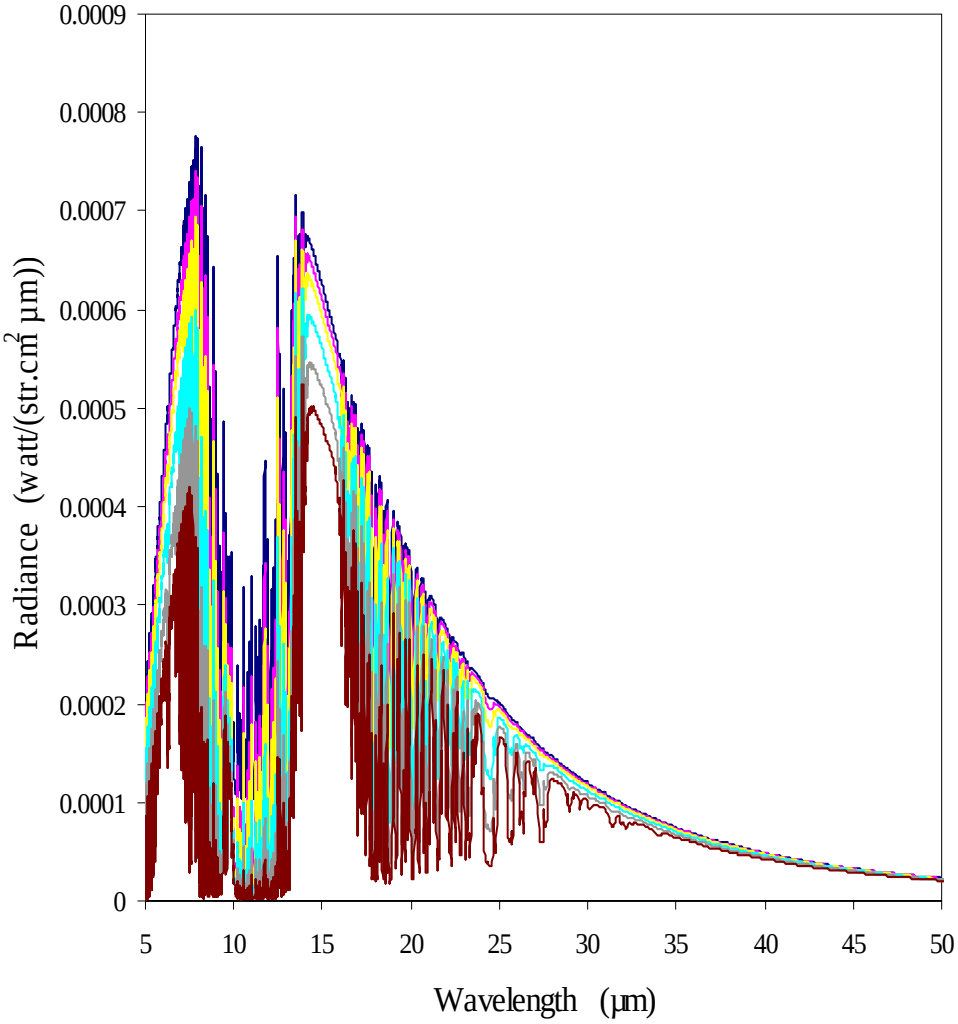

Figure 6. 13. Atmospheric spectral radiance for different altitudes (dark blue 0 km, pink 0.5 km, yellow 1 km, turquoise 2 km, gray 3 km and brown 4 km) obtained for MODTRAN standard MLS summer atmosphere with an amount of 1 cm of PWV.

Table (6.4) presents numerical values of the integrated sky temperatures at the chosen altitude for the two wavelength ranges considered here. Figure (6.14) is a plot of data presented in the table, the sky temperature against the altitude for the two wavelengths. It shows that for both wavelength ranges the sky temperature does decreases as the altitude increase. This is explained as the decrease the amount of the atmospheric water content as the altitude increases, (see table 2.1). The linear fit between these two variables, with a correlation coefficient of 0.99 in both cases, shows the following results:

$$Tsky_{(6.6\mu m-17\mu m)} = -8.8 \times alt - 57.0 \qquad (6.9)$$

$$Tsky_{(6.6\mu m-50\mu m)} = -9.9 \times alt - 12.3 \quad (6.10)$$

where the altitude (*alt*) in both equations in km.

Equations (6.9) and (6.10) indicate that an increase by 1 km in altitude associated with a decrease in sky temperature by 8.8 ^{o}C and 9.9 ^{o}C respectively. Therefore the altitude effect may be considered in studying the IR atmospheric emission in sites at different altitudes.

However, as we shall see in chapter 8, where we present data from different sites in Saudi Arabia, the altitude effect in some circumstances diminished against other important factors such as the screen temperature and water content.

Altitude km	Tsky ^{o}C 6.6µm -17µm	Tsky ^{o}C 6.6µm -50 µm
0	-54.6	-12.2
0.5	-62.9	-18.1
1	-67.0	-22.2
2	-75.1	-31.3
3	-83.5	-41.5
4	-91.6	-52.5

Table 6. 4: Summarises the integrated sky temperature for MLS atmosphere for different altitudes and for the two wavelength ranges considered above.

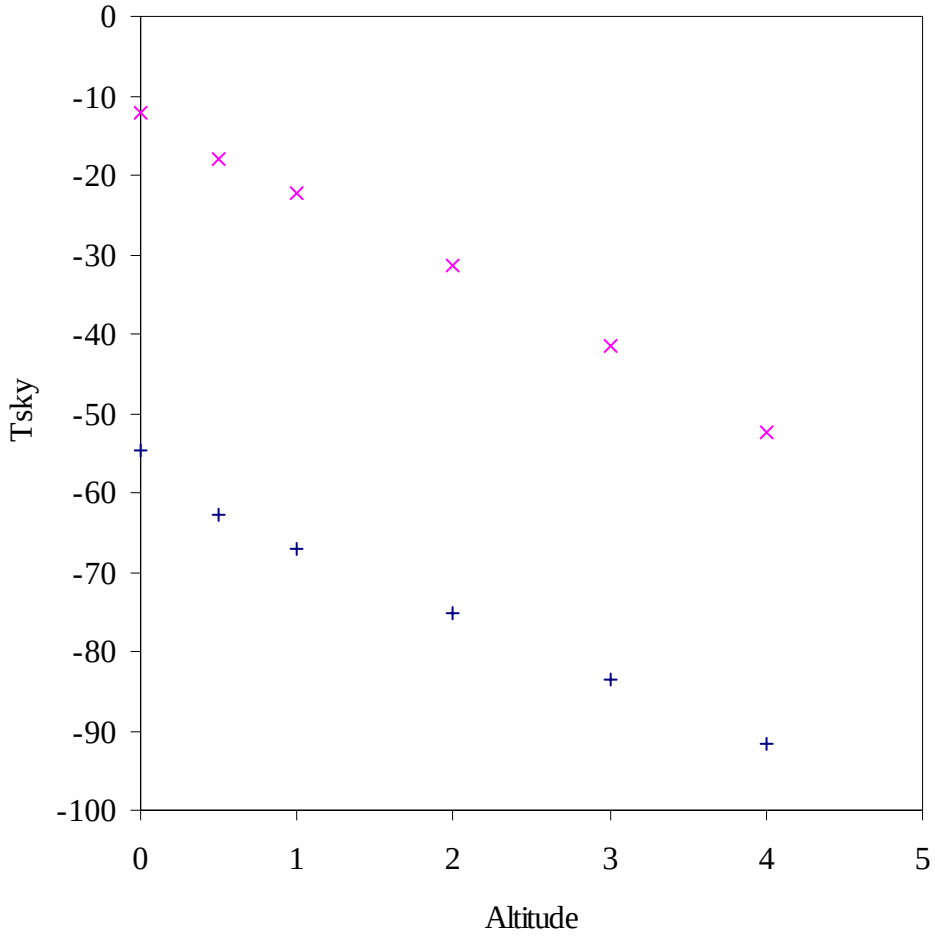

Figure 6. 14. A plot between sky temperature (in ^{o}C) and the altitude (in km) for 6.6 µm - 17µm (pink) and 6.6 µm - 50µm (blue)

6.4.5 Concluding Remarks about The Detector's Wavelength Response

The detection system has been conventionally defined by the filter (lenses or windows, as a weather proof protection tool) /thermopile combination. The short wavelength cut off has been specified by the manufactures of the thermopile and the protective system (see chapter 3). At early times of using the cloud monitors it was thought that the long wave length cutoff of response of the cloud monitors was 17 µm.

At the early stages of using MODTARN for this specific wavelength (for example, for G15 6.6 µm - 17µm) we found that the obtained sky temperatures within this wavelength range were very far from those we have come across. To illustrate this disagreement, a close look to the values of the whole data set of sky temperatures measurements and their statistics presented in tables (4.1) and (4.4) and compare them

with those found in table (6.1) for the wavelength ranges between 6.6 μm to 17μm, we can see that none of the measured (maximum, minimum or average) values have matched or showed any proximity to those simulated for this wavelength range. The minimum value of measured sky temperatures within the whole data set used in this project from Adelaide was -30 ^{o}C, and this value was about 20 ^{o}C and 57 ^{o}C in difference between the highest and lowest MODTRAN simulated clear sky temperature for Tropical and mid-latitude Winter atmospheres respectively. These results between measured and simulated sky temperatures have forced us to examine the cause of such discrepancies. There are four examinations were made to explore these discrepancies.

Firstly we have done several checks to the behaviour of the instruments throughout the whole period of study. Although some of the detectors have shown some irregular behaviors at some periods but we were sure the data of these periods were excluded and an appropriate calibrations were done, so we exclude the possibility that the detection systems are reading incorrect values of the sky temperatures.

The second step was to look carefully to the parameters used as input to MODTRAN or those of default values. The values of these parameters were studied and selected carefully. This include a direct contact to MODTRAN's supplier (Direct contact was made with Gail Anderson at (ganderson@plh.af.mil) during the early time of using MODTRAN), and we were assured that we were using the correct input values. Also, atmospheric inputs were made as close as possible to the real measured atmospheric conditions at Adelaide, and no major changes were found. This confirmed that errors occurring by any misuse of these parameters can be excluded from the investigations.

The third step was to check the steps discussed in section (6.3.3) and used to convert the radiance to sky temperature. The integrated radiances obtained with steps used in this study are comparable with their integrated MODTRAN values found in tape6 output file. Also the scheme of calculating the sky temperature from radiance was based on physical laws and this confirm the elimination of inaccurate calculations of the sky temperature from integrated radiance.

Finally, having these three effects barred from our investigations, we came up with the idea of simulating MODTRAN to wavelengths extending beyond the 17 μm. We then started to run MODTRAN and integrate the sky temperatures for different wavelengths. At each time we compare the obtained sky temperatures with the measured values. This was attained by increasing the upper wavelength of response by 5 μm each time until

we reached the wavelength of 50 µm when we started to get sky temperatures consistent or within an acceptable range of measured values.

In the previous sections we have presented data and results for simulated sky temperatures for two wavelength ranges, the old one 6.6 µm to 17 µm and new one 6.6 µm to 50 µm, for the purpose of comparisons, see equations (6.4) to (6. 9) and tables (6.3) to (6.4) and compare it with table (4.1) and table (4.4).

These results of comparisons showed a great consistency between the measured and simulated temperatures. Consequently, this assured us now that the wavelength of response of G15 cloud monitors is 6.6µm to 50 µm, similar result is applicable to the STD detectors with wavelength ranges from 5.5 µm to 50 µm.

This is an important consequence from using MODTRAN simulations which led to accomplishing one of the goals of this chapter. Hence the theoretical simulations will now help us to optimize the performance of the cloud monitors.

Using this wavelength of response, further studies will be conducted in the following sections.

6.5 MODTRAN Comparisons

This section is dedicated to use MODTRAN simulated sky temperature to compare them with those measured by the G15 cloud monitors. The comparisons will be conducted using firstly MODTRAN standard atmospheres and then using radiosonde profiles over Adelaide.

Similarly MODTRAN simulated sky temperatures for these profiles will also be used to assess the applicability of the experimental clear sky formulae proposed in the previous chapters. This was accomplished by comparing MODTRAN simulated temperatures with temperatures calculated using these models.

These formulae were proposed at the zenith, chapter 4, and at different zenith angles, chapter 5. The functional forms for these models at the zenith for G15 (called model A equation (4.17) and called model B for equation (4.32)) are:

$$Tsky = -31.8 + 0.53\,Tair + 0.60\,PWV \qquad \text{Model A}$$

$$Tsky = -43.9 + 0.75\ Tair + 4.6\ Sqrt(eo) \qquad \text{Model B}$$

Recall equation (5.10) and (5.11) the sky temperatures at any zenith angle for G15 are written here as model C and model D respectively as:

$$T_{\theta} = [(\frac{Tair - Tsky}{2.95}) ln(sec\,\theta)] - [\,31.8 - 0.53\ Tair - 0.60\ PWV\,] \qquad \text{Model C}$$

$$T_{\theta} = [(\frac{Tair - Tsky}{2.95}) ln(sec\,\theta)] - [\,43.9 - 0.75\ Tair - 4.6\ Sqrt(eo)\,] \qquad \text{Model D}$$

6.5.1 MODTRAN Predicted Clear Sky Temperatures Using Standard Atmospheres – Comparisons with Measured and Modelled Data1.

6.5.1.1 At the Zenith

Five of the standard atmospheres available in MODTRAN will be used here for the purpose of this study. These atmospheres are Trop., MLS, MLW, SAS and US standard atmosphere. Figure (6.15) is a plot of the measured sky temperature as a function of the screen temperature, for the data set2 used in chapter 5, also included are MODTRAN results for five atmosphere sky temperatures for 0.5 and 3.5 cm of PWV.

It shows that about 95 % of the measured data are confined between the two regions of the PWV and screen temperatures. In order to accomplish the purpose of this section we will need to run MODTRAN for several PWV values and screen temperatures. The only limitation to this is that, screen level temperatures are fixed for the MODTRAN standard atmospheres and cannot be changed. Therefore we need to find an appropriate method to overcome this inadequacy. To overcome this problem we adopted the following approximations. MODTRAN MLS, Trop., US standard and MLW atmospheres were run to get the measured sky temperatures having screen temperatures

between 19 ^{o}C and 25 ^{o}C, above 26 ^{o}C , between 11 ^{o}C to 17 ^{o}C and below 10 ^{o}C respectively.

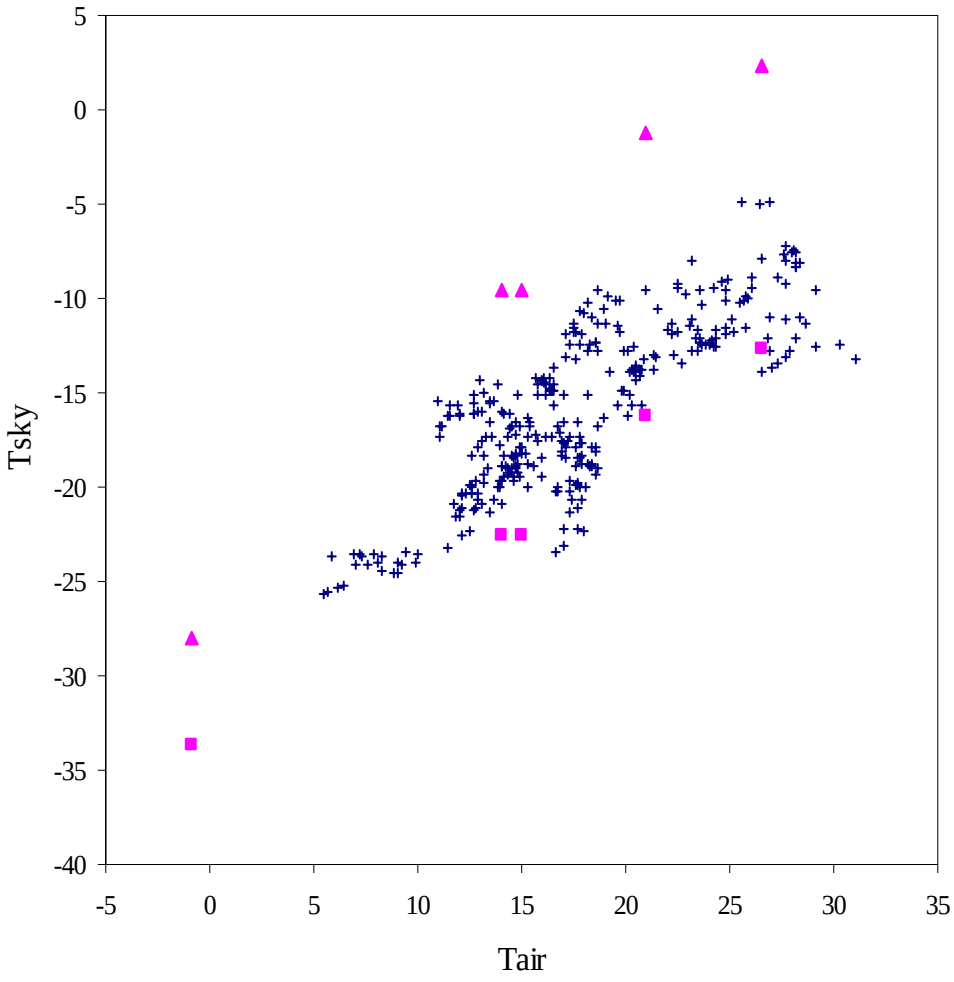

Figure 6. 15: G15 measured clear sky temperature (blue plus) as a function of air temperature- superimposed on MODTRAN simulated sky temperature for the same wavelength ranges for 0.5 (pink squares) and 3.5 (pink triangles) cm of PWV. (The sky and screen temperatures are all in ^{o}C).

For example, the MLS atmosphere was run for different values of PWV having corresponding measured screen temperatures between 19 ^{o}C to 25 ^{o}C. This approximation is reasonable since the range of selected temperatures does not lie far from that of the standard atmospheres. And in this case we are confident that we are not ignoring the effect of screen level temperature.

A total of 44 coincident measured sky temperature data points were found to meet the above criteria. Using the above assumption, MODTRAN was run with the same

parameters used before and the sky temperatures from MODTRAN were calculated. The statistics of the measured and simulated sky temperature values are summarized in table (6.5).

It is obvious from the table that the simulated and the measured values of the sky temperatures are consistent with each other. Their maxima and minima agree within a range of 1 ^{o}C. The mean difference (MBE) between the two temperatures is less than half a degree. Extreme values of the MBE in the maximum and minimum were reported and those may be due to experimental errors or in the approximation of using the standard atmospheres at some screen temperature values. Generally speaking, two important facts can be drawn from these comparisons. One is that, the approximation of using stranded atmospheres, discussed above, is reasonable and close to real. Second, the agreement between the measured and theoretical expectations is good.

The table also gives the predicted temperatures using model A and model B along with their differences (MBE) from MODTRAN simulated temperatures. Sky temperatures predicted using Model A, as we expected, showed better and closer values to MODTRAN values in comparison to those found by model B. For instance, the mean MBE value between Model A and MODTRAN temperatures was less than half a degree, while a value of -3 ^{o}C is found for Model B.

Variable	Range	Minimum	Maximum	Mean
PWV (mm)	17.94	2.34	20.29	12.14
Tair (^{o}C)	17.7	11.4	29.1	19.92
Sqrt(eo) (mb$^{0.5}$)	1.73	2.24	3.97	3.31
Tmeasured (^{o}C)	18.22	-23.12	-4.90	-14.34
TMODTRAN (^{o}C)	21.40	-24.50	-3.10	-14.26
MBE (Tmeasured-TMODTRAN)(^{o}C)	8.39	-4.20	4.19	-0.08
Tmodel(A) (^{o}C)	16.25	-21.73	-5.48	-14.16
MBE (TMODTRAN - Tmodel(A)) (^{o}C)	7.07	-3.58	3.50	-0.10
Tmodel(B) (^{o}C)	14.52	-17.57	-3.05	-11.14
MBE (TMODTRAN - Tmodel(B)) (^{o}C)	14.29	-10.89	3.39	-3.12

Table 6. 5: Summarizes the statistics of the comparisons between MODTRAN simulated sky temperatures (TMODTRAN) for 44 measured data points for the G15 filter wavelength range 6.6µm -50µm, for the five standard atmospheres used here and the measured/modelled sky temperatures (Tmodel (A) and Tmodel (B)). It also shows the MBE between MODTRAN and these temperatures.

A regression analysis between the simulated and measured/predicted temperatures was performed. Fig (6.16) shows plots of the measured/predicted sky temperatures versus the MODTRAN simulated temperatures. The straight line in the figure shows the 1:1 relation and is used here to examine that ratio. There is roughly a 1:1 relation between measured, predicted temperatures using model A and MODTRAN simulated temperature. This relation is not totally evident for model B. Many reasons can cause the divergence of this relation from 1:1, especially for model B. The most likely is the differences between the ground level parameters at the real measurement site and the standard atmospheres. As we pointed out in chapter 4, PWV is a better predictor, as a representative of the atmospheric water, than the screen level value. This may cause the poorer performance of the model B against simulated temperatures.

To conclude, with good accuracy the results of the theoretical simulations conducted in this section showed the compatibility between measured and MODTRAN simulated temperatures at the zenith. It also showed that Model A and Model B sky temperatures are comparable with the theoretical expectations, to which they are applicable, as predictors to the sky temperatures at the zenith.

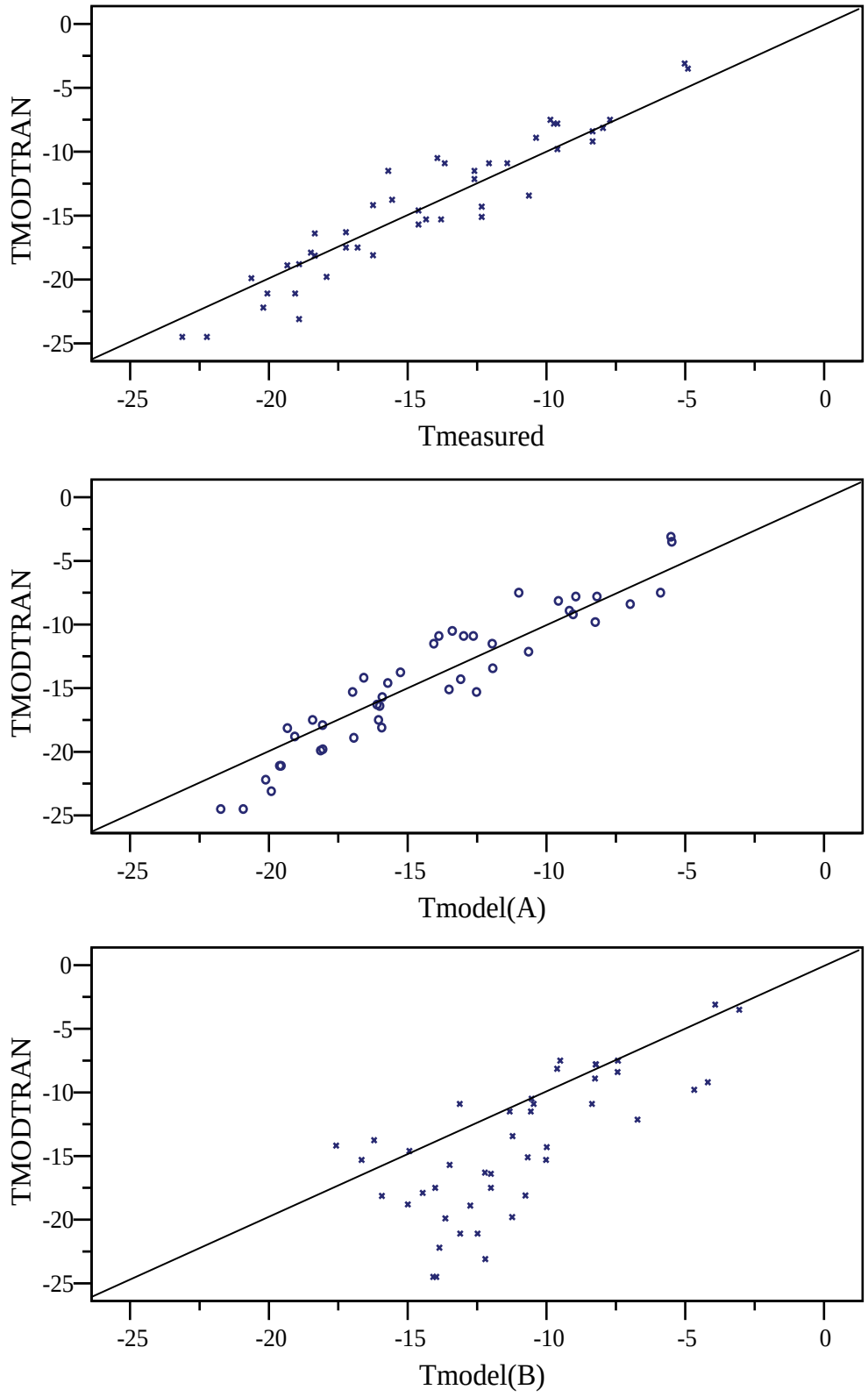

Figure 6. 16: *MODTRAN simulated sky temperatures TMODTRAN using standard atmospheres versus those measured, predicted (model A), and predicted (model B) respectively from top to bottom. All temperatures are in ^{o}C. The solid straight line is the 1:1 ratio line for reference.*

6.5.1.2 At Different Zenith Angles

To investigate the dependence of the sky temperature on the zenith angle using MODTRAN standard atmospheres, four scans were selected and used here. These were selected to have different PWV values, different sky and screen level temperatures, in which the four standards atmospheres can be used. For instance, the US standard atmosphere was run for the scan having a screen level temperature of 16 ^{o}C. The PWV was entered once and the rest of the inputs were as those used in the previous section. For the selected scan MODTRAN was then run for that atmosphere at different zenith angles. Figure (6.17) is an example of the results of the simulations. It shows a plot of the measured, MODTRAN simulated, Model C and Model D temperatures as a function of the logarithm of *sec* of the zenith angle for one scan. It shows that for zenith angles from the zenith up to an 81^{o} the four temperatures agree very well with each other. At 87^{o} MODTRAN and measured sky temperatures are consistent with each other. The reason for the divergence of the two models is discussed in chapter 5 and was due to the assumption of the similarity between the sky temperature and the screen temperature at this zenith angle. The results presented in this section confirm the compatibility between the measured and Model C/Model D predicted temperatures and MODTRAN temperatures over a wider range of zenith angles. They also showed the importance of using the logarithm of the *sec* (zenith angle) as functional form, adapted by this study, to be used to parameterize the sky temperature zenith dependence.

Regression analysis between MODTRAN simulated temperatures for this scan and the logarithm of the zenith angle gives:

$$Tsky(\theta) = 7.7 \times ln(sec\,\theta) - 14.3 \qquad (6.11)$$

with correlation coefficient of 0.99.

The constant and the slope of equation (6.11) are close to, or within, the range of the intercept and the slope of equation (5.2), $Tsky(\theta) = 9.74 \times ln(sec\,\theta) - 16.56$, where their values are found experimentally, see table (5.2).

The whole discussion presented here applies the rest of the scans used in this section. Also, with good confidence, the same results are applicable for the rest of the scans.

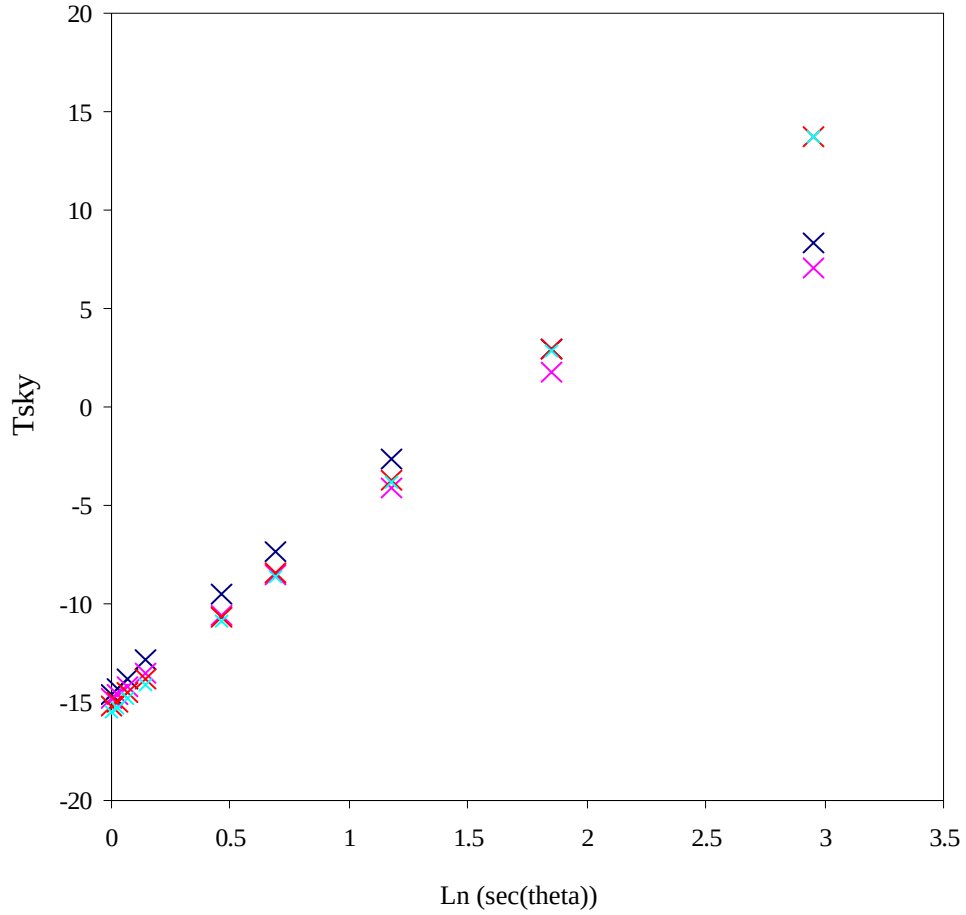

Figure 6. 17: Shows a plot of the measured (blue), MODTRAN simulated (pink), Model C (red) and Model D (turquoise) temperatures (in ^{o}C) as a function of the logarithm of sec of the zenith angle for one scan. MODTRAN US Standard atmosphere was used here, the measured meteorological variables were, Tair = 16 ^{o}C, PWV = 1.3 cm, and the screen vapor pressure, eo, 12.2 mb.

6.5.2 MODTRAN Predicted Clear Sky Temperatures Using *Adelaide Profiles*-Comparison with *measured* and *Modelled* Data2.

6.5.2.1 Approximate Standard Adelaide Profiles Dataset And Running Procedures.

In the previous section we found that MODTRAN standard atmospheres can be used as an approximation for some of the atmospheric conditions at a specific site. However, more accurate investigations required real atmospheric conditions at the site under investigation. A more accurate method is to have radiosonde measurements for most important meteorological variables as an input into MODTRAN. Due to the difficulties

associated with the availability of such information at all times, researchers usually use either atmospheric standard database (such as the TIGR database, which contains more than 2000 atmospheric profiles covering wide ranges of atmospheric conditions over the globe), or build approximate standard atmospheric profiles from radiosonde measurements at that site over some period of time having similar conditions (e.g. summer and winter times). Due to the difficulties of getting access to some of the standard databases, the second approach was adapted for the purpose of this study.

As we discussed in section (6.3.1.2), due to the limited number of radiosonde measurements available for Adelaide, standard summer and winter atmospheric profiles for pressure, temperature and relative humidity were created from the average of the radiosonde data over these two seasons. In this section and throughout the rest of this chapter these two profiles will be used as input into MODTRAN unless otherwise stated. Also profiles for other atmospheric constituents (CH_4, CO, O_2, NO etc) were set to those from the MODTRAN standard mid-latitude summer model, which was assumed to be closest to the conditions at Adelaide in both seasons. Other general inputs were similar to those used before (section 6.3.1.3).

From the available clear sky data used previously to parameterize model A , B, C and D (chapters 4 and 5), 228 data points from the G15 detector (105 from summer data and 123 from winter data) of measured sky and screen temperatures, air pressure, screen water vapor *eo* and PWV, were carefully selected. These data were selected and statistically sampled to cover the whole range of sky and screen level temperatures, PWV and water vapor as exhibited over summer and winter times in Adelaide. Also, data were not selected with time intervals below 30 minutes, in order to avoid spurious data clustering in a limited number of observations over a small range of temperatures or PWV, (table (6.6)).

Having all the required inputs and the dataset available, MODTRAN was run for each set of ground level parameters (temperatures, relative humidity and pressure) as well as the PWV values which were changed to the measured values. The upper air data were left unchanged. MODTRAN integrated sky temperatures were then calculated for each run.

6.5.2.2 MODTRAN Versus Measured

Following the above discussions, *measured* sky temperatures will be compared with MODTRAN simulated temperatures in this section. Table (6.6) gives the statistics of the meteorological and sky temperatures values for the selected data for the two seasons. The last four rows are sky temperatures calculated for this dataset from model A and model B. Generally speaking, the measured and MODTRAN simulated sky temperatures broadly agreed very well with each other in both winter and summer and showed consistent maximum, minimum and mean values. The mean differences (MBE) between the two temperatures were -1 ^{o}C and -2.28 ^{o}C for summer and winter times respectively. The highest MBE values between the two temperatures were -4.6 ^{o}C in winter and 3.9 ^{o}C in summer while over both seasons the lowest MBE was about 2 ^{o}C. These statistical values indicate consistency and compatibility between the measured and the simulated temperatures.

Fig (6.18) shows the relation between the measured temperatures and simulated temperatures for both seasons. The results of the regression analysis and statistical considerations between the two temperatures are presented in row 1 in table (6.7). It shows that the simulated temperatures are generally compatible with those measured with regard to the statistical parameters found in the table for both seasons, particularly summer times. The correlation coefficients between the two temperatures were reasonably good, being 0.87 for winter and 0.90 for summer data. The slopes of the regression lines were reasonably close to the 1:1 relationship, especially for summer with a value of 0.93.

The root mean square errors (RMSE) between simulated temperatures and measured were – 1.6 ^{o}C and 2.7 ^{o}C respectively for summer and winter times.

	Summer profile				Winter profile			
	Min.	Max.	Mean	Std. Dev.	Min	Max.	Mean	Std. Dev.
PWV mm	3.02	20.29	10.87	3.80	1.88	18.23	8.12	3.86
RH %	15.00	90.00	55.50	18.06	35.00	95.00	72.72	17.42
Sqrt(eo) $mb^{0.5}$	2.11	4.70	3.47	0.41	2.38	3.95	3.10	0.30
T air (^oC)	12.90	29.10	19.66	4.37	5.50	20.50	11.56	4.01
Tmeasured (^oC)	-20.83	-6.34	-14.67	3.33	-31.77	-11.70	-21.36	4.74
TMODTRAN(^oC)	-19.99	-5.35	-13.66	3.34	-30.63	-11.15	-19.91	4.25
MB1 (^oC)	-3.91	2.17	-1.01	1.27	-4.61	2.28	-1.45	1.51
T model(A)(^oC)	-16.90	-8.00	-13.48	2.26	-26.45	-10.91	-20.82	3.83
MBE 2(^oC)	-3.77	2.81	-0.18	1.43	-4.18	3.64	0.91	1.63
T model(B)(^oC)	-15.95	-6.92	-12.34	2.08	-25.93	-9.83	-20.15	3.75
MBE 3(^oC)	-6.53	3.34	-1.32	1.88	-7.90	5.26	0.23	3.02

Table 6. 6: Statistics of the meteorological data (T measured, PWV, Relative Humidity RH, vapour pressure, eo, and screen temperature, Tair), measured sky temperatures , MODTRAN simulated sky temperatures TMODTRAN are for G15 detector and sky temperatures calculated using model A , T model A, and model B, T model B (see next section). Also included are the differences (MBE) between Tmeasured – TMODTRAN (MBE1), between MODTRAN-Tmodel1 (MBE2) and between TMODTRAN-Tmodel2 (MBE3).

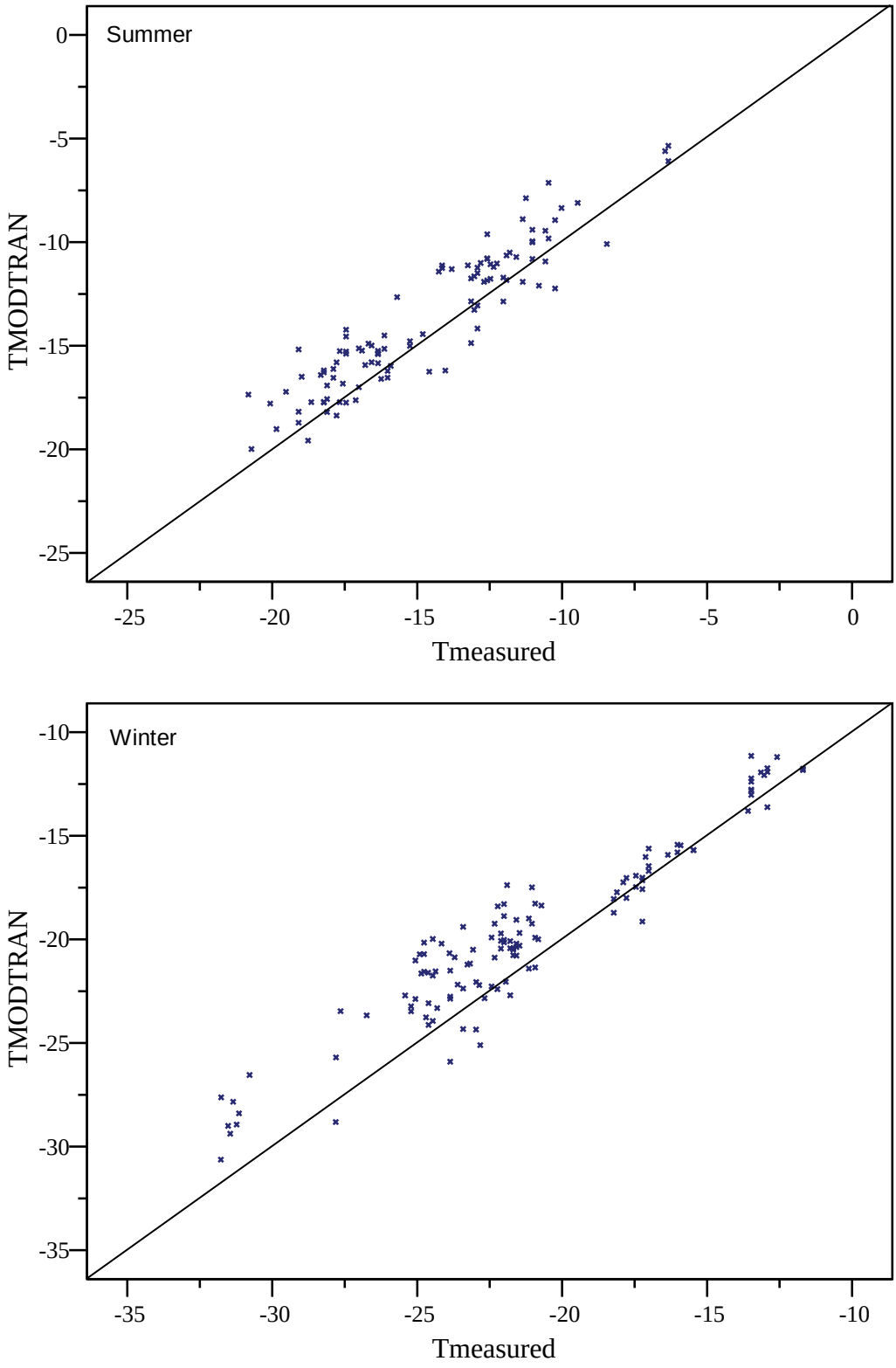

Figure 6. 18: Measured vs. MODTRAN simulated sky temperatures (in ^{o}C) for summer and winter profiles. The solid straight line is 1:1 ratio line for reference.

	Summer profile				Winter profile			
	Inter. ^{o}C	Slope	RMSE ^{o}C	R^2 %	Inter. ^{o}C	Slope	RMSE ^{o}C	R^2 %
MODTRANMeasured	-0.16	0.93	1.6	0.90	1.7	-0.85	2.7	0.87
MODTRAN- model1	5.1	1.3	1.4	0.90	1.3	1.0	3.5	0.85
MODTRAN-model2	3.3	1.3	2.3	0.71	-3.4	0.81	3.00	0.71

Table 6. 7: Summarizes a linear regression analysis between measured and MODTRAN simulated sky temperatures for the G15 detector and sky temperatures calculated using model A and model B.

6.5.2.3 MODTRAN against Proposed Clear Sky Models

The aim of this section is to compare MODTRAN sky temperatures with those calculated using Model A and Model B. An assessment of these comparisons will help in judging the accuracy of the applicability of using these formulae in clear sky temperature predictions.

The sky temperatures for the 228 data points from the G15 detector measurements were calculated using model A and model B for both seasons and their statistics were summarized in the last four rows of table (6.6).

The modelled and simulated temperatures showed different statistical values in winter and summer night conditions. Also, they both showed different behaviour from season to season. Generally speaking, in summer times both models performed better than in winter times.

Model A showed MBE values of less than a degree in both seasons with values of 0.18 ^{o}C and -0.9 ^{o}C in summer and winter respectively. The highest MBE value for model A was in winter, -4.1^{o}C, and the lowest was in summer 2.4 ^{o}C.

Model B, on the other hand, performs differently from one season to another . It showed a mean MBE of 0.23 ^{o}C in winter and -1.3 ^{o}C in summer. In comparison with

model A, model B showed the highest values of MBE with -6.5 ^{o}C in summer and 7.9 ^{o}C in winter.

Most of the observed discrepancies between MODTRAN simulations and both models were found in winter times. Some of these discrepancies may be due to the assumed winter profile, which may not be a good representative of some extreme conditions, especially for clear skies in winter. Inversions, which are found on cold nights in winter, may be another reason for this behaviour.

Fig (6.19) plots the modelled temperatures, predicted using *model A* and *model B*, against their corresponding values of the MODTRAN simulated temperatures for both seasons. The results of the regression analysis and the MBE and RMSE, between the three temperatures are presented in last two rows in table (6.7). Generally, the results showed that the simulated temperatures were reasonably compatible with those modelled with regard to the statistical parameters found in the table.

The correlation coefficients between the MODTRAN temperatures and *model A* were good with 0.90 for summer and 0.85 for winter data. *Model B* correlated less well with MODTRAN, with a value of 0.70 in both seasons. The slopes of the regression lines between model A and simulated temperatures were reasonably close to a 1:1 with a value of 1 for winter and 1.3 for summer data. On the other hand, *model B* showed a similar deviation from 1:1 line to *model A* with value of the 1.3 in summer while in winter has a value of 0.8.

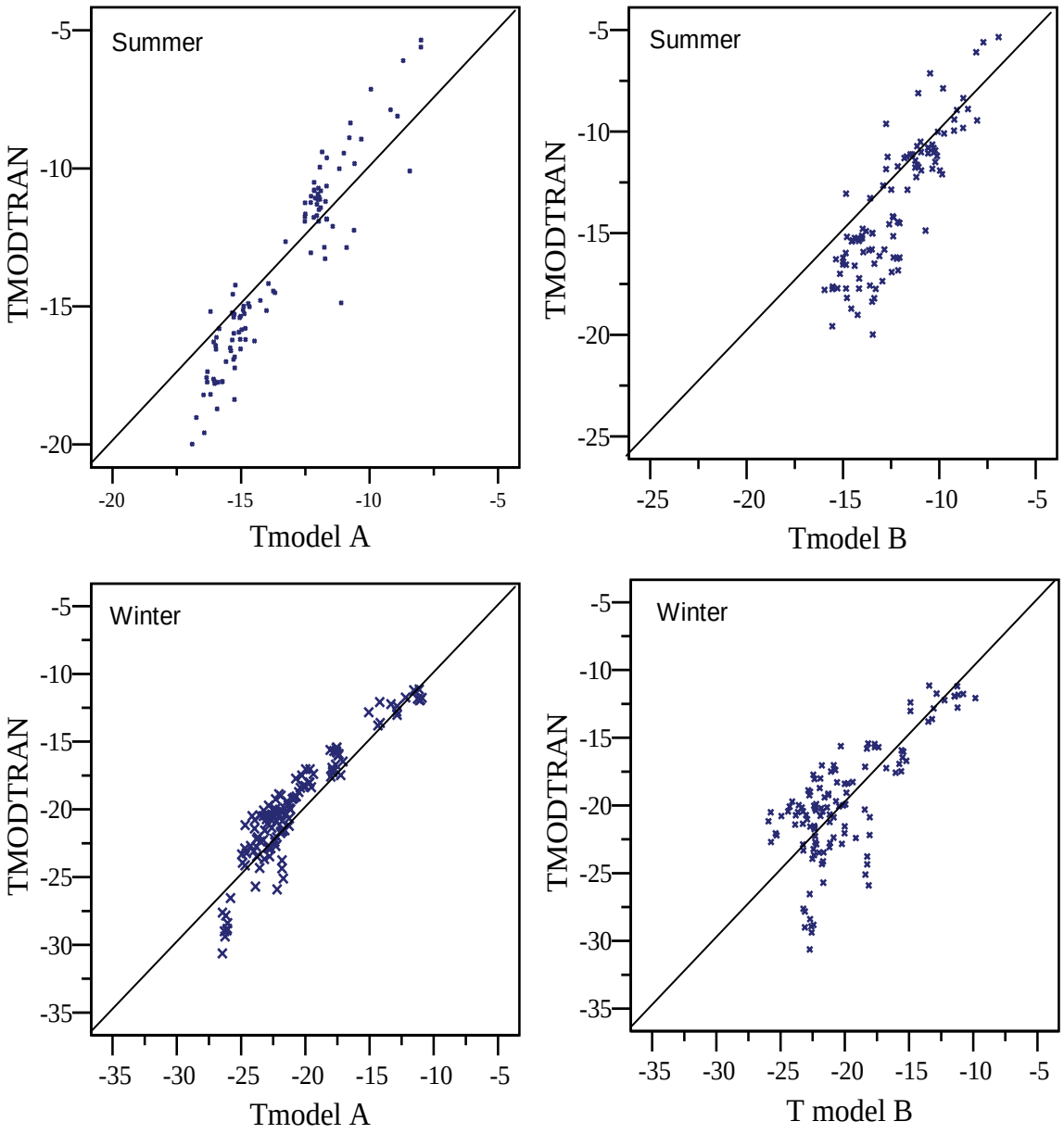

Figure 6. 19: Model A (T model A) and Model B (T model B) predicted temperatures vs. MODTRAN simulated sky temperatures for summer and winter profiles (all are in ^{o}C) . The solid straight line is 1:1 ratio line for reference.

6.5.2.4 Discussion and Comments about the Results

The results presented in the last two sub-sections show the agreements and discrepancies between the simulated, measured and modelled temperatures in summer and winter. It was found that *model B* had a poorer performance and larger statistical biases in comparison with the simulated temperatures, particularly in winter time. On the other hand, both *model A* and measured sky temperatures are in good agreement

with the simulated temperatures, where the latter showed better results than the former. As was concluded in the previous chapter, *model B*, which uses screen level parameters, had a poorer performance in comparison with *model A*. This is due to the fact that the latter includes the total amount of water PWV, which is a good measure of atmospheric water content in contrast to the former which includes the screen level vapor pressure. Figure (6.20) shows a plot of MODTRAN simulated temperatures plotted against the measured and the modelled, using *model A* and *model B*, temperatures for both seasons. It is clear that the compatibility, with more exception for those found at the coldest sky temperatures, between the simulated and the other three temperatures for both seasons is obvious for a wide range of sky temperatures. At the coldest temperatures, the disagreement between the simulated, measured and modeled is larger for *model B*. It is important to notice that more than 95% of the measured and modeled sky temperatures lie close to the 1:1 line to MODTRAN predicted temperatures. Moreover, the most discrepant values of sky temperatures predicted using *model A* and *model B* are not found beyond 2 or 3 standard deviations respectively from MODTRAN 1:1 line.

However it must be stressed that the accuracy of the comparisons depends on many factors:

1- The measured values of meteorological parameters such as T, e_o, and PWV must be accurate.
2- The uncertainty on the measured sky temperatures must be small.
3- The general parameters and the main assumptions input into MODTRAN must be as close as possible to the real.
4- The calculated temperatures by MODTRAN must be reliable and
5- The profiles must be representative of the range of profiles occurring in the real atmosphere.

Other parameters such as the aerosol type may have some impact on the actual comparisons.

Addressing all these uncertainty factors will complicate the comparison procedures and higher accuracies in such situations are difficult to achieve. Our confidence in the first two factors is reasonable. The third factor may be acceptable with confidence. The MODTRAN code has been tested thoroughly and its accuracy is well determined (Berk *et al.* 1998).

Consequently, the main source of errors or spread in the simulated temperatures is the assumption of a representative profile for all measurements, which in some cases include data with extreme conditions. For example on some summer nights the vapor pressure *eo,* falls as low as 4 mb, and 3 mm of PWV, compared to an average value of 12 mb and 10 mm respectively for the season. Due to the extreme conditions toward the end of the seasons, it may not be surprising that the bias of 3 ^{o}C to 6 ^{o}C between the simulated and measured, and modeled temperature is found. Similar arguments can be made for the outlier points in winter times. In some winter nights the level of vapor pressure goes as high as 15 mb, and 18 mm of PWV, compared to an average value in this wet season of about 9 mb and 8 mm of PWV. In both seasons, under such conditions, it is expected that this behavior may be due to the assumptions in MODTRAN of the representative atmospheric vapor density profile over Adelaide. The assumed profiles were approximations for general conditions for both seasons, and this may cause a deviation in simulating the sky temperatures in extreme conditions. Such biases may cause the deviations and may affect the general relations.

Inversions at some clear nights, especially in winter, may cause some of these deviations. Radiosonde data, which were used to create the average profile, may have errors, which can also affect the assumed profile.

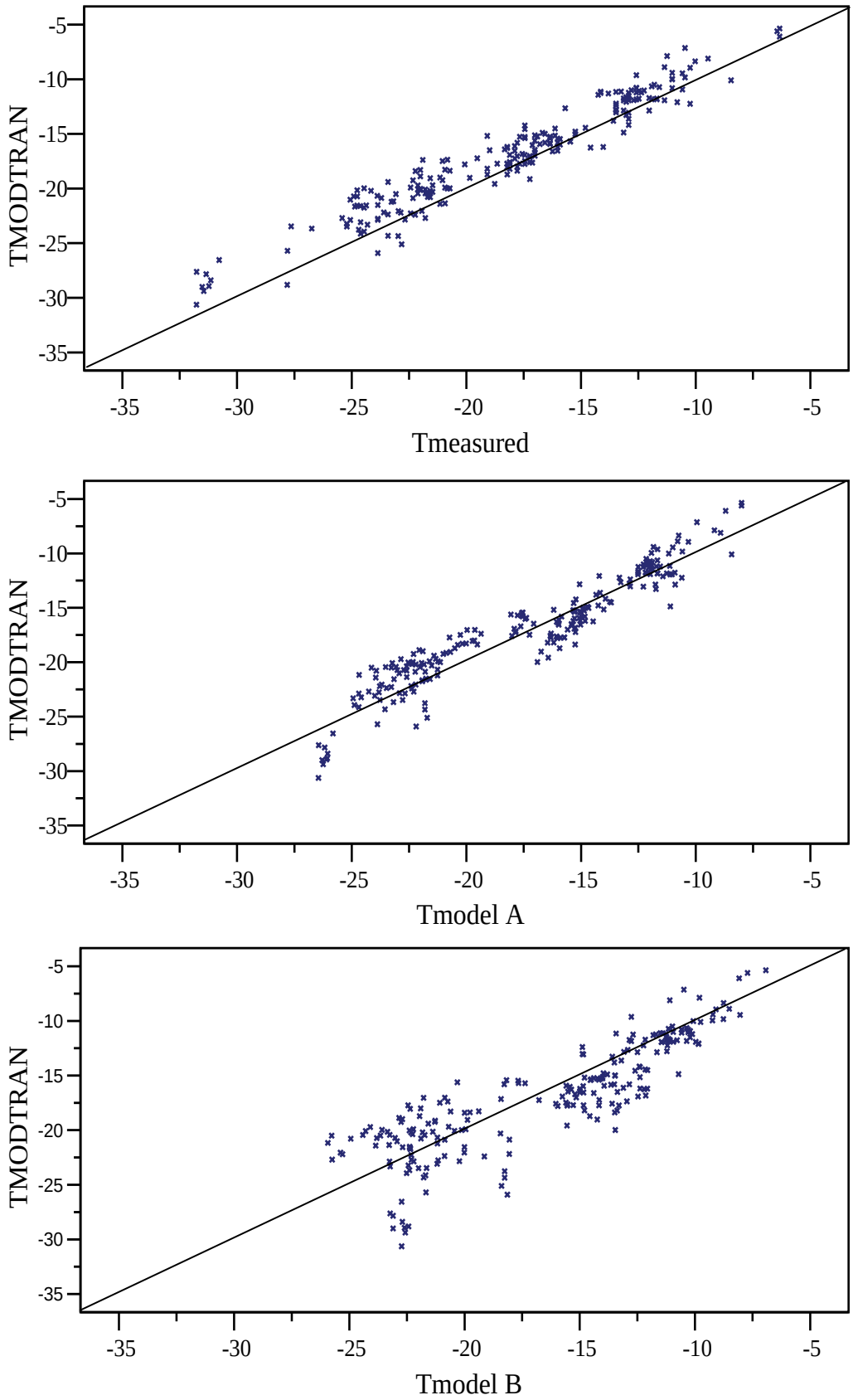

Figure 6. 20: Measured, model A and model B predicted temperatures vs. MODTRAN simulated sky temperatures (all are in ^{o}C) for 6.6µm -50µm for both seasons using Adelaide profiles. The solid straight line is 1:1 ratio line for reference.

6.5.2.5 Zenith Angle Distributions

In this section we will complete the study of MODTRAN simulated sky temperatures and test the applicability of the zenith angle formula, *model C* and *model D*, using Adelaide radiosonde profiles. The representative summer and winter profiles were used as the inputs into MODTRAN. Similar methodology to that used previously to simulate the sky temperatures at the zenith and at different zenith angles (section 6.5.1.2) will be used here. From the available clear sky data from the scanner, see chapter 5, 24 scans of the G15 (14 from summer data and 10 from winter data) measured sky temperatures at different zenith angles were selected and used in the current investigations.

Figure (6.21) shows the variation of the sky temperatures against the logarithmic of *sec* of the zenith angle (ln (sec θ)), for one selected scan from summer data and one from winter data. These angles cover the range from the zenith to 87^o. The figure shows a sample of lines, which describe the relationship between the simulated sky temperatures, measured temperatures and predicted temperatures using *model C* and *model D* as a function of the logarithm of the secant of the zenith. Similar relationships were found for all the selected scans in both seasons. The entire scan showed agreements between the simulated temperatures and those measured, with a reported maximum difference of no more than 3 ^oC from the zenith to 3^o above the horizon. Similarly the MODTRAN temperatures showed comparable and consistent results with those temperatures predicted by the two models with a differences of no more than 4 ^oC at any angle, except at the angle of 87^o where the common observed differences lie in the range of 5 ^oC to 9 ^oC. The linear correlation coefficient between the temperatures and the logarithm of secant angle for all scans was found to be not less than 0.99.

From the above results it can be concluded that MODTRAN has demonstrated that the zenith angle relationship between the sky temperatures and the log of the secants of the zenith angle should be as observed. Theoretically also, we found that the proposed formulae, *model C*, and *model D*, can be used with a good accuracy to predict the sky temperatures at any angles from the zenith to zenith angle as of 84^o.

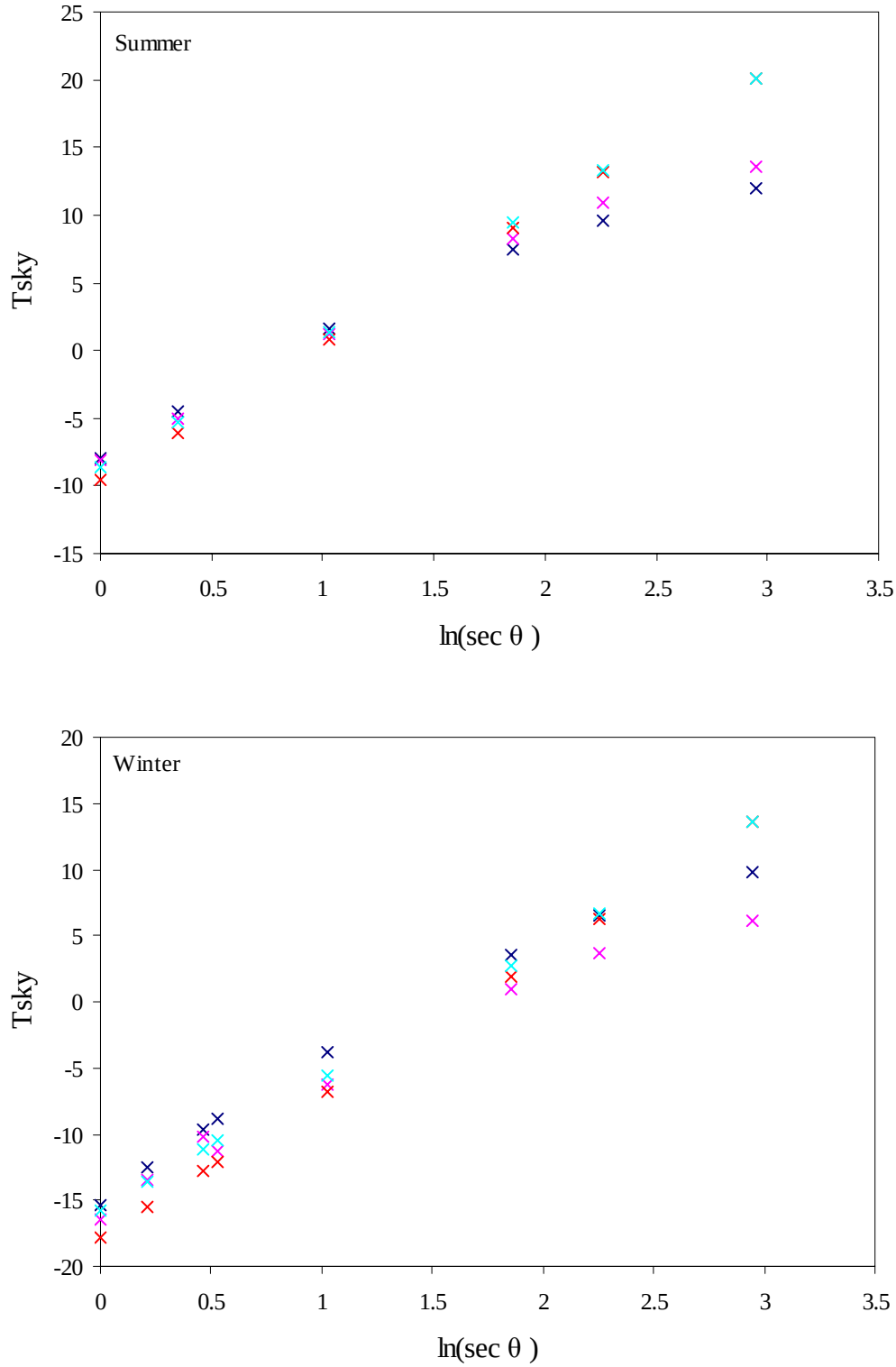

Figure 6. 21: Shows the simulated sky temperatures obtained by MODTRAN(pink), compared with measured(dark blue) and predicted sky temperatures using model C (red) and model D (turquoise) (all are in ^{o}C) as a function of logarithm of air mass. These data are for one scan each for Adelaide summer and winter profiles.

6.6 Conclusion

This chapter has linked the observations with theoretical models and their associated numerical codes using atmospheric profile data represented by the numerical code MODTRAN. The observations had led to empirical formulae to predict the sky temperatures, while the MODTRAN simulations have been used to integrate the spectral temperatures.

Using MODTRAN it was confirmed that the screen level temperatures and the water vapor content, represented here as the PWV, have the greatest impact in determining the broadband IR clear sky temperatures. However, as pointed by some researchers, other parameters may impact on studies of IR sky temperatures, e.g. Ayotte *et al*.(1999) and references therein. Here, we studied the effect of two factors, aerosol type and altitude effect. We have shown that the both these two factors have some effects on the sky temperatures differently.

The 6.6μm -50μm sky temperatures obtained by MODTRAN were found to agree sufficiently with the measured and predicted sky temperatures at the zenith and at different zenith angles. The degree of consistency is high. The assumed atmospheric profiles from radiosonde data for both summer and winter have shown a reasonable approximation to the real atmospheres. The models which used the screen level temperature and the amount of PWV, models A and C, were proven to predict the sky temperatures at the zenith and at different zenith angles with higher accuracy. On the other hand, model B and D, which use the screen level temperature and the screen level vapor pressure, have shown some inconsistency with the simulated temperatures. They can be used to a reasonable approximation as a predictor for the sky temperatures at the zenith and at different zenith angles.

CHAPTER SEVEN

OVERCAST SKY TEMPERATURE MEASUREMENTS

7.1 Introduction

In a recent article, Riordan *et al* (2005) described a study of the IR overcast sky temperatures at the Edinburgh field site in a coastal region of South Australia. They used one year (1999-2000) of measurements using a 3^{o} FOV STD filter viewing the zenith. They had access to a ceilometers data which gives reliable measurements of cloud height. They investigated the relationship between sky temperatures, screen level temperatures and cloud base temperatures. Also, they studied the properties of clouds at different altitudes.

This chapter is the last of four chapters dedicated to the study of clear and overcast skies using data collected from Adelaide sites. These chapters make up the first part of this thesis. The aim of this chapter is two fold. The first is to review some of the results presented by Riordan *et al.* (2005) and to carry out further investigations at the zenith

and at different zenith angles using an independent dataset from other cloud monitors. The second, the ultimate purpose of this work, is to examine the capability of the clear sky formulae proposed in the preceding chapters (at the zenith and at different zenith angles) to discriminate clear skies from cloudy skies and to determine the presence of clouds in the field of view. This step is very important for cosmic ray observatories and for the new generation of robotic telescopes.

In the following section, we describe the observational dataset employed for this analysis. This will include data collection, selection and treatment. The results are divided into two main parts. The first part (section 7.3) is devoted to investigating the characteristics of overcast sky temperatures at the zenith. A proposed parameterization that it is capable of providing better estimates for overcast sky temperatures will be presented in this section. The zenith angle dependence of overcast sky temperatures will also be briefly discussed in this section. In the second part (Section 7.4), comparisons between measured overcast sky temperatures and predicted clear sky temperatures at the zenith and at different zenith angles will be achieved. These comparisons will be then extended to include skies which are partly overcast. Finally, short comments on the results and accuracy of the data used here will be summarized.

7.2 Instrumentation and Data Collection

7.2.1 Data from Cloud Monitors

Data used here are those obtained from four cloud monitors operated on the roof of the Oliphant Wing of the Physics Building, at the University of Adelaide. These monitors are G15 and STD detectors each with 3^o and 90^o FOVs.

Recorded data from these cloud monitors between 2001 to 2005, as described in chapter 4, including the downtime/operation times will be used. Unlike previous work in this thesis, in this study we are restricted to conditions where the sky is totally overcast.

In analogy with selecting clear sky periods, overcast times were selected following the following criteria:

1. The visually observed total cloud cover reported by the Bureau of Meteorology has to be 8 octa.

2. The full sky curve from the scanner has to be at least following a certain pattern of uniform structure at the time that matches 8 octa of cloud cover.
3. As has been discussed in chapters 3 and 4, clear sky temperatures at the Adelaide site are always lower. Sky temperatures at overcast times show substantially higher temperatures. For instance, very low (negative) temperatures correspond to clear sky times, which may be seen between cloudy times (see figure 4.1).
4. It was also required for an overcast measurement to have at least the two previous and the two following cloud cover measurements to be 8 octa.

Unlike the clear sky scanner's pattern, overcast times will not always have a totally smooth structure. This is due to the presence of different cloud types, altitudes and configurations. Figure (7.1) shows an example of different uncompensated sky temperature outputs from the G15 scanner, from east to west through the zenith, for different overcast skies. Each scan from left to right represents a different condition of the sky at that correspondent angle.

The structure and the depth of each curve in the figure are different from one to another according to the type, height and the properties of the clouds. Each curve has its own feature in representing the clouds. For instance the curve at the top represents overcast sky with low-level clouds, while the lowest curve is for mid-level clouds. Also, the blue crosses show an overcast scan with different and irregular features.

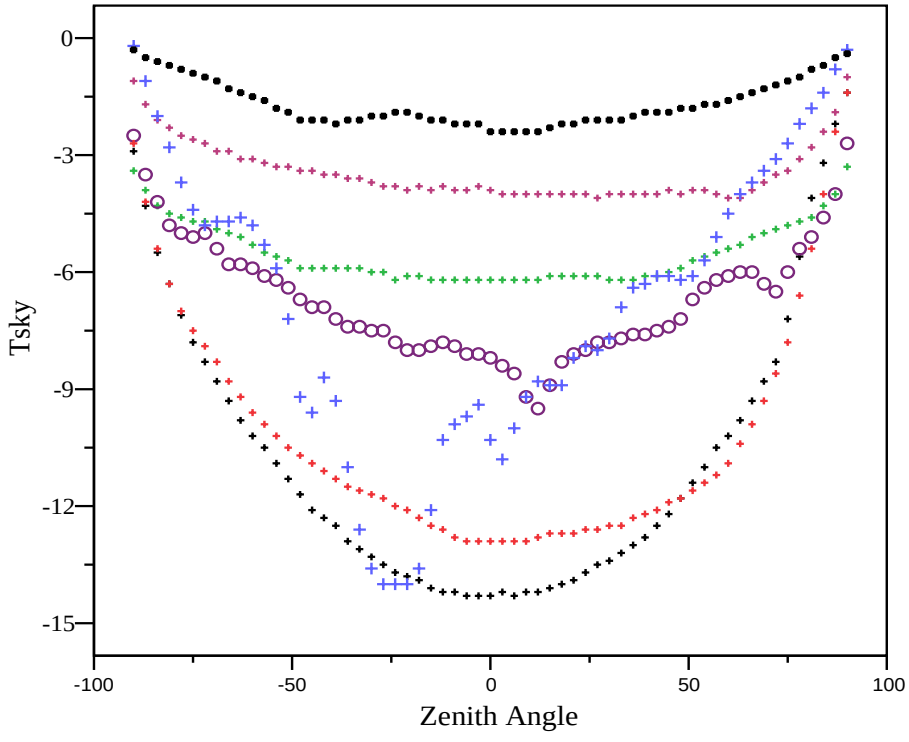

Figure 7. 1: .This example shows the uncompensated sky temperature from a G15 scanner showing structures for different overcast periods.

7.2.2 Meteorological Parameters and Cloud Temperature Estimates

All necessarily meteorological variables were measured by the Australian Bureau of Meteorology at its Kent Town weather station 4 km from the study site. Air temperatures measured by the thermistor inside the cloud monitors were used as representative of the screen level temperature.

Visual cloud observations (obtained by a trained observer) are recorded every half an hour along with the other meteorological parameters. All the data obtained in this project (including those used in this study) are selected from those which have been quality controlled by the Bureau. Recorded cloud information including cloud altitude (cloud height), amount of clouds, and cloud types were also obtained. All these data are recorded, reported and classified according to the World Meteorological Organization (WMO) codes.

The cloud base temperature is usually difficult to measure. Here, it assumed that the cloud base *Tcloud* can be estimated using the air temperature and the standard lapse rate for the lower atmosphere of 6.5 ^{o}C.km^{-1} and cloud altitudes. The equation used in this study is:

$$Tcloud = Tair - 0.0065Zcloud \tag{7.1}$$

This formula was used by many investigators e.g. Riordan *et al.* 2005, Kimball *et al.* 1982 and Lind and Katsaros 1982).

Here *Tcloud* is the estimated cloud base temperature in ^{o}C, *Zcloud* is the cloud altitude (cloud height) in meters from the Weather Bureau estimate and *Tair* is the air temperature in ^{o}C.

This equation gives a very close estimate for the temperature of the base of the lowest cloud layer, but for higher cloud altitudes it may not estimate the temperature accurately. Here, we will assume that the lowest cloud layer will have the most effect on sky temperatures, and therefore equation (6.1) with the assumption of the standard lapse rate will be a good approximation.

7.2.3 Data Set Summary

The dataset used in this study contains half-hour night time measurements of sky temperature measurements from four cloud monitors (two STD and two G15 filters each with 90^{o} and 3^{o} FOVs) plus the corresponding weather and cloud information. A total of 1187 data points of G15 and 578 data points of STD detectors were judged to be completely overcast and were selected to be used for the purpose of this study.

The results presented here will be mainly from the G15 detector with 3^{o} FOV. This is for two reasons. The first is that both the G15 and the STD detectors are peaked at 10 μm (the wavelength of peak cloud emission) therefore we expect similar results are also applicable for the STD detector. Thus, focusing on one detector will avoid repeated discussion. Also, G15 detectors have been in continuous operation since 2001 while STD detectors have had a number of downtimes. The second reason for using the 3^{o} FOV detector is that astrophysical applications often require cloud information on a tiny portion of the sky, hence the emphasis on using the results of 3^{o} FOV detectors in these applications.

The functional form of any parameterization will be given for all detectors while graphical illustrations and result discussions will be considered mainly for G15 detector with 3^{o} FOV.

Table (7.1) and (7.2) show the summary statistics for overcast skies sky temperature measurements from the G15 and STD detectors with 3^{o} FOV and 90^{o} FOV along with some meteorological variables for the data considered in this study.

The results in both tables show some interesting features some of them already stated in chapter 3.

1. The most pronounced is that the overcast sky temperatures measured by the STD and G15 monitors with 3^o FOV have values very close to each other.
2. For both G15 and STD filters, the 90^o FOV differs by about 2 ^oC from that of the 3^o FOV.
3. The mean, maximum, and minimum estimated cloud temperatures were within the same range of sky temperature values measured by both detectors with two different fields of views. From table (7.2), for the STD detector with 3^o FOV for instance, the mean estimated cloud temperature was 9.30 ^oC, which is similar to the measured sky temperature, 9.53 ^oC and 1 ^oC colder than the sky temperature measured by the 90^o FOV. This result is valid for the G15 filter.
4. The range of the overcast measured sky temperatures presented in the tables for all monitors lies between -5 ^oC to 20 ^oC. This evidence provides us with powerful tool to identify either clear sky from cloudy sky or cloudy sky from clear sky using our cloud monitors.

	Range	Minimum	Maximum	Mean	Std. Deviation
Tair ^oC	21.40	6.20	27.60	14.35	3.48
T_{dp} ^oC	16.00	3.10	19.10	10.06	3.15
eo mb	14.44	7.63	22.07	12.57	2.80
Sqrt (eo) $mb^{0.5}$	1.94	2.76	4.70	3.52	0.38
RH %	66.00	33.00	99.00	76.35	11.68
Cloud Height m	2700.	60.	2760.	701.	367.
Tcloud ^oC	26.19	-1.42	24.77	9.79	3.61
Tsky 90^o FOV ^oC	28.63	-5.06	23.57	12.66	4.09
Tsky 3^oFOV ^oC	21.27	-2.32	18.95	9.69	3.64

Table 7. 1: Shows the summary statistics of a total of 1186 of G15 overcast measured temperatures for both 3^o and 90^o FOV. It also shows the weather information, cloud heights and calculated cloud temperature (Tcloud) using equation 6.1.

	Range	Minimum	Maximum	Mean	Std. Deviation
Tair ^oC	18.30	5.70	24.00	13.87	2.96
T_{dp} ^oC	16.00	3.10	19.10	9.91	3.02
$e$omb	14.44	7.63	22.07	12.42	2.65

Sqrt (*eo*) mb$^{0.5}$	1.94	2.76	4.70	3.51	0.36
RH %	64.00	33.00	97.00	77.81	11.16
Cloud Height m	3240.	60.	3300.	706.	536.
Tcloud ^{o}C	25.09	-5.47	19.62	9.32	4.00
Tsky 90^{o} FOV ^{o}C	23.18	-4.18	19.01	10.53	3.61
Tsky 3^{o}FOV ^{o}C	21.16	-2.31	18.86	9.53	3.71

Table 7. 1: Same as table (7.1) but for 578 measurements from STD detectors.

7.3 Results from Overcast Skies at the Zenith

In this section we will review some of the parameters that contribute to the overcast sky temperatures, and the relation between the sky temperature and cloud temperatures. This work was discussed in detail in Riordan *et al.* (2005).

7.3.1 Background

Clouds increase the flux of atmospheric radiation received at the surface because the radiation from water vapor and carbon dioxide in the lower atmosphere is supplemented by the emission from clouds in the atmospheric window (8 μm-14 μm) which lacks gaseous emission (Malek 1997). The IR radiation emitted by a cloud is closely related to the cloud base surface temperature for cloud emissivity characteristics very similar to those of a blackbody. Thus, the long-wave radiation flux measured for totally overcast sky conditions depends strongly on this parameter in all cases where cloud emissivity is close to unity, as occurs in general, in clouds with a high liquid water path Paltridge and Platt (1976). Air temperature and maybe the atmospheric water content also have a considerable contribution to this radiation. The long-wave radiation flux emitted downward by a cloudless atmosphere is appreciably smaller than that emitted by a totally overcast sky or by atmospheres covered by some clouds. For partly overcast skies (broken clouds) the downwelling between the clouds are characteristics of the clear sky. With regard to this, Kondratyev (1969) pointed out that the downwelling infrared radiation flux for fully overcast skies increases considerably as the cloud base height lowers, presenting the highest values in the cases of optically dense and thick clouds having a base altitude close to the ground, mainly because the cloud base temperature is higher, the cloud emissivity is close to unity, and the attenuation of

infrared radiation by the underlying atmosphere is weaker for the radiation emitted by low-altitude clouds than for that coming from high-altitude clouds.

7.3.2 Parameters Influence Overcast Sky Temperature

For fully overcast sky conditions, the main parameters to be considered in the analysis of downwelling IR radiation measurements (represented here by sky temperature) are the true cloud base surface temperature, air temperature and water content.

Figure (7.2) to figure (7.4) show the relations between the overcast measured temperature (for G15 detector with 3^{o} FOV) and these three variables for the full data set. Apart from the group of high level clouds in the left corner of the figures (this set of data may be due to extreme weather conditions at the time of measurements or other factors other than those discussed here) the figures show a clear correlation between the measured sky temperature and the three parameters for clouds at different altitudes. However, the scatter and the dependency are different from one figure to another.

Figure (7.2) indicates that, over the whole range of air temperatures, low-level clouds showed a reasonable correlation, with more proportionality than those found for high level clouds, with sky temperatures. In some occasions clouds at different altitudes have measured sky temperatures the same as those of the air temperatures. This suggests that the clouds appear as a perfect black body with temperatures close to those at the ground level (i.e. they may be efficiently reflecting the ground radiation).

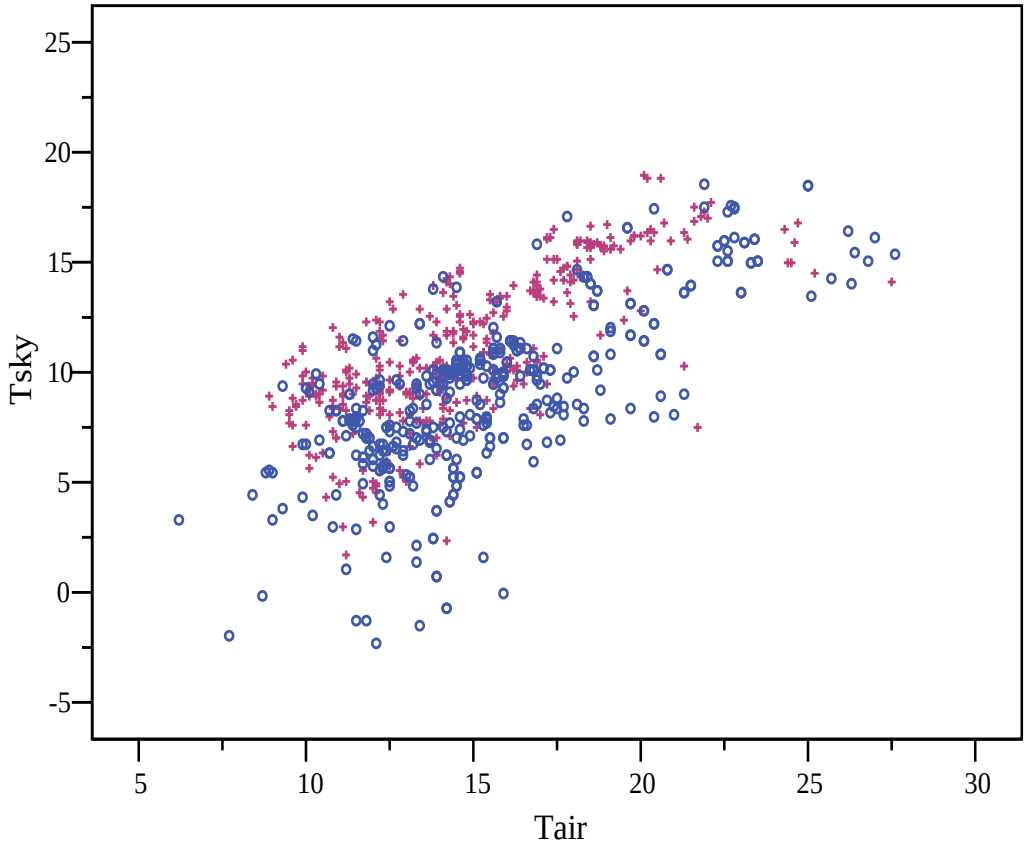

Figure 7. 2: The relation between the air temperature(Tair) and the overcast zenith sky temperature(Tsky) G15 detector with 3° FOV (both in °C). Blue○ represents data for cloud higher than 750m and red+ are for clouds below 750 m. Cloud heights are come from Bureau of meteorology estimate.

Figure (7.3) shows that more than 85% of the cloud estimates lies close to the line of equality of the sky and cloud temperatures. In this case, as suggested by Riordan *et al.* (2005), the cloud monitor measures the cloud base temperature. In this case, the cloud temperature is related to the cloud properties rather than to the water vapour in the intervening atmosphere. This suggests that the measured sky temperature depends on the ground temperature where the cloud emissivity is close to unity, and the attenuation of infrared radiation by the underlying atmosphere is weaker for the radiation emitted by low altitude clouds than for that coming from high-altitude clouds. For those low level cloud data, where the cloud base temperatures do not lie in the equality line with the measured sky temperatures the cloud does not act like a perfect blackbody. This means other factors such as the water content below the cloud may be considered.

On the other hand, the predominant characteristic of measured sky temperatures for high level clouds is that they are far from the equality line with cloud base temperatures. In this case the measured sky temperatures are warmer than the cloud temperature

which suggests that other factors may cause these deviations. This deviation may be due to not allowing for the effect of amount of water vapour in the intervening atmosphere or inaccurate assumption of temperature lapse rate of 6.5 ^{o}C/km used in calculating the cloud base temperature. This implies an actual lapse rate from radiosonde measurements is recommended.

However, some high level clouds actually fall in or close to the equality line. Similar conclusions drawn above for low level clouds can be suggested for those higher clouds which show cloud base temperatures close to the measured sky temperatures.

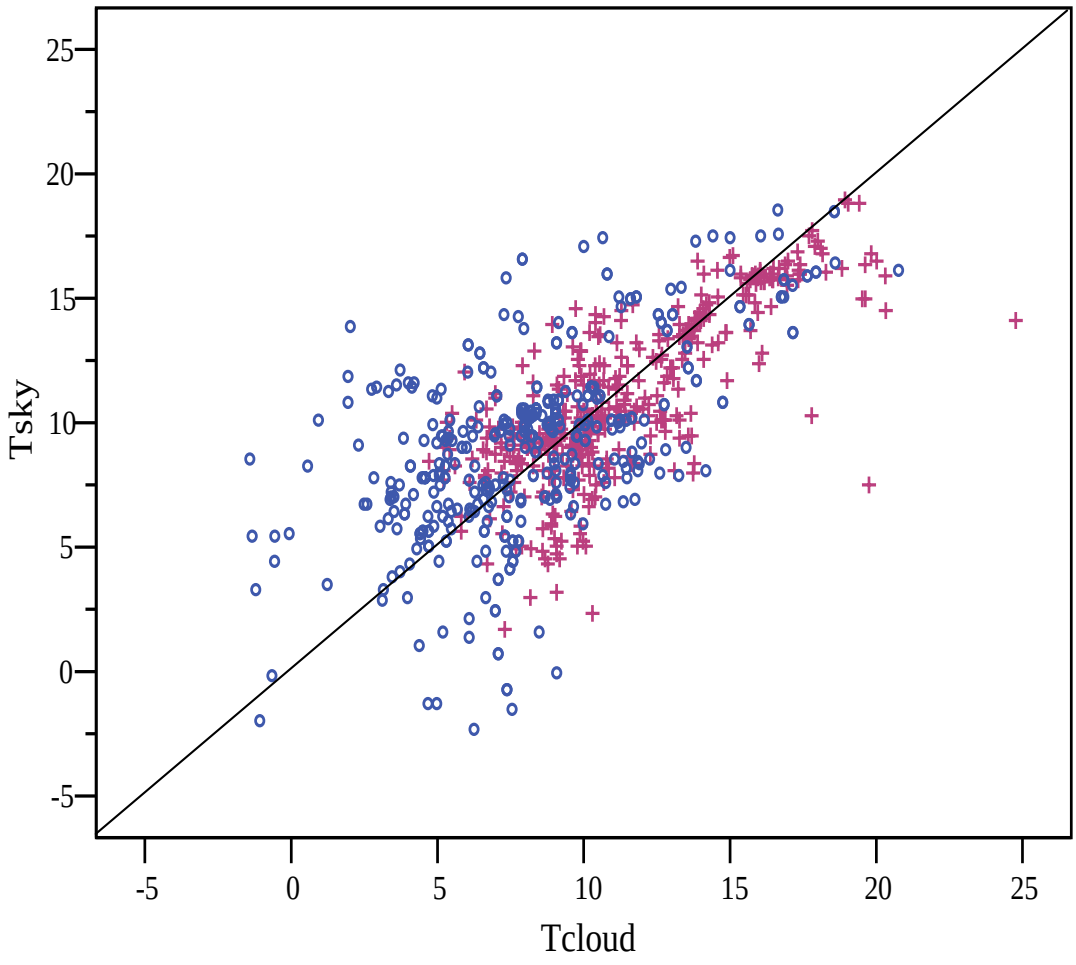

Figure 7. 3: Cloud base temperature, Tcloud, estimated from equation (6.1) vs. measured sky temperature, Tsky ,for the G15 detector with 3^{o} FOV (both in ^{o}C). Blue○ represents data for cloud higher than 750m and red+ are for clouds below 750 m. The line indicates equality of the sky and cloud temperatures.

Figure (7.4) shows the relation between the water vapour content (represented by the square root of vapour pressure) and the measured sky temperatures. Generally speaking, the measured sky temperatures for all level of clouds increase linearly with the amount of the atmospheric water content. The regression analysis (for the G15 detector with 3^{o} FOV) between vapour pressure and the measured sky temperature for *low level* clouds shows a slope of 7.9 and intercept of -18 ^{o}C, while the *high level* clouds shows a slope of 7.29 and intercept of -15.6 ^{o}C. The overall regression line for high and low altitude together shows a slope of 7.3 and intercept of -16.3 ^{o}C which suggests that the amount of atmospheric water, to some extent, has an effect on the measured overcast sky temperatures for cloud at different altitudes.

The dependence of the measured sky temperature of high level cloud on the water vapour content can be explained if the IR atmospheric emission originates below the cloud base where most of the atmospheric water absorption and emission occur. This was found to agree with Allen (1970) and Riordan *et al.* (2005) conclusions. Moreover, the impact of water content on the sky temperatures for low level clouds may be due to presence of low level atmospheric water in some humid nights enhanced by water contents of the clouds themselves. Even at nights with moderate humidity, we may expect a reasonable relation between water contents and sky temperatures. This may be due to the presence of water vapour at low altitudes (see table 2.1) yet below the low level cloud base.

It is advantageous to mention that, in addition to the peak response at 10 µm where the cloud emission occurs, the cloud monitor has a spectral response, which includes spectral regions where the water vapour absorption and emission occur, e.g. (between 5.5 µm - 7 µm and beyond 15 µm). This may assist in explaining the dependence of the overcast sky temperatures on the of water content.

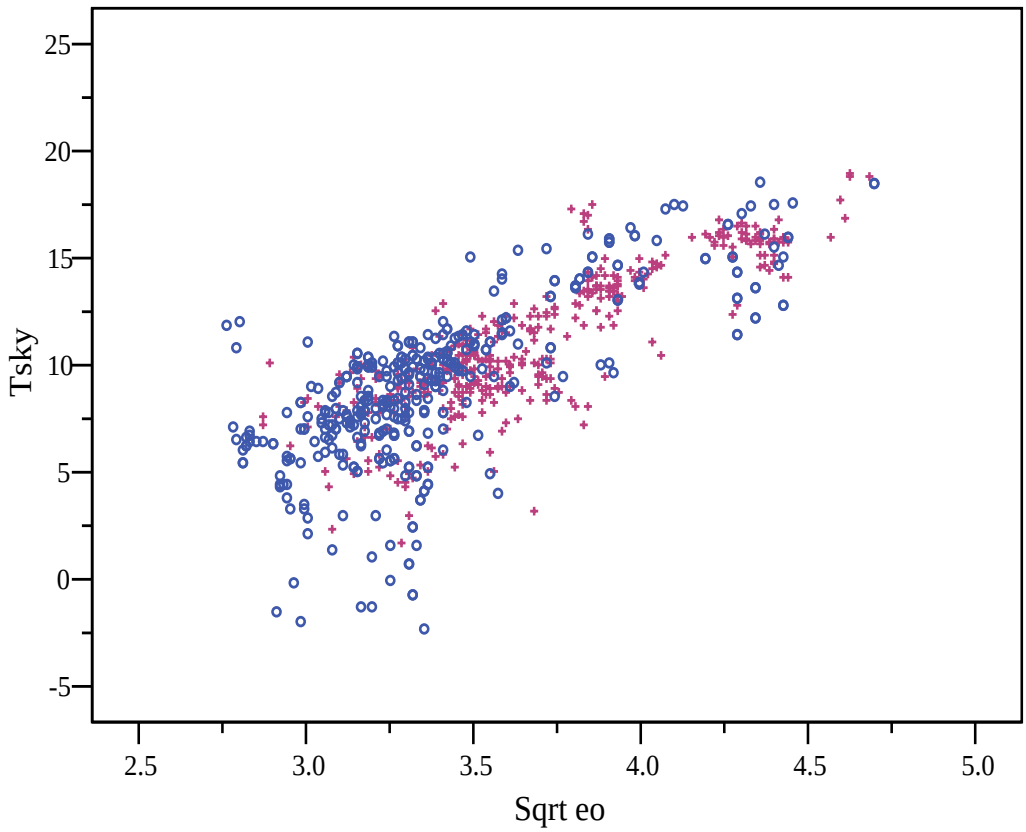

Figure 7. 4: The relation between the square root of vapour pressure Sqrt eo(in $mb^{0.5}$) and the overcast zenith sky temperature for the G15 detector with 3^o FOV (in ^oC). Blue○ represent data for cloud higher than 750m and red+ are for clouds below 750 m.

7.3.3 Parameterization of Overcast Sky Temperature at the Zenith

Although the aim of this thesis is not concerned with further analysis of overcast skies, it is still interesting to see how overcast IR sky temperature is modelled using ground level parameters which can physically describe it.

In the literature, to account for the increase of the cloud's contribution to the IR radiation, authors previously applied empirical corrections to their clear sky estimate. As we discussed in chapter two, this correction is always achieved by having an empirical factor which varies with the cloud amounts and cloud types (Geiger 1965, Sellers 1965).

A multiple regression analysis between the overcast sky temperature and the three parameters described above was performed here. Those parameters are air temperature, vapour pressure and the cloud base temperature as determined from the above assumed lapse rate. The reason of choosing the first two is their physical relation with the

atmospheric conditions between the ground and the cloud base. Additionally, the cloud base temperature is taken into account since it is the most significant parameter defining the intensity of the grey body emission processes of the clouds themselves.

Table (7.3) summarizes the results of the regression analysis (equation of fit, MBE, R^2 and RMSE) and for all filters with 3^o FOV and 90^o FOV for low and high level clouds.

The dependence of overcast sky temperature on these parameters is clear and it is different from one parameter to another as we found before. It is obvious, as it was expected, that the screen temperature is the dominant factor need to be considered. According to the coefficients of the other two parameters, the dependence of the sky temperature on these parameters is weaker. However, as it was found from figures (7.3) and (7.4) that both parameters are necessary to be included in the calculations. Since the cloud temperature factor is linked to the cloud properties (altitude), while the vapor pressure factor is linked to the atmosphere between the observer and the cloud base. Although the correlation coefficients for the parameterizations are not very high, the statistical parameters of the models show low values of MBE and RMSE errors.

Figure (7.5) shows the measured overcast sky temperature plotted against the predicted sky temperature using the formula for G15 detector with 3^o FOV.

Apart from a spread for some low and high level cloud (lower left part of the figure) most of the data distribute evenly around the equality line. This means that, to some extent, the model can predict the overcast sky temperatures with reasonable accuracy using a measurable ground level air temperature and vapour pressure with an appropriate lapse rate.

Filter	FOV	Regression Fit Equations	MBE ^{o}C	R^2	RMSE ^{o}C
G15	3	$Tsky = -12.78 + 0.12Tcloud + 0.28Tair + 4.85Sqrt(eo)$ (7.2)	-0.15	0.82	2.10
G15	90	$Tsky = -11.64 + 0.020Tcloud + 0.67Tair + 4.07Sqrt(eo)$ (7.3)	0.01	0.88	2.10
STD	3	$Tsky = -11.89 + 0.11Tcloud + 0.51Tair + 3.71Sqrt(eo)$ (7.4)	-0.03	0.81	2.2
STD	90	$Tsky = -7.90 + 0.08Tcloud + 0.72Tair + 2.16Sqrt(eo)$ (7.5)	0.10	0.84	2.03

Table 7. 2: Shows the regression equation of the overcast sky temperature in ^{o}C as a function of cloud base temperature (Tcloud), air temperature (Tair) both in ^{o}C, and square root of vapour pressure (Sqrt(eo) in $mb^{0.5}$). It also shows the MBE, R^2 and the RMSE of the regression results.

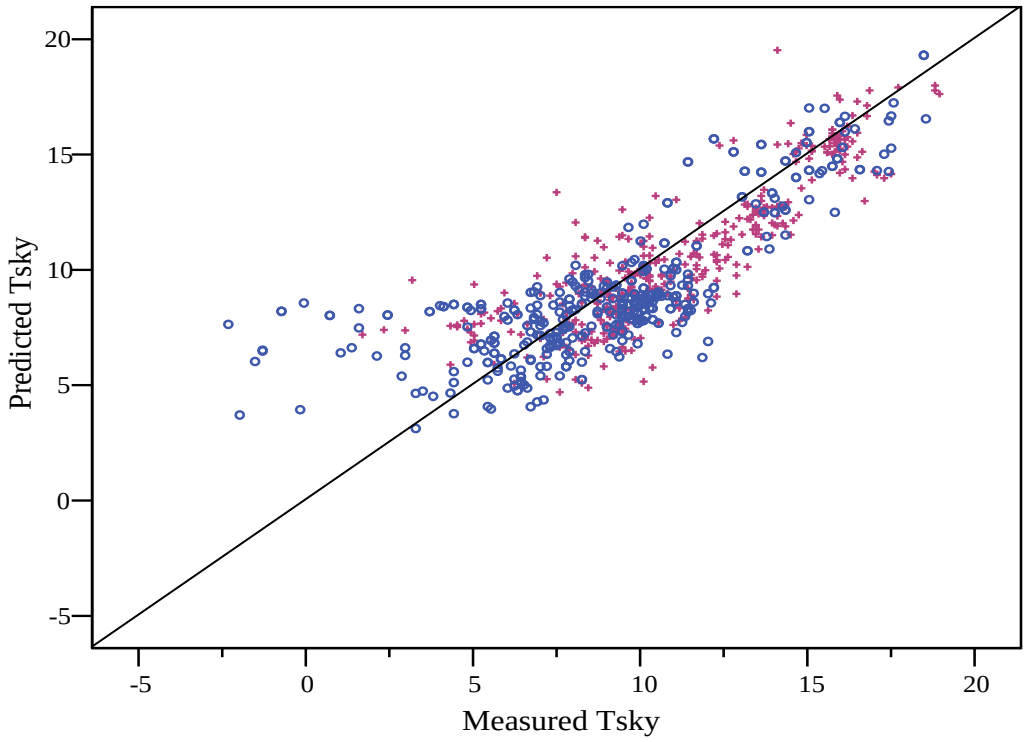

Figure 7. 5: Measured overcast sky temperature for the G15 with 3°FOV (in °C) versus the predicted sky temperature using equation (7.2) for low level clouds (red +) and high level clouds(blue○)t . The straight line is 1:1 for reference.

7.3.4 Zenith Angles Dependence of Overcast Sky Temperatures

Figure (7.6) shows the relation between the overcast sky temperatures and the zenith angle from the zenith to the horizon. It is based on the average values of 1186 observations from G15 detectors. The outstanding features of the graph are the negligible increase of sky temperature from the zenith down to a zenith distance of 30° and the large increase from 70° toward the horizon where the sky temperature reaches almost that of the blackbody temperature of the air temperature. At the horizon, the overcast temperatures, as was suggested for clear sky temperatures, are very close to the ground (or screen level temperature). The sample of overcast sky temperature dependence on the zenith angle is similar to that found for clear skies, compare figure (5.1) with (7.6)

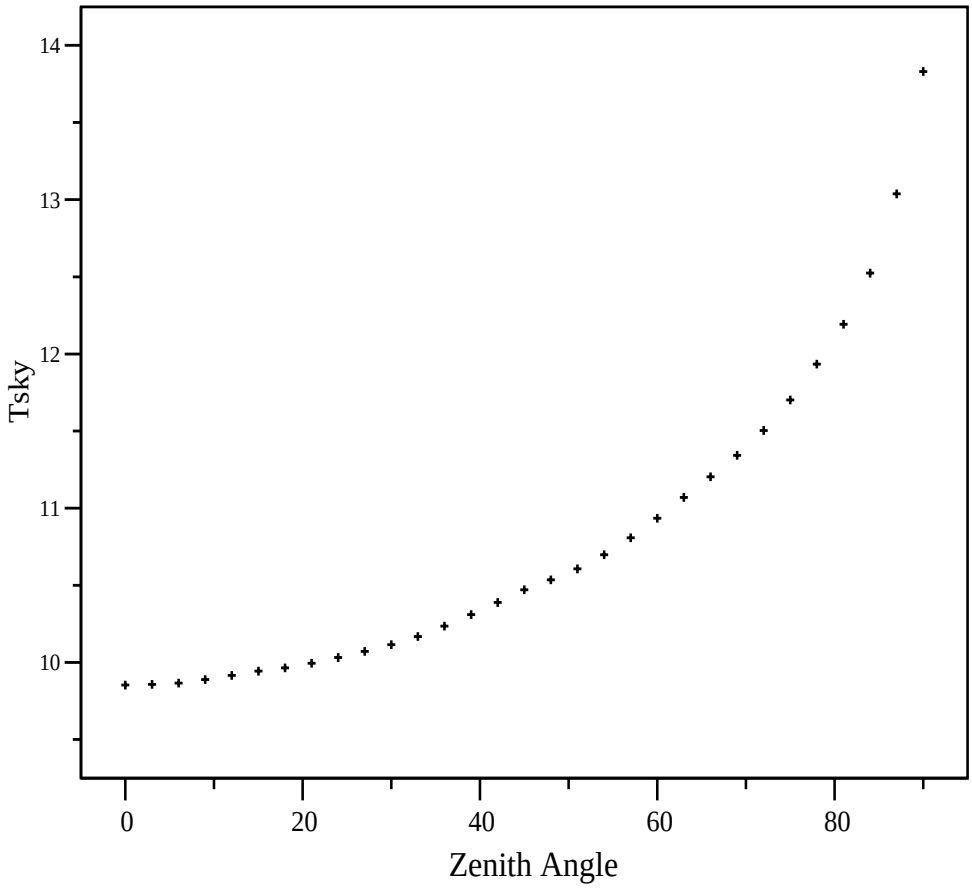

Figure 7. 6: Zenith angle variations of the averaged overcast sky temperatures over the period of study for the G15 detector. The average meteorological variables are Tair 14.34, Tdp 10.05 ^{o}C, eo 12.56 mb, Sqrt eo, 3.52 $mb^{0.5}$, Tcloud 9.78 ^{o}C (units as table (7.2).

7.4 Discrimination between Clear Sky and Cloud

7.4.1 Totally Overcast Skies

In chapter 4 we proposed a model for predicting clear sky temperatures at the zenith using the screen level temperature and water vapour pressure. This model was then extended in chapter 5 to predict the clear sky temperature at different zenith angles close to the horizon.

We now consider the use of the clear sky models (at the zenith or at any zenith angle) in predicting the presence of clouds. Additionally, a level which discriminates between clear sky and cloudy skies either partly or totally overcast, will be set. In the rest of this section the proposed formulae for G15 detector will be used similar results can be

applied for the STD detectors. Also, the models considered here are those having the screen level parameters in their functional forms e.g. for G15 equations (4.32) (5.11).

A Mathematica procedure was designed to accomplish the purpose of this section and the following section. The code works as the following.

1. The code reads each overcast sky scan individually from the data base.
2. At each zenith angle, the code calculates the expected clear sky temperatures from the clear sky models.
3. The measured sky temperatures, clear sky predicted temperatures and the difference between these two temperatures at every zenith angle are then stored.
4. The above steps are then repeated for all the scans in consideration.

Figure (7.7) shows a comparison between the measured overcast temperature and clear sky predications based on the clear sky parameterization at different zenith angles for all the 1186 scans. The intention is that one would measure the screen level parameters and compare the predicted clear sky temperature with the actual measured temperature. A substantial deviation of the observed temperature from the clear sky prediction would indicate the presence of cloud in the field of view.

Figure (7.8) concludes the results of this section. It shows the relationship between the zenith angle and the *mean* temperature difference between measured overcast skies and clear sky predictions (MBE). From the zenith to 63^o the difference is always more than 20 ^{o}C, which means that the overcast sky is at least 20 ^{o}C warmer than the clear sky under the observed physical conditions at those zenith angles. This discrimination falls almost linearly with angle from about 15 ^{o}C at 80^o to about only 3 ^{o}C at a zenith angle of 87^o.

Hence, except under the most extreme conditions, a discrimination condition for recognizing cloud can be readily defined and used in practice to discriminate between clouds and clear sky.

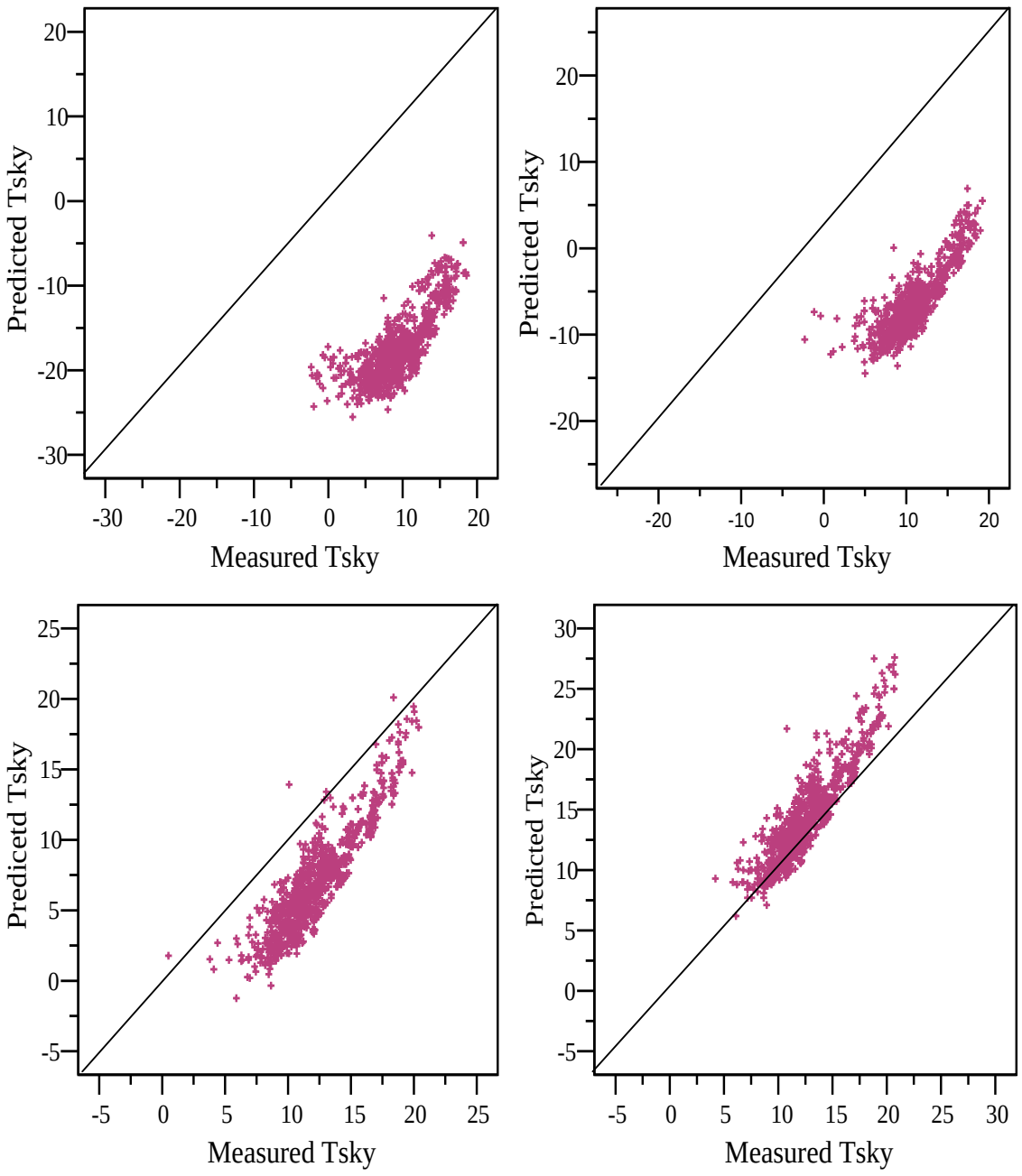

Figure 7. 7: Comparisons between the predicted temperatures using the clear sky model (in ^{o}C) and the overcast measured temperature at zenith angles from top left (0^{o}, 70^{o}, 84^{o} and 87^{o}). The straight line is 1:1 for reference.

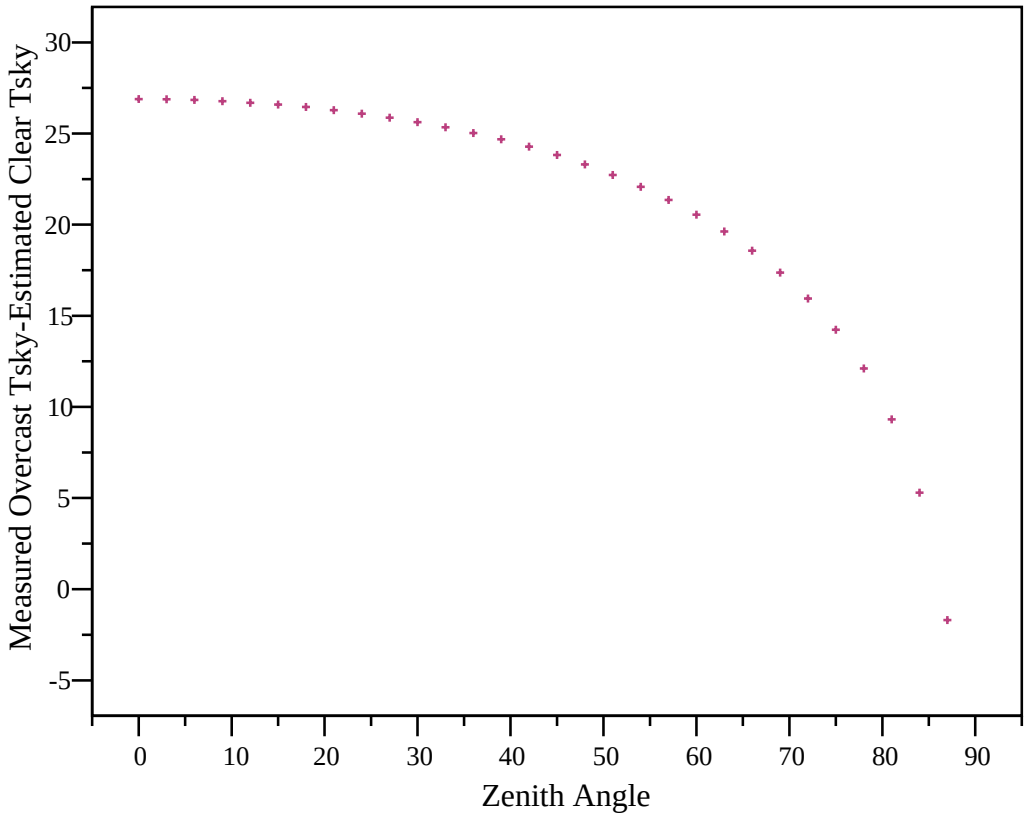

Figure 7. 8: Shows the relationship between the mean difference between the observed and predicted clear sky temperatures (in ^{o}C) and the zenith angle for G15 detector for the full dataset.

7.4.2 Partly Overcast Skies

We usually deal with partially overcast skies, where the sky exhibits both clear and cloudy conditions at the same time. The aim of this subsection is to investigate the selection of clear areas of sky out of partial cloud cover.

In the case of partly overcast skies, we can assume that the thermal emission (or sky temperature) measured over a sky containing both clouds and clear sky can be estimated in direct proportion to the cloudless and cloudy-sky fractions. Thus the sky temperature coming from partly overcast sky can be evaluated as algebraic sum of partial contributions made separately by cloudless and cloud covered parts of the sky

On the basis of studying partly overcast skies, data used here are limited to sky conditions between clear and overcast skies. The steps of selecting partly overcast sky data were referred to in chapter 3 and will be reviewed here.

In selecting partly overcast skies, two steps were taken. Firstly, the data was limited to those data having an amount of clouds greater than 2 octa and less than 7 octa.

Secondly, scans were selected on the basis of irregular structure from the scanner detectors (see figure 3.17). The general rule (and expectation) is that the sky temperatures of partly overcast sky will be in the range of temperatures between clear sky (cold temperature) and overcast sky (warm temperature) for the same atmospheric conditions of air temperature and water vapour. This means that the structure of partly overcast sky is expected to lie between those two ranges of temperatures. It turns out that this is always the case for partly overcast temperatures from the scanner detectors. Figure (7.9) shows an example of from the scanner from the zenith to the horizon for the three sky conditions. The clear sky is represented by a curve, which shows cold temperatures, and the overcast sky has a curve with warmer temperatures. On the other hand the partly overcast smooth curve moves between these two curves.

A total of 230 night-time data points were selected randomly during the period from 2001 to 2004 and judged to meet the above criteria.

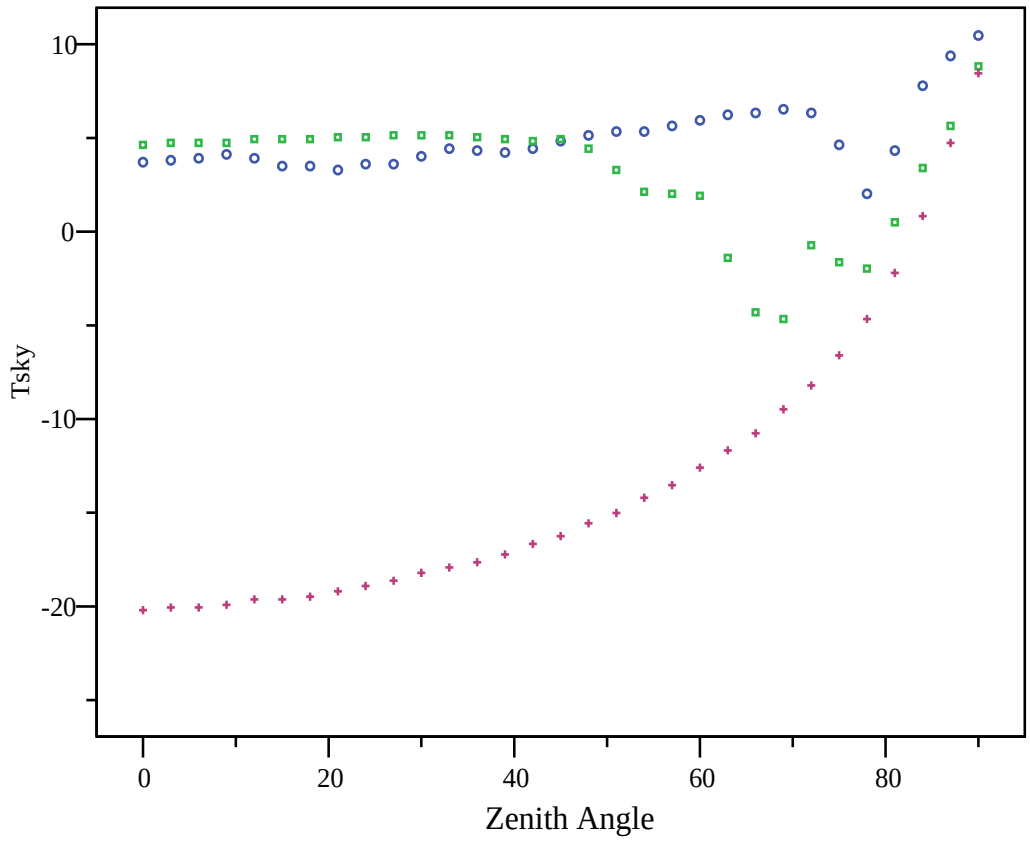

Figure 7. 9: Shows an example of three scans from the zenith to the horizon from a G15 detector having the same air temperature and atmospheric water contents from zenith to horizons. It shows the variation of the sky temperature for clear sky (Red +), totally overcast sky (Blue ○) and partially overcast sky (Green □) with zenith angle.

Following the same procedure as in subsection (7.4.1), the clear sky models for G15 were also used here to compare the predicted clear sky with measured partially overcast sky temperatures. Figure (7.10) shows a histogram of difference between the predicted clear sky temperature and the measured temperature at the zenith for partially overcast skies. In this case the actual cloud cover was unknown. However, the figure shows clustering close to a temperature difference of zero, which indicates that clear sky can be correctly identified. On the other hand, large differences between the predicted and measured temperatures showed the pattern exhibited by overcast skies.

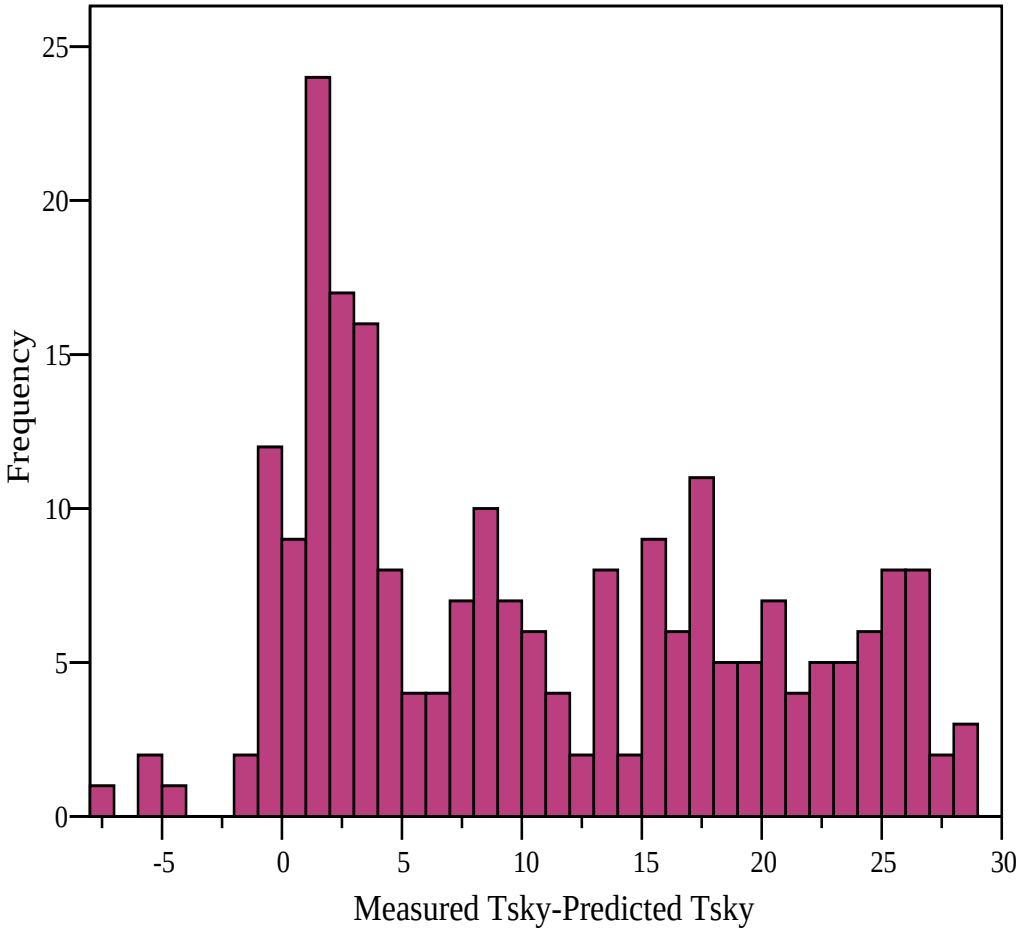

Figure 7. 10: Histogram showing the difference between the predicted clear sky temperature and the measured temperature at the zenith for partially overcast skies.

7.5 Comments on the Accuracy

Although different data sets and different period of times were considered, the results presented in this chapter showed compatibility with those found by Riordan *et al* (2005). However, the effect of the screen water vapour was not considered in their investigations for low-level clouds, while here it is assumed that it has an effect on both low level and high-level clouds. Also, radiosonde data were used in their study to determine the actual lapse rate and a ceilometer was used to determine the cloud altitudes, where here data, particularly cloud altitudes, were used as provided by the Weather Bureau.

It is worth mentioning that the errors in either measurements or results found in this chapter may be considered under one of the following categorise:

1- Error in measured sky temperatures.
2- Errors in screen level measurements of temperature and water vapour.
3- Errors in cloud height measurements and informations
4- Errors due to not considering the cloud types, at the same height.
5- Errors in the assumed lapse rate, in which the actual lapse rate is necessarily for more accurate results.
6- Ceilometer and radiosonde data were also desired to give more reliability to the results presented here.
7- Cloud emissivity was not evaluated nor considered in this study and the cloud base temperature was assumed to be the parameter that represents the cloud properties.

The first two errors are less probable since the cloud monitors are calibrated and throughout the period of interest have shown a stable performance. Moreover, the screen level measurements of temperature and vapour pressure are assumed to be correct and are quality controlled by the Weather Bureau.

Cloud height measurements, cloud types and cloud covers were obtained from the Weather Bureau without any information about the methods used to measure them. However, the Bureau estimations of these parameters are usually determined by visual observation from trained observers. Some errors in determining the actual cloud base altitude are expected. The impact of different types of cloud at the same level can cause substantial errors in the results. For example low level cloud has more than several types in which the features of each type are different from each other in distribution, water liquid contents and shape. This effect was not considered either in

this study or by Riordan *et al.* (2005). The assumption of constant lapse rate may be considered as one of the major impacts on the determination of the cloud base temperatures particularly high-level clouds. It differs from time to time and from season to another, and real lapse rate is desirably needed. This sounds impractical in most of the circumstances but at least it is practical to have a reasonable lapse rate for different seasons. Radiosonde data which can be used to determine the cloud height (in addition to ceilometer measurements) and used to define the actual lapse rate are important in such investigation to give better results.

While these errors are important in assessing any investigations it was expected that their contributions to the final results, especially to those presented in the first part of the study, will not be more than 5-10% of the actual values of sky temperatures either measured or predicted. With or without considering these errors the results of comparisons presented in the second part of this study can be considered to be reliable and accurate. This is because the factors considered to have impact on the results (such as cloud heights) are not considered in comparison situations.

Results presented in the second part of this study have shown promising results for the clear sky models proposed in this thesis in predicting the presence of clouds in the field of view of any astronomical or astrophysical observatories having similar conditions to those found in Adelaide.

CHAPTER EIGHT

DATA FROM FOUR SITES IN SAUDI ARABIA

8.1 Introduction

The aim of this chapter is to study the IR sky temperature measured with the cloud detectors by operating them in different climate conditions, extending beyond those found in Adelaide (chapter 4) and Auger (chapter 9) sites. It also examines the performance of these detectors when they operate at extreme weather conditions and optimizes their capabilities of measuring atmospheric radiation and cloud predications. Successful results from this chapter will help the author to initiate a proposal for atmospheric monitoring program in Saudi Arabia using these monitors.

Direct measurements of IR sky temperatures obtained by cloud monitors and meteorological parameters from four sites in Saudi Arabia in the years 2004-2005 were collected, analyzed and their results are presented here.

The chapter starts with a summary of the geographical locations and climatological properties for the four sites. The instrumentation and data collection will be discussed in section 8.3. The analysis procedures and data treatment will be reviewed in this section too. The results, section (8.4), will be discussed in two main parts. The results obtained from 90^{o} FOV cloud monitors will be presented in the first part. Here, data from each site will be presented separately. Results from these sites will be put together for evaluation and unified conclusions from all sites will be given at the end of this part. In the second part results from a 3^{o} FOV cloud monitor will be discussed.

8.2 Sites Description

IR sky temperature measurements were made at four sites in Saudi Arabia. These were Jeddah, Abha, Tabouk and the capital Riyadh. The sites were selected to have a wide range of atmospheric conditions ranging from extreme warmth and moisture to extreme dryness. Abha lies at about 1600 km southwest of Riyadh; Jeddah is located approximately 1000 km southwest of Riyadh while Tabouk is approximately 1200 km northwest of Riyadh, see figure (8.1).

Abha is located at (18° 13′ N; 42° 30′ E, 2200 m a.s.l) in the southwest of the Kingdom. The southern region is the relatively fertile area of coastal mountains in the extreme southwest (near Yemen). Mountain peaks rise to 3,000 m and there is ample rainfall to support natural vegetation and cultivation. Abha's altitude of 2200 m above sea level gives it a relatively moderate climate. Temperatures remain within a narrower band than is the case in many other parts of the Kingdom. The Abha region also has the highest level of rainfall of any part of Saudi Arabia. For much of the year there are cloudy skies, particularly in winter. Clear conditions tend to occur during summer.

Riyadh lies in the central region at (24° 43 ′N; 46° 40′E, 692 m a.s.l). The central region is considered to be a vast eroded plateau 600 meters above sea level, consisting of areas of uplands, broad valleys and dry rivers. The area also contains a number of marshes. These are thought to be the remnants of inland seas, which existed in ancient geological times.

A costal city, Jeddah is located in the western coast part of the country at (21° 31′N; 39°13′E, 10 m a.s.l), on the shore of the Red Sea. A tropical climate is dominant in Jeddah with the relative humidly reaching 98 % sometimes. Average temperatures are 23^{o}C in January and 32^{o} C in July. High levels of water vapor are always found in Jeddah.

Tabouk is situated in northwestern Saudi Arabia at (28° 23′ N; 36° 34′ E, 620 m a.s.l). Standing high above sea level, it has an equitable climate with an average temperature of 22 °C.

Figure 8. 1: Map of Saudi Arabia shows the geographical location for the four sites used in this study.

8.3 Observation and Data Collection

8.3.1 Instrumentation and Data Collection

The experiment started at the four sites on the summer of 2004 although it was not simultaneous at all sites. For instance, the first set of collected data for some sites started in June while other sites started in July, but still in the same season.

IR sky observations were made using a STD filtered cloud monitor described in chapter 3. Except for Riyadh, which had a 3^o FOV, all the three sites were equipped with a 90^o FOV monitor. Data from the Jeddah site were obtained for the summer of 2004 (June-August) and the following winter of 2005 (January-March). Similarly, data from the Abha site were acquired for the summer of 2004 (August-September) and the next winter of 2005 (January-February). Tabouk is the only site which has data for the winter of 2005 (January-March). Riyadh has data for about two years including two summers, two winters and one spring.

In Abha and Tabouk the experiments were conducted at their airports. At Riyadh, the detector was placed on the roof of the King Abdulaziz City for Science and Technology (KACST), 30m above the ground, at 10 km from Riyadh Airport. On Jeddah the detector was installed at the roof of King Abdulaziz University (KAAU), 25 m above ground and 12 km from Jeddah Airport.

The data acquisition systems were XR5-8-A-SE data loggers manufactured by Pace Scientific. In addition to the three outputs from the cloud detectors, the loggers have internal sensors to measure the humidity and the surface temperature. The data from each of the loggers and from the cloud detector are recorded in 10 minute intervals. The accuracy of the logger's sensor measurements is +/-2 % humidity and +/ -0.15 ^oC at a temperature of 25 ^oC.

Hourly data were used in the analysis to avoid clustering of data over a short range of conditions. Ground level measurements of meteorological data, cloud visual observations and radiosonde measurements were obtained directly at the study site or from the nearest weather station (or airport) operated by the Saudi Meteorological and Environmental Protection Agency (MEPA).

The dew point temperature, T_{dp} and vapor pressure were, *eo*, calculated using the measured relative humidity and air temperature from equations (3.19) to (3.18).

The data from MEPA were used for comparison and for checking the accuracy of the air temperature and relative humidly measured by the loggers as well as the calculated dew point temperature. No major differences were found between logger/calculated records and those measured by the MEPA. For example, the difference between the calculated T_{dp} and the measured values was always below 2 ^{o}C.

The routine radiosonde launch times are near 0300 and 1500 local standard time (LST). Night time radiosonde measurements at 0300 were used for selecting clear sky times as well as calculating the total amount of atmospheric water PWV.

At each site, the assembly of the cloud monitor and the logger was installed in a stand especially designed by KACST for the purpose of this study. At the top of the stand the cloud monitor was installed vertically. Underneath, the logger sat inside a ventilated box figure (8.2).

During the period of operation all the cloud monitors showed a linear and stable performance. No significant changes in the detector and the logger system sensivity have been identified, even after continuous exposure to extreme weather conditions. Regular hardware checks were carried out for the systems. Apart from changing the batteries at some stations no major breakdown or any faults were found

Figure 8. 2: Shows the setup of the monitor/logger system at the field site.

8.3.2 Clear sky selection

Night time clear sky data were selected for each site and used in this study. In selecting suitable clear sky times, three methods were used.

1. The visually observed total cloud cover reported by MEPA at or near the site has to be less than one octa. However, cloud information is kept in daily files in MEPA database, hence information for some periods during specific nights were not available. Yet, this method was used as an initial tool to identify the clear sky nights.
2. Plotting sky temperature versus time for the desired night when the cloud cover less than 1 octa was then performed. As we saw in chapter 3 cold temperatures represent clear sky and warm temperatures indicate low cloud. High-level clouds may well not be detected using this technique. Such clouds have a minimal impact on the ground level atmospheric radiation. This method is illustrated in figure (8.3).
3. A third method was used when radiosonde data were available. Here air, and dew point temperatures were plotted against the height, if they met each other this means that the relative humidity was 100% and that the ascent of the radiosonde was probably intersected by a cloud. Having taken these criteria into accounts, the clear sky data were selected and became available for the analysis.

These there methods together form excellent procedures for selecting clear sky times. However, in the absence of radiosonde data the first two methods can be adequately used with good confidence in selecting clear skies.

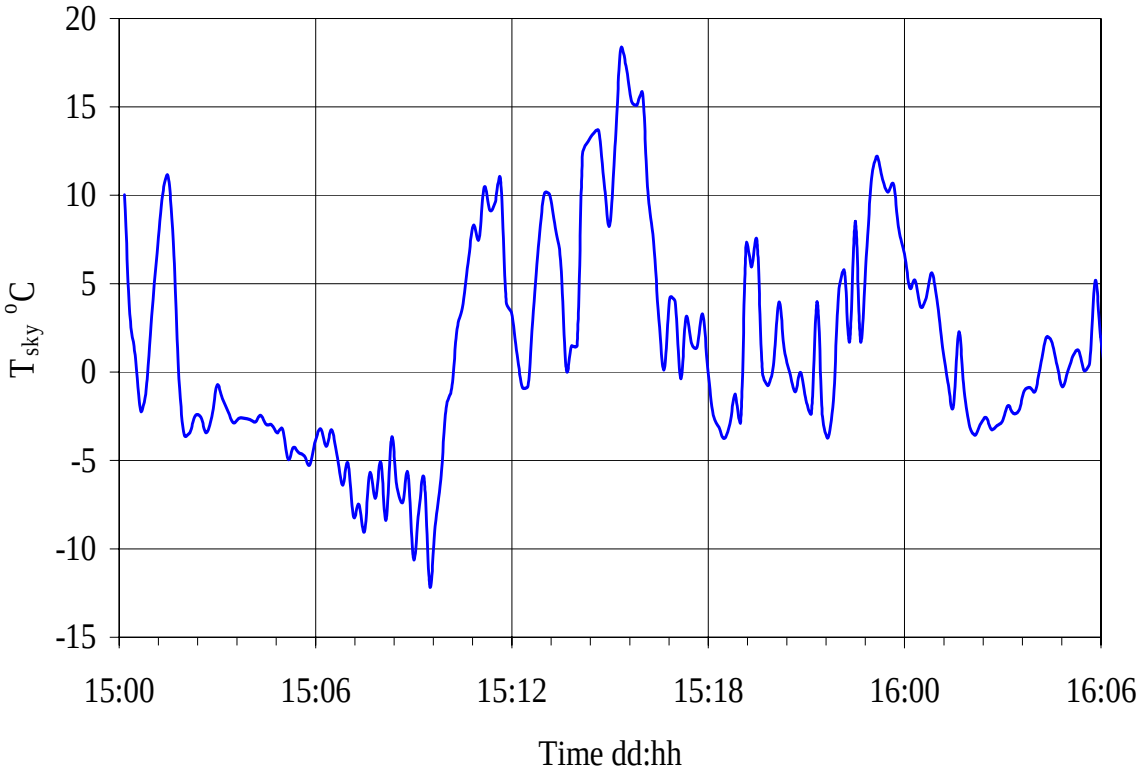

Figure 8. 3: Example shows a plot for two nights with different sky conditions between 15.8.2004 midnight to 16.8.2004 morning. The night starts with some clouds (positive T_{sky}) and then the sky becomes clear (negative T_{sky}) between 3am to 9 am. The sky conditions then varied between clear and cloudy until the next morning.

8.3.3 Procedures and Data Analysis

Selected night time data for clear skies described in the previous section were used in this study. Sky temperature corrections using the calibration formulae described in chapter 3 for the STD 3^o FOV and 90^o FOV filters were applied.

For a single site the procedure for analyzing the data is similar to that discussed in chapter 3 and followed in chapter 4. This is briefly discussed here.

Firstly the clear sky temperatures were correlated with a single independent meteorological parameter. Multiple regression analysis was then applied to establish the models that optimize the prediction of the clear sky temperatures and minimize the errors. The resulting formulae for each site were considered as the preferred ones in predicting the clear sky temperatures. Comparisons were then made between measured and predicted sky temperatures, using these formulae, against some of the bulk models found in the literature were then performed.

A unified model, if it could be found, containing data from all sites was then investigated.

8.4 Results from 90^{o} FOV Detectors

The average measured values of data for selected clear sky times for the three sites are presented in table (8.1). The table summarizes some of the measured/calculated meteorological variables and sky temperature for the corresponding period of running the experiment. The PWV was obtained by integrating the radiosonde profile up to 11 km. (See chapter 4.)

From the point of view of climatic characteristics, the three study sites lie in the transition area from tropical to continental climate zones, thus possessing relatively mild and moderately humid climates.

Each site has unique climatological characteristics. In winter periods, for example, Abha is warmer than Tabouk despite its greater altitude. It also has greater PWV. The sky temperature on the other hand, does show a decrease (toward negative values) with altitude, and an increase (toward positive values) with the PWV and air temperatures.

In the following discussion there will be an emphasis on variations of the clear sky temperature with the three parameters that have a major impact on it. These are vapor pressure, air temperature, and PWV.

	N	RH %	PWV mm	T_{dp} ^{o}C	Sqrt eo mb$^{0.5}$	Ta ^{o}C	Tsky ^{o}C	Period
Abha	230	41.92	12.87 (29)	1.59	2.68	18.72	-6.87	Aug-Sep 04,
	152	63.61	10.2 (16)	4.46	2.94	11.66	-8.78	Jan-Feb05
Tabouk	233	50.47	8.46 (48)	-1.23	2.38	9.27	-6.70	Jan-March 04
Jeddah	166	69.22	28.9 (41)	22.46	5.22	30.82	11.78	June-Aug 04
	171	79.19	23.97 (46)	16.67	4.37	22.03	14.44	Jan-March2005

Table 8. 1: Shows the mean values of the measured meteorological variables and the sky temperature at the 3 sites, which have 90^{o} FOV detectors. These values are RH,PWV, T_{dp} , Square root of vapor pressure (Sqrt (eo)), T_{air}, sky temperature T_{sky} and the period of measurements. N is the number of observations. The numbers in brackets in the PWV column represent the number of the coincident radiosonde ascents during this period of time.

8.4.1 Abha

Figure (8.4) shows the relation between the sky temperature and three parameters considered in this study for Abha over the two seasons. In this figure, the general trends between the sky temperature and those parameters are evident. There is an increase in the sky temperature with the increase of any of these variables. However, the degree of dependence is known to be affected by other factors, e.g. wind speed or air pressure variations, and may be slightly different from season to season.

The seasonal variations are apparent in this graph. The spread in the data is also obvious, being different for each season. Apart from overlap between the two seasons around 17^{o}C, the air temperature between the two seasons is well separated. The range of summer temperature for Abha was between 14 and 25 ^{o}C, while the range of winter temperatures was between 5 and 17^{o}C. This seasonal behavior of the air temperature has a great effect when parameterizing the sky-air temperature relationship. For example the slope and the intercepts of the regression between sky temperature and air temperature changed from 1.7 to 0.7 and from –28.4^{o} to –19^{o}C respectively from winter to summer. The PWV in both seasons also vary from night to another according to the atmospheric conditions. For example higher values of PWV are reported on cold winter times and vice versa, which mean that other factors may be added. Screen vapor pressure correlated better with the sky temperature over the two seasons with slightly different slopes. This seasonal dependence is not discussed much in the literature. Several investigators such as Swinbank (1963) and Berdahal (1982) have presented data from different sites with different atmospheric conditions for different seasons but rarely found such non-overlapping data in the atmospheric conditions.

Moreover, in analyzing Adelaide data seasonal variation was not truly evident. The cause of the extreme seasonal variations in Saudi Arabia may be due to the instability of the atmospheric conditions, as well as the impact of the micro-climatological factors over a single site. The sky temperatures for summer and winter times range between –17^{o}C to 0 ^{o}C and –23^{o}C to 3 ^{o}C respectively. These ranges are reasonable and they match those measured in Adelaide with the same conditions and the same filter.

The results of the multiple regression analysis (functional forms, MBE, RMSE and R^2) for Abha, Tabouk and Jeddah sites are summarized in table 8.2.

In the following discussions, *model1* will be used to define the model that contains the ground level air temperature and the square root of vapor pressure while the model which contains the air temperature and the PWV measured by radiosonde as fitted

parameters will be called *model2.* This is applicable in the discussion for the other three sites

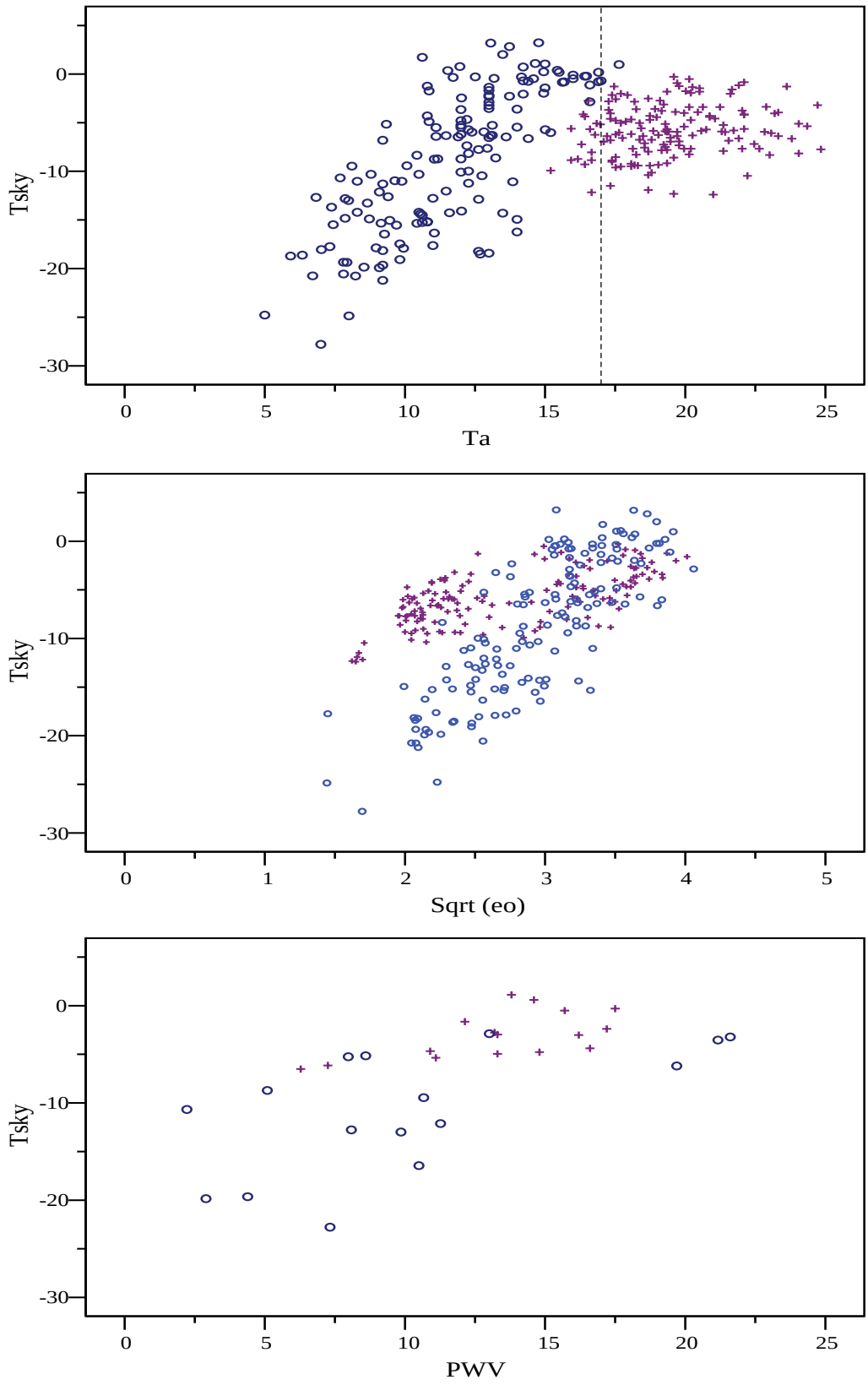

Figure 8. 4: Shows the variations of the sky temperature Tsky ^{o}C with air temperature Ta ^{o}C(top), square root of vapor pressure $mb^{0.5}$ (middle) and PWV mm (lower), for Abha for both seasons, summer violet + and winter blue ○. The line in the top panel was set at reference Ta at 17^{o} C, the boundary between the two seasons.

	N	Functional Form	MBE ^{o}C	RMSE ^{o}C	R^2 %
Abha	382	$Tsky = -23.36 + 5.36Sqrt(eo) + 0.52Ta$ (8.1)	–0.16	2.9	0.80
	55	$Tsky = -23.8 + 0.48PWV + 0.78Ta$ (8.2)	-0.55	3.0	0.83
Tabouk	233	$Tsky = -18.85 + 1.83Sqrt(eo) + 0.97Ta$ (8.3)	-0.10	2.5	0.87
	48	$Tsky = -17.7 + 0.21PWV + 1.44Ta$ (8.4)	1.1	3.3	0.88
Jeddah Summer	166	$Tsky = -31.06 + 3.5Sqrt(eo) + 0.71Ta$ (8.5)	0.37	3.2	0.6
	41	$Tsky = -41.4 + 0.29PWV + 1.49Ta$ (8.6)	-0.09	3.8	0.7
Jeddah Winter	171	$Tsky = -20.109 + 2.5Sqrt(eo) + 1.062Ta$ (8.7)	-0.25	1.16	0.95
	46	$Tsky = -13.9 + 0.20PWV + 1.16Ta$ (8.8)	1.1	1.2	0.94

Table 8. 2: Summarizes the parameterization of the clear sky temperatures as a function of (Ta, Sqrt (eo)) and (Ta, PWV) for the three sites. It gives the number of observations (N column), equation of the regression, MBE (difference between measured and predicted temperatures using the model) RMSE and correlation coefficient.

Figure (8.5) shows the measured sky temperatures versus the predicted temperatures using *model1* and *model2,* equations (8.1) and (8.2) respectively, for Abha site. The straight lines in the figures show the 1:1 ratio for reference. For a reasonable amount of data and wide range of temperatures both models can fit the measured sky temperatures with good accuracy. The RMSE for *model1* and *model2* were 2.9 and 3.0 ^{o}C respectively, while the MBE were –0.16 and –0.55 ^{o}C respectively. However, deviations from the measured values by more than 7 ^{o}C were found in some predictions using these two models. There are many reasons that may explain these deviations such as extreme conditions in some nights over the period of interest. For example the change of thickness of the water vapor layer in some winter nights may be the reason for the deviation of the group of points from the 1:1 line in the left part of figure (8.5). But generally speaking, the predicted sky temperatures are reasonably distributed about the equality lines in both figures.

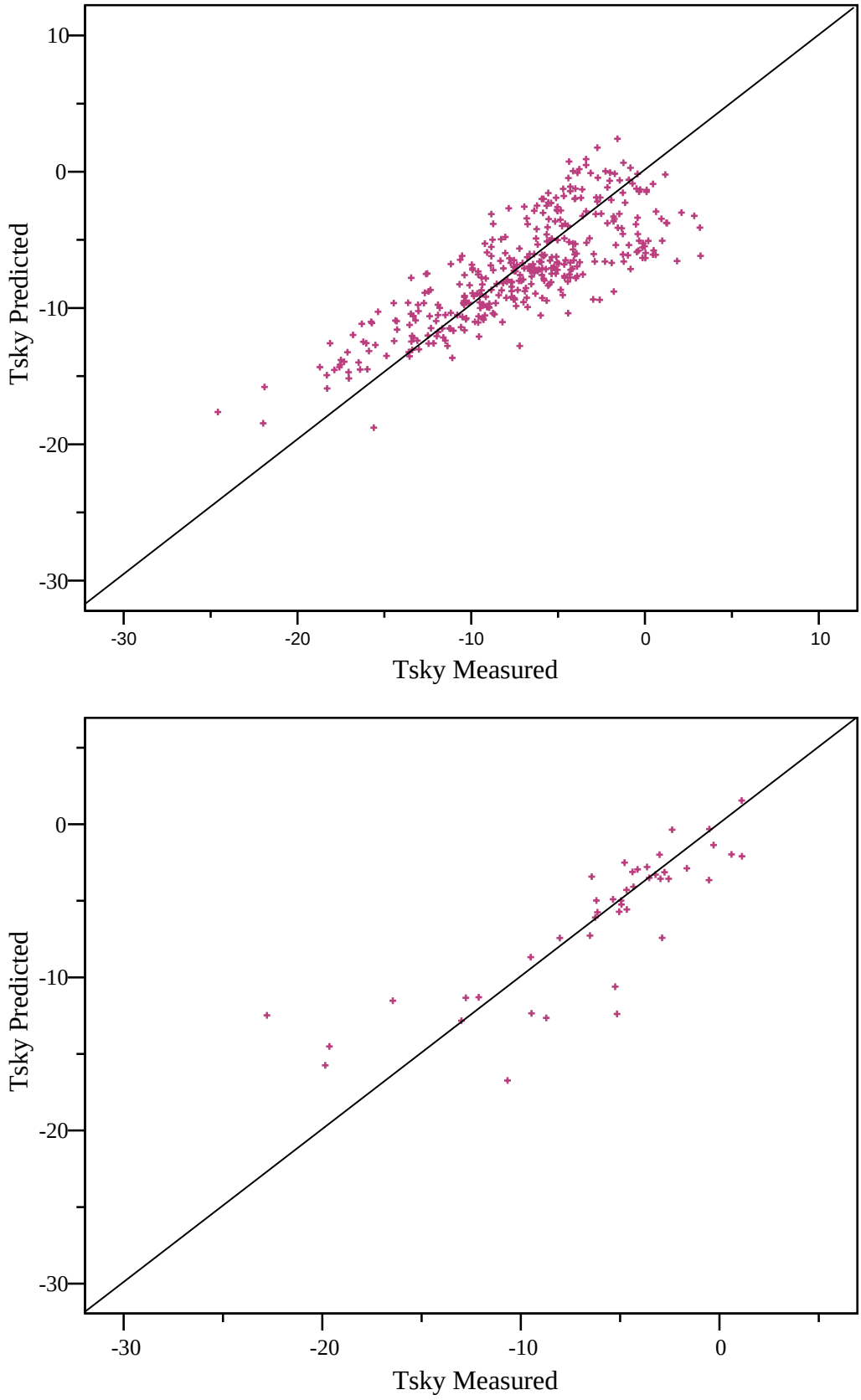

Figure 8. 5: Hourly clear sky temperature estimated from model1 (top) and from model2 (bottom) versus the measured Tsky for Abha site over summer and winter The straight line is the 1:1 line.

8.4.2 Jeddah

Figure (8.6) shows the relation between the sky temperatures and the three meteorological variables considered before for Jeddah site. In Jeddah the situation is almost the same as Abha in terms of the non-overlapping of the data from season to season. However, the situation in Jeddah is more observable and the air temperature over the two seasons is well separated as a consequence of the extreme difference in conditions between summer and winter in Jeddah. Jeddah has a tropical climate and the temperature ranges are confined to a small range. For example in winter the temperature range in Jeddah is between 14 ^{o}C and 26 ^{o}C while in summer the range is between 27 ^{o}C and 34 ^{o}C. In this case there is no overlap between the two regimes. This non-overlap in the data is slightly evident in the relation between the sky temperature and the vapor pressure. Unlike the above behaviors, the relation between the sky temperature and the PWV has an overlap for the two seasons. This must be due to the major impact of the air temperature in the lower atmosphere, which controls the atmospheric radiation, originating in the ground level. In other words the upper air atmospheric conditions in both seasons may be the same and the differences between summer and winter originated in the lower atmosphere.

Sky temperatures in both seasons are always above zero, and are found within the same range between 1 ^{o}C and 20 ^{o}C. These temperatures are higher than those found in either Adelaide or Abha. In Adelaide, which has a Mediterranean climate even in summer times, sky temperatures above 5 ^{o}C are always represent emission from cloudy skies. However, Excel (1977) presented sky temperatures measured in Bangkok, Thailand, like those found in Jeddah.

A single independent variable correlation analysis was performed independently between the sky temperature and Sqrt (eo) and Ta for the two seasons. The intercepts and slopes for were remarkably different. For the Sqrt (eo) versus Tsky, the slope for summer and winter changes from 4 to 7 respectively, and the intercepts differ for summer and winter by 8 ^{o}C, being –9 ^{o}C for summer and –17 ^{o}C for winter. Similarly, for Ta correlated with Tsky the slope changes from 1.4 for winter to 1.1 for summer, while the intercepts were modified from -17.2 ^{o}C in winter to –21 ^{o}C in summer.

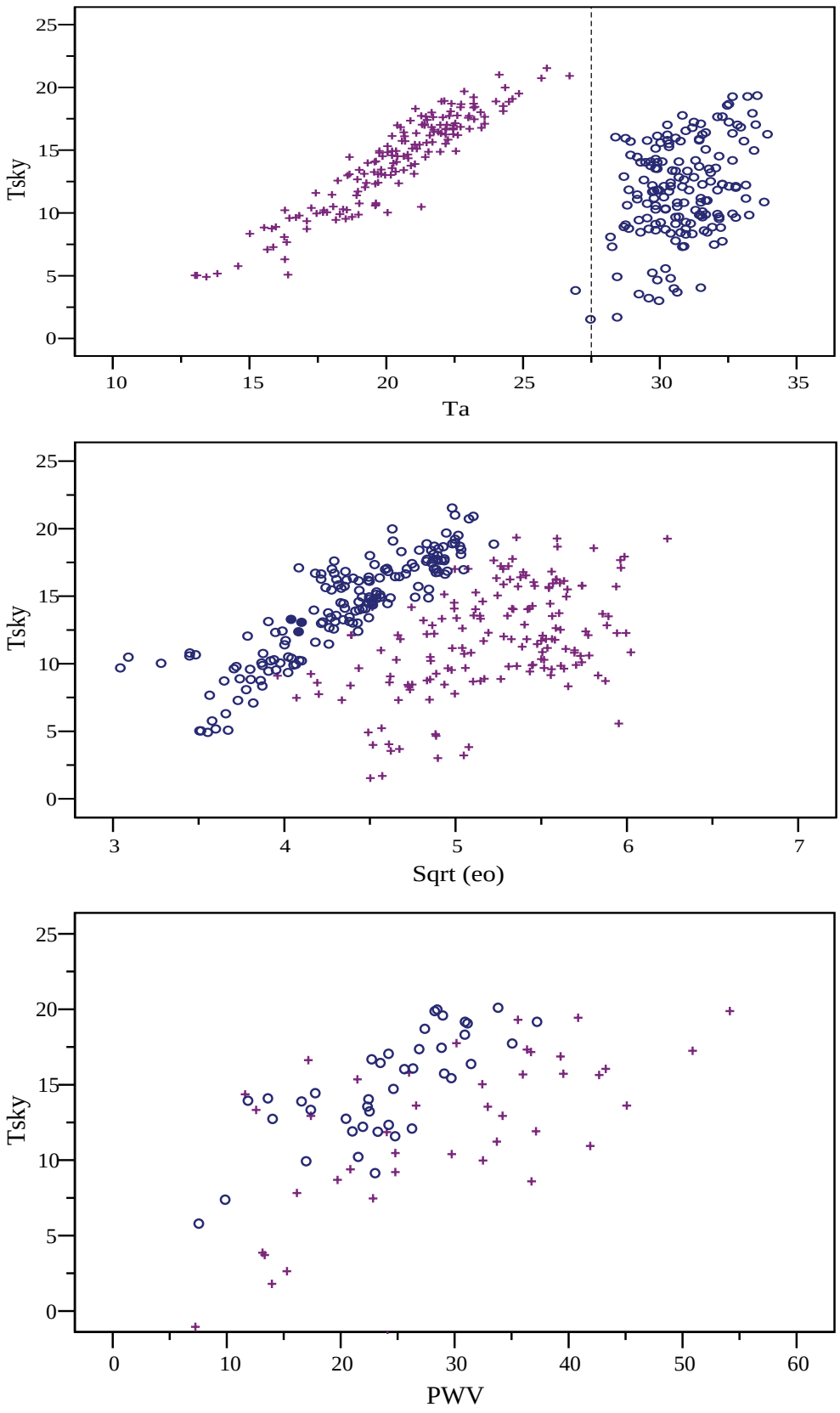

Figure 8. 6: Shows the variations of the sky temperature Tsky ^{o}C with air temperature Ta ^{o}C (top), square root of vapor pressure (Sqrt(eo)) $mb^{0.5}$ (middle) and PWV mm (lower), for Jeddah for both seasons, summer violet + and winter blue ○. The line in the top panel was set at reference Tair at 27.25 ^{o}C the boundary between the two seasons.

On the other hand, the slopes in the case of using the PWV as a single variable do not change much, while the intercepts shows a difference of about 3 ^{o}C from season to season. For summer the slope and the intercept were 0.29 and 3.3 ^{o}C respectively, while in winter the slope was 0.37 and the intercept was 5.9 ^{o}C.

It is obvious from the above discussion that it is not ideal to model the sky temperature with a single formula for both seasons and it is more practical to develop formulae for each season.

For summer seasons where the temperature Tair > 25 ^{o}C the results of two-parameter fits are summarized in table (8.2). In summer both *model1* and *model2* showed RMSE of about 3 ^{o}C and 4 ^{o}C respectively, low R^2, and different values of MBE. The intercepts of both models are unusual and showed very large negative values. Although the coefficient (slope) of air temperature in the second model shows a value greater than one, all other slopes in both formulae are within a physically acceptable range when compared to results from other sites.

The predicted versus measured sky temperature results using these models are shown in figure (8.7). The models either overestimate or underestimate the sky temperature at some temperature values. Although there were no large differences between the RMSE and MBE for both models, *model2* showed better performance than *model1*. This is apparent in the bottom panel of the figure where the predicted temperatures are distributed close or around the 1:1 line with the measured temperatures. On the other hand, 40 % of the predicted temperatures lie in parallel lines and far from the 1:1 line with the measured temperatures. The cause of this poor performance can be expected to be due to other factors in addition to those used in this model. Large aerosol particles, dust and smoke trapped up in the lower part of the atmosphere are possible factors expected to have a major effect in this time of the year in Jeddah. In Jeddah, summer is usually the time of the monsoons coming from the east bringing in dust to the whole province. This causes inhomogenity in atmospheric conditions, which may be extreme from day to day or from time to time in the same day.

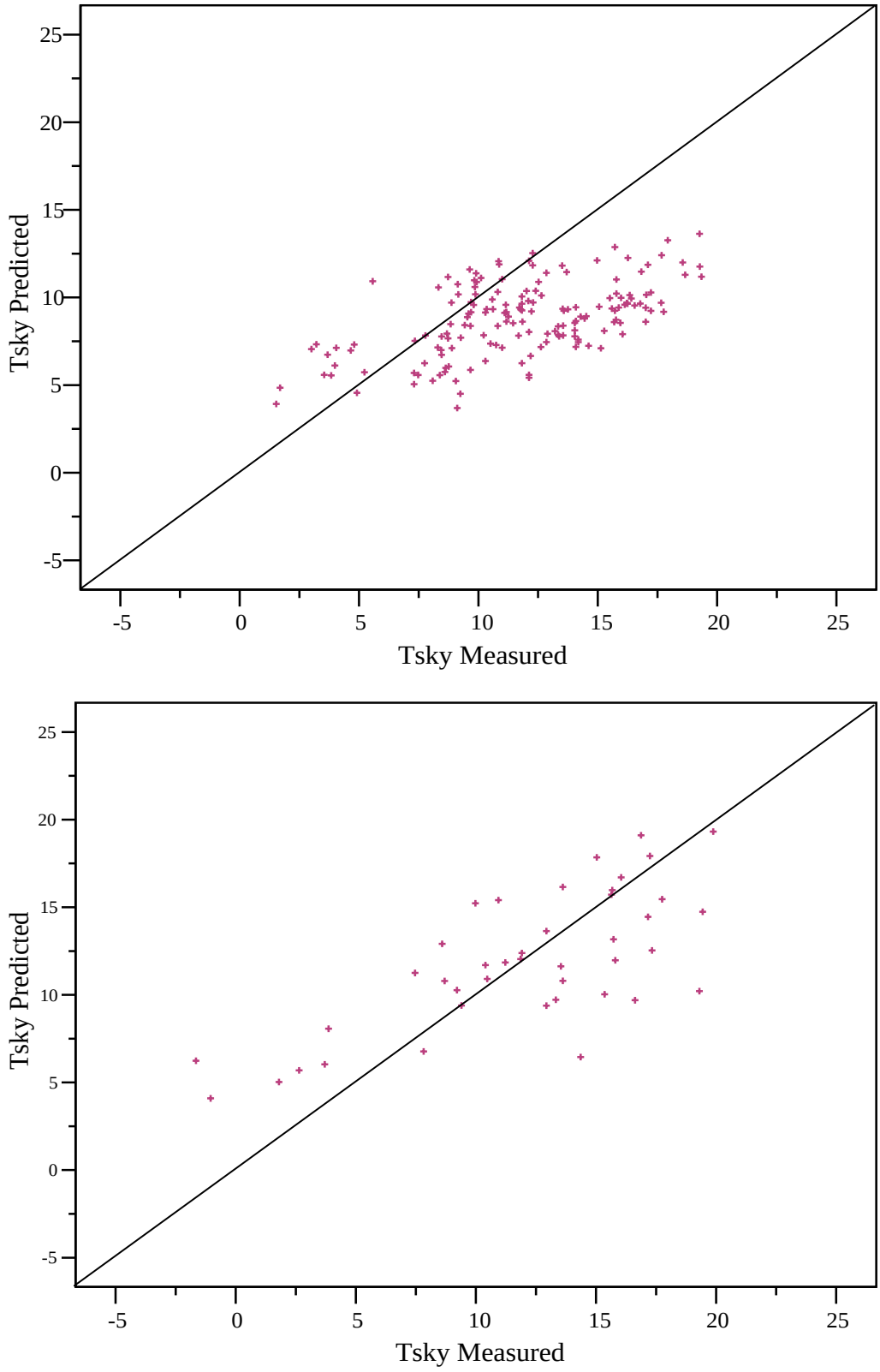

Figure 8. 7: Hourly clear sky temperature estimated from model1 (top) and from model2 (bottom) versus the measured Tsky for Jeddah site in summer. The straight line is the 1:1 ratio line for reference.

In winter the situation is completely different. For the expected range of temperature in winter times in Jeddah, $0 < T_{air} < 27\ ^{o}C$, the parameterizations of the clear sky temperature are given in table (8.2).

These models showed a lower RMSE, MBE of about 1 ^{o}C and high correlation coefficient for both models. The RMSE, , R^2, and MBE for *model1* were 1.1^{o}C, 0.95, and –0.26 ^{o}C respectively, while they were 1.2 ^{o}C , 0.94 and 1.2^{o}C respectively for *model2*. Also, the values of the intercepts and the slopes of the atmospheric water (either screen level vapor pressure or the PWV) of these models lie with in acceptable range. The slope coefficients of the air temperature in both models were more than 1 which is higher than the normal values.

Figure (8.8) shows the predicted versus measured sky temperatures using these models. *Model1* showed a superior distribution of the predicted data around the1:1 line with the measured temperatures in comparison with *model2*. This may be due to the greater stability of the lower atmospheric conditions in winter compared to summer in Jeddah. However, for both models the predicted data are close to the 1:1 line. This means that the models can be used to predict the clear sky temperature in Jeddah in this season with higher accuracy.

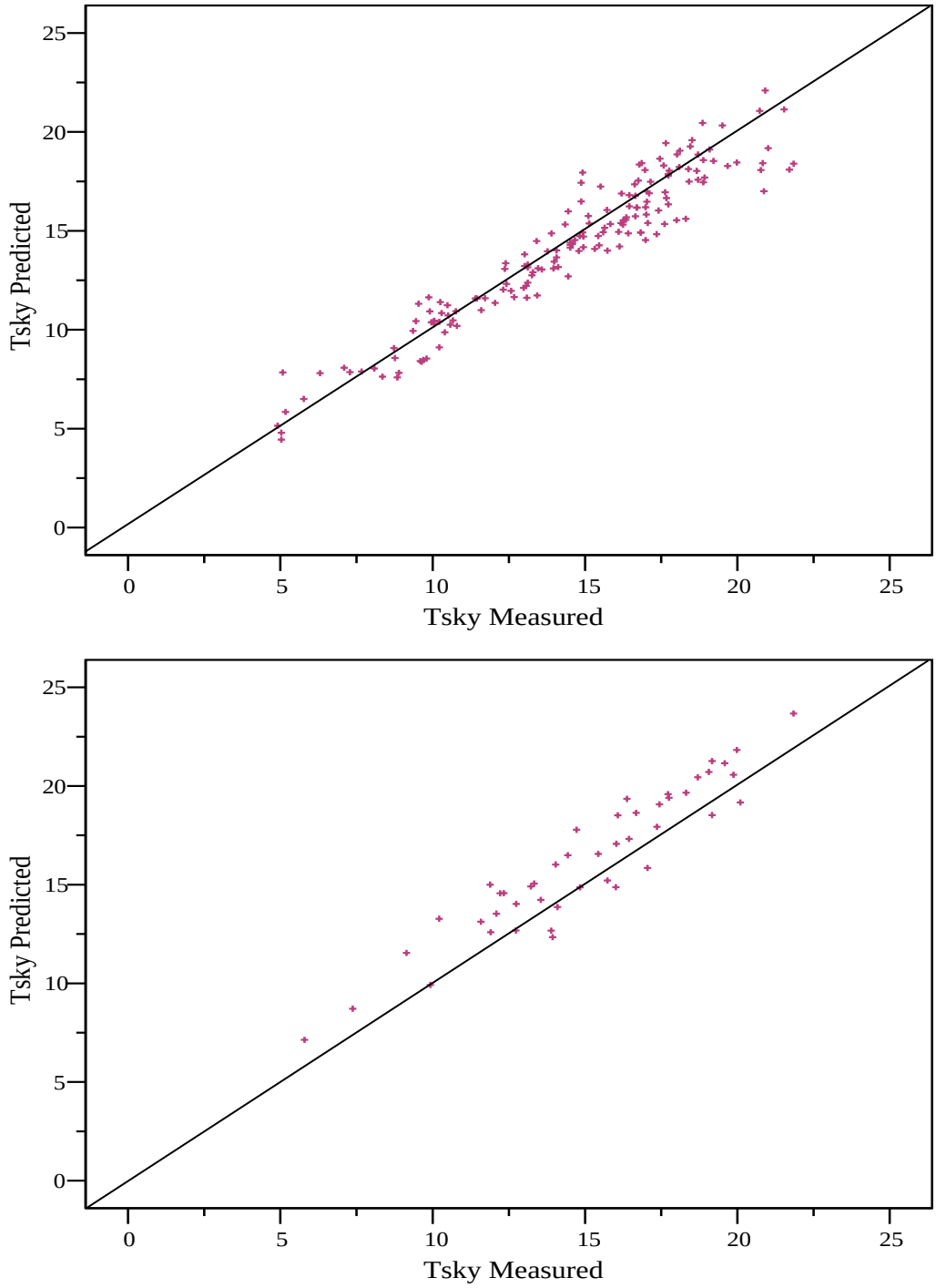

Figure 8. 8: Same as figure (8.7) but for winter times in Jeddah.

8.4.3 Tabouk

In Tabouk the situation is more or less between the above two sites. Although the data for this site do not go beyond a single season, we believe that more data from another season will not make a significant difference not show any seasonal behavior similar to that found in Abha or Jeddah. This is because the atmospheric conditions in Tabouk are moderate, and similar to the Mediterranean conditions found for example in Adelaide. However, the collection of more data is desirable at this site to cover a wider range of temperatures and amount of water vapor.

The relation between the sky temperature and the three parameters is shown in figure (8.9). Sky temperature is well correlated with air temperature. On the other hand there is no clear correlation with the PWV and vapor pressure. This may be due to the limited range of water vapor values measured in this season. However, the general trend is evident; increasing the amount of the atmospheric water can increase the sky temperature.

Table (8.1) shows the multiple regression analysis between the sky temperature and the parameters considered in this study for Tabouk site.

The MBE for both formulae were less than half a degree and the RMSE were 2.5 ^{o}C for *model1* and 3.3 ^{o}C for *model2*. The correlation coefficients, R^2, for *model1* and *model2* were 0.87 and 0.88 respectively. Both models showed reasonable statistics in term of their RMSE and R^2 although *model1* showed better values that *model2*.

Figure (8.10) shows a plot between the predicted temperatures against those measured for this period of time in Tabouk. Apart from some underestimation for both models under some conditions, both temperatures (predicted versus modelled using both models,) are not far from the 1:1 line and distributed around it with no more than 3 standard deviations.

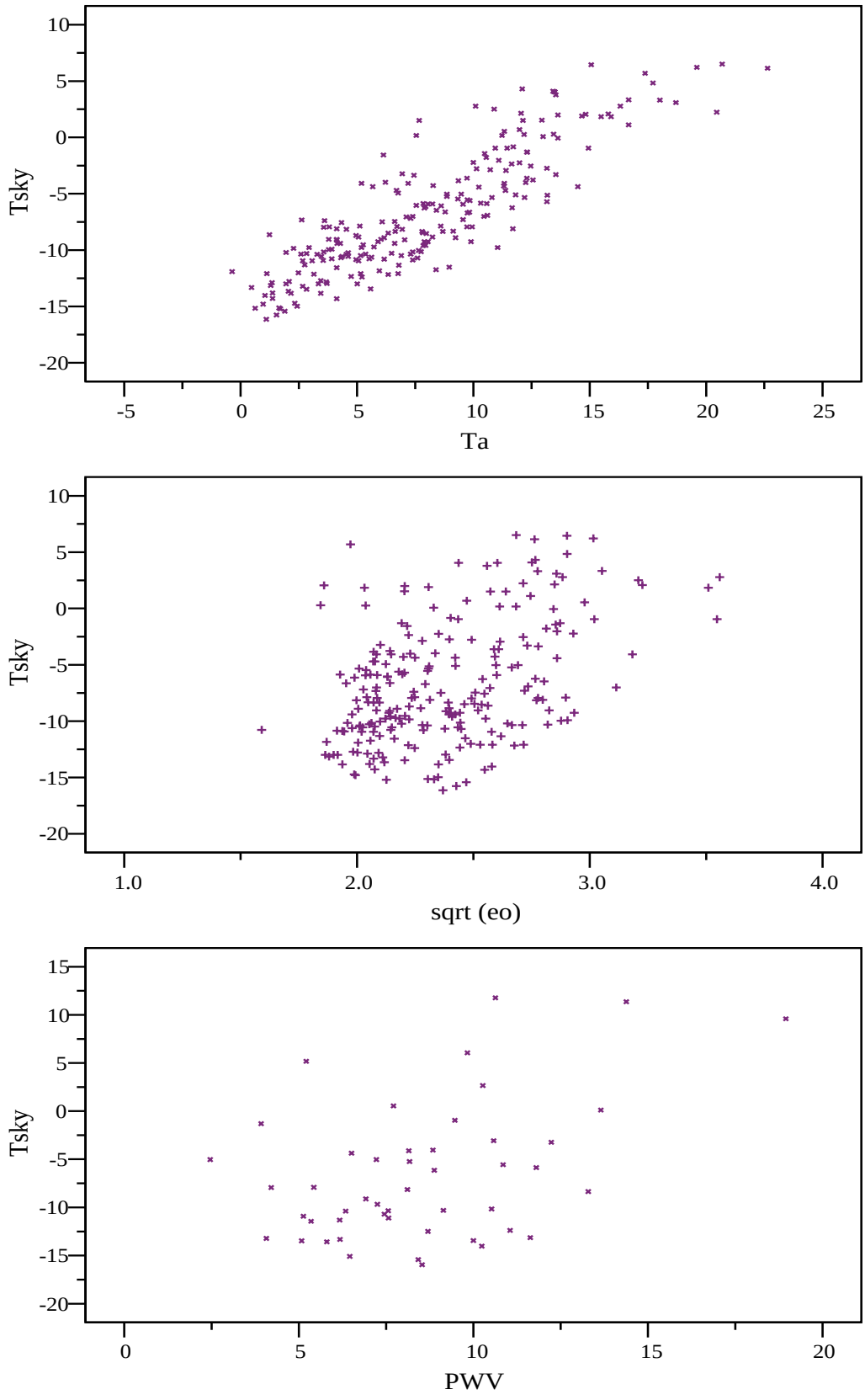

Figure 8. 9: Shows the variations of the sky temperature T_{sky} ^{o}C with air temperature Ta ^{o}C (top), square root of vapor pressure; sqrt(eo) $mb^{0.5}$ (middle) and PWV mm (lower), for the Tabouk site.

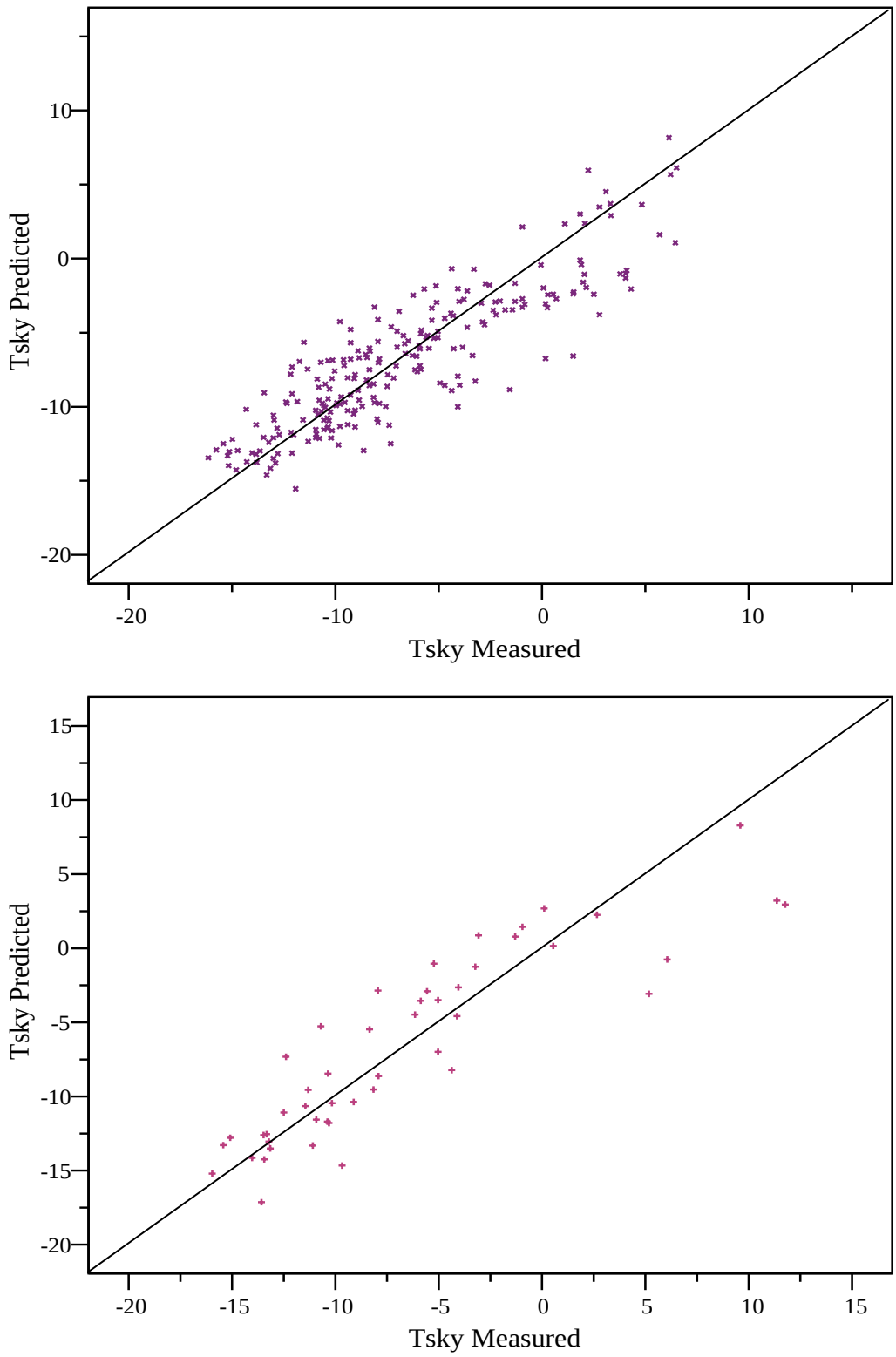

Figure 8. 10: Hourly clear sky temperature estimated from model1 (top) and from model2 (bottom) versus the measured Tsky for the Tabouk site. The straight line is the 1:1 ratio line for reference.

8.4.4 Comparisons with Other Bulk Formulae

Table (8.3) presents the average measured sky temperatures for each site at the period of study, along with the averaged sky temperatures calculated from *model1* as proposed above for each site. The reason of using *model1* not *model2* to compare with other models is discussed in chapter 4. The table also shows the calculated sky temperature from ten bulk formulae found in the literature. The formulations of these models were presented in chapter 2. These models are different in nature, locality, atmospheric conditions and the parameters they use. Here, these models are used in their original form, and the required meteorological variables are substituted in these models.

Table (8.4) shows two statistical parameters, MBE and RMSE, of the regression analysis between the measured/predicted temperatures. These parameters were used to assess the predictability of these models to the measured clear sky temperatures at each site. The response for each model is different from site to another. Some models showed superior predictions at some sites and poorer for another. Moreover, at the same site, some models predict better in one season but are poor in the other.

Model	Abha	Jeddah Summer	Jeddah Winter	Tabouk
Measured T sky	-7.16	11.78	14.67	-5.11
Predicted T sky (*model1*)	-7.18	8.80	14.37	-5.42
Brunt (1932)	-7.44	22.03	9.18	-14.29
Angstom (1918)	-1.44	16.11	7.84	-6.98
Efimofa (1961)	0.17	25.13	12.43	-7.28
Swinbank (1963)	-1.32	19.96	7.53	-10.53
Brutsaert (1975)	-5.57	21.09	9.47	-14.00
Berdahl and Fromberg (1982)	-6.35	17.57	6.60	-14.36
Idso and Jackson (1969)	-0.83	20.86	8.05	-9.46
Idso (1982)	-7.73	5.84	13.33	-8.55
Prata (1996)	-3.50	7.83	9.30	-8.39
Izmon *et al.* [2003]	-5.65	19.28	7.66	-13.41

Table 8. 3: Shows measured Tsky for each site along with those calculated from model1 and those calculated from different models.

	Abha		Jeddah Summer		Jeddah Winter		Tabouk	
	MBE	RMSE	MBE	RMSE	MBE	RMSE	MBE	RMSE
Model1	-0.016	2.9	-2.98	3.19	-0.25	1.16	-0.10	2.5
Brunt (1932)	-0.28	2.86	10.25	10.77	-5.49	5.73	-9.18	9.69
Angstrom (1918)	5.71	6.50	4.33	5.61	-6.83	7.03	-1.87	3.44
Efimofa (1961)	7.33	8.24	13.35	13.76	-2.23	2.64	-2.17	3.56
Swinbank (1963)	5.84	8.32	8.18	8.94	-7.14	7.26	-5.42	6.30
Brutsaert (1975)	1.59	3.75	9.31	9.84	-5.20	5.38	-8.89	9.51
Berdhal and Fromberg (1982)	0.81	3.43	5.79	6.60	-8.07	8.15	-9.25	9.74
Idso and Jackson (1969)	6.33	8.63	9.08	9.77	-6.62	6.75	-4.35	5.30
Idso (1982)	-0.57	4.78	-5.94	7.16	-1.34	2.19	-3.44	4.54
Prata (1996)	3.66	5.02	-3.95	5.20	-5.37	5.52	-3.28	9.03
Izmon *et al.* (2003)	1.51	3.73	7.50	8.15	-7.01	7.14	-8.30	8.80

Table 8. 4: RMSE and MBE in ^{o}C as statistical indicators between the measured and predicted sky temperatures using different models for each site.

In Abha, the Brunt; Idso; Berahal and Fromberg; Izmon *et al* and Brutsaert models performed extremely well in predicting clear sky temperatures. They showed very small MBE values against the measurements with a maximum RMSE of about 3.7 ^{o}C. The Prata model showed a reasonable MBE, while the rest of the models overestimate the predication by large MBE and RMSE.

For Jeddah the situation is different and more complex, with great variability from season to season. In summer all the models, according to their MBE and RMSE, substantially overestimate the measured sky temperature being lower for the Prata model and higher for the Efimofa model.

However, in winter times in Jeddah, the situation is totally different. In addition to *model1,* Idso and Efimofa models showed superior MBE and RMSE values and gave an excellent prediction for the sky temperatures. All the rest of the models underestimated (negative MBE values) and showed larger deviations from the measurements with Berdhal and Fromberg, Izmon *et al.* presenting the largest MBE and RMSE. It is interesting to notice that Efimofa model showed the lowest prediction of sky temperature in summer times in Jeddah and was one of the best predictors in winter times.

For Tabouk, all the models underestimate the measured sky temperatures with two different extremes. Four models showed a prediction no more than 4 ^{o}C in difference. The Angstrom model was the best with MBE of –1.8 ^{o}C, while the Efimofa has a MBE of

–2.17 ^{o}C. The Idso and Prata values were within a 3 ^{o}C range. Brunt, Berahal and Fromberg, Brutsaert and Izmon *et al.* showed the largest MBE and RMSE. Swinbank and Idso and Jackson had values between the two extremes, with MBE between (-5 ^{o}C, 6 ^{o}C) and RMSE between (-4 ^{o}C, 5 ^{o}C).

It is interesting to see that some of these models have shown an excellent performance in the prediction of sky temperatures for some sites with their original coefficients, which means that the situation in these sites may be similar to those in which the empirical models were first proposed.

Comparisons between the performances of *model1* for each site with the bulk formulae were presented also in tables (8.3) and (8.4). In all sites and seasons, models, which performed well in predicting the measured clear sky temperatures, gave comparable temperatures with those predicted using *model1* and vice versa.

For example, in Abha the Brunt model had a MBE -0.28 ^{o}C and RMSE of 2.86 ^{o}C in predicting the measured sky temperature. *Model1* shows a MBE of -0.01 ^{o}C and RMSE of 2.9 ^{o}C.

8.4.5 Ability of Model1 in Cloud Prediction: Example Case Abha

In this section the proposed models for clear sky temperatures will be tested against their capability of predicting clouds against the clear sky background. For simplicity, model1 for the Abha site, because Abha has the largest amount of cloudy sky in Saudi Arabia throughout the year. However, similar results are expected to be applicable to the rest of the sits.

Figure (8.11) shows night time data from the cloud monitor for the period from midnight of 16 August 2004 to midnight of 19 Aug 2004. Hourly detailed cloud observations during this period were obtained from a reliable website[1]. Meteorological data found in this site showed identical values with those made and reported by the Weather Bureau records.

The upper line represents the measurements and the lower line represents temperatures calculated from *model1*. The sky conditions were variable from clear to overcast with different cloud cover throughout this period. Temperatures with values close to or above zero degrees indicate the presence of cloud. On the other hand, negative temperatures show clear sky conditions. The model shows a clear level of discrimination between cloudy and clear skies, not less than 7^{o}C, and can be used effectively to identify the presence of cloud. However, the model has predicted temperatures about 2 to 4 ^{o}C lower than the measured values during some clear sky periods. This range of is still within one standard deviation of the model predictability.

[1] http://www.wunderground.com/global/SD.html

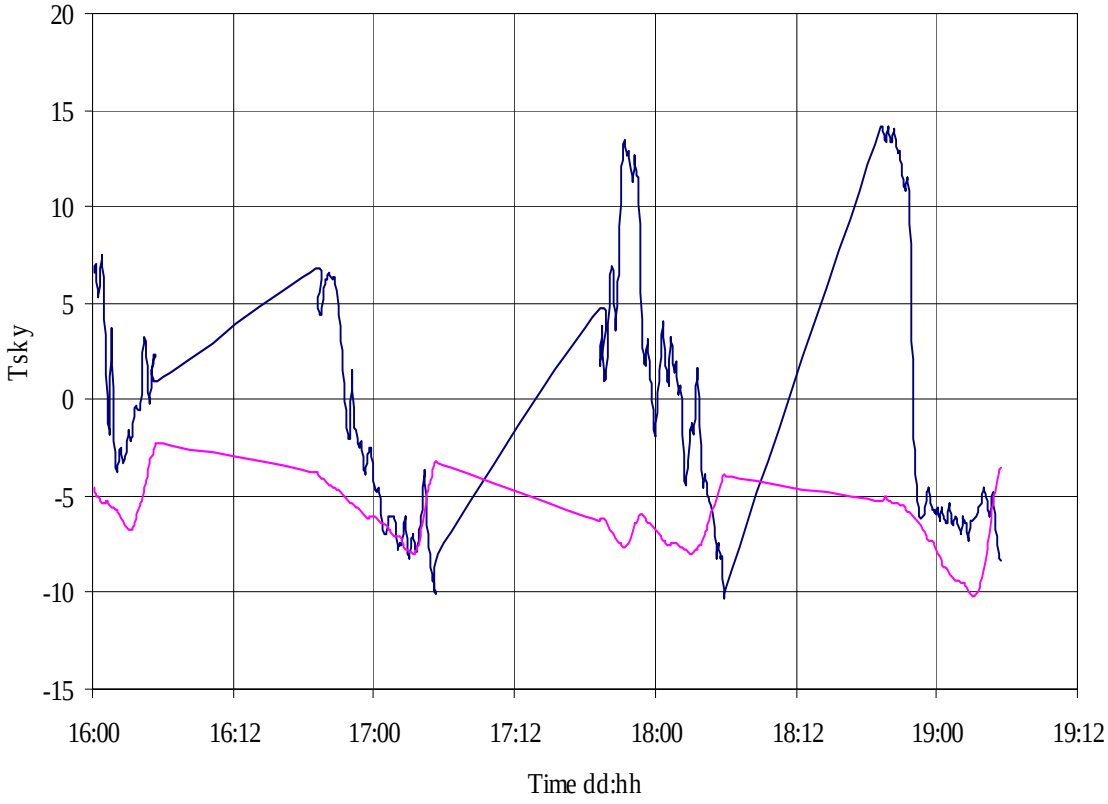

Figure 8. 11: Night time sky temperature (in ^{o}C) data from the cloud monitor at Abha site between 16 to 19 August 2004, for sky with different conditions. The upper line represents the measured Tsky while the lower is Tsky predicted from model1. The straight line connects the night time data when daytime data were excluded.

8.4.6 Data from All Sites

We conclude this section by examining the final picture of the data from all the sites to see how the data look when they all are put together, in which we outline a final conclusion. Figures (8.12) to (8.14) show plots of the clear sky temperature against the three variables used before. These figures summarize the form of behavior that sky temperatures exhibit for various atmospheric conditions of air temperature and the amount of atmospheric water content as well as the altitudinal effects. A general increase in sky temperature is apparent by increasing any of these parameters except the altitude which has an opposite effect.

In figure (8.12), data from Abha (both seasons) and Jeddah (in summer) lie in a line extending from lower to higher air temperature. On the other hand, Tabouk and Jeddah winter data form a line of data parallel to the first line with data from the Abha winter extending between the two extremes. In figure (8.13) and (8.14), apart from the Jeddah data from both seasons, there is no clear separation between summer and winter data for the other two sites.

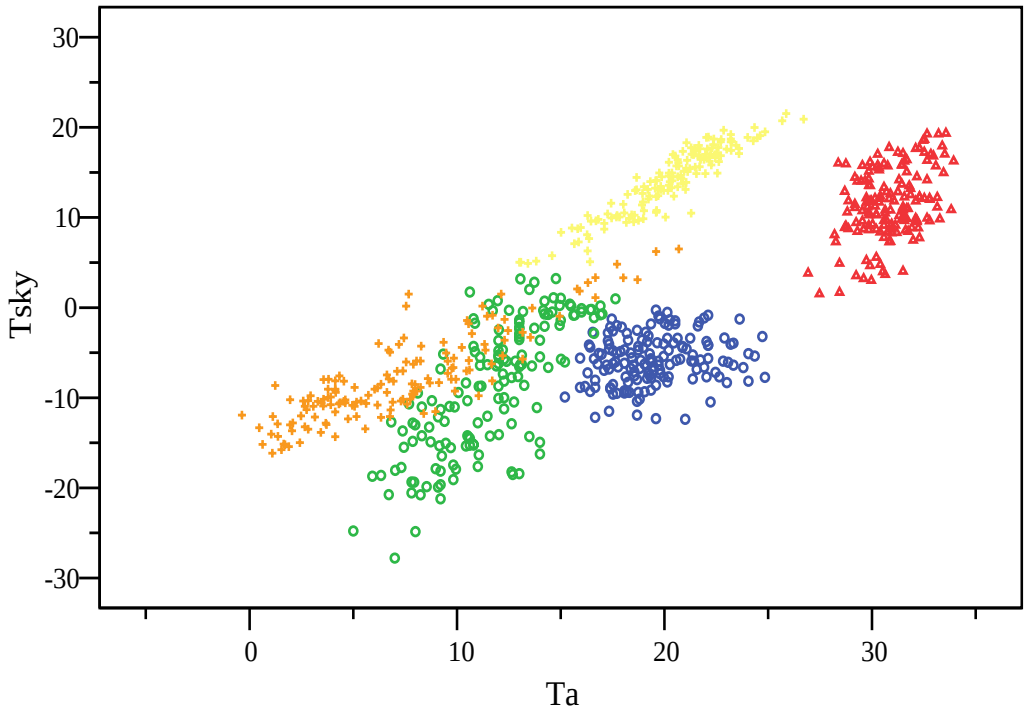

Figure 8. 12: Tsky in ^{o}C vs. Tair (in ^{o}C) for all sites from all seasons (Blue Abha summer, Green Abha Winter, Orange Tabouk, Red Jeddah summer and Yellow Jeddah winter).

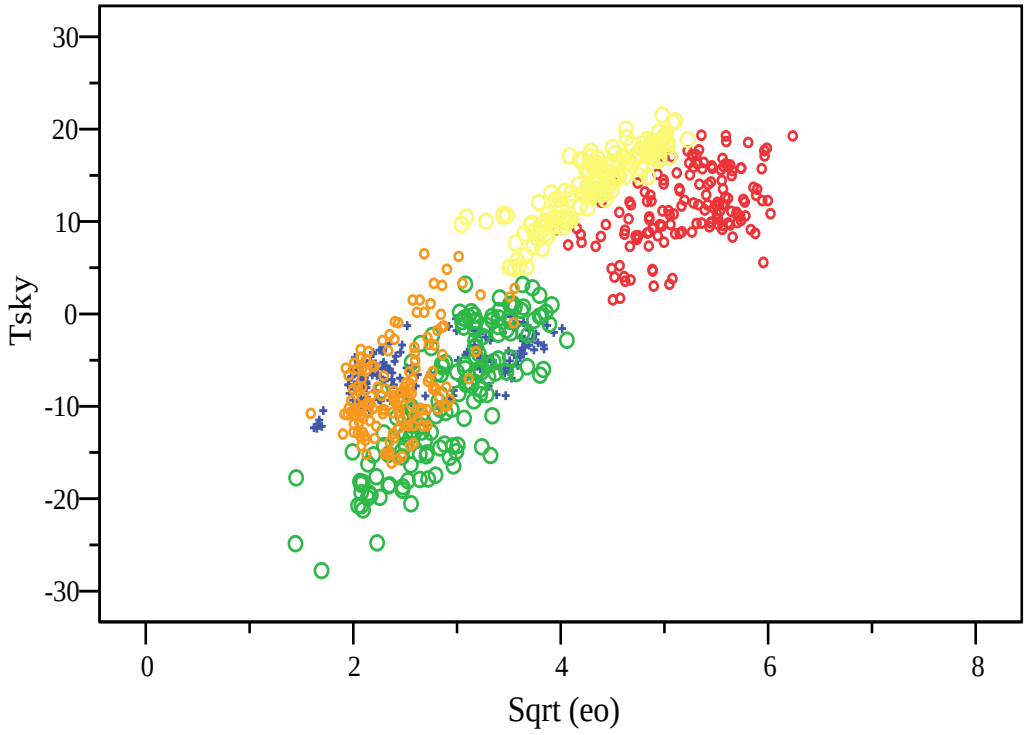

Figure 8. 13: same as figure (8.12) but for Tsky vs. Sqrt(eo) in $mb^{0.5}$. The color codes for all sites and seasons are the same as figure (8.12).

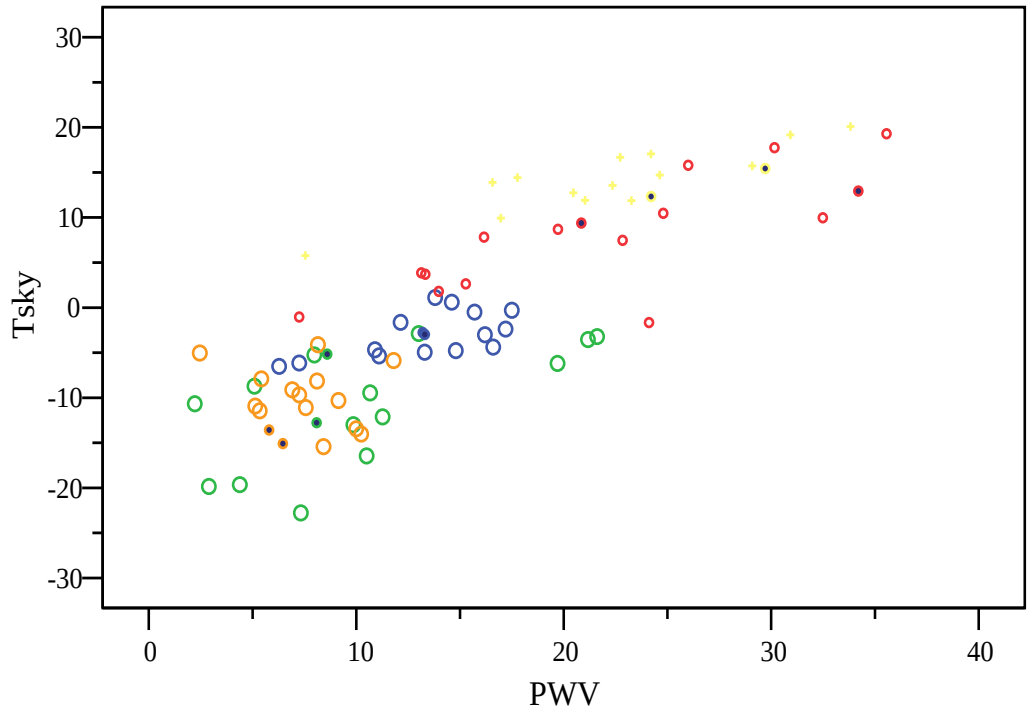

Figure 8. 14: The same as figure (8.12) and (8.13) but for Tsky vs. PWV in mm.

Following the same procedures like to that followed for each individual site, multiple regression analysis between the clear sky temperature and three parameters. For the purpose of doing these regressions the dataset was divided into two groups according to the available parameters. The first is *set1* which includes the whole measurements for the sky temperatures and the ground level parameters. These are those found in figures (8.12) and (8.13) and have a total of 951 data points. The second is *set2* which comprise sky temperature measurements, air temperatures and the PWV. This data set contains 181 data points as used to produce figure (8.14). The statistics of these two sets along with the results of the regression analysis (see below) are summarized in table (8.5).

The resultant formula for the multiple regression analysis between the sky temperature and the screen level parameters of the temperature and the square root of vapor pressure - *set1*- was:

$$Tsky = -26.9 + 6.2Sqrt(eo) + 0.313Ta \qquad (8.9)$$

Similarly, the sky temperature in term of screen temperature and PWV–*set2*- was:

$$Tsky = -15.6 + 0.45PWV + 0.60Ta \quad (8.10)$$

The MBE and RMSE of the predictability of these two models to the measured temperatures are given in table (8.5). The correlation coefficients for the two models were 0.87 and 0.88 for (8.9) and (8.10) respectively.

The *average measured* sky temperature value for *set1* and *set2* were -0.05 ^{o}C and 3.29 ^{o}C respectively. The *average predicted* sky temperature using equation (8.9) was -0.12 ^{o}C with MBE and RMSE being 0.07 ^{o}C and 5.2 ^{o}C respectively. Similarly, the average predicted sky temperature by equation (8.10) was 3.20 ^{o}C with MBE of -0.08 ^{o}C and RMSE of 5.9 ^{o}C. The mean MBE values of these two equations showed excellent fit for the measurements when the data considered as a whole. However, MBE values up to 14 ^{o}C and 16 ^{o}C were found in predicting sky temperatures using (8.9) and (8.10) respectively. These large deviations are expected since the models were built to find the best fit and reduce the deviation as much as possible for the whole data, where in some occasions this becomes impossible.

Figure (8.15) shows the measured versus predicted sky temperatures using equations (8.9) and (8.10).

The effects of the season and the site characteristics are also evident in the figures. Apart from the Jeddah site, when both seasons are considered, both formulae can reasonably predict the sky temperatures, especially data from the Abha and Tabouk sites where there predictions lie close to the 1:1 lines. However, the estimation may not be totally accurate if the formulae are intended to be used for a single site. In that case one of the previously obtained formulae may be used more accurately.

Set1 (N = 951)				
	Range	Minimum	Maximum	Mean
Sqrt(eo) ($mb^{0.5}$)	4.79	1.44	6.24	3.40
Ta (^oC)	32.68	1.26	33.94	18.00
Tsky Measured (^oC)	49.63	-27.79	21.84	-0.05
Tsky Predicted (^oC)	37.78	-15.59	22.18	-0.12
MBE (^oC)	28.84	-14.08	14.76	0.07
RMSE (^oC)	14.75	0.01	14.74	5.2
Set2 (N = 181)				
PWV (mm)	51.93	2.22	54.15	18.02
Ta (^oC)	33.87	-0.42	33.45	17.89
Tsky measured (^oC)	44.63	-22.78	21.84	3.29
Tsky Predicted (^oC)	40.13	-13.28	26.85	3.20
MBE (^oC)	31.35	-14.91	16.44	-0.08
RMSE (^oC)	16.41	0.03	16.44	5.94

Table 8. 5: Shows (top part) the summary of the statistics of screen level temperature (Ta) , square root of vapor pressure (Sqrt (eo)),the measured sky and predicted sky temperatures using (8.9) and the MBE and RMSE of these predictions for data set1. It also shows (lower part) the statistics of the PWV, the screen temperature (Ta), along with measured and predicted sky temperatures using equation (8.10) and the MBE and RMSE of these predictions for data set2.

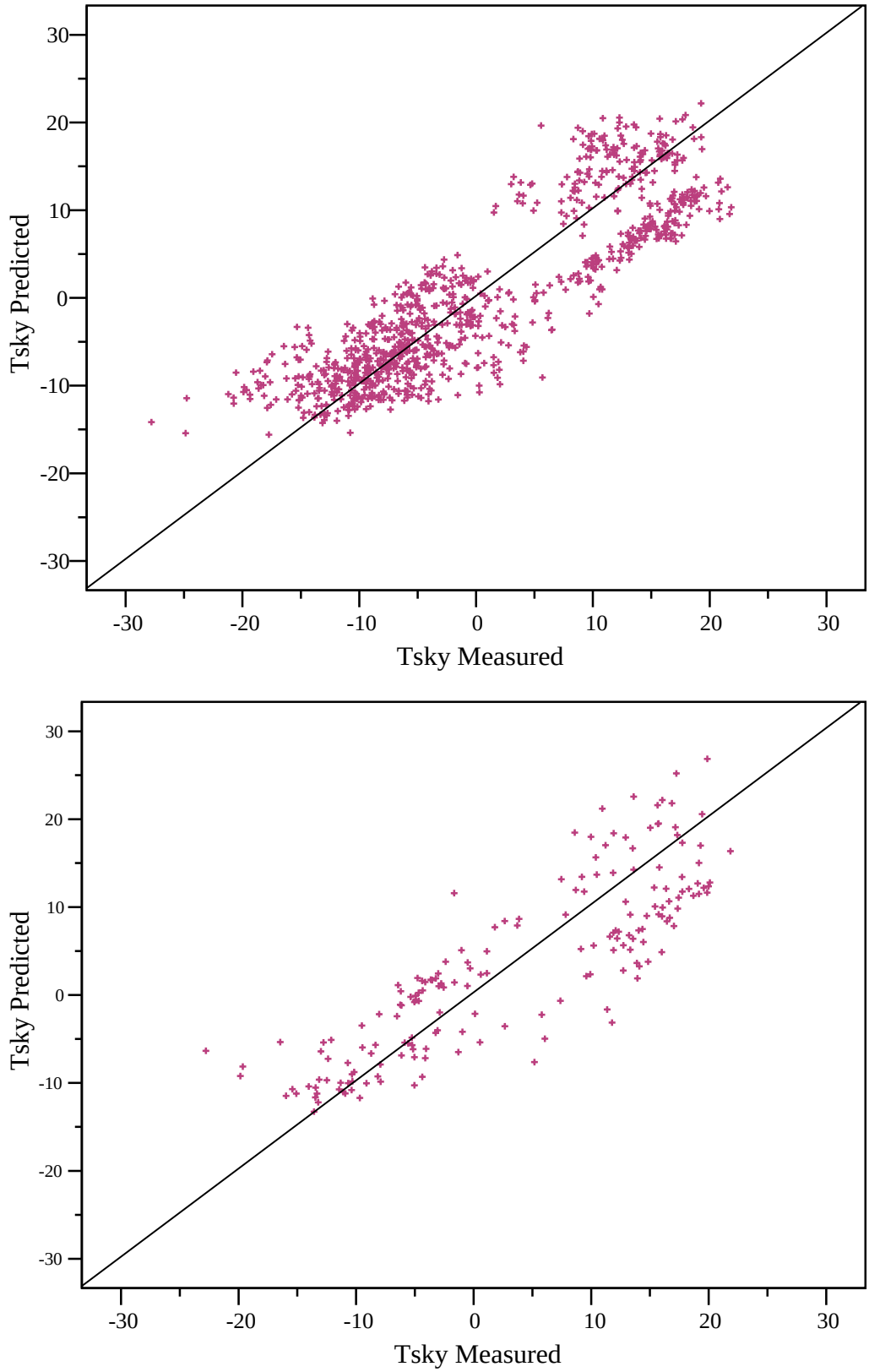

Figure 8. 15: Hourly clear sky temperature estimated from equation (8.9) (top) and from equation (8.10) (bottom) versus the measured Tsky for all sites over all seasons. The straight line is the 1:1 ratio line for reference.

8.5 Results from the Riyadh Site (3o FOV detector)

8.5.1 Results and Discussions (Parameterizations)

In Riyadh the experiment was conducted through 2004- 2005. The data gathered so far are those for the following period of times: August 2004 to September 2004, December 2004 to March 2005, June 2005 to August 2005 and October 2005 to December 2005. The reason for the incomplete sequential data for some months is due to overwriting of recorded data in the logger when the collection time exceeded three months. Although there is some incompleteness in the data within the full two years, we are confident that the collected data well representing the real atmospheric conditions over Riyadh in different seasons. Thus, the results found in this study, with a very high level of confidence, are correct for the Riyadh site. Except for the use of a 3^{o} FOV STD cloud monitor at the Riyadh site, the instrumentation, clear sky selection, data treatment and analysis procedures, were similar to those discussed above.

Table (8.6) presents a summary statistics of half-hourly meteorological parameters and sky temperatures at the Riyadh site for the period of study. Precipitable water vapor data from coincident radiosonde ascents were used in this study and are also presented in the table.

Set1 (N = 1620)					
	Range	Minimum	Maximum	Mean	Std. Deviation
Sqrt ($eo_)(mb^{0.5}$)	2.8	1.71	4.52	2.53	0.36
Ta (^oC)	37.55	4.15	41.7	24.1	8.99
Tsky (^oC)	51.79	-29.03	22.76	1.24	10.89
Set2 (N = 126)					
PWV (mm)	26.61	3.74	30.35	13.15	5.64
Ta (^oC)	30.77	4.82	35.59	22.31	8.38
Tsky (^oC)	46.99	-26.2	20.79	1.29	10.9

Table 8. 6: Hourly statistics of the square root of vapor pressure (Sqrt eo), air temperature Ta and the measured sky temperature Tsky for the data set1 which has the available screen level measurements (1620 data points). The last three rows represent the PWV derived from coincidence Radiosonde(RS) ascent times, screen temperature Ta, and sky temperatures at Tsky at those time corresponding to the PWV measurements (126 data points). These data are for the Riyadh site in Saudi Arabia during all the period of investigation (see text) between 2004-2005.

The data in the table show that the site exhibited a wide range of meteorological conditions. The sky temperature ranged from –29 ^oC for clear sky winter times to 22 ^oC for hot clear summer nights. Also, the air temperature varies between 4 ^oC to 41 ^oC, whilst the vapor pressure changes from 3 mb to around 20 mb. Generally speaking from a meteorological point of view (especially vapor pressure and PWV) Riyadh is a dry site and may be considered as the driest among any of the three sites presented here (plus the Adelaide and Auger sites (see chapter 4 and chapter 9)).

The values of measured Tsky and Ta at the times of coincident radiosonde ascents do not differ much from those measured at other times in term of their mean values.

Following the same procedures used for the other three Saudi sites, the clear sky temperatures versus the Ta, Sqrt (eo) and PWV are shown in figures (8.16) to (8.18).

The three figures show the general behaviour of sky temperatures against the three parameters considered. That is, any increase of one of these parameters is accompanied by an increase in sky temperature. This sort of trend is least pronounced between the sky temperature and vapor pressure (see below). In figure (8.16), although there is some scatter in the data, air temperature varies linearly with sky temperature over the whole range of data. However, there are three clouds of spread in the observations, which can be identified. The lower, higher ones and some of those in the middle lie close to a representative straight line, with some data of the middle set of data flattening

away from this linear line. This flattening might be explained by a higher systematic error of measurements during this period of time or there may be another cause, which is not clear at this stage.

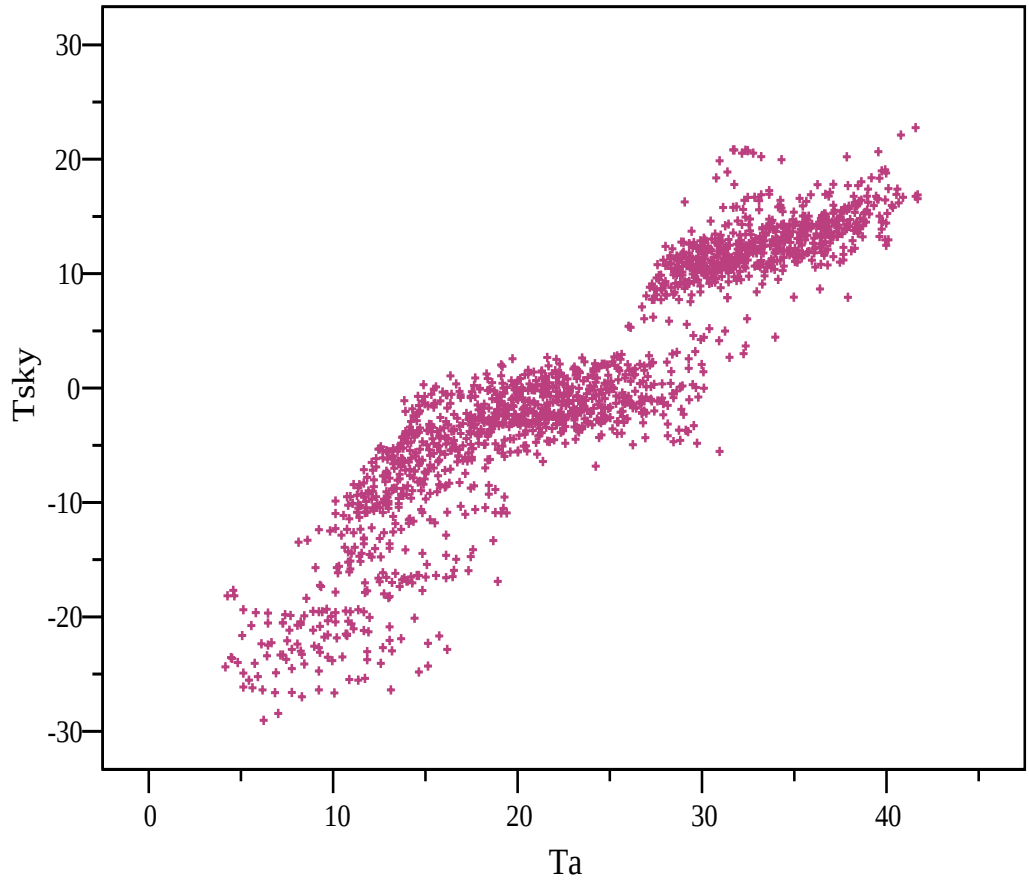

Figure 8. 16: Tsky vs. Ta (both in ^{o}C) for the Riyadh site during the period of investigation.

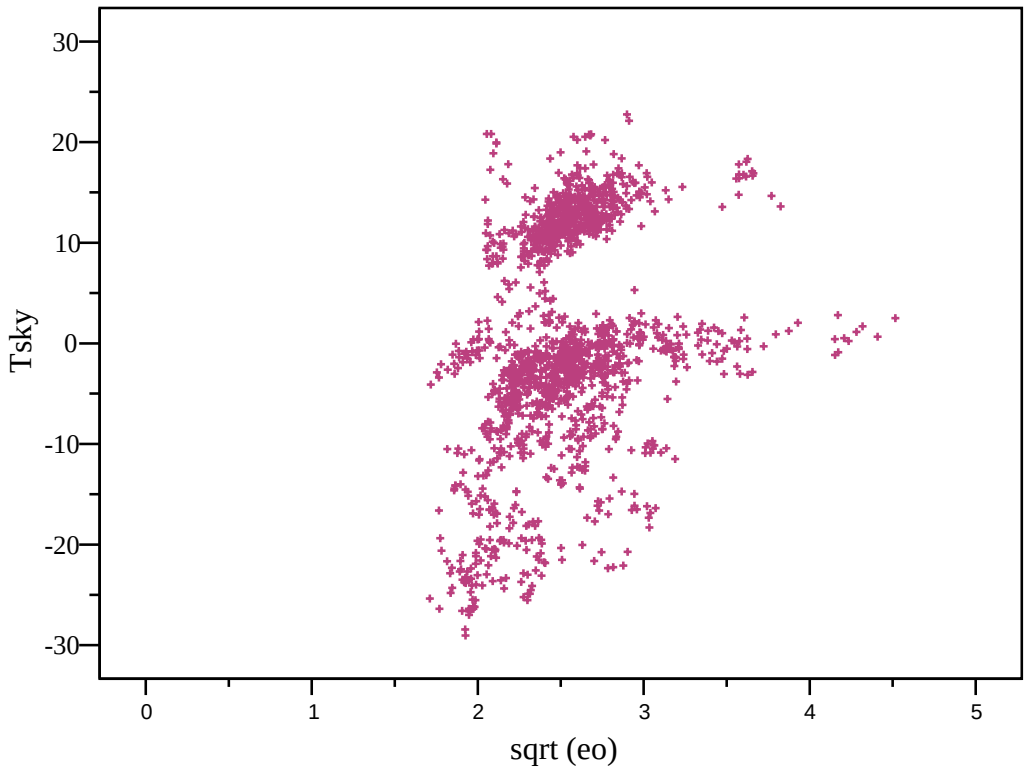

Figure 8. 17: Same as figure (8.16) but for Tsky vs. sqrt(eo) in $mb^{0.5}$.

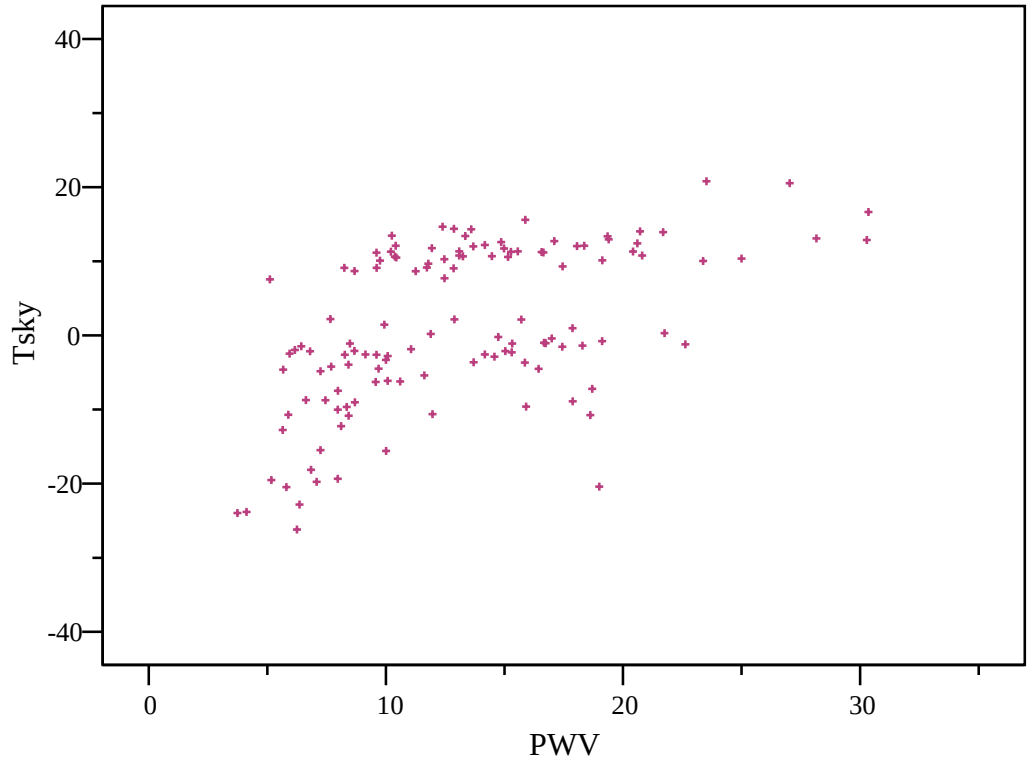

Figure 8. 18: Same as figure (8.16) and (8.17) but for Tsky vs. PWV in mm.

Interesting features of sky temperatures versus the vapor pressure are shown in figure (8.17). The sky temperature is poorly correlated with the vapor pressure when the whole data set (*set1* table 8.6) is considered. Again, three clusters or "clouds" of data lie horizontally parallel to each other over a narrow range of vapor pressure values, with the exception of the middle one, which extended to higher values. For the same value of Sqrt (eo), the sky temperatures changed dramatically from one group to another. For example at Sqrt (eo) of 2 $mb^{0.5}$ the sky temperature was dramatically varied in three different occasions, represented by those three groups above, to be –30 ^{o}C, -5 ^{o}C and 15 ^{o}C from the lower, middle to higher group respectively. Swinbank (1963) found the same pattern when he compared observations from Aspendale in Australia with observations from the Indian Ocean for the same range of air temperatures. However, here at this single site the case is a little different and temperature variations may be causing this trend. Other parameters are expected to play roles, for example aerosols, wind speed, dust and pollutions. Riyadh lies in the middle of the desert and severe weather conditions are observed over short periods of time. This issue will be discussed in more detail in chapter 10.

Finally the PWV shows a degree of linearity with the sky temperature somewhat between the two above parameters, *set2* table 8.6 and figure (8.18). Here there are two

groups of data, those at lower part of the figure, for which the sky temperature increases clearly with increasing the PWV, becoming less clear around medium PWV values. The other group, which is parallel to the first one, shows slight increases of sky temperature with PWV. This may be associated with the fact that in Riyadh, as for other Saudi sites, temperature inversions are commonly found and result either from clear winter cold nights, or from the presence of sky heat caused by the aerosols and dust over some sites like Jeddah in summer time.

The parameterizations of the sky temperature for the Riyadh site (3^o FOV) using the above three parameters (using multiple regression analysis) are given by:

$$Tsky = -31.6 + 2.75Sqrt(eo) + 1.05Ta \quad (8.11)$$

$$Tsky = -28.22 + 0.286PWV + 1.15Ta \quad (8.12)$$

Equation (8.12) was produced by a multiple regression analysis for the 126 data points of *set2* in table (8.6). The average predicted sky temperature using this formula was 1.20 ^{o}C, compared with the averaged measured of 1.29^{o}C, with a MBE of -0.89 ^{o}C, RMSE of 2.9 ^{o}C and R^2 of 0.96. The statistics of this equation showed that this model could be used in predicting clear sky temperatures when using these two parameters. Figure (8.19) shows the resulting measured versus predicted sky temperature.

In obtaining equation (8.11) the entire data *set1* was split into two groups, with more than one half of the data,1022 data points, were utilized for the modelling (producing equation (8.11) and the other 599 points were used for the validation. The average predicted temperature was 3.24 ^{o}C, compared with average measured of 3.60 ^{o}C. The regression results between the measure and predicted sky temperatures give MBE of –0.35 ^{o}C, RMSE of 3.15 ^{o}C and R^2 of 0.96. The average measured temperature for the second half of the data was –2.79 ^{o}C and the predicted value using (8.11) was –3.6 ^{o}C. The MBE in this case was 0.8 ^{o}C. Finally in utilizing this model to predict the whole data set, 1620, the average measured, average modelled and MBE were 1.24 ^{o}C, 1.30 ^{o}C and -0.06 ^{o}C respectively.

The results of these comparisons are illustrated in figures (8.20)-(8.22).

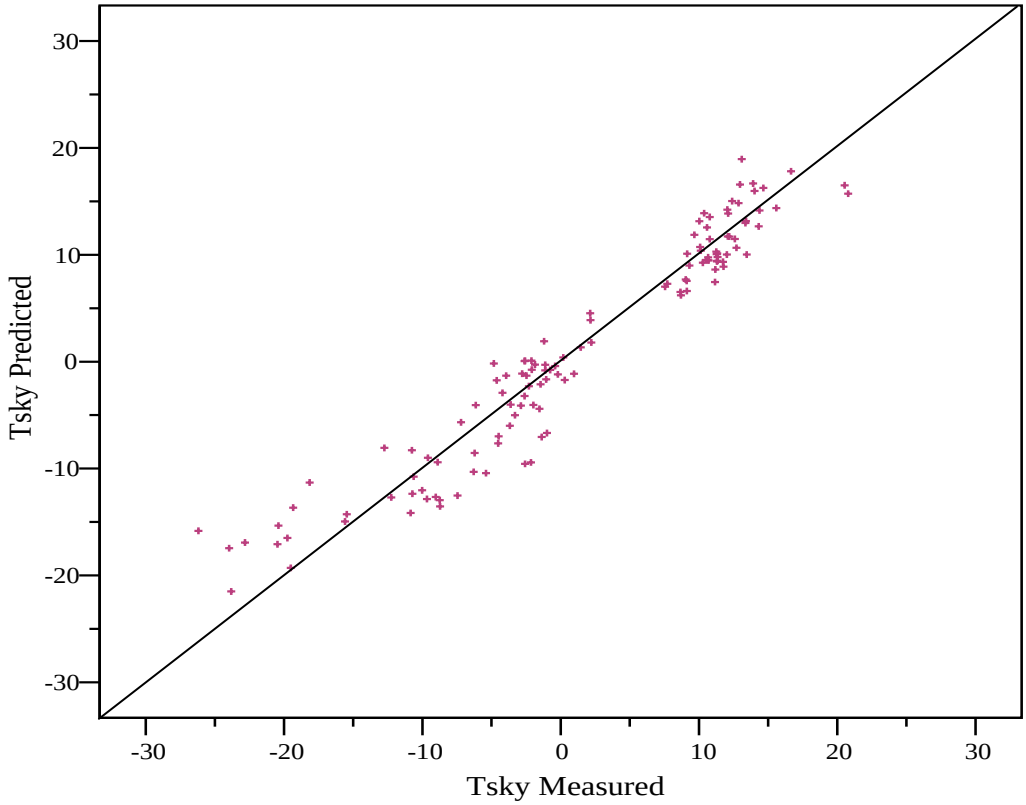

Figure 8. 19: Measured Tsky vs. predicted Tsky (in ^{o}C) using equation (8.12). The straight line is the 1:1 ratio line for reference.

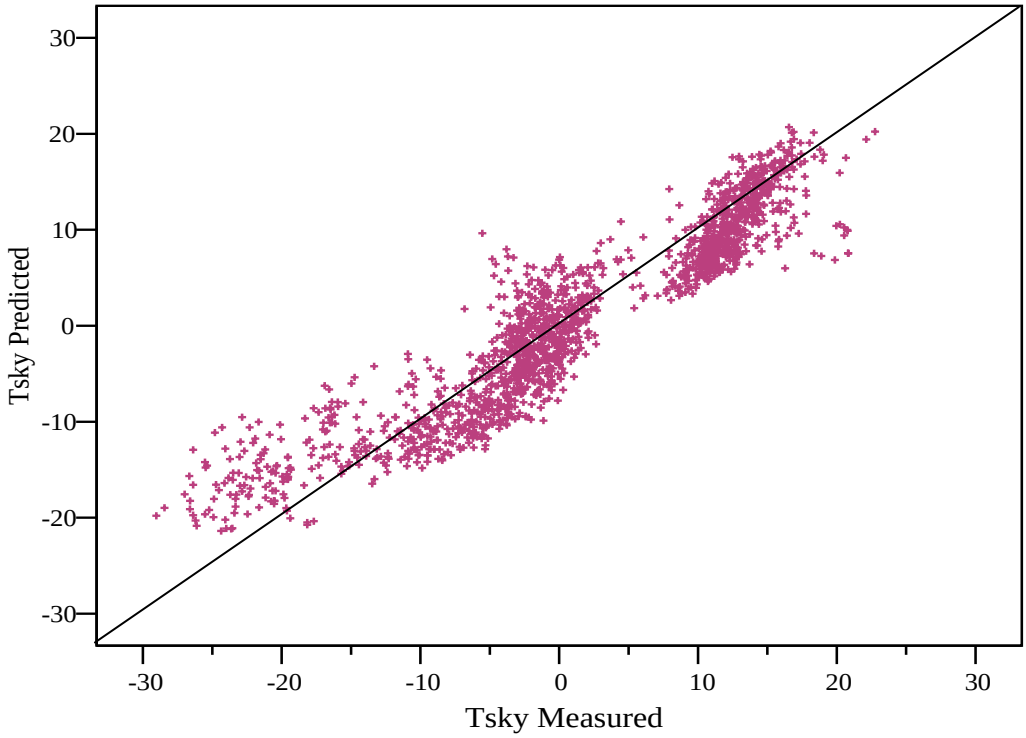

Figure 8. 20: Measured Tsky vs. predicted Tsky (in ^{o}C) using equation (8.11) for the data set1 used for the parameterizations (n=1022 points). The straight line is the 1:1 ratio line for reference.

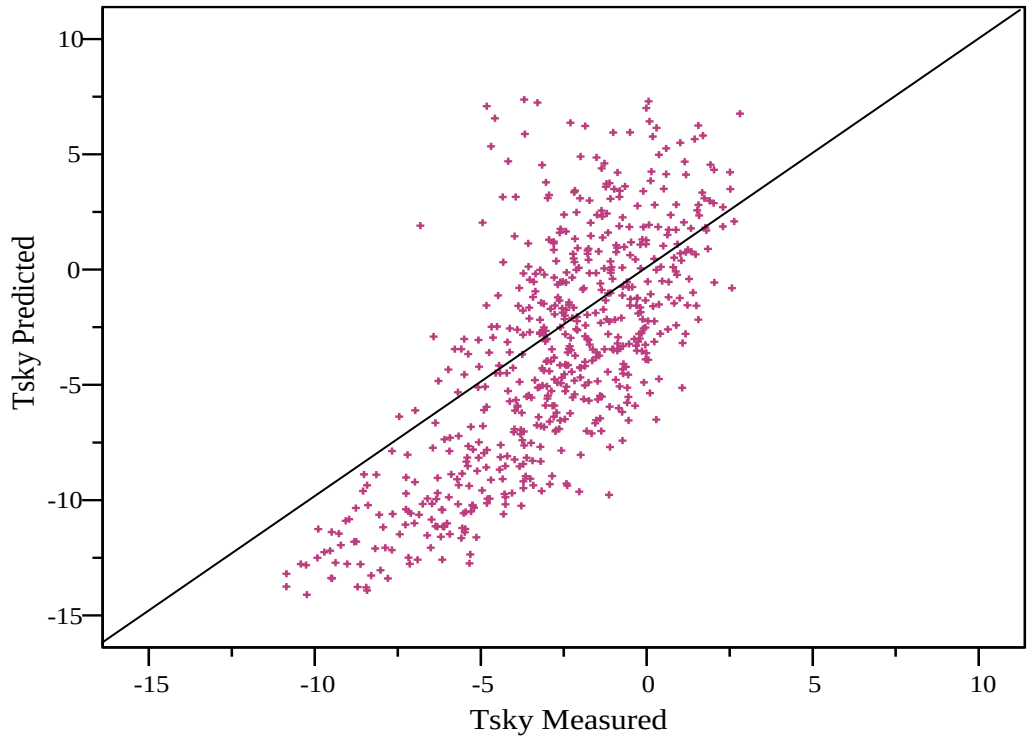

Figure 8. 21: Measured Tsky vs. predicted Tsky in ^{o}C using equation (8.11) for the independent data set used for validation (n=695 points). The straight line is the 1:1 ratio line for reference.

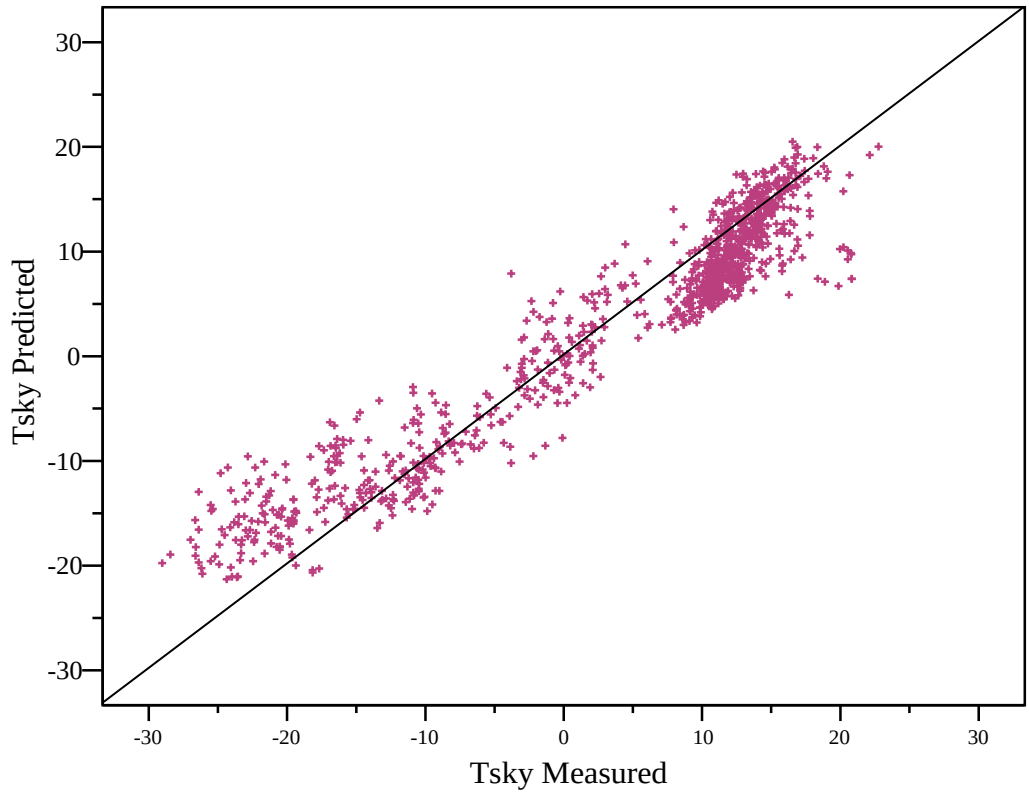

Figure 8. 22: Measured Tsky vs. predicted Tsky in ^{o}C using equation (8.11) for the whole data (1621 data points) including data used for parameterization and those used for validation. The straight line is the 1:1 ratio line for reference.

Although the figures showed a pattern of under-estimations (lower part of figures 8.20 and 8.22) or over-estimations (top part of figures 8.20 and 8.22) using equation (8.11) in predicting the measured clear sky temperatures, it is notable that over wide ranges most of the data in all figures lie in the vicinity of the 1:1 lines. The under-estimations or over-estimations of the sky temperatures can be attributed to other factors affecting the atmospheric conditions at some period of times at the Riyadh site other than air temperature and vapor pressure. As we mentioned earlier these factors might be heavy aerosol particles, wind speed, and directions and atmospheric inversions.

8.5.2 Comparisons with Other Models

In this subsection, following the same procedures as with the other three sites, measured and predicted sky temperatures using equation (8.11) will be compared with some models found in the literature and used throughout this study in their original forms. The work conducted in this section is mainly based on data *set1* of table (8.6).

Table (8.7) summarizes the statistical values of the measured and calculated sky temperatures using eleven models including those calculated using equation (8.11). The table also gives the MBE and the RMSE values between the measured and modelled temperatures.

By examining their statistical parameters, the models of Idso and Jackson, Swinbank, Efimofa and Angstrom showed the poorest performance. The first two models showed the largest maximum, minimum, mean, MBE, and RMSE differences in prediction. On the other hand, the Berdhal and Fromberg and Brunt models perform the best. Both of these models are independent of air temperature. The Berdhal and Fromberg model is a function of dew point temperature while the Brunt model is a function of vapor pressure. The Efimofa formula depends solely on the square root of vapor pressure but is considered as the one with the worst performance. Although there is little difference in the functional dependence between Brunt (dependent on the *square root* of vapor pressure) and Efimofa (dependent on vapor pressure), their performance was quite different. Surprisingly, these results may violate the expected trend as considered from figure (8.16) and figure (8.17). In these figures, sky temperatures have a good linear dependence over the whole period of time with air temperature. This may be compared with the relation with vapor pressure, which was diminished in some periods of time.

Except for the Berdhal and Fromberg model, all the models with two independent variables, (mainly air temperature and vapor pressure) showed a very good results in terms of their statistical parameters considered here. The Izmon *et al*. Brutsaert, Prata and Idso models, in order of success, were able to perform well in predicting measured sky temperatures and being compatible with those predicted using equation (8.14). For example Izmon *et al* showed a MBE of less than a degree in comparison with the mean measured and predicted temperatures. Although all models including those with the best performance, either single or two independent variables, and equation (8.14) have shown compatible results with either the mean or/and the maximum measured values of sky temperatures, it is noteworthy that none of these models have predicted or reached the minimum measured temperature value. For example our proposed model and that of Brutsaert, which were considered as the best predictors here, have predicted temperatures with a minimum of –21.28 ^{o}C and –21.12 ^{o}C respectively and this is still about 7^{o}C above the minimum measured sky temperatures. This may not be due to a deficiency of these models in predicting such low temperatures, but is likely to be due to the complicated atmospheric conditions found and exhibited by the Riyadh site.

Model	Min	Max	Mean	Measured-Model		Predicted-Model	
				MBE	RMSE	MBE	RMSE
Measured Tsky	-29.04	22.76	1.24	-	-	-	-
Predicted Tsky eq. (8.11)	-21.28	21.68	1.30	-0.06	3.84	-	-
Brunt (1932)	-20.78	21.33	0.12	-1.12	2.07	-1.18	4.33
Angstrom (1918)	-13.09	25.80	7.56	6.32	7.46	5.02	2.07
Efimofa (1961)	-12.81	25.64	7.01	5.77	12.86	5.71	7.46
Swinbank (1963)	-17.76	35.83	10.39	9.15	7.10	9.09	12.86
Brutsaert (1975)	-21.12	21.60	0.18	-1.06	5.85	-1.12	7.10
Berdhal and Fromberg (1982)	-20.86	20.11	0.03	-1.21	10.37	-1.27	5.85
Idso and Jackson (1969)	-15.73	36.24	11.06	9.82	9.59	9.76	10.37
Idso (1982)	-14.28	22.19	4.45	3.21	4.43	3.15	9.59
Prata (1996)	-16.98	22.00	2.81	1.57	2.39	1.51	4.43
Izmon *et al.* (2003)	-19.20	19.86	0.51	-0.73	4.28	-0.8	2.39

Table 8. 7: The first half (first 3 columns) summarizes the minimum, maximum and mean, values of the measured clear sky temperatures and those calculated with from 11 models including values predicted using equation (6.11), all in unit of ^{o}C. The second half (4 columns) shows the comparisons results between the estimated and measured clear sky temperatures over the period under consideration with 1620 data points. Tabulated values are MBE and RMSE, all with units of ^{o}C,. These two statistics were determined in each case, for the 11 different models, with respect to the measured values (Measured-Model Column) and the modeled temperature by eq.8.11 (Predicted – Model Column).

8.5.3 Cloud Prediction over Riyadh

In this subsection the capability of the parameterized clear sky temperature formula, equation (8.14), in predicting the presence of clouds will be tested. Also, the level of discrimination between the clear sky and overcast sky temperatures will be investigated. Overcast data were selected using the same method used in selecting overcast times in Abha, section (8.4.5). Selected data used here were those for overcast times between December 2004 to March 2005, which are mainly in winter time. We aimed to have overcast periods for both summer and winter times in Riyadh to cover wider range of atmospheric conditions to test the model. Unfortunately, no overcast periods were reportedly found in summer times, since, in summer, the Riyadh sky is mainly considered as a cloud free atmosphere. To achieve the goal of this section we will progress with the available data, and more data may be available in the future.

Table (8.8) shows the statistics of the air temperature, vapor pressure, measured overcast sky temperatures and predicted sky temperatures using equation (6.14). The difference between the two temperatures for the selected 383 overcast data points is also presented. It is clear from the tabulated data that there is a mean separation of about 17 ^{o}C between the measured (cloud) and predicted (clear) sky temperatures. The model has a very good ability in predicting the presence of the cloud in the FOV of the detector.

Figure (8.23) shows a histogram of the difference between the measured overcast temperatures and those predicted using the clear sky model over the desired periods and for the considered data. The graph shows that more than 85 % of the differences between the two temperatures are above 17 ^{o}C, which means that both temperatures are well separated from each other. This indicates that the model is at least working well discriminating the cloudy periods in winter time at Riyadh.

However, a difference of only 1 ^{o}C was found on one or more occasions. In such conditions the discrimination of the cloudy sky becomes unpredictable.

	Range	Minimum	Maximum	Mean	Std. Dev
Ta (^oC)	15.02	7.81	22.83	14.40	3.64
Sqrt (*eo*) ($mb^{0.5}$)	1.71	2.78	4.48	3.56	0.41
Tsky measured (^oC)	25.87	-6.44	19.43	11.09	3.74
Tsky predicted (^oC)	18.66	-15.19	3.47	-6.70	4.44
T_{dif} (^oC)	25.48	-0.89	24.59	17.78	4.90

Table 8. 8: Range, Minimum, maximum, mean and the standard deviation of the key meteorological parameters used in this investigations Ta, Sqrt(eo) (square root of vapor pressure), sky measured temperature predicted sky temperature and T_{dif} is the difference between the measured and predicted temperatures using (8.11)

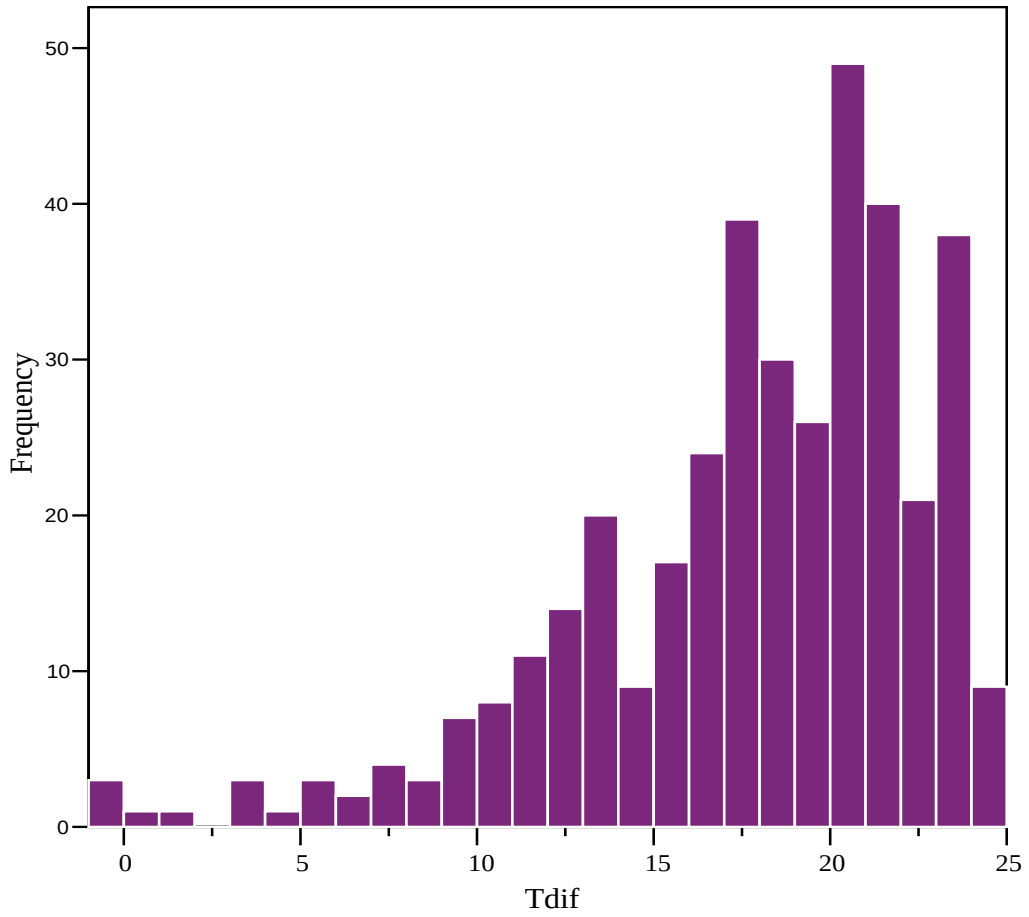

Figure 8. 23: .Frequency distribution for the difference of the measured overcast sky temperatures and sky temperatures predicted using the proposed clear sky model (equation 8.11).

CHAPTER NINE

CLOUD MONITORING FOR THE AUGER COSMIC RAY SITE USING A SINGLE PIXEL IR CLOUD DETECTOR

9.1 Introduction

Atmospheric monitoring is critical for air fluorescence detectors used in the Auger project. That project uses the atmosphere as a detector medium for ultra high energy cosmic rays. At the Auger cosmic ray site, a number of experiments have been carried out in the atmospheric monitoring program. In particular, in April 2005 the University of Adelaide deployed a single pixel IR cloud monitor at the central laser facility site

(CLF) in the centre of the Auger observatory, for monitoring sky temperatures to support its cloud camera activities.

The aim of this chapter is to use the sky temperature data collected from the cloud monitor to study the characteristics of the clear skies over the site and formulate the clear sky temperature as a function of measurable observational quantities. We hope then that the obtained model is able to predict the presence of clouds over the site in a similar way to models obtained for the Adelaide and Saudi sites. Over a wide range of air temperatures and quite reasonable amounts of water vapor, we propose a formula that accurately predicts clear sky temperatures. It is hoped that this formula can support the ongoing research currently carried out by the fluorescence group at the observatory to set cloud detection criteria for sky images taken by the IR cloud cameras.

The first two sections of this chapter will give a brief introduction to the Auger project and a brief summary of the atmospheric monitoring programs there. Data sets and the methods for selecting clear sky times will be discussed in section (9.4). Data analysis, parameterizations, and results will be detailed in section (9.5). The results section (9.6) is divided into three subsections, the formulation of the clear sky temperature and associated statistical tests will be given in the first. The second subsection is devoted to comparisons between the proposed formula and some bulk models. The ability of the proposed formula in setting a discrimination level between clear and cloudy skies will be investigated against data from overcast periods in the third subsection.

9.2 The Pierre Auger Observatory

The Pierre Auger Project is an international collaboration to study the nature of the highest energy cosmic rays. It is designed to unveil the secrets of those Ultra High Energy Cosmic Rays (UHECR) through the observation of the Extensive Air Showers (EAS) they produce in the atmosphere (Bertou 2005). The importance of the Pierre Auger Project lies in the fact that, at the very highest particle energies, deflection from galactic and intergalactic magnetic fields is small and so directional studies are possible. To overcome the problem of very low UHECR fluxes, the Pierre Auger Observatory employs an enormous collecting area, covering 3000 km^2 on an elevated plain in western Argentina near Malargue, a town in Mendoza Province that lies just east of the Andes Mountains. This area is covered by an array of 1600 $10m^2$ base, 1.5 m deep water Cherenkov detectors on a 1.5 km triangular grid (Dawson and Sommers 2001).

This is called the Surface Detector (SD). Also, air fluorescence detectors (FD) (Fly's Eye-type) monitor the atmosphere above the array. They will be distributed in 4 stations around the edge of the surface detector array and will view the atmosphere on moon-less nights. At present, three of these four fluorescence sites have been completed and are in operation. Two of them, Los Leones and Coihueco, have been working since January 2004, the third, Los Morados, began working in March 2005 (Bellido. 2005). The fourth site at Loma Amarilla will be in operation early 2007. The array of water Cherenkov detectors and a fluorescence eye makes up a hybrid detector. This then has the ability to describe the detailed nature of EAS. The fluorescence detector provides measurement of the longitudinal development profile of the total shower energy. The surface detector, on the other hand, records the shower front parameters. Details of the fluorescence and surface detectors can be found, for example in Abraham *et al.* (2004), Bellido (2005) and reference therein, and Auger collaboration papers in the 27^{th} and29^{th} International Cosmic Ray Conference (ICRC)

9.3 Atmospheric Monitoring for the Auger FD

Atmospheric correction to fluorescence data is an essential part of the reconstruction process of a shower. The prime uncertainties in the fluorescence measurements arises from uncertainties in atmospheric transmission, light scattering, and cloud correction to the fluorescence data (Matthews and Clay 2001). Analysis of the fluorescence data relies on a detailed knowledge of the scattering and absorption properties of the atmosphere between the sites of emission and detection in order to reconstruct the original cosmic ray's direction and energy. If, for example, the emitted fluorescence light passes through cloud, the scattering and absorption it suffers will change with respect to a clear sky due to the cloud's particle content, its higher water vapour and its ice content. Reconstruction of the cosmic ray cascade from the fluorescence data then, requires information about cloud cover at the time of the observation.

As part of the Auger atmospheric monitoring program a number of experiments were conducted and different instruments were installed to develop a good knowledge of local atmospheric conditions, e.g. Roberts (2001), Wiencke (2001). The Auger Central Laser Facility (CLF), optical depth monitor, aerosol phase function monitor and cloud detectors are all examples of the experiments used in this program. As its contribution to the program the University of Adelaide has installed commercial IR cloud cameras at

the each of the three completed fluorescence sites. Also a single pixel IR detector with STD filter and 3^o FOV, as described on chapter 3, was deployed at the centre of these sites adjacent to the CLF site. The cloud cameras operate between 7 μm to14 μm. The need for this single pixel detector arises from the fact that these cameras are not radiometric. They produce IR images but have no absolute physical criteria for cloud discrimination.

Data from the cloud monitor will be used in this study to formulate the clear sky temperature.

9.4 Site Descriptions and Data Collection

The cloud monitor was placed viewing vertically at the CLF site. The site is located at the center of the Auger observatory. The fluorescence detectors or the eyes of the observatory are located at three sites, Los Leones, Coihueco and Los Morados. Figure (9.1) shows the locations of the three sites and the CLF site where the cloud monitor is placed. The CLF site is located at an altitude of 1412 m above sea level with distances of 30 km, 26 km and 31 km from Coihueco, Los Leones and Los Morados respectively.

The primary observational dataset consists of measurements of the sky temperatures and surface meteorological conditions during the period of operations. The CLF measurements have been made since April 2005, the time when the cloud monitor started work. Sky temperature measurements were obtained from the STD cloud monitor with a 3^o FOV for which the spectral range of the detected radiation is 5.5 μm to 50 μm. Corrections for sky temperature were made using the absolute calibration formula described in chapter 3.

The data used in this study were those covering the period between April 2005 and December 2005. Sky temperature measurements were recorded every 5 minutes and logged to the CLF database unit via an on site logging system. These data are saved in daily files and can be viewed in a daily or monthly basis from the Auger website[1]. They can also be extracted from the above website as text files. Measurements of surface weather data were recorded by the weather station at the CLF. The recorded weather information are ground level temperature, relative humidity, wind speed and direction, average wind speed and atmospheric pressure. These data are collected every 5 minutes and sent daily to the database at Lyon in France. Dew point temperature, which is used

[1] http://www.physics.utah.edu/~wiencke/auger/clf_cldmon/.

to calculate the vapour pressure, is calculated using the methods described in chapter 3, (Equations (3.18) to (3.20)). Cloud cover information was obtained from the IR cloud cameras placed at the three fluorescence sites mentioned above.

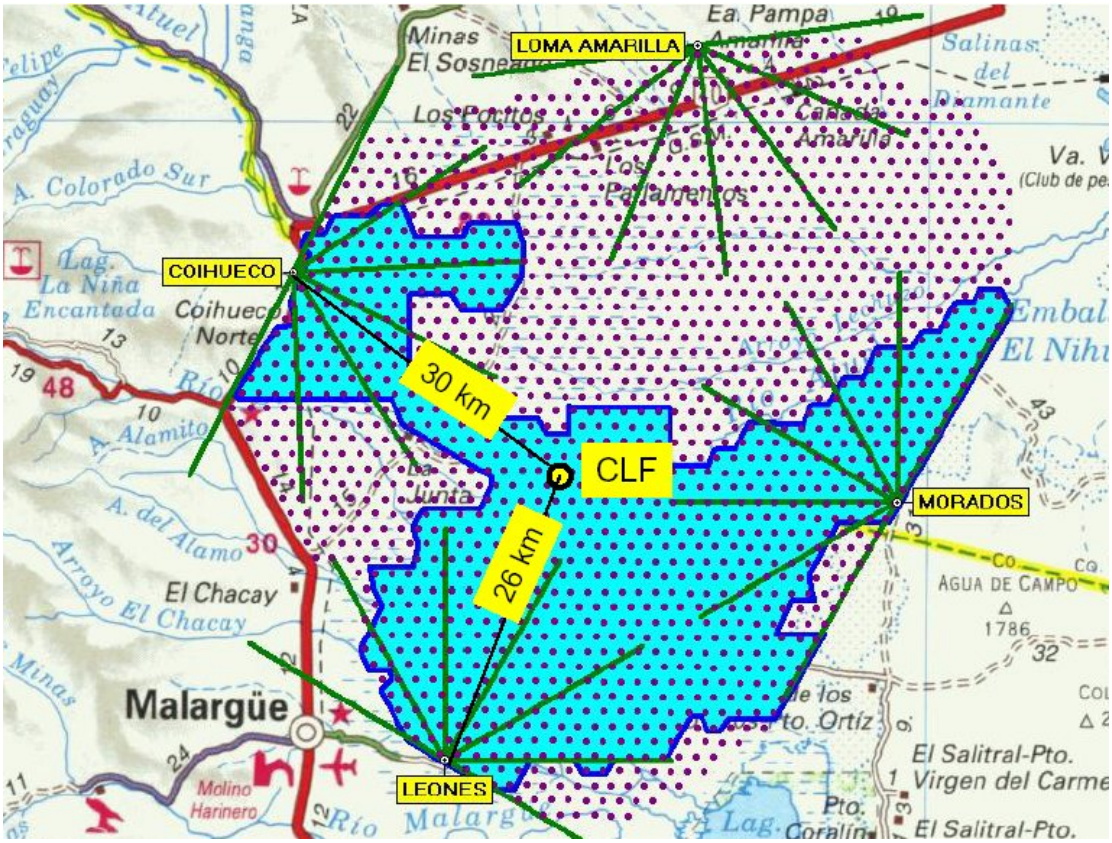

*Figure 9. 1: Shows the arrangement of the four FD sites and the CLF site , where the cloud monitor was placed, located approximately in the middle of the three eyes.(Bellido 2006 private communication***).**

9.5 Clear Sky Selection and Setting the Database

The clear sky data was selected according to the following processes. The CLF is located at the middle of 3 sites equipped with IR cloud cameras. At a certain time, if all the three images from the cameras are recorded as a cloud-free, this means that the CLF was also a cloud free site. This criterion is believed to be valid when at least the last hour and the following hour images were clear at the three sites. Figure (9.2) shows a clear sky image taken with the IR cloud camera at Los Morados. This selection method is an approximation and based on the cloud motion from one place to another.

For example if the cloud images at a specific hour from the three sites are clear and the images for the next hour are also clear, this means that the sky dome at the CLF within the area at that time at these three sites is cloud free. Selecting clear skies using this method enabled us to reduce the data to certain times, in which we were almost confident of their clearness. Further, the data selected for these times were then checked by plotting each selected period individually and checking the sky temperature variations during this period. This assessment was used because the clear skies are colder than cloudy skies and the presence of the cloud, which emits also IR radiation and hence is warmer, may cause dramatic change in the sky temperature measurements. This method was used in chapter 8.

Based on the above two criteria a total of 136 data records of clear sky temperatures and corresponding values of surface weather are ready for the analysis.

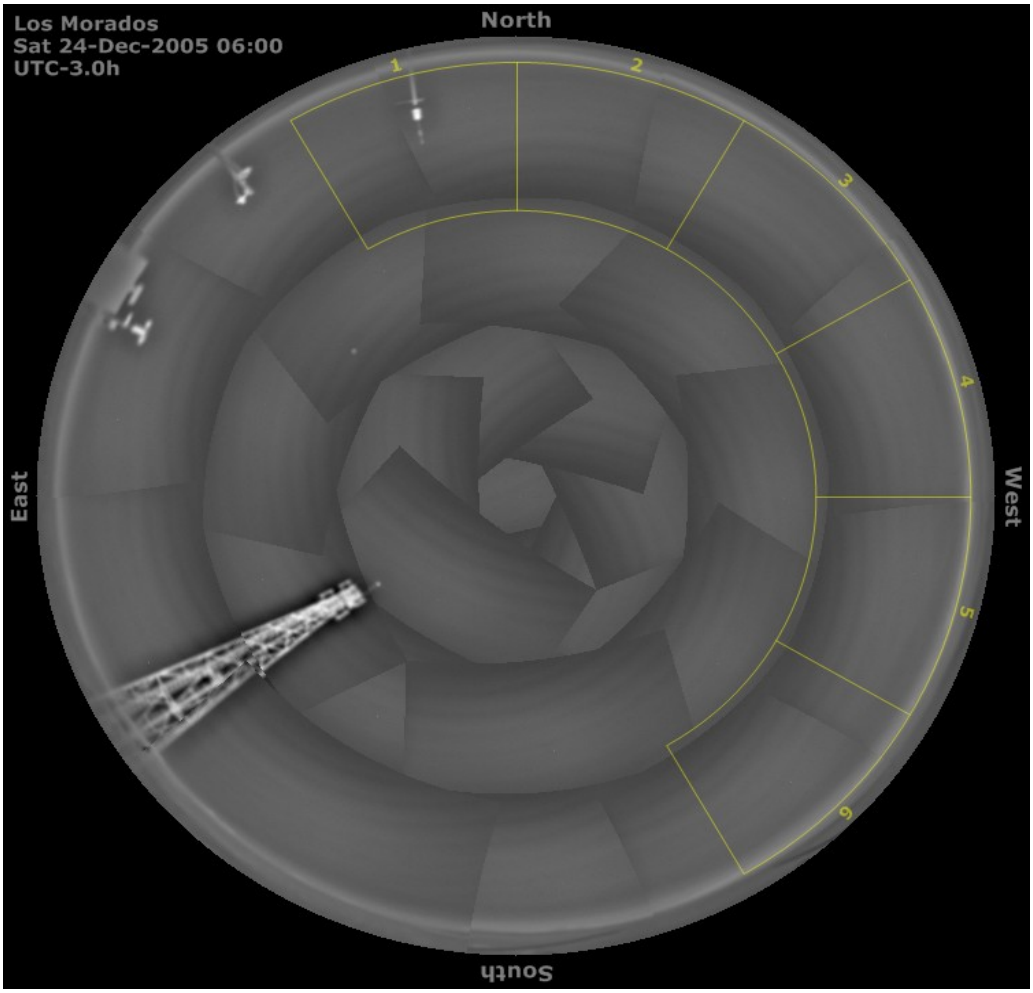

Figure 9. 2: Shows an example of a clear sky image taken by the IR cloud camera at Los Morados site on 24 December 2005 at 6 am UT.

Calibration corrections were then applied to the selected sky temperatures by applying the calibration formulas obtained from the detector calibrations outlined in chapter 3. The statistics of the key meteorological variables and the measured sky temperatures for the clear periods are presented in Table (9.1). The clear sky temperature ranged from –39 ^{o}C on very cold dry clear nights to –7 ^{o}C on warm wet nights. The screen level temperature varied from –8.8 ^{o}C to 20.5 ^{o}C and the temperature measured by the thermistor from –6 ^{o}C to 20 ^{o}C. The surface water vapour pressure lies within a 2-11 mb range and the relative humidity from 12 % to around 90 %. Although, the dataset has a small number of measurements, it contains a considerable range of the measured quantities, in contrast to measurements obtained from Adelaide and Saudi sites. The main aspect is a wider range of sky and air temperatures with values that have not been reached in Adelaide or in Saudi sites. This is an important factor towards assisting in later formulating the unified clear sky temperatures for all the sites.

	Range	Minimum	Maximum	Mean	Std. Deviation
Air Pressure (mb)	21.28	853.73	875.01	862.49	5.05
RH (%)	78.15	11.75	89.90	57.87	22.40
T_{dp} (^{o}C)	20.89	-12.36	8.53	-3.48	4.90
Vap. Pressure *eo* (mb)	8.74	2.37	11.11	5.00	1.77
Ta (^{o}C)	26.45	-6.40	20.05	5.53	6.78
Tsky (^{o}C)	28.25	-39.82	-11.57	-24.62	6.61

Table 9. 1: Descriptive Statistics of the clear sky meteorological and sky temperature measurements at CLF site for the period of 6 months between April to December 2005. Tsky is the corrected sky temperatures using the calibration formula,. Ta is the air temperature measured by thermistor inside the detector. RH is the relative humidity and Vap. Pressure (eo) is the vapor pressure. Air pressure is the atmospheric pressure and T_{dp} is the dew point temperature .

9.6 Results and Discussion

In the first step, a model based on a regression between the sky temperature and the vapour pressure and air temperature will be proposed. In the second step, the proposed model as well as the measured sky temperatures will be compared with some of the existing models found in the literature. Finally, the new model will be used for some selected overcast sky conditions to observe its capability to define the level of change from clear to overcast sky conditions.

9.6.1 The New Model

The procedure of analysing the data here is same as that followed in chapters 4 and, in which we attempted to find a best approximation for the clear sky temperatures using the ground level measured quantities. Figure (9.3) shows the relation between clear sky temperature (*Tsky*) and air temperature (*Ta*). Although there is some scatter the relation between the two temperatures over the whole range of air temperatures is quite linear. The regression analysis of a linear fit between the two temperatures gives the following:

$$Tsky = -28.77 + 0.75 \times Ta \tag{9.1}$$

The correlation coefficient of this regression was 0.65 with a RMSE of 4.2^{o}C and MBE of 0.01 ^{o}C. Although the average value of MBE was small for this fit, a range from - 10 ^{o}C to 7 ^{o}C was found (see table (9.2)).

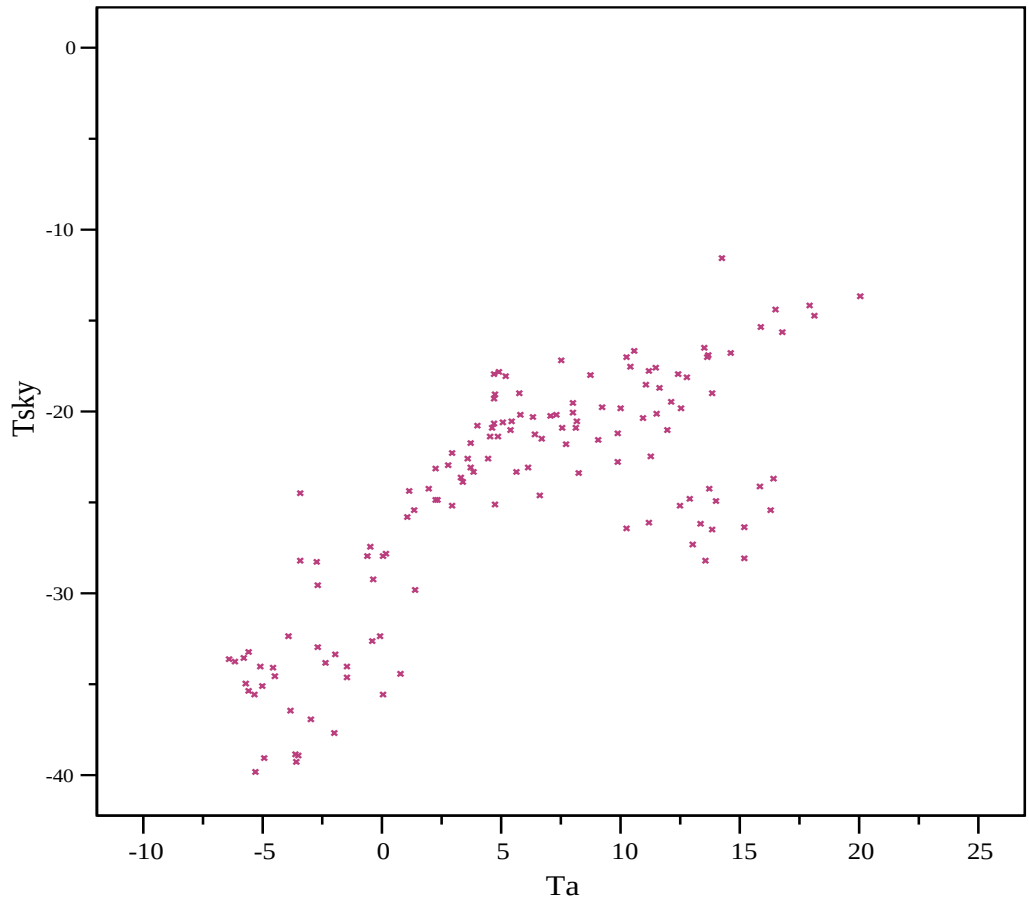

Figure 9. 3: Clear sky temperature as a function of the air temperature for CLF site.

The behaviour of the clear sky temperature under various conditions of water vapor pressure was then investigated. Figure (9.4) shows the relation between the sky temperature and the square root of vapor pressure. The relation is roughly linear with a spread in the data forming two parallel groups of data, which may be due to the combination of two different extremes of wet and dry conditions.

The regression analysis between the two variables was:

$$Tsky = -49.6 + 11.38 Sqrt(eo) \tag{9.2}$$

The correlation coefficient was 0.6, RMSE was 5 ^{o}C and the average MBE was -0.05 ^{o}C. Large differences with more than 11 ^{o}C were found between measured and predicted sky temperature using the square root of vapor pressure as a single parameter (see table (9.2)). It is noteworthy to mention that the intercept and the slope of equation (9.2) were extremely high in comparison with those found for Adelaide or Saudi sites

when this single variable is considered. This may be due to the extremely low sky temperatures observed over the CLF which force the regression coefficients to higher values.

Both air temperature and vapor pressure were then, together, considered to parameterize the sky temperature. The multiple regression result gives the following:

$$Tsky = -45.59 + 8.05Sqrt(eo) + 0.561Ta \qquad (9.3)$$

The statistics of this multiple regression along with those single parameter discussed above are summarized in table (9.2). The average MBE of this fit was zero, the RMSE was 2.74 ^{o}C and the correlation coefficient R^2 was 0.92. These statistical values are better than those found when a single independent variable was used. The maximum and minimum MBEs found in using the single parameter formulae (equations 9.1 and 2.2) were reduced to lower values. For example, equation (9.3) showed a minimum MBE of -5.9 ^{o}C in comparison with -11.33 ^{o}C for equation (9.2) and -10.70 ^{o}C for equation (9.1). This is about 6 ^{o}C and 5.5 ^{o}C reduction in the MBE from (9.1) and (9.2) respectively when equation (9.3) was used.

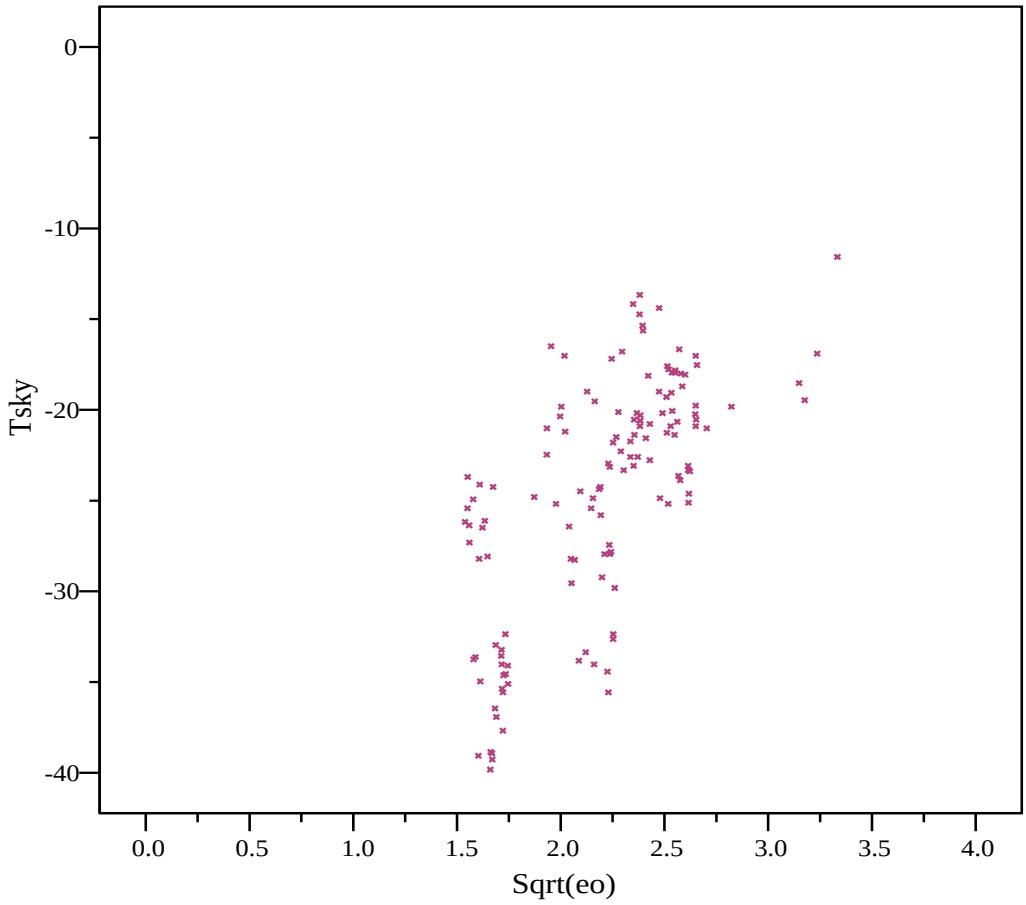

Figure 9. 4. Clear sky temperature versus the square root of vapor pressure (Sqrt (eo)) for CLF site over the period of study.

The fit of this model to the measured data is illustrated in figure (9.5) which shows the estimated sky temperature plotted against the measured values.

The distribution of the residuals of this equation (MBE) compared to the ideal normal distribution is shown in figure (9.6). The statistics of equation (9.3) suggest that this equation can be used with very good accuracy to predict the clear sky temperature with an error of less than 3 ^{o}C. The maximum deviation observed for this model was no more than 2 to 3 standard deviations. It is also important to mention that anomalous observations were expected to cause some of the deviations for the predictions. These may be due to errors in the measurements, either failure in the detector/logger system or in the measurements of some of the meteorological variables.

The linear relationship between the observed and predicted values was also statistically tested on a simple linear regression test at a significance level of (α = .05 i.e. 95 % Confidence Interval). The results indicted that the regression was statistically significant with a slope close to unity (0.89) and with R^2 = 0.92, suggesting a strong 1:1

relationship, see figure (9.5), between the model predicted and observed clear sky temperatures.

However, perfect performance is not expected from this model, hence, the data used here are for a limited range of atmospheric conditions. More observational data for longer period of times are preferable for better estimations and higher accuracy.

	Range	Minimum	Maximum	Mean	Std. Deviation
Tsky measured	28.25	-39.82	-11.57	-24.62	6.61
Tsky of Eq.(9.1)	19.84	-33.57	-13.73	-24.62	5.09
MBE of Eq(9.1)	18.00	-10.70	7.30	0.01	4.20
Tsky of Eq(9.2)	20.42	-32.10	-11.68	-24.56	4.51
MBE of Eq(9.2)	22.22	-11.33	10.90	-0.05	4.83
Tsky of Eq(9.3)	27.43	-37.73	-10.30	-24.62	6.01
MBE of Eq(9.3)	14.10	-5.94	8.17	0.00	2.76

Table 9. 2: Summarizes the statistics of the measured and predicted sky temperatures using equations (9.1) to (9.3) as well as the MBEs between the measured and predicted temperatures using the same equations. The units of all the variables in the table are ^{o}C.

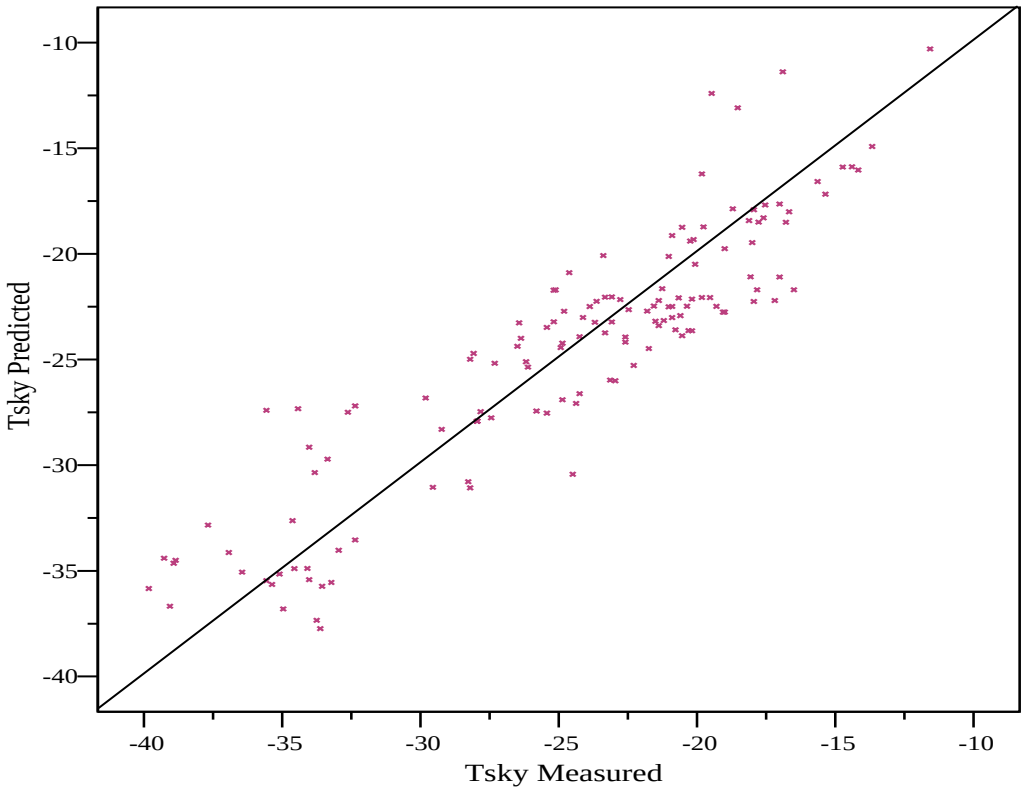

Figure 9. 5: Comparison between model and measured values of sky temperatures of the CLF atmosphere for clear sky conditions; the straight line is the 1:1 line.

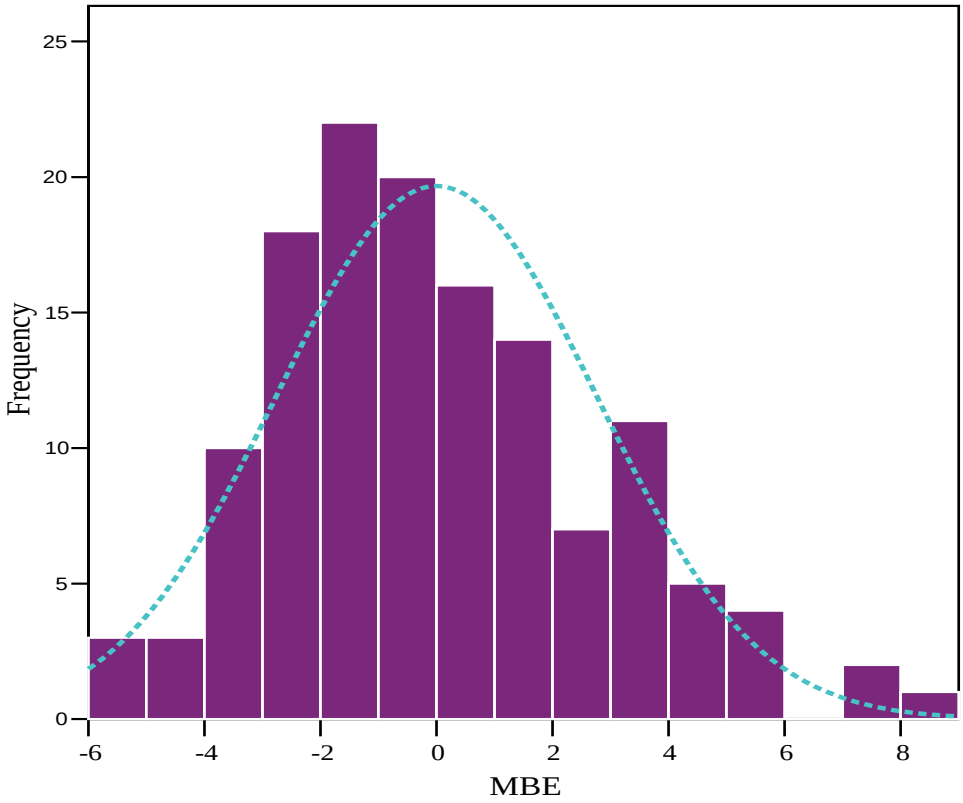

Figure 9. 6: Histogram (frequency distribution) for the difference between the modeled and measure sky temperature values, superimposed with a normal distribution curve. The mean of this distribution is not far from zero and the standard deviation was 2.5 ^{o}C.

9.6.2 Existing Models

Some of the widely reported clear sky formulae mentioned in chapter 2 were compared with the measured sky temperatures and with sky temperatures predicted by equation (9.3) referred here as *model1*. The functional forms of these models are summarized in chapter 2. The procedure of calculating the sky temperatures from these models are also discussed in chapter 2 and followed in chapters 4, 7 and 8.

The mean, maximum, minimum and the standard deviation of the measured and predicted temperatures from *model1*, and from those formulae are presented in table (9.3). The mean range of the modelled temperatures for all the published models was between

–11 ^{o}C to –20 ^{o}C. None of these models have shown proximity to the measured temperatures. However, Brutsaert, Brunt and Berdhal and Fromberg have shown closer values than the others with a mean of about 6 ^{o}C warmer than the measured values. Izmon *et al.* with the constant values substituted for mountain site showed the closest

values to the measured/predicted temperatures with a difference of about 4 ^{o}C. (Izmon *et al.* in their parameterization have developed model for low land site and high site, and for each site the proposed model have different constants, where here in this study and for Abha, and Tabouk sites in Saudi Arabia high site constants were used and for Adelaide, and the rest of the Saudi sites low land values were used). The models of Angstrom, Idso and Jackson and Efimofa have shown the warmest temperature, which are quite far from the measured values. Moreover, the statistical parameters of the regression analysis between the calculated sky temperatures from these bulk formulae against those measured/predicted for the CLF data were calculated and presented in table (9.4).

The average range of the estimated MBE between the measured/*model1* sky temperatures and the published formulae is between 4.2 ^{o}C to 13.5 ^{o}C. This means that the sky temperature has been overestimated. The Brunt, Brutsaert, Berdhal and Fromberg, Izmon *et al.* and Idso models have shown the minimum values of the average MBE, lie in the range between 4.2 ^{o}C and 7.8 ^{o}C. Angstrom, Efimofa and Idso and Jackson have shown the maximum MBE. Also, all the formulae are encumbered with significant higher values of RMSE which have values ranging from 5.8 ^{o}C to 14 ^{o}C, from measured temperatures or predicted temperatures. The correlation coefficients between each model, and both the measured and *model1* sky temperatures were also obtained. For the former the correlation coefficient R^2 values were (0.56 -0. 8), being lowest for the Idso and Jackson model, while higher values of R^2, between (0.6 – 0.9) were found between the *model1* versus models using published formulae. If all the three statistical criteria are taken into account, the majority of the published formulae discussed here in their original coefficients are in poor agreement with both empirical data and predicted data for the model proposed here. Those formulae were derived for various regions with diverse atmospheric conditions.

Model	Mean	Max	Min	STDEV
Measured Tsky	-24.62	-10.30	-37.73	6.04
Predicted Tsky eq. (4.32)	-24.62	-10.30	-37.73	6.01
Brunt (1932)	-18.64	-3.45	-35.47	7.84
Angstrom (1918)	-11.38	3.89	-29.13	7.92
Efimofa (1961)	-11.08	3.13	-26.10	7.37
Swinbank (1963)	-15.43	5.16	-35.44	10.32
Brutsaert (1975)	-18.70	-2.39	-36.86	8.17
Berdhal and Fromberg (1982)	-18.54	-3.68	-35.23	7.79
Idso and Jackson (1969)	-13.05	5.59	-26.79	8.25
Idso (1982)	-16.82	-3.60	-29.85	6.68
Prata (1996)	-15.19	-1.13	-30.83	7.44
Izmon *et al*. (2003)	-20.39	-7.15	-31.78	6.23

Table 9. 3: Summarizes the statistics of the measured clear sky temperatures and those temperatures calculated with from 11 models including values predicted using equation (9.3).

	Measured - Model			Predicted - Model		
MODEL	MBE	RMSE	R^2	MBE	RMSE	R^2
Predicted Tsky eq. (8.11)	0.00	2.74	0.92	-	-	-
Brunt (1932)	5.98	7.01	0.78	5.98	6.45	0.95
Angstrom (1918)	13.23	13.71	0.79	13.24	13.23	0.93
Efimofa (1961)	13.53	14.13	0.69	13.54	13.86	0.85
Swinbank (1963)	9.19	11.29	0.61	9.19	10.95	0.74
Brutsaert (1975)	5.91	6.88	0.82	5.92	6.36	0.98
Berdhal and Fromberg (1982)	6.07	7.09	0.77	6.07	6.54	0.94
Idso and Jackson (1969)	11.57	12.78	0.56	11.57	12.48	0.69
Idso (1982)	7.80	8.93	0.61	7.80	8.50	0.75
Prata (1996)	9.42	10.15	0.74	9.42	9.76	0.90
Izmon *et al.* (2003)	4.22	5.84	0.64	4.22	5.18	0.77

Table 9. 4: Comparisons of the estimated and measured clear sky temperatures at the CLF site during the period from April to December 2005. Tabulated values are the (MBE), (RMSE), all with unit of ^oC, and R^2. These three statistics have been determined in each case, for the ten different models, with respect to the measured values (Measured-Model Columns) and the modeled temperature by equation(.9.3) (Predicted – Model Column),. The sample contained 136 estimates.

Some of these bulk formulae have been calibrated by adjusting their constants to be useable in other places. For example Buckley *et al.* (1998) adjusted the coefficient of the Idso-Jackson formula to be appropriate for the H.E.S.S site in Nambia. Garicia (2004) has performed coefficient adjustments to Brunt, Brutsaert, Berahal and Fromberg and Prata equations to fit the IR radiation measured over Spain.

Here, as an illustration, the original coefficients of Brunt and Brutsaert were adjusted to be suitable in describing the clear sky at the CLF site. The Brunt formula with its original coefficients $\varepsilon = 0.55 + 0.0066 \times Sqrt(eo)$ was modified with new coefficients to fit the CLF data the equation becomes $\varepsilon = 0.545 + 0.0420 \times Sqrt(eo)$. The resultant MBE and RMSE of these adjustments were 0.7 ^{o}C and 3.7 ^{o}C respectively. Likewise,

the Brutsaert model in its original form was $\varepsilon = 1.24(\frac{eo}{T})^{\frac{1}{7}}$ and with a new coefficient has the form of $\varepsilon = 1.12(\frac{eo}{T})^{\frac{1}{7}}$ and gave a MBE of –0.4 ^{o}C and RMSE of 3.4 ^{o}C. Figure (7.8) shows the relation between the measured sky temperature and those predicted by the Brunt and Brutsaert with their modified coefficients.

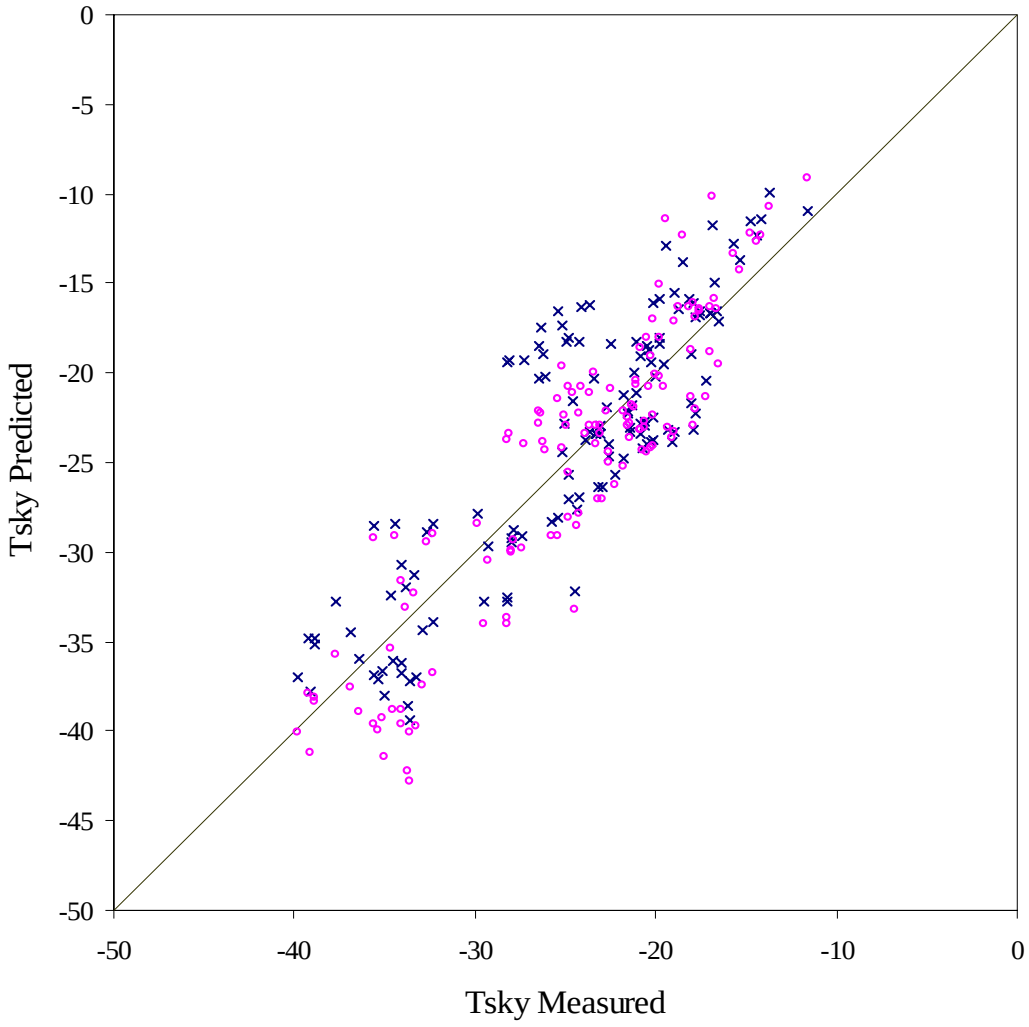

Figure 9. 7: Comparison between measurements and estimation of T sky for modified Brunt (blue +) and Brutsaert (pink ○) according to the local conditions at the CLF.

9.6.3 Testing the Model in Predicting clouds

We finish this chapter by looking to the capability of *model1* (equation 9.3) for predicting the presence of cloud. This was achieved as follows. Overcast periods were selected first, using the same method for selecting clear skies. However, here the cloud images from the IR cloud cameras from the 3 sites have to be totally overcast. Figure (9.8) shows example of an overcast image at Los Morados site. Figure (9.9) shows the overcast measured sky temperatures (warmer temperatures) along with the sky temperatures predicted using equation (9.3). The level of discrimination is clear with a difference of about 10 to 20 ^{o}C. The figure also shows the applicability of the formula of tracing the change of sky conditions from overcast, partly cloudy, to clear skies.

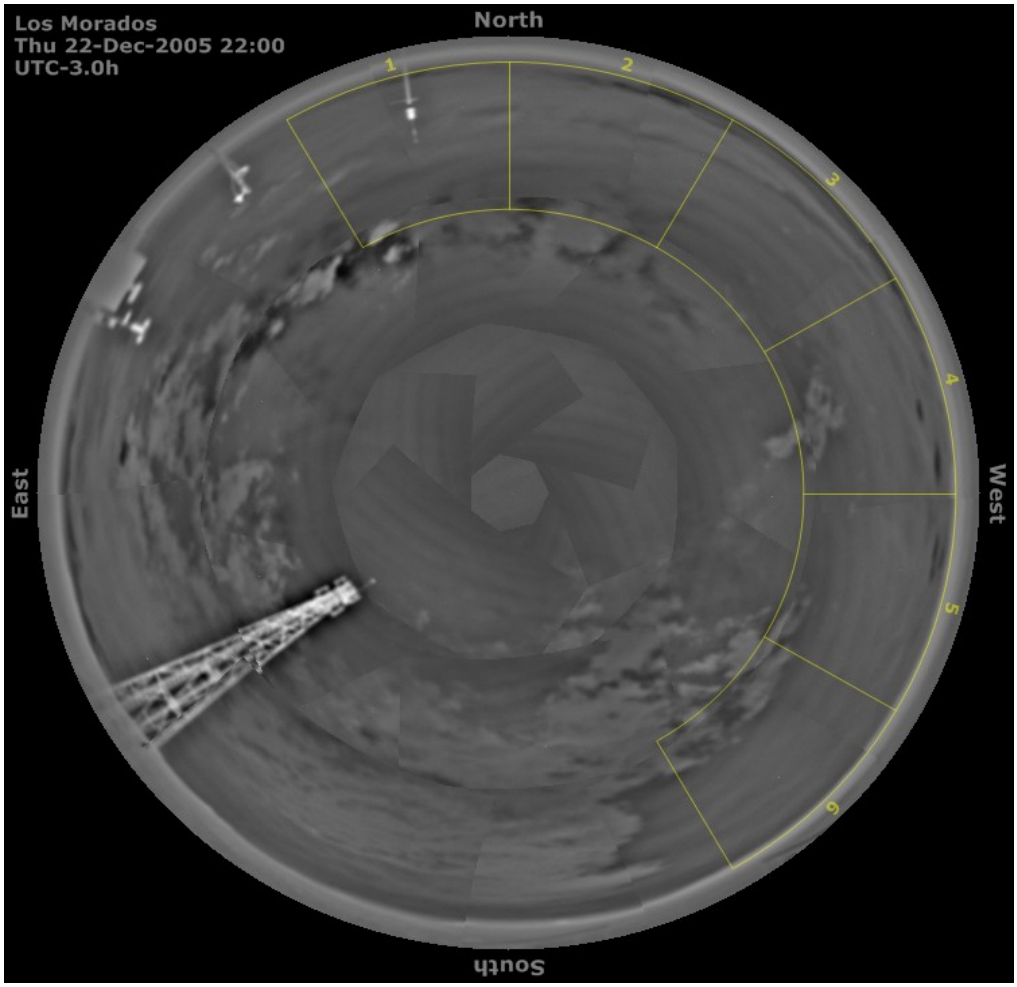

Figure 9. 8: Shows example of an overcast sky image taken by the IR cloud camera at Los Morados site on 22 December 2005 at 22 UT time

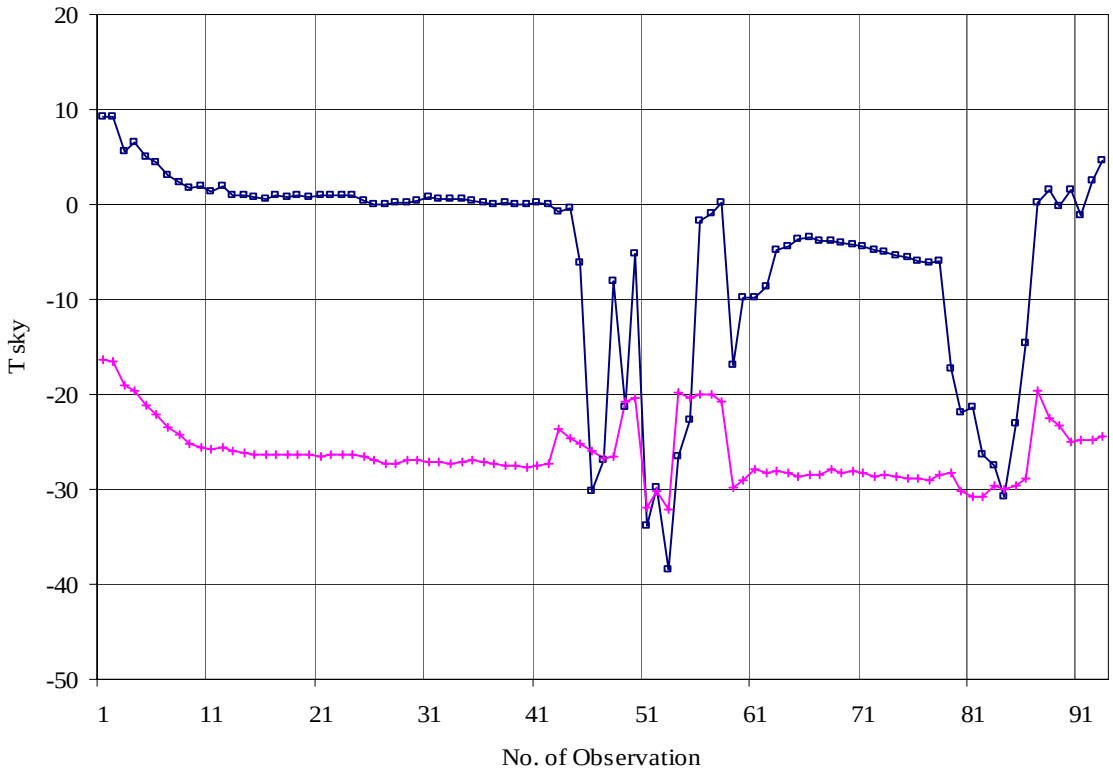

Figure 9. 9: Comparison between the measured sky temperatures with different sky conditions (overcast/clear) blue □, with temperatures predicted using the proposed model equation (9.3) pink + both are in ^{o}C. The abscissa is the sample number between April to December 2005. There is a clear discrimination between the upper line for observed overcast skies and the clear sky model line below.

9.7 Conclusion and Further Work

Data from a cloud monitor at the Auger observatory were compared with previously published formulae and a newly developed parameterization for clear sky temperatures. The data was less than a year of measurements during three seasons of operations. The developed model was evaluated and it showed a better performance against the measured temperatures. This empirically derived formula could be used in the future to set up some specific criteria toward establishing a certain level for changes between clear and overcast in the sky images recorded by the IR cloud cameras. Although the predictions of this model have less scatter than previously published predictions, it is not necessarily superior for Auger or other similar sites, in general, because they have been tuned with limited quantities quantity of data. Nonetheless, until more data become available, the model is recommended for use during clear skies in Auger.

Finally, the Auger cloud monitor data will be used further in this project to derive a unified model for data from Saudi Arabia and Adelaide.

CHAPTER TEN

TOWARD A UNIFIED SCHEME FOR THE CLEAR SKY TEMPERATURE

10.1 Introduction

In chapters 4, 8 and 9 we modelled the sky temperature as a function of screen level temperature and the atmospheric water content.

In those chapters we found that each site has its own formulation in predicting the clear sky temperatures. These formulae may differ from season to season for the same site. However, it was also found that a single useful formula could be developed if the data for more than one site is considered (section 8.4.6). The resulting general formula has some associated underestimation or overestimation at a particular site or under particular conditions. This is due to differences in other intrinsic properties of the site itself.

In this chapter, we are trying to draw a picture for the variations of the clear sky temperatures when data from all sites are considered together. This will include the study of the relationship between the clear sky temperatures under various conditions of the commonly used parameters, mainly the air temperature and the water vapour content. Other parameters will not be investigated; however, their effects may be discussed.

The sites considered here are Jeddah, Tabouk, Abha and Riyadh in Saudi Arabia, the Adelaide site in Australia and the CLF site at the Pierre Auger cosmic ray project in Argentina. The results are divided into two main parts. The first presents the analysis of data collected by the 3^o FOV detectors from Riyadh, Adelaide (at the zenith from the scanner) and the Auger site. The second part shows the results from sites having detectors with 90^o FOV. These are Jeddah, Abha, and Tabouk from Saudi Arabia and the Adelaide site in Australia. All the data used here and the presented results are those at night time measured by the STD detectors which have a spectral response of 5.5 μm to 50μm.

10.2 Data Sets

Data used here are those presented and described in the previous chapters. Table (10.1) and table (10.2) show the average statistics of the whole data set for sites having detectors with 3^o FOV (2773 data points) and sites with 90^o FOV (1934 data points) respectively. Data presented are the main meteorological variables and the sky temperatures. The data in the tables show a wider range of meteorological variables as well as sky temperatures than those covered by any individual site. For example, data from 3^o FOV detectors covered a range of air temperatures extending from -6 ^{o}C observed at the CLF site to the extreme warm temperatures found in Riyadh in summer. The last two rows in both tables represent the PWV and the coincident measured clear sky temperatures. The PWV data were obtained either by GPS sensors, at the Adelaide site, or from radiosondes at the Saudi sites. No measurements of PWV were available for this study from the CLF site.

	Range	Minimum	Maximum	Mean	Std. Dev.
RH %	91.15	5.85	97.00	42.27	26.56
Tdp ^{o}C	31.26	-12.36	18.90	2.60	4.94
eo mb	19.43	2.37	21.80	7.77	2.73
Sqrt(eo) mb$^{0.5}$	3.13	1.54	4.67	2.75	0.48
Ta ^{o}C	48.10	-6.40	41.70	19.34	9.73
Tsky ^{o}C	62.58	-39.82	22.76	-6.85	13.30
PWV mm (555)	28.42	1.86	30.28	11.16	4.08
Tsky ^{o}C (555)	50.07	-29.29	20.79	-13.41	10.01

Table 10. 1: Shows the mean values of some of the measured meteorological variables and the sky temperature at the 3 sites, Riyadh, Adelaide and CLF, which have 3^{o} FOV detectors. These values are RH T_{dp}, vapor pressure (eo) and Square root of vapor pressure (Sqrt e_o), Ta, sky temperature T_{sky}. The last two rows represent the measured PWV for the Adelaide and Riydah sites and their corresponding Tsky. The numbers in the brackets in the PWV column represent the number of the PWV observations.

	Range	Minimum	Maximum	Mean	Std. Dev.
RH %	86.00	11.00	97.00	63.75	19.80
Tdew ^{o}C	42.49	-13.95	28.53	7.30	7.46
eo mb	36.81	2.08	38.89	11.49	6.48
Sqrt(eo) mb$^{0.5}$	4.79	1.44	6.24	3.28	0.87
Tair ^{o}C	32.68	1.26	33.94	15.73	7.16
Tsky ^{o}C	54.56	-32.71	21.84	-4.91	10.20
PWV mm (613)	52.29	1.86	54.15	12.83	7.42
Tsky ^{o}C (613)	51.13	-29.29	21.84	-11.38	11.92

Table 10. 2: Same as table (9.1) but the data here are for those detectors with 90^{o} FOV placed at the 4 sites The last two rows represent the measured PWV for the four sites and their corresponding Tsky. The numbers in the brackets in the PWV column represent the number of the PWV observations.

10.3 Results and Discussions

The results of the analysis of the data used here will be discussed according to the detector's field of view. In the first sub-section, the results from 3^{o} FOV detectors will be presented while the second subsection will discuss the results from the 90^{o} FOV detectors.

10.3.1 Sites with 3o FOV Detectors

10.3.1.1 Ground Level Measurements

Figures (10.1) and (10.2) show the relationships between the sky temperature and the air temperature and the square root of the screen level vapour pressure respectively. They show that for each site the relationship between the sky temperature and these two parameters is different and exhibits different sorts of behaviour. This variation is evident, and the aim here is to investigate the factors that cause it.

For example for the same air temperature and water vapour values the sky temperature in Riyadh varies by 10 ^{o}C over two seasons. Also, for the same amount of water vapour over the whole range of sites the sky temperatures are different.

As we saw previously, the Riyadh site has shown clearly different regimes of weather conditions and sky temperatures between the seasons.

Seasonal variations at the same site and altitude effects from one site to another have been reported and studied in different articles e.g. Berger *et al*. (1987), Swinbank(1963) and Izmon *et al*. 2003. In studying the atmospheric radiation in two sites (lowland and mountain land) in southwest Germany for more than three years, Izmon *et al*. (2003) found that a difference in the elevation of the study sites results in a significant contrast in their climatology and hence their longwave radiation regime.

Similarly, Swinbank (1963) reported data from different sites, in which he showed a similar sort of behaviour to that presented in figures (10.1) and (10.2). In his article, he presented data from Australia, UK and the Indian Ocean. He concluded that that the screen level temperature is the only parameter responsible for this behaviour and this parameter can be utilized to parameterize the atmospheric radiation. Moreover, even over a small scale range of distances (less than 2 km) Clay *et al.* (2007) recently discussed a pilot study in the southern suburbs of the Adelaide metropolitan area which examined the magnitude of changes in the clear sky temperature as the observation location is changed on a local neighbourhood scale, figure (10.3). Their measurements were conducted using a STD detector with 3^{o} FOV. They claimed that this finding may be expected due to the geographical structure, altitude differences and microclimatology effects over small distances.

Unlike the above observations, over longer period of time, seasonal patterns were not totally evident in data obtained from Adelaide site (chapter 4). Single models were developed to predict the sky temperatures over a period of more than 4 years. Evidence

found by Martin and Berdhal (1982) supports this finding. Their results showed that the clear sky emissivity observed over three sites in the United States tend to show no lower or higher values for the same value when allowance was made for the water vapour effect.

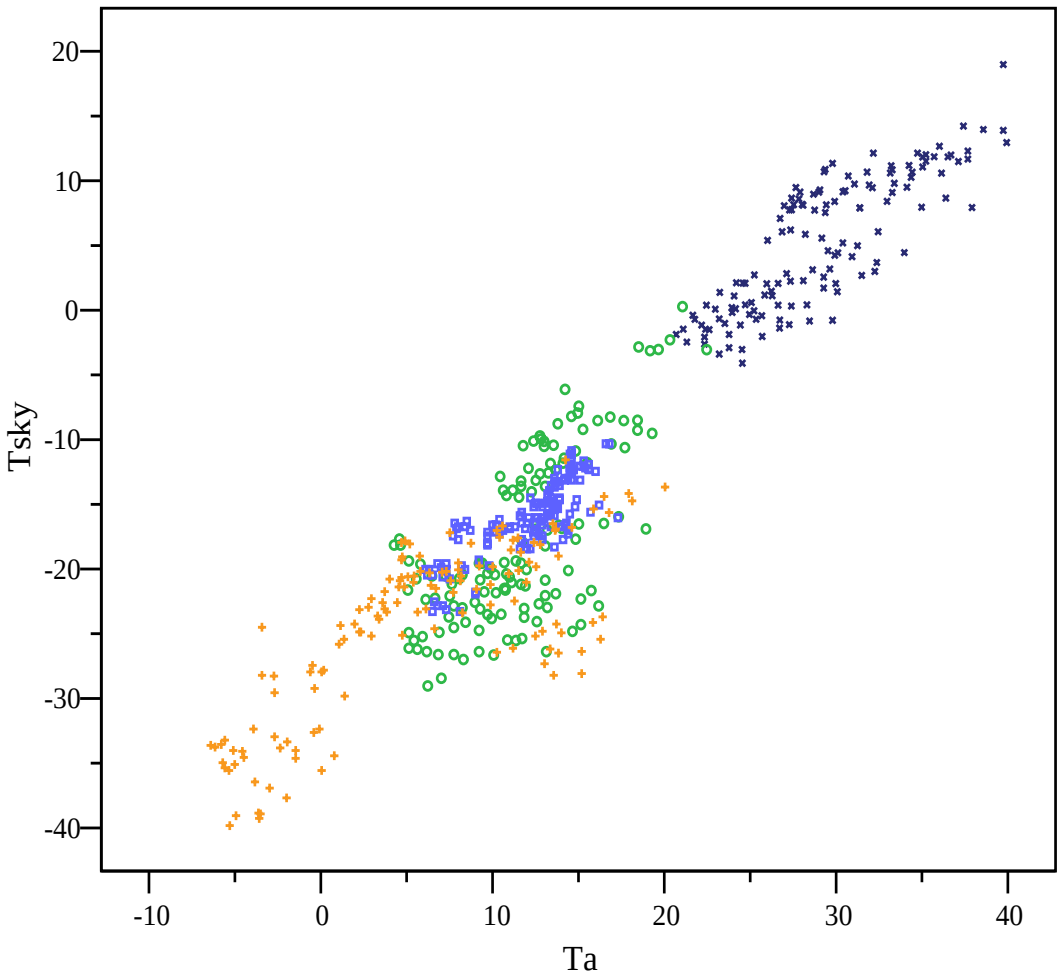

Figure 10. 1: Tsky vs Ta for clear skies at three sites having 3^o FOV detectors . Light blue □ Adelaide , green ○ Riyadh winter, orange + CLF and dark blue × Riyadh summer both temperatures in ^{o}C.

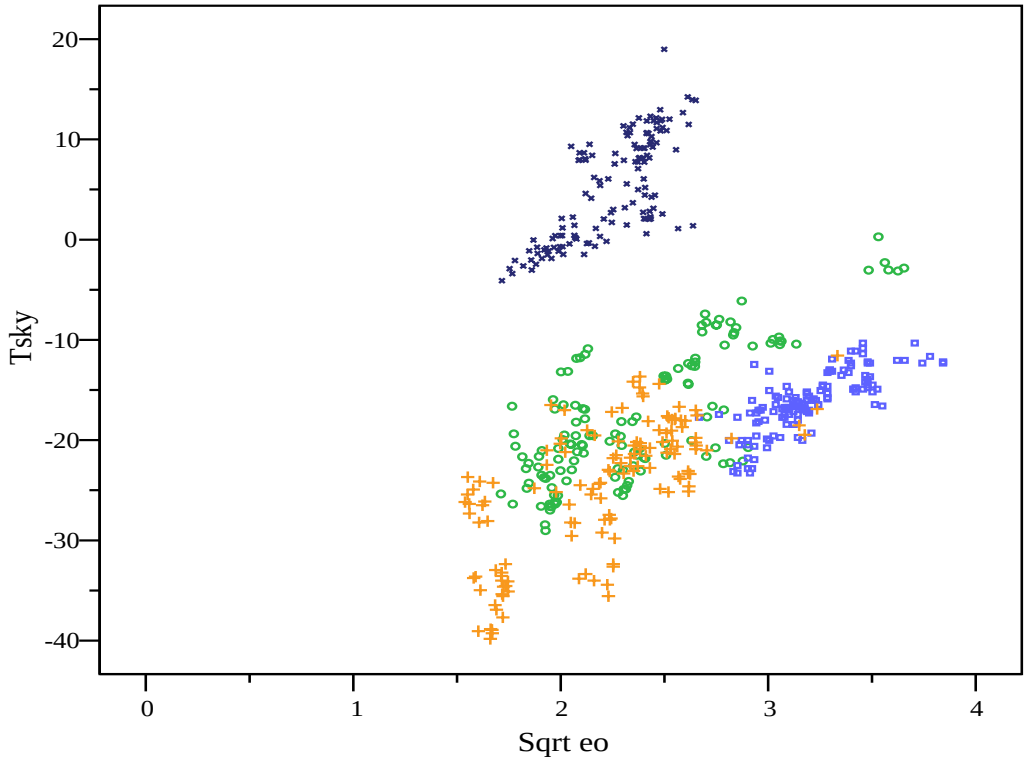

Figure 10. 2: Tsky (in ^{o}C) vs Sqrt (eo) in $mb^{0.5}$. for the three sites having 3^{o} FOV detectors Light blue □ Adelaide , green ○ Riyadh winter orange + CLF and dark blue × Riyadh summer

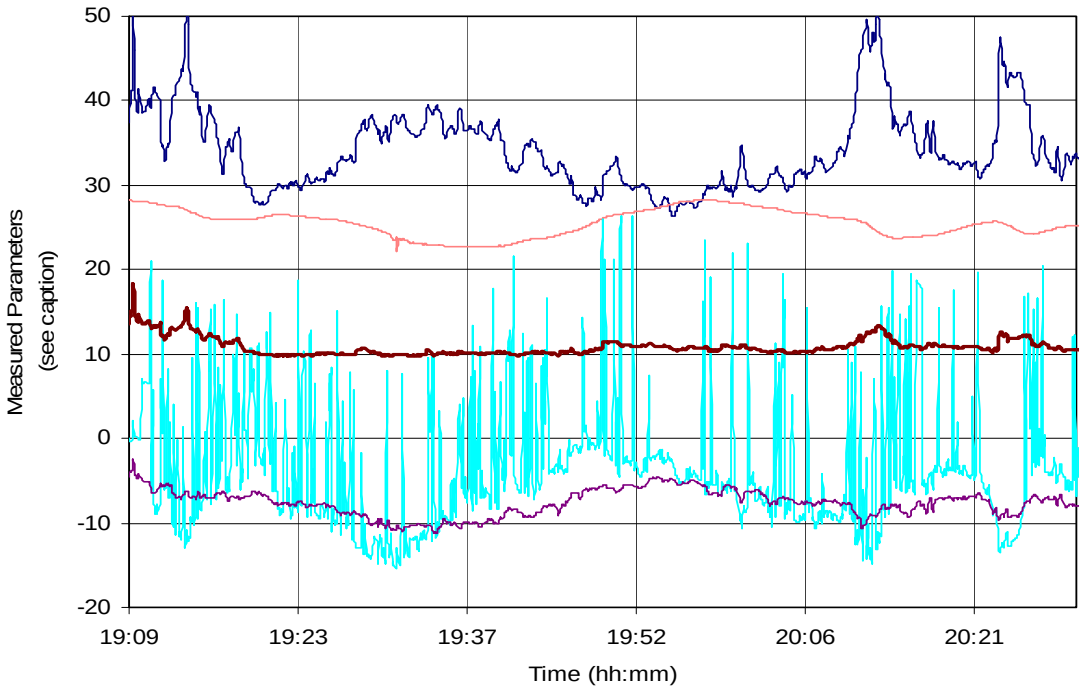

Figure 10. 3: Shows the variation of sky temperature over distances as small as hundreds of meters over the full range of altitudes accessible in the Adelaide metropolitan area, from the coast to the summit of Mount Lofty at an altitude of approximately 700 m. The lines (from the top) correspond to relative humidity% (blue), air temperature ^{o}C (red) vapor pressure mbar (dark red), sky temperature ^{o}C (turquoise), and predicted sky temperature ^{0} C (violet) using equation (4.29) for the Data taken on 24 March 2006. The many vertical lines are due to various thicknesses of tree canopy above the clear-sky baseline. Adapted from Clay et al. (2007).

Although, there is some spread in the data, figure (10.1) shows that over the whole range of air temperatures clear sky temperature correlate reasonably well with the screen temperature

The regression analysis between the two parameters in ^{o}C is:

$$Tsky = -31.5 + 1.27 \times Tair \qquad (10.1)$$

The intercept value of this equation looks reasonable and lies within an expected range of the average of its values found before for the three sites. The slope however, is larger than expected and indicates the need for other factors to be considered. The statistics of this analysis gives R^2 of 0.93, RMSE of 5 ^{o}C., MBE of 0.085 ^{o}C and average measured and predicted temperatures were -6.85 ^{o}C and -6.94 5 ^{o}C respectively. This equation can be used as an approximate predictor of the sky temperature over the whole range of temperatures. The deviation from this single regression model for the three sites over different seasons can be interpreted as being due to the fact that the sets of measurements are not homogenous where the observations made and that they were made at different distinct temperature and humidity regimes. This is in agreement with Swinbank's claims when using this parameter in parametrizing atmospheric radiation. Some of the large biases between the predicted and the measured sky temperatures at some temperatures may be due to the lack of the inclusion of other parameters, such as water content, which could give a much better estimate.

Figure (10.2) shows the relationship between the sky temperature and the amount of atmospheric water. The general pattern of the relationship between the two variables lies in parallel lines for the sites one to each other. However, for each individual site the relation is linear and evident. At the same value of the vapour pressure, different values of the sky temperatures were found. For example at the vapour pressure value of 2.8 $mb^{0.5}$ the reported sky temperatures were -26 ^{o}C, -20 ^{o}C, -12 ^{o}C and 14 ^{o}C for Adelaide , CLF, Riyadh winter and Riyadh summer respectively. This is in some way similar to figure (2) of Swinbank's article. Unlike the results reported by Swinbank and found in previous chapters, the correlation analysis applied between the sky temperature and the screen level vapour pressure now yields a negative relation. This means that an increase in the vapour pressure is accompanied by a decrease (colder temperatures) in the sky temperatures. The cause of this trend was due to the Riyadh summer data, which is located at the top of the figure. In these circumstances the use of the screen level water

vapour parameter to estimate the sky temperature is meaningless. Such behaviour violates the real physical relation found for individual sites between the sky temperature and the amount of atmospheric water in the atmosphere which showed that more water results in high sky temperatures. It also contradicts the theoretical implication of radiation transfer theory as well as empirical established models such as that of Brunt. A better physically based correlation between the sky temperature and the vapour pressure can be found if the Riyadh summer data are excluded. We expect that this group of points is associated with high screen temperatures and this is clear from the top of both figures (10.1) and (10.2). A multiple regression fit between the sky temperature and both screen temperature and vapour pressure was also conducted. The results gave a negative coefficient for the vapour pressure variable which is still contracting the expectations. Figure (10.4) is a 3-D plot, with two different views, for the sky temperature along with the square root of vapour pressure and the screen level temperature. As it can be seen from the figure, the relation between the three parameters, as a whole, is not obvious and factors other than those considered here may be needed if the Riyadh data are to be included.

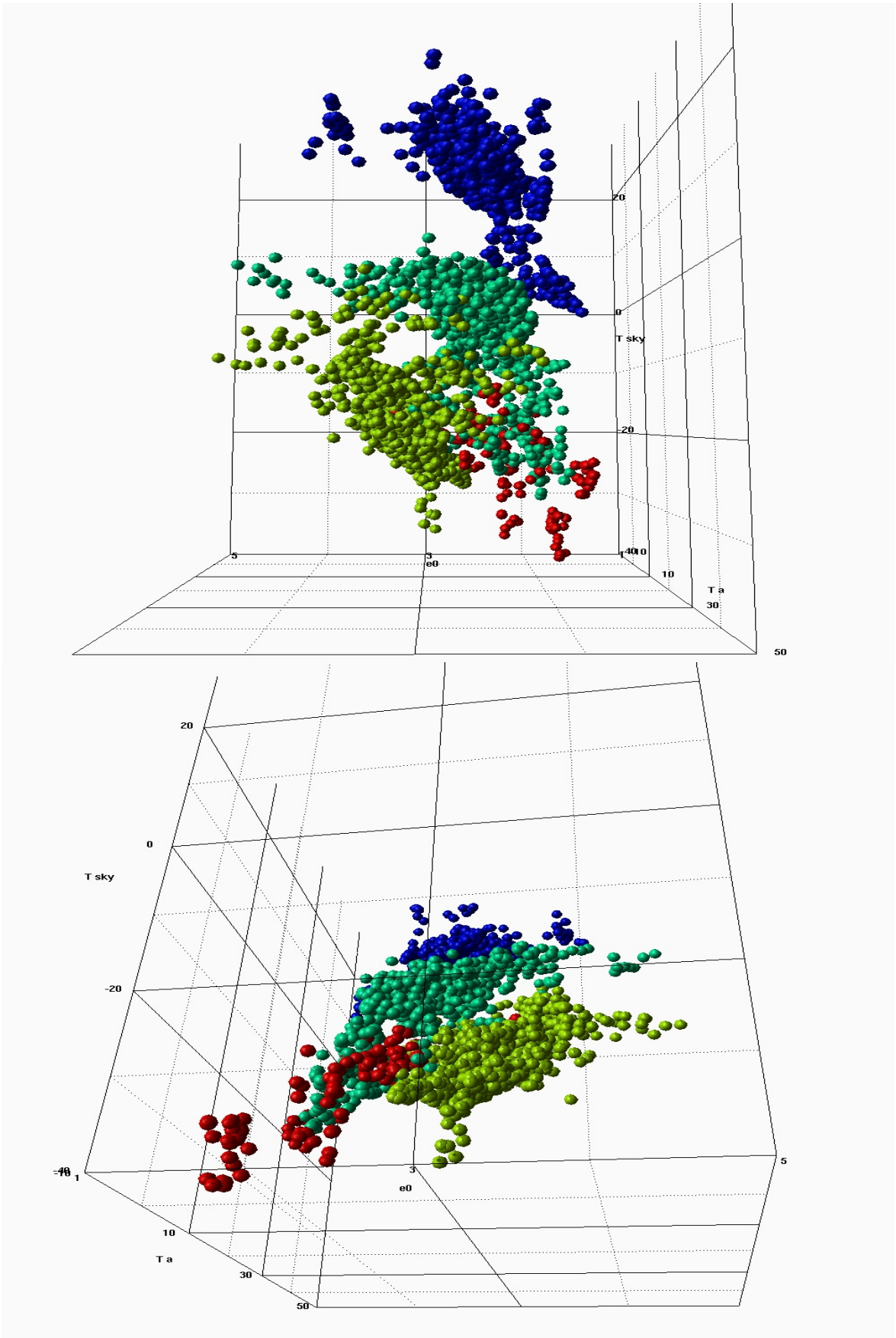

Figure 10. 4: 3-D plot with different views shows the relationship between the sky temperature (^{o}C) and both the square root of vapor pressure, Sqrt(eo) ($mb^{0.5}$), and temperature (^{o}C) for Riyadh summer (blue), Riyadh winter (dark green) Adelaide (green) and CLF (red).

Our first attempt to understand the combined dataset was to model the sky temperature individually for each site in different seasons at each site. Then the proposed model from one site at a particular season was used to predict the measured values from the rest of the sites. This resulted in biases, which were then subtracted from each site to superimpose the data and draw the final conclusions.

A multiple regression analysis was carried out previously for all sites. However, Riyadh showed seasonal variations of the sky temperature mainly with the screen level water vapour, which was not investigated in chapter 8. For the purpose of this chapter it was decided to find the seasonal formulation for Riyadh for both seasons. Because data from the Adelaide site have shown no seasonal trend, and due to the limited available data for the CLF site, it was not desirable to parameterize each season individually for them.

Table (10.3) presents the functional form, MBE, R^2 and the RMSE of the multiple regression analysis between the sky temperature and the air temperature and the square root of vapour pressure for the Riyadh site along with those found previously for Adelaide and the CLF. The associated errors for the intercepts, the coefficients of water vapour and air temperature for each of these formulae were 0.95 ^{o}C, 0.5 ^{o}C mb$^{-0.5}$, and 0.025 ^{o}C respectively. With the exception of the difference in the intercepts, the values of the slopes of the air temperature and the vapour pressure were almost the same for the Riyadh site in both seasons. Also, air temperature coefficients are almost the same and not too dissimilar to these for Adelaide and the CLF. The vapour pressure coefficients, on the other hand, for the Riyadh site in both seasons are not far (of the order of two standard deviations) from Adelaide and of order of four standard deviations from that for the CLF.

Site	season	Regression Fit Equations	MBE ^{o}C	R^2	RMSE ^{o}C
Riyadh.	Summr	$Tsky = -22.62 + 5.2Sqrt(eo) + 0.64Ta$ (10.2)	-0.15	0.81	2.5
Riyadh	Winter	$Tsky = -35.05 + 5.0Sqrt(eo) + 0.69Ta$ (10.3)	0.01	0.88	4.0
Adelaide	both	$Tsky = -39.2 + 3.5Sqrt(eo) + 0.79Ta$ (10.4)	0	0.87	2.7
CLF	Winter	$Tsky = -45.59 + 8.05Sqrt(eo) + .56Ta$ (10.5)	.0	0.92	2.7

Table 10. 3: The formulation, MBE, R^2, and the RMSE of the sky temperatures using the screen level temperature and the square root of the vapour pressure, , for the three sites over the specified season.

The Adelaide model was then chosen to be used as a predictor to the measured sky temperature at the other sites. The mean biases between the predicted and measured sky temperatures were 16 ^{o}C, 10 ^{o}C and 2 ^{o}C for Riyadh summer, Riyadh winter and CLF respectively. The source of these biases can be attributed to many factors: the difference in altitude between the sites, the amount and the distribution of water vapour content above the site and the amount of aerosol dust and smoke over the site. These are all examples of the sources expected to cause these biases.

These biases were then subtracted from the measured values for each corresponding site. For example, 16 ^{o}C was subtracted from every measured sky temperature at the Riyadh in summer time. This was done to superimpose the data and to help in finding a unified model which may lead to physical interpretations of the manners of the data found above. Figures (10. 5) and (10. 6) are similar to figures (10.1) and (10.2) with the data superimposed using the above procedures. In figure (10.5) the data were shifted by the amount of the subtracted bias without any major change to the actual pattern found in figure (10.1). Similarly the data in figure (10.6) were also shifted, with a remarkable change of the pattern. Here the Riyadh summer data were shifted closer to the data of Adelaide, Riyadh winter and CLF. The relationship between sky temperature and the screen vapour pressure now tends to become physically reasonable. The spread in the data is large but does not violate the physics of the relationship. A multiple regression analysis between the sky temperature and both the air temperature and water vapour using the superimposed data gives:

$$Tsky = -41.27 + 4.2Sqrt(eo) + 0.798Ta \quad (10.6)$$

The R^2, MBE and the RMSE for this relation were 0.92, -0.03 ^oC and 3.3 ^oC respectively. The standard deviation of the intercept was 0.5 ^oC, for the vapour pressure coefficient was 0.130 ^oC $mb^{-0.5}$ and for the air temperature was 0.006 ^oC. Despite different intercept values and slight difference for the CLF site, the slopes of the two parameters (Ta and Sqrt (e*o*)) were not significantly different from those found for the individual site. (See table (10.3)). The differences in the intercepts are expected to be due to intrinsic properties of the site.

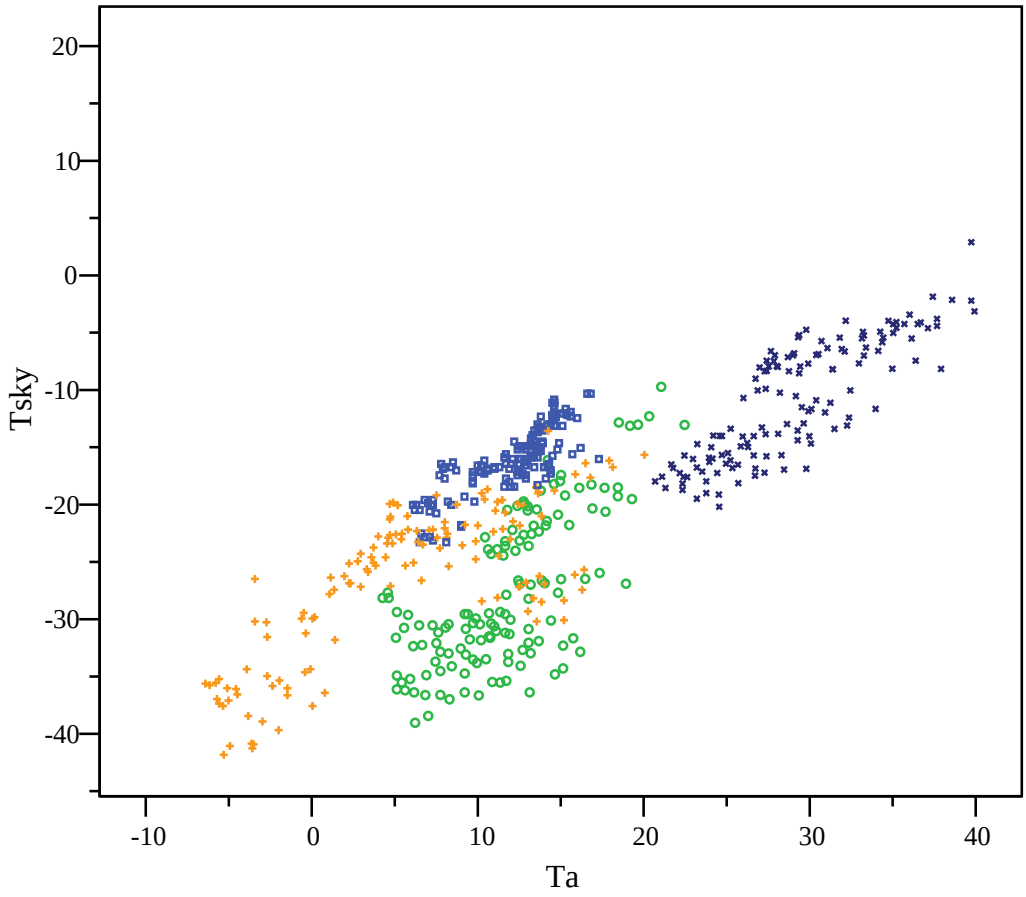

Figure 10. 5: Same as fig (10.1) , here data were shifted using the biases subtracted (see text for details) Light blue □ Adelaide , green ○ Riyadh winter orange + is CLF and dark blue × Riyadh summer

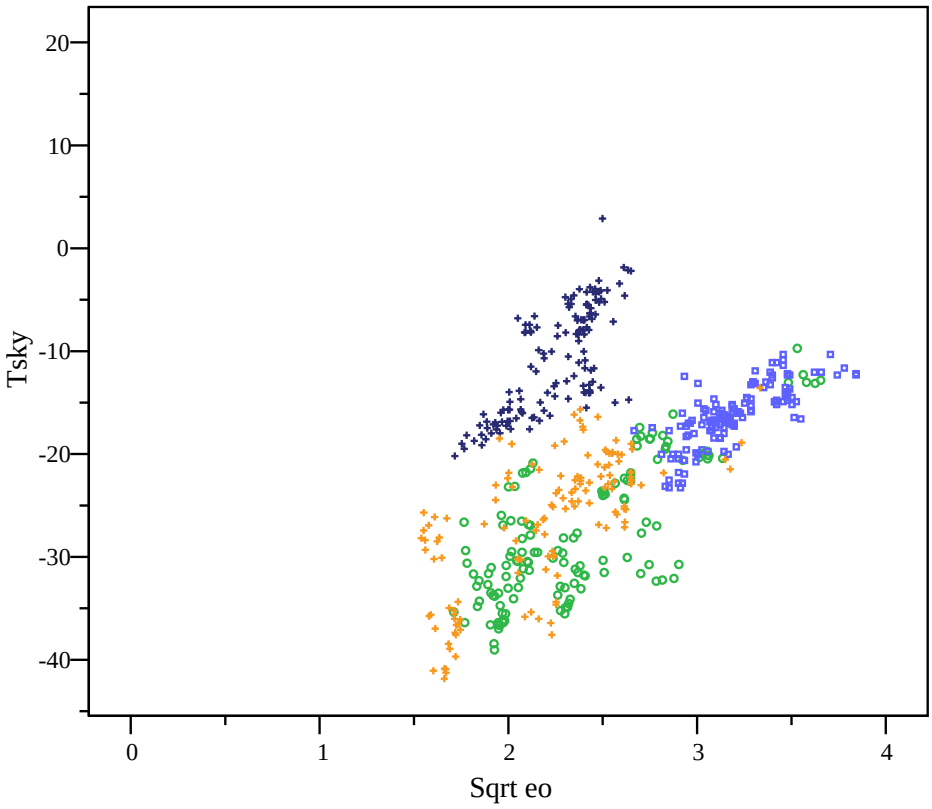

Figure 10. 6: Same as fig (10.2) , here data were shifted using the biases subtracted (see text for details) Light blue □ Adelaide , green ○ Riyadh winter orange + is CLF and dark blue × Riyadh summer

10.3.1.2 PWV Data

In the previous subsection we tried to understand the irregular relation between the sky temperature and the screen level variables, especially vapour pressure. We manipulated the data in such a way that a unified model could be produced. Our efforts, to some extent, were reasonable but not totally absolute since we did not account for the effect of the total amount of atmospheric water content as well as other parameters (e.g. aerosol effects). The former will be investigated here while the later will be the subject of the next subsection.

Figure (10.7) illustrates the relationship between the sky temperature and the PWV. The data used are those from radiosonde launches at Riyadh airport for summer and winter periods (see chapter 9) and from GPS receivers at the BP field site near Adelaide (see chapter 4). These data were not superimposed and are in their original form. The CLF site has no radiosonde data available for the current study.

The data lie in parallel lines with different values of sky temperature for the same amount of PWV. For example at the PWV of 10 mm the sky temperatures were -21.5 ^{o}C, -6.4 ^{o}C and 10.6 ^{o}C for Adelaide Riyadh winter and Riyadh summer respectively. This is similar to the pattern found in figure (10.2) where here the lines are closer. A correlation analysis between the PWV and the sky temperature gives:

$$Tsky = -29.13 + 1.40PWV \tag{10.7}$$

Although the statistics of this equation is poor (R^2 = 0.5, RMSE = 8.2 ^{o}C), it shows the physical meaning of the relation between the two parameters, an increase in the atmospheric water associated with an increase in the sky temperature. This is opposed to what we found when we related the sky temperature to the screen vapour pressure. The value of the PWV coefficient, 1.4, is high and different from those found for individual sites (see chapters 4 and 8). The prediction of the sky temperature using this equation compared to the measured sky temperature is somehow ambiguous and indicates that an inclusion of another parameter, such as air temperature, is required.

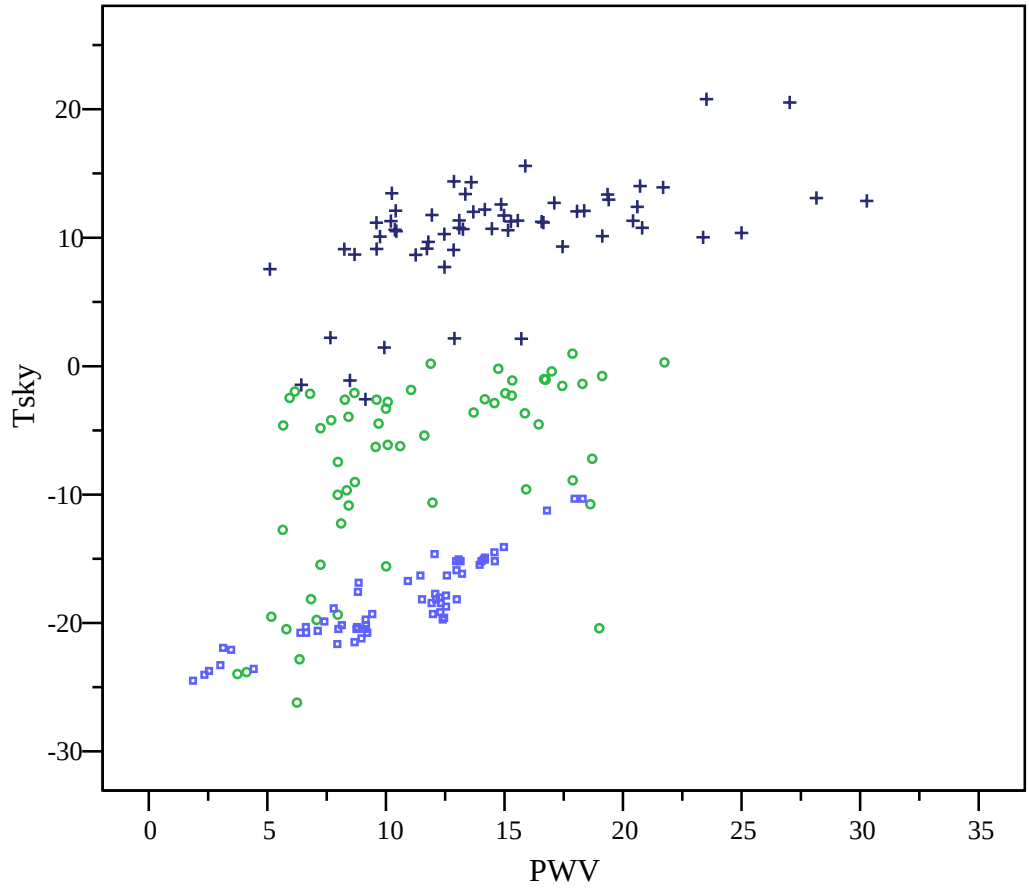

Figure 10. 7: The relation between the sky temperature ^{o}C and the PWV, for + Riyadh summer, ○ Riyadh winter and for Adelaide.

A two-variable fit between the sky temperature and both the PWV and the air temperature gives:

$$Tsky = -37.7 + 0.61PWV + 1.00T_{air} \qquad (10.8)$$

The correlation coefficient, MBE and the RMSE of the above equation were 0.82, 0.072 ^{o}C and 5.7 ^{o}C respectively. The standard deviations for the intercept, PWV and air temperature coefficients were 0.7 ^{o}C, 0.06 $^{o}Cmm^{-1}$ and 0.04 ^{o}C respectively.

The above formula shows coefficients which may be different from those found for each site individually. The coefficient of the PWV and the air temperature are related, in the two-parameter fit, in a way such that they tend to compensate each other. For example, if the PWV coefficient has a low value this corresponds to higher values in the air temperature coefficient. Although having higher value RMSE, about 5 ^{o}C, it is

noteworthy to say that this model performed reasonably well even though it was produced from data obtained from sites with complicated characteristics. Figure (10.8) shows the measured versus predicted sky temperatures using equation (10.8). It shows that the prediction was successful for a number of the points which lie in or close to the 1:1 line. On the other hand, we can see diversity between the two temperatures by 2 to 3 standard deviations from the equality line.

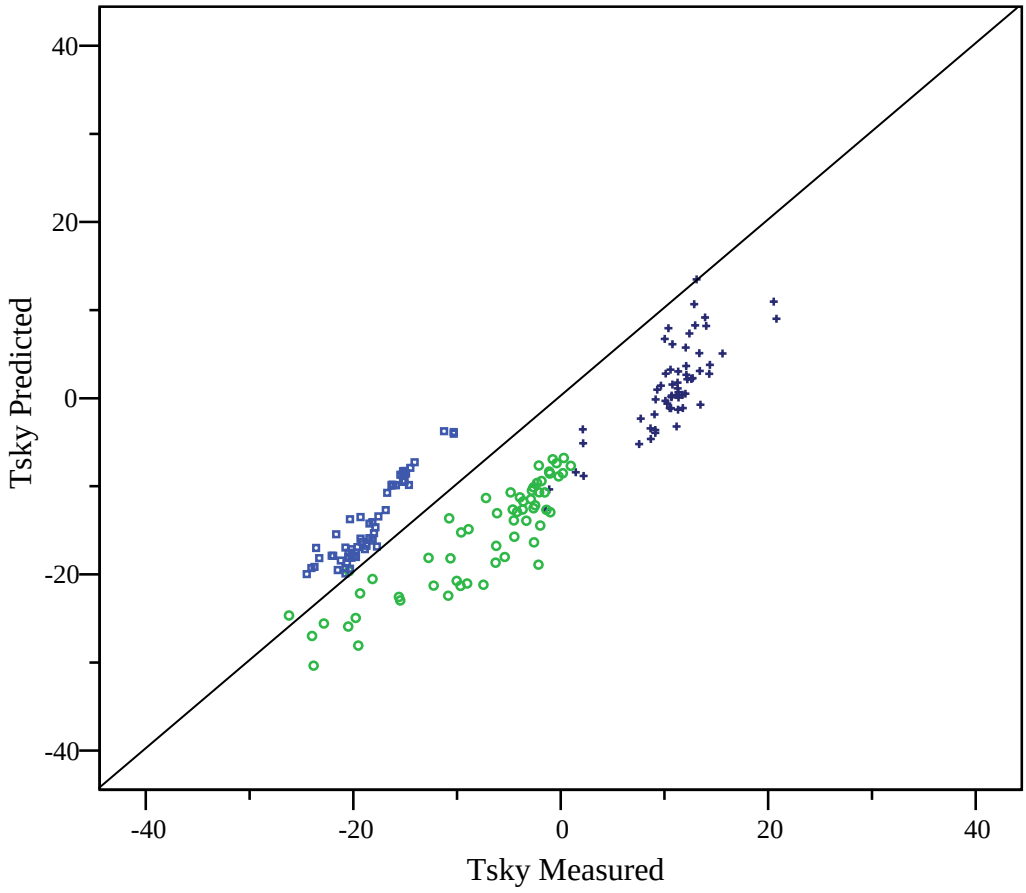

Figure 10. 8: Comparisons between measured and predicted (equation 10.8) sky temperature (in ^{o}C), dark blue + Riyadh summer, green ○ Riyadh winter and light blue for Adelaide. The straight line is a 1:1 line for reference.

The distribution of the water content at a specific site at a certain time may cause large biases in the prediction on a number of occasions, in which need to be investigated.

The scale height of water vapour for each data set (Riyadh summer, Riyadh winter and Adelaide) was calculated using available radiosonde information. The scale physically

relates the screen level water content and the total amount of PWV (see for example Ritan 1963 and equation (2.16)). Here it was obtained for each data set by performing a linear regression analysis between the PWV and the screen level vapour pressure. The inverse of the slope of the regression line is the required scale height. The average values of the scale height were 3.3 km, 2.3 km and 1.1 km for the Riyadh summer, Riyadh winter and Adelaide sites respectively. Their ranges were (1 to 6 km) for Riyadh summer, (0.5 to 5 km) for Riyadh winter and (0.2 to 4 km) for Adelaide. It is noteworthy to see that over one site the average scale height varies from one season to another and also in the same season. This has two important consequences. One is that the difference in scale height from one site to another and from one season to another may contribute to higher RMSE of equations (10.6) and (10.7) which were produced from sites having different scale heights. The second is that the screen level water content (represented either by vapour pressure, dew point or relative humidity) cannot be used to accurately represent the amount of water, at some times even at the same site. In this case, we are not accurately accounting for the stratifications of the real atmosphere over certain conditions.

10.3.1.3 Aerosol Effect Using MODTRAN

Since no data or measurements for other atmospheric parameters, such as aerosols or dust content, were available for this thesis it was desirable to find another way of conducting further investigations. These further investigations include the cause for the biases between the Adelaide predicted temperatures and the measured temperatures at the other sites (especially Riyadh), see section (10.3.1.1). MODTRAN software was used here to do part of this investigation and to find a clue to a possible explanation.

Two radiosonde profiles for one summer night and one-winter night for Riyadh are shown in figure (10.9 a, b) respectively. These profiles were chosen as representative of atmospheric conditions to be found in both seasons. They were used as inputs into MODTRAN. The reason of choosing this site is the common anomalistic features exhibited and the fact that data from this site caused the large biases. The figure shows the real atmospheric situations in different seasons. For example the winter profile (10.9 b) shows a temperature inversion starting from ground level to about 2 km above the ground.

Such low-level inversion types are common over many Saudi Arabia sites. The causes of these inversions are either the existence of warm air above cold ground, or because dust and pollution trapped in the higher atmospheric levels act as a lid for the air below. The former is most common on very cold clear winter nights, as the case of some winter nights in Riyadh. The latter is ordinarily found in polluted areas by the dust, smoke and larger aerosols. This type is commonly found over industrial cities in Saudi Arabia like Jeddah or in Riyadh at summer times.

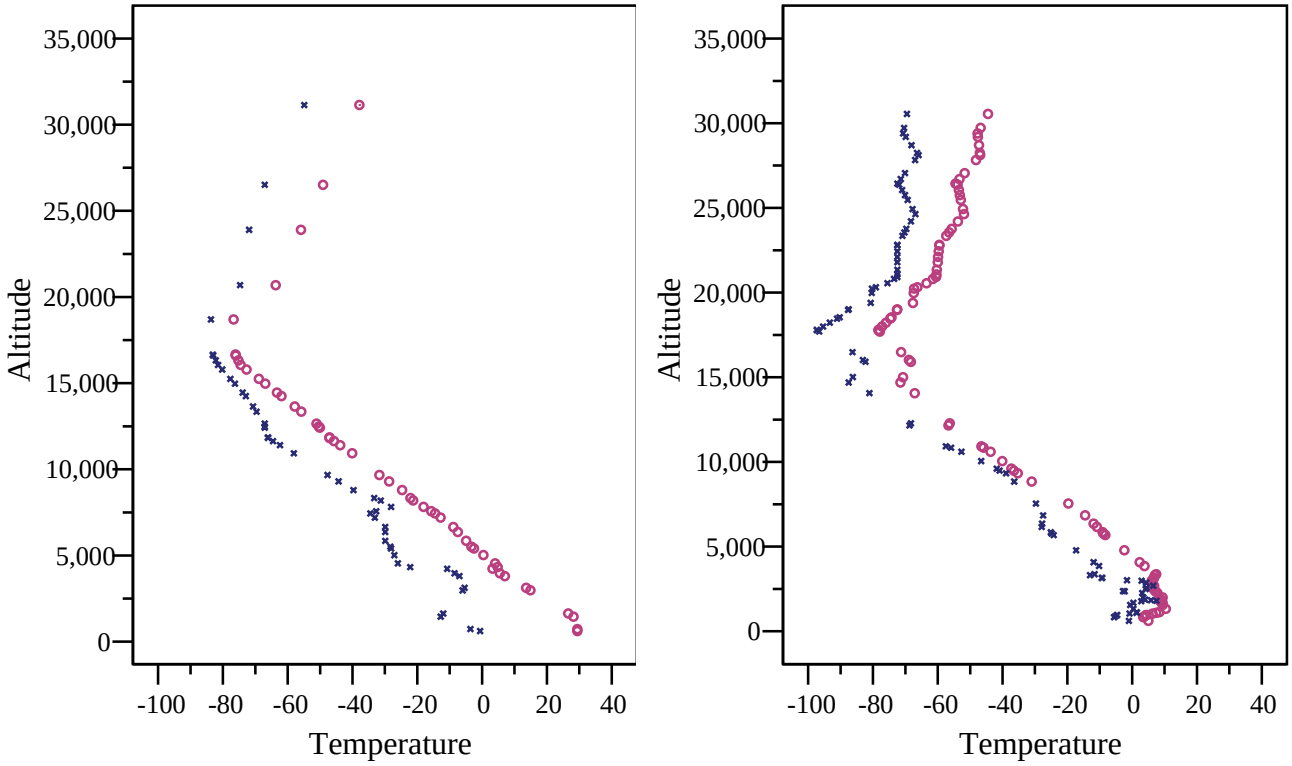

Figure 10. 9: Atmospheric profiles for air temperature (blue crosses) and dew point temperature (red circles) and altitude in m for (a) summer night- left- (13.06.2005) and (b) winter night-right-(19.12.2005) for the Riyadh site.

Carbon dioxide was set in MODTRAN to the value of 373 ppmv. Ozone and other minor atmospheric gases were set to the default values of the mid-latitude summer atmosphere found in MODTRAN. Other general inputs were similar to those used and described in chapter 6. For the selected winter profile, the measured sky temperature by the detector was -20.1 ^{o}C and the PWV was 1.9 mm. MODTRAN was then run using the desired inputs/outputs and the sky temperatures were calculated using the procedures detailed in section (6.3.3). With an urban aerosol profile (visibility of 23 km, a very clear winter night) the spectral distribution of this profile obtained by

MODTRAN is shown in figure (10.10). The integrated predicted sky temperature between the wavelengths of response of the detector was -17.5 ^{o}C, which is about 2.5 ^{o}C warmer than the measured value. If we account for the error in the measurements of the atmospheric parameters and sky temperatures this value looks reasonable.

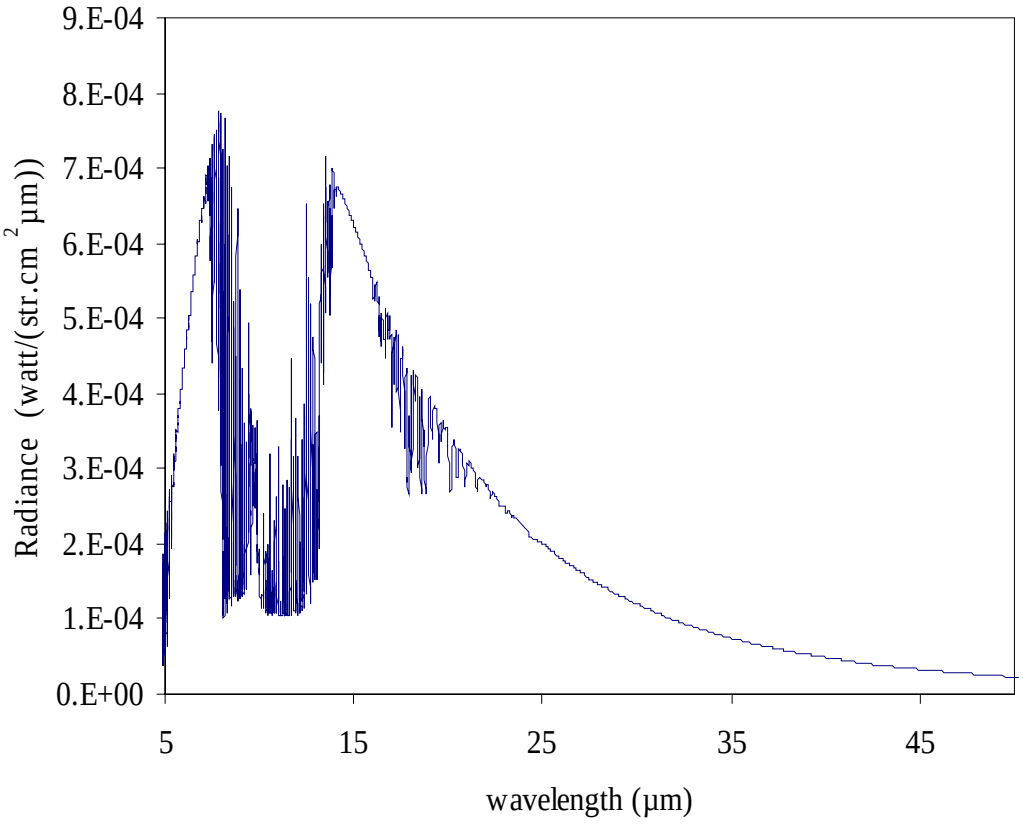

Figure 10. 10: MODTRAN output shows the spectral distribution of the Riyadh winter profile of (13.6.2005).

Following the same procedures for the summer profile, with a measured sky temperature of 9.66 ^{o}C and a PWV of 1.7 mm the MODTRAN predicted sky temperature was –3.57 ^{o}C, which is about 13 ^{o}C colder than the measured value. In order to investigate the cause of this difference, different tests were carried out. Since the effect of the two important parameters (atmospheric temperature and water content) were considered utilizing the real atmospheric profile, it was advantageous to seek other factors causing this difference. The influences of these factors are expected to be in the wavelength region between 8 µm to 14 µm (the atmospheric window). This is because the atmospheric emission outside this region is mainly due to water vapour which is

related to the air temperature, which already accounted for. One can see from figure (10.10) that outside this range the atmosphere is already radiating as a black body.

MODTRAN was then run by assigning different values of the carbon dioxide, aerosol type, background, visibility, and other available potentials found in MODTRAN. No major changes in the predicted sky temperature were found by changing the amount of carbon dioxide, the background or the available default aerosol types (e.g. urban, rural, and maritime). However, by setting up the visibility of the urban aerosol model to a certain value MODTRAN gave us a closer answer to the actual measured value. At the visibility of 1.5 km the MODTRAN predicted sky temperature was 7.8 ^{o}C, which is 2 ^{o}C warmer than the measured value.

Meteorological visibility refers to the transparency of air: in darkness, meteorological visibility is still the same as in the same air in daylight. Various weather stations report this as haze (dry) or mist (moist). Fog and smoke can reduce the visibility to near zero. The same can happen in a sandstorm in and near desert areas, or with forest fires.

Figure (10.11)[2] shows a typical example of who the sky looks like in some summer days in Riyadh. .

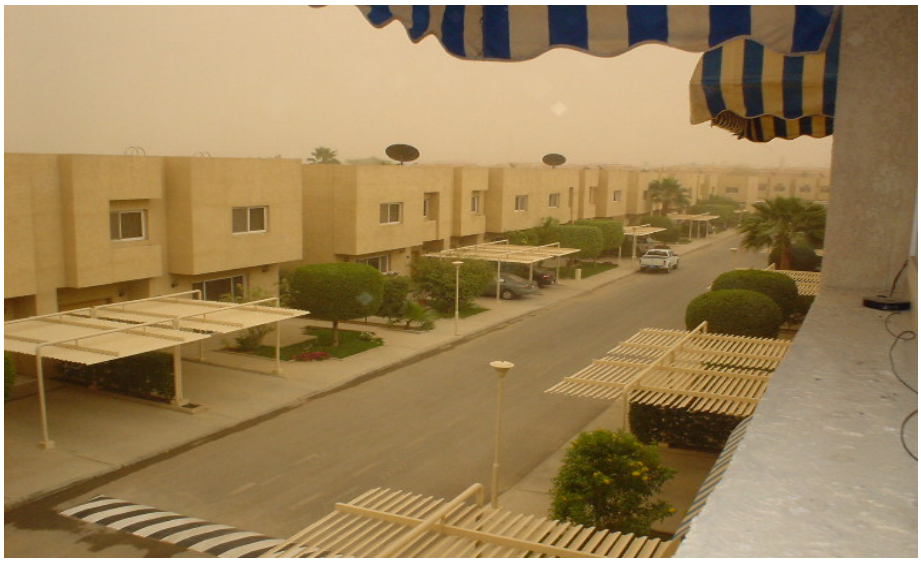

Figure 10. 11: The visibility on such polluted sky is greatly reduced by dust storm in Riyadh especially in summer times.

[2] *http://www.wunderground.com*

It is clear that the visibility factor, which is related to the presence of aerosols in the atmosphere, has an effect on the visible range of wavelengths. However, this effect may be extended to the IR part of the spectrum if the size of the aerosol particles becomes comparable with the IR wavelengths (see section 6.4.4.1). MODTRAN takes account of this, and has an aerosol size distribution to account for this effect.
Figure (10.12) shows the spectral distribution of the Riyadh summer atmospheric profile simulated by MODTRAN with a visibility of 1.5 km.

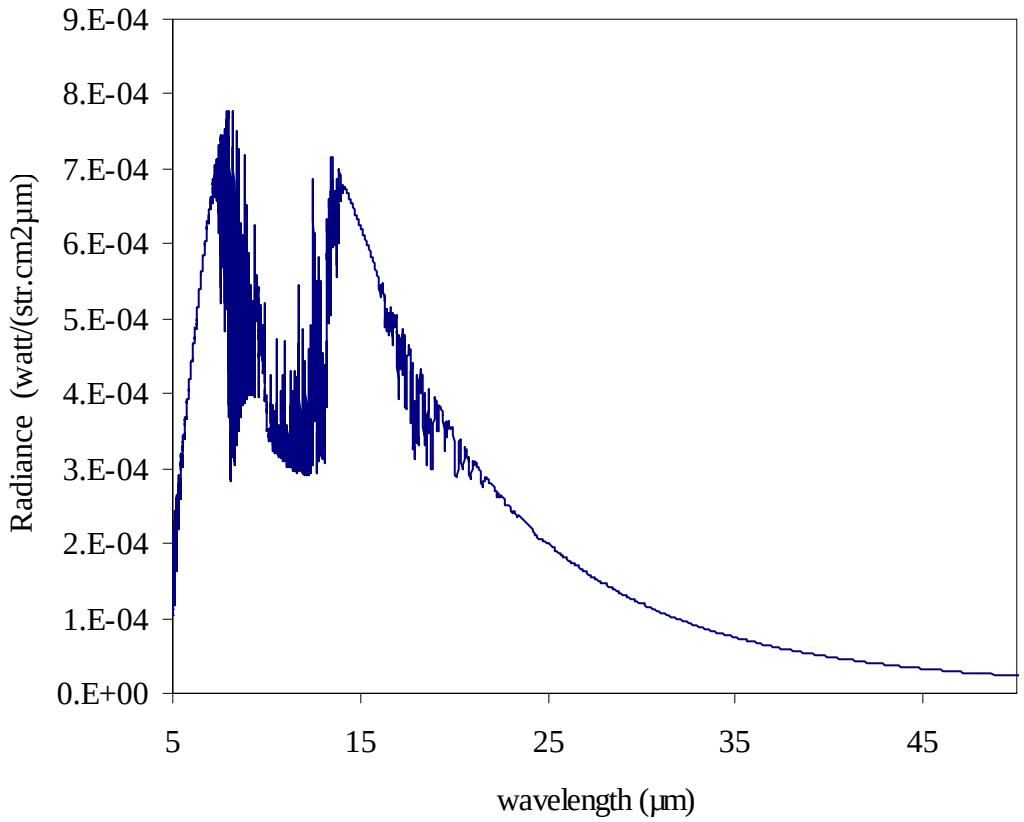

Figure 10. 12: MODTRAN output shows the spectral distribution of the Riyadh Summer profile of (19.12.2006).

The effect of emission of atmospheric water and other atmospheric gases outside the atmospheric window remains the same and the effect of the aerosols is evident in the portion of the atmospheric window of the spectral distribution when comparing figure (10.12) and (10.10). Moreover, the presence of larger sizes of aerosols, dust and smoke may work as a lid (similar to the effect of clouds), which causes more emission in this part of the spectrum. This value of the visibility may look rather low. However, in the atmospheric conditions found in most of the Saudi Arabian sites this may really be the case. As we mentioned above, Riyadh is the capital of the country, located in the desert

in which dust is found to hang in the atmosphere at most of the times, especially in summer. Also, it is considered as an industrial city where smoke and aerosols are always present.

The effect of aerosol, smoke and haze on the atmospheric radiation has been well studied and established. For example for Yakutsk in the former USSR, Evfimov(1951) found that the atmospheric radiation increases at the appearance of haze by about 31 % in a given month. He also found that in some individual cases, greater increases of the atmospheric radiation were observed when the formation of haze was accompanied by fog. In the same sense, smoke present near the Earth's surface was found to increase the atmospheric radiation by 15 to 80 % Berland (1948), Krasikov (1948) and Berland (1952).

Other suggestions to explain the deviation in the sky temperature from one site to another or at the same site in different seasons may be one of the following factors.

1. The altitude effect which may contribute to the bias of 2 ^{o}C between the Adelaide site and CLF. Although Riyadh is higher than Adelaide, this effect is not pronounced between these two sites.
2. Also, over an extreme range of temperatures such as those found in the Riyadh summer, the formula used to calculate the vapour pressure (equation (3.18)) may not be totally accurate.

Thus, the effect of air temperature, water content, local parameters such as those mentioned above and others related to the geography of the site, are some possible factors cause these differences in the sky temperatures. These factors can be accounted for and may explain the differences in the constants of the models proposed for each site (equations in table 10.3) and their difference from the unified model, equation (10.6).

10.3.2. Sites with 90o FOV Detectors

Data collected by detectors with 90^{o} FOV at four sites were studied in detail in chapters 4 and 8. The average statistics of the data from these are presented in table (10.2)

Figures (10.13) to (10.15) show the relationship between the sky temperatures and the screen level temperature, screen level vapour pressure and the PWV for the combined data The general pattern for the variations of the sky temperature with the three parameters is shown as groups of parallel lines having different sky temperatures for the same amount of the variable under consideration. This is similar to the shape of the

data from the three sites having 3^{o} FOV detectors. However, the general relationship is roughly linear over the whole range of values. This linearity is evident, although the scatter is large and the combined data are less correlated. This form of linearity follows our physical expectations, which suggest that an increase in any of these variables is accompanied by an increase in the sky temperature. Unlike the anomalies found in the previous subsection the screen level vapour pressure is positively correlated with the sky temperatures.

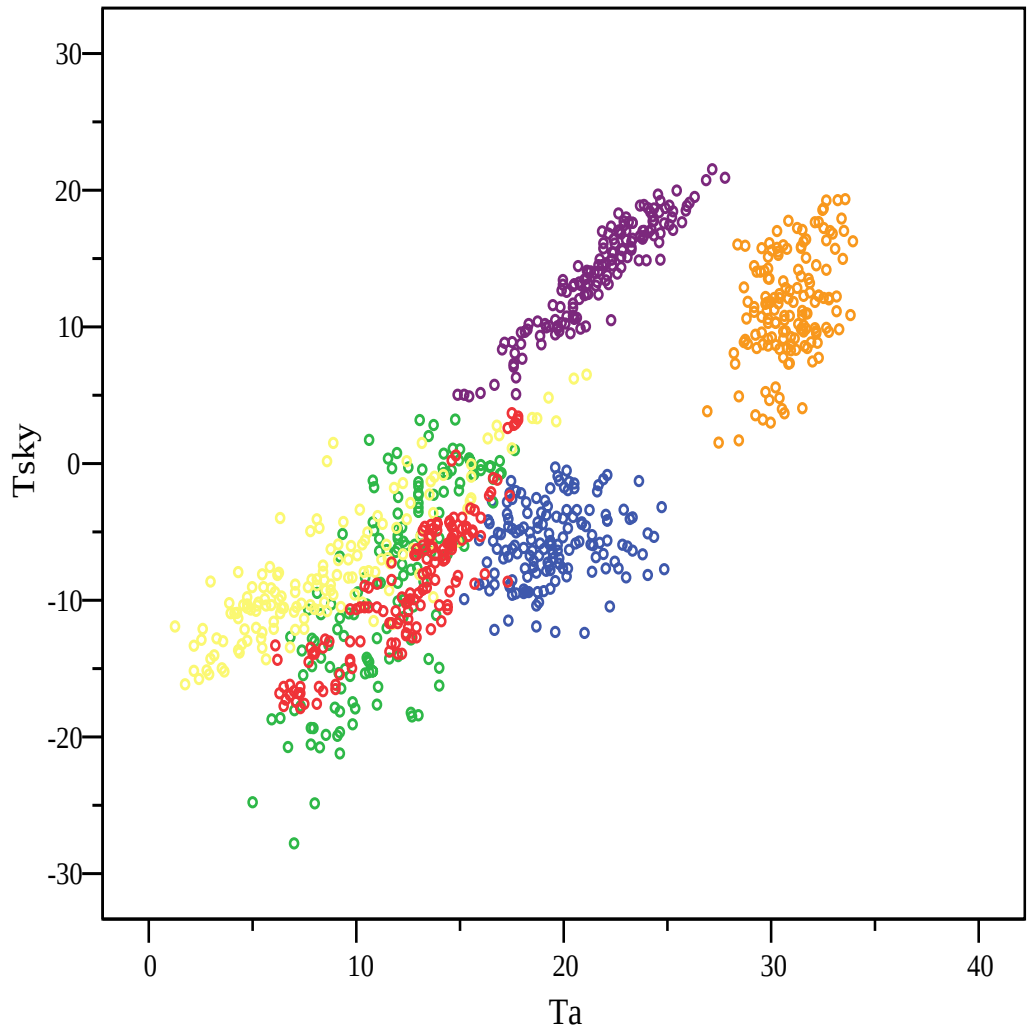

Figure 10. 13: Tsky vs Tair for four sites (90^{o}): Blue Abha summer, Green Abha winter, Orange Jeddah summer , Purple Jeddah winter Yellow Tabouk and Red Adelaide.

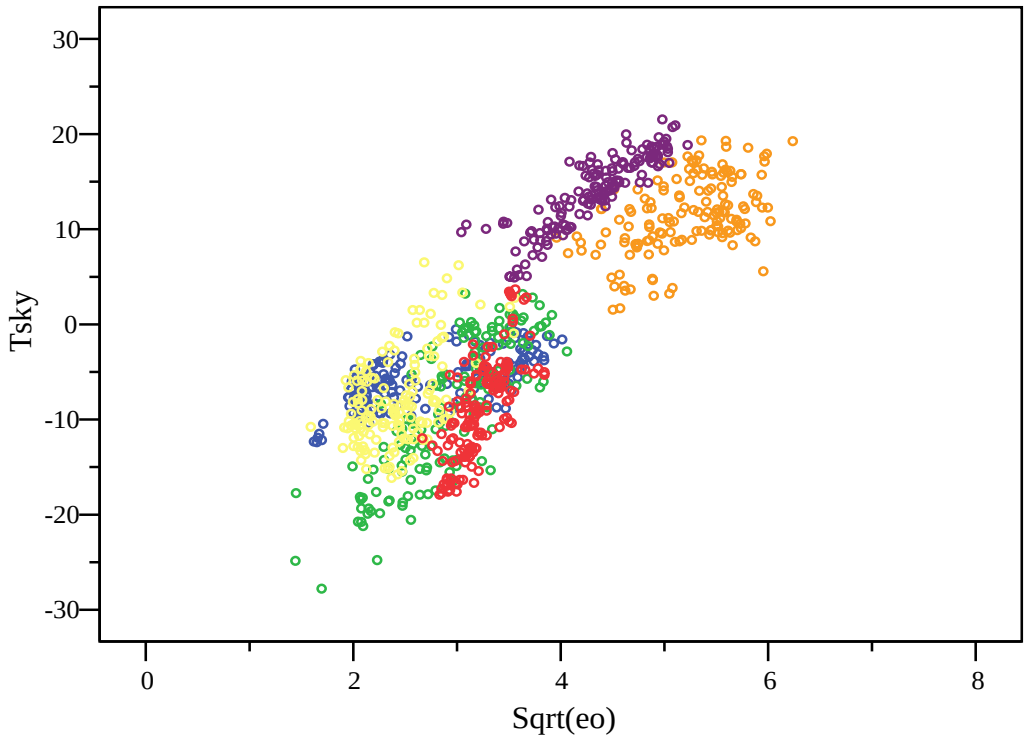

Figure 10. 14: Tsky vs Sqrt (eo) for four sites .Blue Abha summer, Green Abha winter, Orange Jeddah summer, vilot Jeddah winter Yellow Tabouk and Red Adelaide.

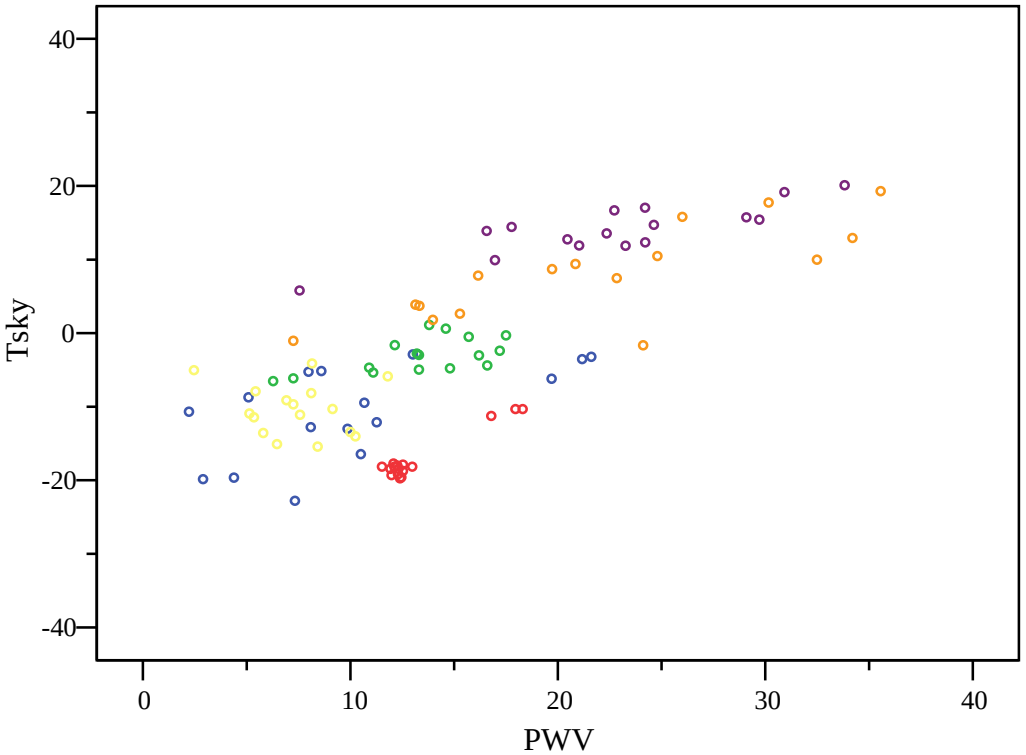

Figure 10. 15: Tsky vs PWV for four sites .Blue Abha summer, Green Abha winter, Orange Jeddah summer, Purple Jeddah winter Yellow Tabouk and Red Adelaide.

Tables (4.6), (4.3) and (8.2) show the proposed models for all sites having STD detectors with 90^o FOV. Those models were developed for each individual site. With the exception of rare occasions, these models were able to give an accurate fit to the measured data. A single model for the combined three sites in Saudi Arabia was also proposed.

Here we are trying to extend the model and the data range by the inclusion of data from the Adelaide site. Table (10.4) shows the simple and multiple regressions analyses for the data from all sites.

Both single variable and two variable formulae (equations 10.9- 10.13) are able to predict the sky temperature with reasonable accuracy, although they all show poorer correlation coefficients and higher values of RMSE in comparisons with a single site formulations presented in the chapters 4 and 8.

Figures (10.16) and (10.17) show the predicted versus measured sky temperature using the two variables model, equations (10.12) and (10.13) respectively.

Function	Regression Fit Equations	MBE ^oC	R^2	RMSE ^oC
Tsky(Tair)	$Tsky = -22.6 + 1.12Tair$ (10.9)	0.07	0.79	6.26
Tsky(PWV)	$Tsky = -27.54 + 1.25PWV$ (10.10)	0.12	0.73	7.3
Tsky(Sqrt(eo))	$Tsky = -33.1 + 8.6Sqrt(eo)$ (10.11)	0.03	0.73	6.9
Tsky (Sqrt(eo), Tair)	$Tsky = -30.7 + 4.12Sqrt(eo) + 0.78Tair$ (10.12)	0.02	0.83	5.5
Tsky (PWV, Tair)	$Tsky = -29.8 + 1.12PWV + 0.243Tair$ (10.13)	0.01	0.80	7.2

Table 10. 4: The formulation of the sky temperatures using the screen level temperature, the square root of the vapor pressure, and the PWV as single variable or two variables for the combined data from three sites having 90^o FOV detectors.

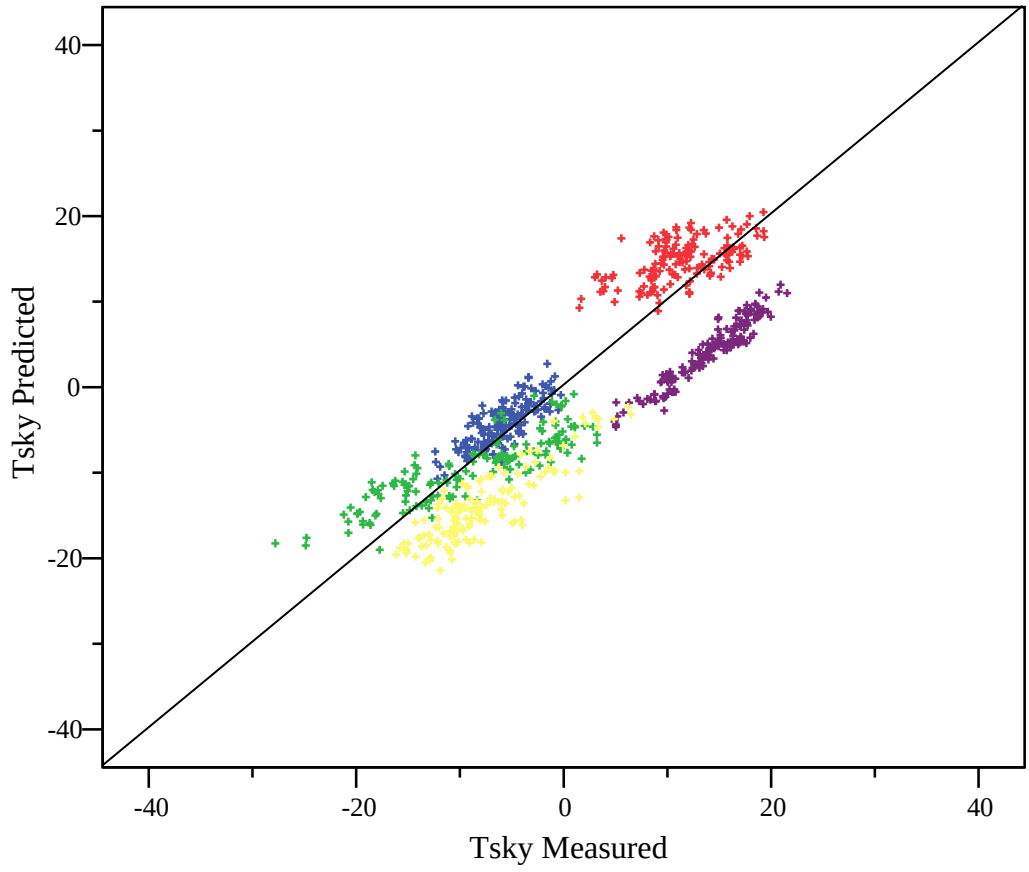

Figure 10. 16: Comparisons between measured and predicted (equation 10.12) sky temperature (in ^{o}C) for Abha; blue, Jeddah; Summer red, Jeddah winter; green, Adelaide; yellow and Tabouk; vilot. The straight line is a 1:1 line for reference.

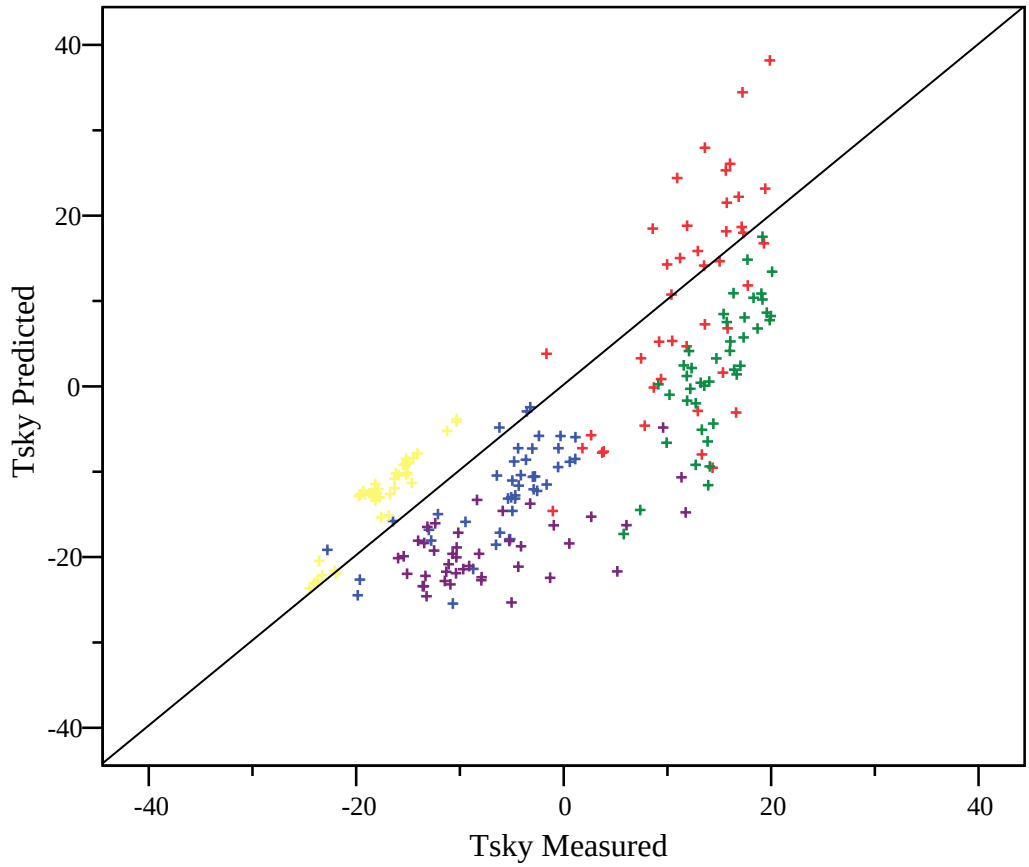

Figure 10. 17: Comparisons between predicted (equation 10.13) and measured sky temperatures (^{o}C) Abha; blue, Jeddah Summer red, Jeddah winter green; Adelaide; yellow and Tabouk; violet. The straight line is 1:1 line for reference.

With a closer look at the equations found in the table we notice the following:

- There are no major improvements in using the two variable models over those using a single parameter. The RMSE values of the predictions are not far from each other. For example, the maximum and minimum MBE values were 16 ^{o}C and -16 ^{o}C respectively using equation (10.9) compared to 14 ^{o}C and -18 ^{o}C respectively using equation (10.12).
- The slopes of equations (10.9) to (10.11), (single variable models) are higher than those obtained for a single site.
- The coefficient of the PWV in equation (10.13) was higher than expected while the coefficient of the Ta was lower than we expected. This suggests that there is some other local factor which is not yet accounted for in either model. Hence, the RMSE's are not far from each other.

Comparisons between equations presented in table (10.5) for 90^o FOV sites with those (equation (10.1) to equation (10.4)) for the 3^o FOV detectors shows the following:

1- There is a great similarity in the slope values of the air temperature and the PWV between (10.1) and (10.7) and equations (10.9) and (10.10). However, they all differ from each other in their intercept values. We expect warmer intercepts for 90^o FOV detectors which view larger zenith angles.
2- Apart from the difference in the intercept, the superimposed multiple regression fit equation (10.6), is similar to equation (10.12) using the same parameters, although they were produced from detectors with different FOV.

Two unified models using data from STD detectors with 90^o FOV from different sites were obtained without any complications. The first parameterizes the clear sky temperature as function of both screen level vapour pressure and air temperature. The second contains the PWV and the air temperature. Although having large MBEs and RMSEs, the ability of these models in predicting the measured data was reasonable. At a specific site, it is recommended to use an individual formula for accurate predictions.

CHAPTER ELEVEN

CONCLUSION

From the results presented in the previous chapters we can reach to the following conclusions.

The clear sky temperature (atmospheric radiation) mainly depends on the screen level temperature and the amount of water in the atmosphere, represented either by the screen level vapour pressure or by the PWV. The reason for the choice of the first parameter is that it is associated with strong dependence of the atmospheric radiation on the black-body emission law applied to the various atmospheric layers. The second parameter is generally needed, since atmospheric water vapour strongly absorbs the infrared radiation as a result of both infrared continuum and selective absorption by its vibro-rotational and rotational absorption bands centred at infrared wavelengths longer than 5 μm. That is, within the spectral range characterised by the most intense atmospheric emission.

Data used from six sites around the world enabled us to model the clear sky temperature using these two parameters with a high degree of accuracy. We found that

the dependence of the atmospheric radiation on these two variables for all the sites is consistent with what has been found previously in the literature. The dependence on those two parameters is different from one place to another and the degree of difference exhibited can be an impediment in producing a perfect general model for predicting atmospheric radiation

Two different groups of models were produced for each site. The first are those which use the screen level temperature and the PWV (PWV, Tair). The second are those which use the screen level temperature and the screen level water vapour pressure (Sqrt(eo),Tair). Due to the unavailability of the PWV data at the Auger site, only a model from the second group was developed. Generally, it was found that models using (PWV, Tair) gave better performance than those using the (Sqrt(eo),Tair). This is because the PWV accounts for the real amount of the water in the atmosphere. However, models using (Sqrt(eo),Tair) have advantages since they use easy-to-measure screen level variables.

For the purpose of detecting the presence of clouds, models which have screen level parameters ((Sqrt(eo),Tair)) were tested and shown to be reliable in finding clouds under different atmospheric conditions. For each site these models were checked against some clear sky models found in the literature.

Other physical local factors may also have some influence on the measured sky temperature and cause a deficiency in producing a very accurate model at single site or a reasonable global formulation for clear sky temperatures over different sites with extremely different screen and upper air conditions. Their effects on the sky temperature can be either major or minor depending on local circumanstances. These parameters can be divided into two groups. The first is related to the weather conditions at the time of measurements such as wind speed, dust, aerosols, smoke, air pressure etc. The second group, on the other hand, includes intrinsic site considerations such as the altitude and the geography of the site. The influence of some of these factors was confirmed theoretically using MODTRAN in chapters 6 and 10. However, actual measurements of such parameters are recommended and desirable for accurate estimations.

Seasonal variations as well as anomalous behaviour of the clear sky temperature were observed at the four Saudi sites. Data from both the Auger CLF and Adelaide sites have not revealed pronounced variations over the seasons nor any other anomalistic features like those found in Saudi sites. Moreover, CLF and Adelaide data have covered a wide

range of moderate atmospheric conditions and the latter employed a very large dataset to ensure that the resulting models are more reliable.

The uniqueness of the work of this thesis was in the effort toward finding a unified model in the data from all the sites. Those sites exhibited greatly differing atmospheric conditions. Although there were severe complications in achieving this goal and associated difficulties, a unified model was found which predicted the night time clear sky temperatures with reasonable accuracy. Individual models found for each site are more accurate, and are advisable to be used at the sites studied here, or at other sites having similar conditions. The results presented in chapter10 confirm the conclusions drawn above. There is little doubt that there are systematic differences between the data set due to the necessary non uniformity of methods of measurements or in the data treatment (see e.g. clear sky selection).

The zenith angle dependence of the clear sky temperature was also investigated experimentally using data from the Adelaide scanner. It was found that the sky temperature does vary with the zenith angle being coldest at the zenith from which it progressively increases as the viewing angle increases, until the temperature is close to the ground temperature at low elevation angles.

Most of the above discussions and the findings were supported theoretically using MODTRAN software, chapter 6. For example, the dependence of clear sky temperature on, air temperature, water vapour, zenith angle, the effect of aerosol and site altitude were all investigated using MODTRAN.